# EXPERIMENTAL AND COMPUTATIONAL STUDIES OF PROPERTIES OF THIN FILMS OF CADMIUM-TIN-OXIDE FOR MANUFACTURE OF MICRO-ELECTROMECHANICAL SYSTEMS AND FOR NOISE CONTROL

**BY**

**ONGWEN NICHOLAS OGADA**

**A THESIS SUBMITTED IN PARTIAL FULFILMENT OF THE REQUIREMENTS FOR THE DEGREE OF DOCTOR OF PHILOSOPHY IN PHYSICS**

**SCHOOL OF PHYSICAL AND BIOLOGICAL SCIENCES**

**MASENO UNIVERSITY**

## DECLARATION

This thesis is my original work, and has not been presented in any institution of higher learning that I know of, for the award of a degree certificate.

ONGWEN NICHOLAS OGADA

PHD/SC/00022/2019

Signature……..…… Date……..……

This thesis has been submitted for examination with our approval as the supervisors:

1. Dr. Erick Ogam,

   Laboratory of Mechanics and Acoustics,

   UMR 7031 AMU – CNRS,

   Marseille – France.

Signature…… Date……...…….……..

2. Dr. Henry Otunga,

   Department of Physics and Materials Science,

   Maseno University,

   P. O. Box 333 – 40105,

   Maseno – Kenya.

   Signature……..... Date…….……

## ACKNOWLEDGEMENT

My foremost sincere gratitude goes to the Almighty God for giving me this opportunity (life, health, mind, and strength) to come up with this work. He has guided me to this far I have reached, providing me with knowledge.

I acknowledge my supervisors, led by Dr. Erick Ogam, whose timely advice and continued support assisted immensely in the progress and completion of this work. His vast knowledge, network, and experience in research work helped in the conceptualization as well as resource mobilization (human and financial) to ensure the success of the study. He always worked tirelessly to ensure that this study was carried out successfully, by giving me directions (both in the experimental and the computational aspect of the work) and making corrections in the work, up to the final draft.

Special thanks go to Dr. Henry Otunga for being the second supervisor for the study and also for providing me with supervision on the computational study, including connecting me to the Center for High Performance Computing (CHPC in Cape Town, South Africa), which enabled the computations in this study to be carried out successfully. He was always with me whenever I needed his assistance.

Sincere gratitude goes to my loving wife, Celestine Achieng, who has been giving me constant encouragement, moral support, care, and a conducive study environment in order to come up with this work. She was supportive throughout the period of my study.

I will not forget the assistance that I received from the laboratory technologist in the University of Nairobi, Mr. Boniface Muthoka. He gave me all the experimental experience that I needed in order to carry out the study successfully. He showed me how to use the equipment that I needed for the research (spray pyrolysis and surface profiler).

## DEDICATION

The Almighty God

My loving and caring wife, Celestine Achieng

## ABSTRACT

The recent advancements in electronics have stimulated the high demand for semiconductor substrates for printing electronic circuits, some of which are used in the Micro-Electromechanical Systems (MEMS) devices. The most commonly utilized substrate for the printing of these devices is silicon (Si), which is preferred because, compared to the other substrates like silicon nitride and gallium arsenide, it: has better electrical, mechanical, and thermal properties that are desirable for the production of MEMS, and is also readily available. Despite the advantages above, Si has many drawbacks, including rarely occurring as a pure element, as well as being brittle, which call for alternative substrates such as cadmium-tin-oxide (CTO), whose thin films (TFs) have been studied and proved to possess excellent optical and electrical properties. However, the acoustical, mechanical, and thermal properties of CTO have not been explored. This study employed both experimental and computational techniques to study the properties of CTO as a possible substitute to Si in the manufacture of MEMS, and also as a possible laminate on window panes for noise control, with the main aim of determining its structural, acoustical, mechanical, and thermal properties. The specific objectives of the study were: (i) to investigate the effect of concentration of cadmium on the structural properties of CTO; (ii) to develop a simpler method that applies stress and strain in calculating elastic constants of materials; (iii) to investigate the effect of concentration of cadmium on the acoustical, mechanical, and thermal properties of CTO; and (iv) to investigate the effect of pressure on the mechanical and thermal properties of CTO. The TFs of CTO were prepared by dissolving cadmium chloride and tin II chloride separately in distilled water to form each solution, after which they were mixed at different ratios by volume. The final solutions were subsequently sprayed onto the pre-heated microscope glass substrates by spray pyrolysis at a temperature of 450 °C to form the TFs. The X-Ray diffraction measurements of the prepared samples were taken using Expert Pro, while their chemical compositions were measured using X-Ray Fluorescence. The *ab initio* calculations were done using density functional theory with PBESOL functionals as implemented in the Q*uantum Espresso* code. A new and simpler method that employs stress and strain was developed for calculating the mechanical properties, where we modified the complex matrices for the existing energy-strain method. The simulation of acoustic transmission loss was done using Maple software. The outcome of the study showed that the properties of CTO are very sensitive to the number of cadmium atoms. The optimum properties obtained were: density of 7.636 g/cm$^3$, bulk modulus of 149.1 GPa, shear modulus of 53.2 GPa, Young's modulus of 142.7 GPa, Vickers hardness of 3.757 GPa, Poisson's ratio of 0.367, Pugh's ratio of 3.422, Debye temperature of 377.7 K, melting temperature of 2295.1 K, Debye vibrational energy of 8.557 x $10^{-2}$ Ry/cell, Gibbs free energy of 0.1584 Ry/cell, entropy of 7.984 x $10^{-4}$ Ry/cell/K, specific heat at constant volume of 2.659 x $10^{-4}$ Ry/cell/K, and acoustic transmission loss of 136.4 dB. Due to its comparable mechanical and thermal properties to those of Si as observed in this study, CTO can substitute Si in the manufacture of most MEMS. Its soft and ductile nature is ideal for the manufacture of flexible MEMS such as biomedical MEMS and microbolometers. The high acoustic transmission loss is good for noise reduction on window panes in houses near noisy places such as those close to airports.

## TABLE OF CONTENTS

## LIST OF ABBREVIATIONS AND ACRONYMS

| | |
|---|---|
| bioMEMS | Biomedical Microelectromechanical Systems |
| BZ | Brillouin Zone |
| CTO | Cadmium-Tin-Oxide |
| DFT | Density Functional Theory |
| Ecut | Kinetic energy cut-off |
| Ecutrho | Charge density cut-off |
| EFM | Equivalent Fluid Model |
| FWHM | Full Width at Half Maximum |
| GGA | Generalized Gradient Approximation |
| IB | Integral Breadth |
| LAPW + lo | Linear Augmented Plane-Waves plus local orbitals |
| LAPW | Linear Augmented Plane-Waves |
| LB | Langmuir-Blodgett |
| LCD | Liquid Crystal Display |
| LDA | Local Density Approximation |
| MEMS | Micro-Electromechanical Systems |
| PAW | Projector Augmented Wave |
| PBESOL | Perdew-Burke-Ernzerhof functional for SOLids |
| PP | Pseudopotential |
| QE | Quantum Espresso |
| QHA | Quasi Harmonic Approximation |
| SCF | Self-Consistent Function |

| | |
|---|---|
| SEM | Scanning Electron Microscope |
| SPT | Spray Pyrolysis Technique |
| TCO | Transparent Conducting Oxide |
| TF | Thin Film |
| UV-Vis | Ultraviolet-Visible |
| Vc-relax | Variable-cell relaxation |
| XC | Exchange Correlation |
| XRD | X-Ray Diffraction |
| XRF | X-Ray Fluorescence |

## LIST OF CHEMICAL SYMBOLS

| | |
|---|---|
| Cd | Cadmium |
| $CdCl_2 \cdot H_2O$ | Cadmium chloride monohydrate |
| $Cd_2SnO_4$ | Cadmium stannate |
| Ga-As | Gallium arsenide |
| HCl | Hydrochloric acid |
| $HNO_3$ | Nitric (V) acid |
| La | Lanthanum |
| O | Oxygen |
| Si | Silicon |
| SiC | Silicon carbide |
| $Si_3N_4$ | Silicon nitride |
| Sn | Tin |
| $SnCl_2 \cdot 2H_2O$ | Tin II chloride dihydrate |
| $SnO_2$ | Tin IV oxide |

## LIST OF SYMBOLS

| | |
|---|---|
| $\alpha$ | Tortuosity |
| $\beta$ | Compressibility modulus of the fluid |
| $\gamma$ | Specific heat ratio of the gas |
| $\mu$ | Poisson's ratio |
| $\tau$ | Transmission loss |
| $\theta_D$ | Debye temperature |
| A | Elastic anisotropy |
| B | Bulk modulus |
| $c_V$ | Specific heat capacity at constant volume |
| $\mathfrak{D}_1$ | Rigidity of the plate |
| dB | Decibel |
| E | Young's modulus |
| $E_{vib}$ | Debye vibrational energy |
| F | Gibbs free energy |
| $f_c$ | Cut-off frequency |
| G | Shear modulus |
| $H_V$ | Vickers hardness |
| $k_1$ | Wave number in the medium |
| $k_f$ | Compressibility of the gas saturating the pores |
| $m_p$ | Mass of the plate |
| n | Pugh's ratio |
| $P^C$ | Cauchy pressure |

| | |
|---|---|
| S | Entropy |
| $T_m$ | Melting temperature |
| $w_1$ | Displacement of the wave from the mean position as a function of the boundary of the plate |

## LIST OF TABLES

## LIST OF FIGURES

## LIST OF APPENDICES

# CHAPTER ONE
# INTRODUCTION

## 1.1 Background of the study

Thin film (TF) technology is a very fast-growing field, with a lot of research on different materials being investigated for different applications. One of the currently researched areas includes the incorporation of the TF technology into the Micro-Electromechanical Systems (MEMS) device manufacture and design, which has been identified as one of the promising technologies for the 21st century (Prime, 2002). MEMS technology combines the traditional semiconductor electronics with microelectronics, and the MEMS systems are able to sense, control, and actuate on very small scales (within micrometres). Figure 1.1 shows the general composition of MEMS.

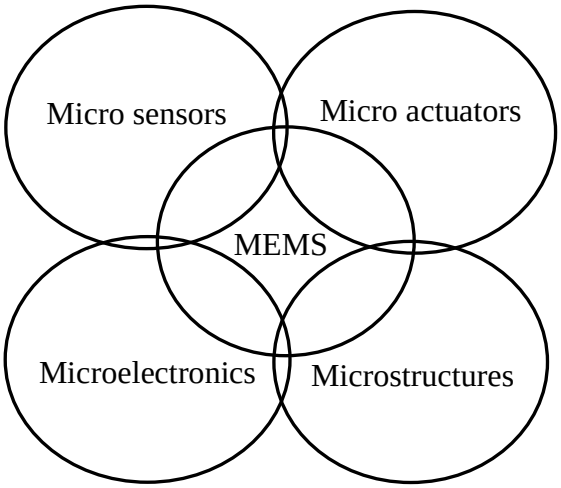


***Figure 1.1: General composition of MEMS***

The MEMS technologies are used to fabricate tiny devices in the order of millimetres or even micrometres in size, which are used by scientists in building minute materials, which could not be possible or too expensive to be manufactured using other technologies. MEMS devices are found in various systems such as in automotive, communication, defence, electronics, and medical. MEMS have existed since 1950s, and have slowly evolved into day-to-day life devices. Some of the MEMS commercial products in the market today include accelerometers (in controlling pressure sensors), in inkjet printer heads, and in projection screens, as well as in airbag deployment in automobiles. The ultimate potentials for MEMS devices lie in their utilization in telecommunications, biomedical, and process data control areas (Srinivasa et al., 2012).

The dominant substrate material that is currently being utilized in the fabrication of MEMS devices is silicon (Si) (Pratap & Arunkumar, 2006). This is because Si: is abundant; is relatively cheap and can be processed to unparalleled purity; possesses high definition; is mass produced; and photolithography is ideal for reproducing Si device geometries at high levels of MEMS precision. Moreover, Si possesses the desirable properties (electrical, mechanical, and thermal) that are ideal for the manufacture of MEMS devices (Hull, 1999). Other crystalline semiconductors such as silicon nitride ($Si_3N_4$), silicon carbide (SiC), gallium arsenide (Ga-As), and diamond, are also being utilized as substrate materials because they have comparable intrinsic properties to Si, although Si stands out from them because when exposed to steam, it easily oxidizes to form a surface layer of silicon IV oxide, which is chemically inert and also electrically insulating (Prime, 2002).

Moreover, Si has virtually no hysteresis (perfect Hookean material) and hence, almost no energy dissipation. This makes Si MEMS very reliable for the highly repeatable motions that they undergo, since they suffer extremely little wear and tear, and they can be used for billions to trillions of cycles before breaking (Dutta & Datta, 2010). Si (111) is preferred to the other crystallographic orientations because most of the mechanical properties are isotropic on it. Some of the properties of Si (electrical, mechanical, and thermal) are listed in table 1.1 (Hull, 1999) (Auciello et al., 2008) (Finot, Passian, & Thundat, 2008) (Hopcroft, Nix, & Kenny, 2010) (Keesom & Seidel, 1959) (Yang & Jiang, 2005).

Despite the advantages mentioned, Si has its own drawbacks as a substrate for the manufacture of MEMS devices. Firstly, it rarely occurs as a pure element, implying that it has to be purified before use, a process that is not only tedious, but also expensive; secondly, it is not flexible; and lastly, it is brittle, implying that Si substrates cannot be made very thin (less than 1 mm thick) (Weast, 1984). Moreover, Si is becoming less attractive as a substrate for the manufacture of most MEMS devices due to its narrower band gap as well as its loss of mechanical reliability in harsh environmental conditions such as at high temperatures of above 500 $^{o}$C (Cimalla, Pezoldt, & Ambacher, 2007) (Gerberich, Stauffer, Beaber, & Tymiak, 2012). These harsh-environment MEMS

include sensors and actuators such as those in the oil sector, and combustion processes. The main advantages of micro components compared to the conventional macro components include their higher reliability, affordability, as well as their ability to incorporate more complex functions (Varadan, 2003).

Silicon carbide (SiC) is an excellent wide band gap semiconductor with better mechanical, chemical, and thermal stability. It has already been explored as a substrate material for MEMS. Moreover, it has already been incorporated into the Si micromachining technology (Cimalla et al., 2007). The much higher Youngs modulus of SiC of 410-422 GPa (Messaoud et al., 2019) (Reddy, 2007) implies that it can maintain a linear relationship between the applied load and the induced deformation compared to Si, which has an effective Youngs modulus of only 130 GPa (Hopcroft et al., 2010). Moreover, SiC has a much larger ratio of Young's modulus to density (about 127) compared to that of Si (about 56), hence making beam structures to have greater resonant frequencies and better quality factors (Coakley, Splett, & Janezic, 2003). This property makes micromechanical resonators advantageous for frequency filtering in high-speed communication transceivers.

***Table 1.1: Some of the electrical, mechanical and thermal properties of silicon***

| **Property** | **Value** | **Unit** |
|---|---|---|
| **a) Electrical** | | |
| Electrical conductivity | $1 \times 10^3$ | S/m |
| Electron mobility | 1,400 | $cm^3/V/s$ |
| Electrical resistivity | $1.0 \times 10^{-6}$ | Ω-cm |
| Band gap (indirect) | 1.2 | eV |
| **b) Mechanical** | | |
| Young's modulus | 130-169 | GPa |
| Bulk modulus | 80 | GPa |
| Density | 2,330 | $kg/m^3$ |
| Poison's ratio | 0.26 (Si (1 1 1)) | |
| **c) Thermal** | | |
| Melting temperature | 1,687 | K |
| Specific heat | 0.7 | J/kg/K |
| Thermal conductivity | 148 | W/m/K |
| Linear thermal expansion | $2.6 \times 10^{-6}$ | $K^{-1}$ |
| Debye temperature | 636 | K |

Downhole pressure sensors and diesel engines in in-cylinder pressure sensor movement applications operate under high pressure regions of above 0.3 GPa. However, among the major shortcomings of SiC as a MEMS material is it brittleness, just like Si. It is therefore not suitable for manufacture of flexible MEMS such as sensors, micro fluidic components, and biomedical MEMS (bioMEMS). Previous studies have shown that flexible substrates are sensitive to temperature and therefore, only low-temperature materials such as polymers are currently being utilized in such MEMS (Tu, 2014).

The rapid advancement of TF growth techniques has sparked academic and industrial research on the development, production, and testing of TF-based products (Mariana, Rodrigo, Marcos, & Homero, 2012). In addition to lower cost and better performance, the use of TFs in place of the traditional bulk semiconductor materials enables the manufacture of electronic devices with smaller volumes, lower weights, and greater flexibility. The investigation of wide band gap semiconductor materials to replace Si as the base material in the manufacture of these devices is receiving a lot of attention at the same time that there is a trend in the shrinking of electromechanical devices.

The use of TF materials for MEMS device applications has however not extensively been researched on, despite the numerous advantages that TFs offer such as dielectric functions, encapsulation, and anti-stiction surfaces in MEMS devices. A good example is the use of TFs to create membranes with the desired properties for microphones, opto-acoustic modulators, and cantilevers (Lazerand & Lishan, 2014). The few TF materials that have been utilized in MEMS include: silicon nitride ($Si_3N_4$) for capacitive switches (Koutsoureli et al., 2017), titanium nitride for MEMS shape memory alloys (Yongqing, Hejun, Weimin, Sam, & Min, 2010), and SiC in sensors (Mariana et al., 2012).

***Table 1.2: Some of the electrical properties of cadmium-tin-oxide thin films***

| **Property** | **Value** | **Unit** | **Reference** |
|---|---|---|---|
| Electrical conductivity | 1,666.67 | S/m | Krishna et al., 2010 |
| Electron mobility | 100 | $cm^2/V/s$ | Bhuvaneswari & Velusamy, 2013 |
| Electrical resistivity | $1.19 \times 10^{-4}$ | Ω-cm | Barbara, Castanedo, & Zelaya-Angel, 2016 |
| Band gap | 3.3 | eV | Zhu et al., 2021 |

Cadmium-tin-oxide (CTO), also known as cadmium stannate ($Cd_2SnO_4$), has emerged as an n-type semiconductor with excellent optical and electrical properties. Some of the electrical properties of CTO are shown in table 1.2. Due to its wide band gap of 2.9-4.6 eV, high optical transmittance in the Ultraviolet-Visible (UV-Vis) spectrum of up to 98%, and excellent electrical properties comparable to those of Si, the TFs of CTO have found wide applications as transparent conducting oxides (TCOs) in the front panel of TF solar cells, liquid crystal display (LCD) screens, and smartphone touchscreens.

Windows can be described as the 'eyes' of buildings, since they allow light to enter the buildings as well as allowing the individuals inside the buildings to view the outside. External noise is becoming more and more of a nuisance by the day to the individuals inside the buildings, especially in the cities where a lot of economic activities that produce a lot of low frequency sound are carried out, as well as in those buildings situated near airports. Moreover, modern buildings have large windows that are covered with glass. Therefore, sound insulation properties of the window panes is increasingly becoming a critical factor to consider when constructing buildings. Due to the high optical transparency of CTO in the UV-Vis spectral range that has been considered for use in LCDs (Ali, Mohamed, Wakkad, & Hasaneen 2009), it is a possible candidate as a laminate on window panes, which can attenuate sound without compromising the transmission of light into and out of buildings.

The acoustical, mechanical, and thermal properties of CTO have not been explored extensively however, although they equally play a very vital role in the functioning of MEMS substrates as well as possible application as a laminate on window panes for noise control. The experimental attempts to mechanically characterize CTO have come up with just bits of information. For instance, Diliegros-Godines, Flores-Ruiz, Castanedo-Pérez, Torres-Delgado, & Broitman (2018), who studied the mechanical and tribological bulk properties of CTO prepared by the Sol-gel, found out a Young's modulus of 88.90 GPa. However, it is worthwhile to note that the nanoindentation method that was employed in the study relies heavily on the axis of the sample that is in contact with the nano indenter, and if care is not taken, one may end up with the axial elastic moduli instead of the global elastic modulus of the material.

In an attempt to provide an alternative MEMS substrate to Si and SiC, as well as to find an acoustic attenuating laminate on window panes, we undertook both experimental and computational studies of the structural properties (XRD and chemical composition); mechanical properties (bulk modulus (B), shear modulus (G), Young's modulus (E), Poisson's ratio ($\mu$), Vickers hardness ($H_V$), Pugh's ratio (n), Cauchy pressure ($P^C$), and elastic anisotropy (A)); thermal properties (Debye temperature ($\theta_D$), melting temperature ($T_m$), Debye vibrational energy ($E_{vib}$), Gibb's free energy (F), entropy (S), and specific heat capacity at constant volume($c_v$)), and acoustical properties (acoustic transmission loss) of TFs of CTO, a wide band gap semiconductor, which is a highly attractive candidate as a substrate in the manufacture of MEMS sensors and actuators, and for noise control. To the best of our knowledge, the acoustical, mechanical (other than the Young's modulus reported by Diliegros-Godines et al., 2018) as well as thermal properties of CTO, have not been documented.

The experimental study in this work involved the determination of the chemical composition as well as the crystal structures of the CTO samples from XRD, while the computational study involved simulation using density functional theory (DFT) as implemented in the *Quantum Espresso* (QE) code (Giannozzi et al., 2017) in order to determine the mechanical and thermal properties of the CTO samples at zero GPa pressure, and as functions of the applied pressure. The calculations were made possible by use of the generalized gradient approximation (GGA). Perdew-Burke-Ernzerhof functional for SOLids (PBESOL) functionals. The study of the acoustical properties involved the use of Kirchoff-Love theory of plates. A new and simpler method that applies stress-strain relationship was developed and utilized in calculating the mechanical properties of CTO. In order to demonstrate the effectiveness of the method, we also calculated the mechanical properties of Si and SiC, two materials whose mechanical and thermal properties are known, and are also extensively being utilized in the manufacture of most MEMS. The calculated values of the mechanical properties of the two materials (Si and SiC) were compared with those that are available in the literature. The Kirchoff-Love theory of plates (Love, 1888) requires the density of the material as well as the elastic constants as inputs. Both the density and elastic constants of CTO were determined in this study for the first time.

## 1.2 Statement of the problem

The most common and widely known (and utilized) substrate material for the fabrication of MEMS devices is Si. This is because Si, compared to the other semiconductors like SiC, $Si_3N_4$, Ga-As, and diamond, has electrical and mechanical properties that are desirable for the fabrication of most MEMS. Si is impervious to fatigue, and also can be processed to unparalleled purity for better transport of charge carriers, besides there being available and well-developed surface micromachining technologies for its processing. Moreover, Si is readily available, and also relatively cheaper than the other semiconductors that are also being utilized in the fabrication of MEMS. However, it has the existing drawbacks, which include rarely occurring naturally as a pure element, and being non-flexible. The relatively low Young's modulus of Si of 130-190 GPa also makes it not suitable for use in the fabrication of mechanical sensors. The above drawbacks limit its commercial deployment. SiC on the other hand, could be an ideal substrate for MEMS that operate under harsh environmental conditions such as those in the oil industry, owing to its much larger Young's modulus of above 400 GPa, and much higher Vickers hardness of 32 GPa compared to that of Si at 10 GPa, had it not been brittle also, just like Si. To produce a pure, optically transparent and flexible semiconductor with higher Young's modulus, explorative research is ongoing to identify alternative ductile substrate materials to Si. TFs of CTO are potential candidates as substrates for the manufacture of MEMS devices due to their already explored excellent electrical and optical properties. Moreover, due to the constant exposure to noise pollution by people living in noisy places such as those near airports, TFs of CTO have become a prime candidate as a laminate on the window panes for noise control, owing to its high optical transparency in the UV-Vis spectrum.

## 1.3 Objectives of the study

### 1.3.1 Main objective

The main objective of the study was to employ both experimental and computational techniques in order to study the structural, acoustical, mechanical, and thermal properties of the thin films of cadmium-tin-oxide at zero pressure and as functions of the applied pressure, and then relate them to applications as a substrate for the manufacture of Micro-Electromechanical systems devices and also for noise control as a laminate on window panes.

### 1.3.2 Specific objectives

The specific objectives of the study were:

1. To investigate the effect of concentration of cadmium on the structural properties (crystal structure, crystallite size, and chemical composition) of thin films of cadmium-tin-oxide.
2. To develop a simpler computational technique that applies stress and strain in calculating elastic constants of materials.
3. To investigate the effect of concentration of cadmium on the acoustical, mechanical, and thermal properties of thin films of cadmium-tin-oxide.
4. To investigate the effect of the applied pressure on the mechanical and thermal properties of thin films of cadmium-tin-oxide.

## 1.4 Null hypothesis

TFs of CTO possess desirable mechanical properties (bulk modulus, shear modulus, Young's modulus, Poisson's ratio, Pugh's ratio, Vickers hardness, Cauchy pressure, and elastic anisotropy), thermal properties (Debye temperature, melting temperature, Debye vibrational energy, Gibb's free energy, entropy, and specific heat capacity at constant volume), and acoustical properties (acoustic transmission loss), which can find good use as a substrate for manufacture of MEMS devices, and as a laminate on window panes for noise control.

## 1.5 Justification of the study

Electronics are of paramount importance to our day-to-day lives. This is because it has enabled the development and printing of electronic circuits, which are found almost everywhere, from communication in radiation actuators and radio frequency MEMS, to entertainment in high-definition televisions. Most of the current MEMS devices are fabricated on Si as the substrate. This is because Si has the desirable electrical, mechanical and thermal properties that are ideal for the fabrication of most MEMS devices. Moreover, fabrication technologies for the manufacture of MEMS devices such as micromachining and bulk machining are well developed for Si. The mechanical properties determine how strong materials are, and play a crucial part in many aspects, including resistance to shape change, shear, abrasion and scratch, as well as ductility. The thermal properties on the other hand, are related to the properties of a material such as melting temperature, specific heat capacity, thermal expansion, and thermal conductivity, which should be considered when designing MEMS that operate under harsh environmental conditions such as in high temperature and pressure. Such MEMS include sensors and actuators for oil sector and combustion processes.

The above-mentioned drawbacks of Si (rarely occurring as pure element, brittleness, rigidity, narrow band gap, and loss of mechanical reliability in harsh environmental conditions such as at high temperatures of above 500 $^{o}$C) call for relatively pure semiconductors that are not only easily foldable (ductile), but also have better mechanical and thermal properties. CTO being a semiconductor and whose pure TFs can be deposited at desired thicknesses and at a relatively cheaper cost, provides an opportunity of obtaining an alternative foldable material for use as a substrate in the fabrication of MEMS devices, especially those in the medical field. However, not much information is available in the literature about the properties of CTO apart from its optical. The high optical transparency of CTO is ideal for its application as a laminate on window panes for noise control. The physical properties of CTO such as density, and the mechanical and thermal properties (such as melting and boiling temperatures) were not available in the literature at the time of carrying out this study. Apart from determining the acoustical, mechanical and thermal properties of CTO, the ab initio calculation was also used to determine the density of CTO for the first time.

## 1.6 Significance of the study

TFs of CTO have been tested and proved to possess very good optical and electrical properties. Moreover, CTO has also been analysed and found to be an n-type semiconductor. The study of its acoustical, mechanical, and thermal properties in this study provides an opportunity of obtaining an alternative semiconductor material to Si as a substrate for fabrication of flexible MEMS such as: nanoscale imaging, sound transducers, flexible displays, accelerometers, microbridges, drug delivery analysis, molecular assembly, tissue engineering, biosensor development, and genomics and proteomics; and also as an acoustic laminate on window panes for noise control in building that are situated in places that suffer from noise, owing to its optical transparency in the UV-Vis wavelength range.

## 1.7 Assumptions of the study

In the study of the acoustic transmission loss through the double and triple-glazed window panes, there is the possibility of multiple reflections of the acoustic wave between the panes, which can interfere with the results. However, when a wave is reflected, its amplitude is attenuated at each reflection, and it becomes smaller and smaller at each subsequent reflection. Thus, we only considered the acoustic reflection for the first wave, since the approximation can be neglected.

TFs deposited by SPH have the point and extended defects. However, both the experimental and ab initio calculations carried out in this study assumed that the TFs of CTO are pristine.

## 1.8 Scope of the study

This study investigated only the structural, acoustical, mechanical, and thermal properties of CTO. Thus, other properties such as optical, electrical, and electronic were not considered. In the study of structural properties, we only explored the XRD analysis to determine the crystal structures and the lattices parameters, the grain size, as well as the chemical composition of the synthesized samples. Other structural properties such as scanning electron microscopic (SEM) and X-ray photoelectron spectroscopic studies were not considered. In the study of mechanical properties, we only explored the bulk modulus, shear modulus, Young's modulus, Poisson's ratio, Pugh's ratio, Vickers hardness, Cauchy pressure, and elastic anisotropy. Other mechanical properties such as yield strength, ultimate strength, creep, and resilience were not considered. In the study of thermal properties, we only investigated the Debye temperature, melting temperature, Debye vibrational energy, Gibb's free energy, entropy, and specific heat capacity at constant volume. Other thermal properties such as thermal conductivity, thermal diffusivity, and thermal expansion were also not studied. In the study of acoustical properties, we only explored the acoustic transmission loss. Other acoustical properties such as acoustic reflection and porosity of the CTO samples were not considered.

# CHAPTER TWO
# LITERATURE REVIEW

## 2.1 Introduction

In this chapter, the previous work that has been done on CTO (both experimental and computational) is discussed, including the previous applications. The structural studies of materials by XRD, the crystal physics and mechanical properties (including the energy- strain method for calculating elastic constants of materials, elastic constants, and elastic anisotropy), the thermal properties, as well as the acoustical properties of materials, are also discussed. The common materials that have been utilized as substrates in the manufacture of MEMS devices, together with their properties and limitations, are also discussed. The chapter closes with the applications of MEMS, including microactuators, sensors and coating materials.

## 2.2 Previous work on cadmium-tin-oxide

### 2.2.1 Experimental studies

#### 2.2.1.1 Deposition methods

TFs of CTO have been deposited by many methods, including spray pyrolysis technique (SPT) (Agnihotri & Gupta, 1980) (Ortiz, 1982) (Haacke, Ando, & Mealmake, 1977), thermal treatment of coprecipitated salts (Sidorak, Ivanov, Shubin, & Shubin, 2011), radio frequency magnetron sputtering (Baratto, Ponzoni, Ferroni, Borgese, Bontempi, & Sberveglieri, 2012), and sol-gel (Velásquez, Campero, & Ortiz, 2003). Doping of the compound has also been done using gases like argon and fluorine (Bhuvaneswari & Velusamy, 2013); and metals such as zinc (Patil, Dea, & Kaushik, 2012), yttrium (Cristaldi, Impellizzeri, Priolo, Gupta, & Gulino, 2012), and iron (Ongwen, Oduor, & Ayieta, 2019). Introduction of the dopant has been observed to improve the properties of the deposited TFs, especially the optical and electrical.

Of all the deposition methods that have been utilized, SPT is the most preferred because it is simple to use, and also easy to apply in large-scale production. Moreover, this method is relatively cost-effective; does not require a vacuum, which may be difficult to maintain due to pump leakages; and does not require high-quality substrates (Perednis & Gauckler, 2005). The following factors have been kept constant in depositing the TFs of CTO by SPT: 35 cm as the distance between the spray nozzle and the substrate, with a 45° spray angle; the carrier gas flow rate at 50-61/min at 6.0-6.5 x $10^4$ Pa pressure, with the substrate distance from the spray nozzle being 30-35 cm; the spray angle of 45.1 °C; the spray time of 1-3 s; and the spray interval of 30 s to 2 min (Ongwen et al., 2019) (Bhuvaneswari & Velusamy, 2013) (Agnihotri & Gupta, 1980) (Ortiz, 1982) (Haacke, Ando, & Mealmake, 1977).

The deposited TFs of CTO have been obtained with thicknesses in the range of 200-600 nm (Barbara et al., 2016), and 143-199 nm (Zhu et al., 2021) at different deposition temperatures of 300 °C (Alnaimi & Al-Dileamy, 2007), 500 °C (Zhu et al., 2021), room temperature (Meng et al., 2012), and 400 °C, 450 °C & 500 °C (Krishna et al., 2010). Annealing has also been done on the deposited TFs at different temperatures of 550 °C (Meng et al., 2012), 400 °C (Nasir et al., 2013), and 500 °C (Patil et al., 2012), after which the optical properties of the deposited TFs have been observed to improve.

#### 2.2.1.2 Precursors used

The precursor solutions that have widely been utilized in depositing the TFs of CTO are the compounds of cadmium (Cd) and tin (Sn). The alkanoates or nitrates of the two metals are the most preferred because they are highly soluble in most of the solvents that are commonly used (Perednis & Gauckler, 2005). Most of the precursors have been dissolved in alcohols, mostly ethanol and methanol (absolute ethanol/ methanol, 99.99 % pure) (Patil et al., 2012), although some researchers have also dissolved the precursors in ethanoic acid (Agnihotri & Gupta, 1980) and water (Bhuvaneswari & Velusamy, 2013). The precursors have also been prepared at different concentrations, ranging from 0.02M (Bhuvaneswari & Velusamy, 2016) to 0.2M (Alnaimi & Al-Dileamy, 2007). The precursor solutions have been mixed at different ratios of 1:1 (Patil et al., 2012), and 2:1, 4:1 & 6:1 (Krishna et al., 2010).

Since the compound formed by solutions of Cd and Sn salts is insoluble (forms a white precipitate), small amounts of acids such as lactic acid (Barbara et al., 2016), and hydrochloric acid (HCl) (Bhuvaneswari & Velusamy, 2013) have been added. This leads to dissolution of the white precipitate in order to form a colourless solution of CTO. The resulting solution is then left for some time, usually two to three days in order to become homogeneous. It is usually colourless, with a strong smell of acetic acid in case cadmium acetate is used as one of the starting compounds.

#### 2.2.1.3 Properties studied

The properties of CTO (structural, optical, electrical, and electronic) have been investigated. The structure and morphology of the TFs of CTO have been studied by XRD (Blackmore & Cattell, 1990), electron spectroscope (Golestani-Fard, Hashemi, Mackenzie, & Hogarth, 1983), and SEM (Kurbanov, Amirdzhanova, Movsum-zade, & Panakh-zade, 1986). Sawat, Shinde, Deokate, Bhosale, Chougule, & Rajpure (2009) observed the crystalline forms of CTO in the cubic structure along the (1 1 1) orientation. Cubic structures with strong peaks along the (3 1 1) direction have also been obtained by Nasir et al. (2013), while Ongwen et al. (2019) observed the orthorhombic structure along the (2 0 0) direction. The morphology of the deposited TFs shows that some have smooth surfaces, while others have rough surfaces. Krishna et al. (2010) found that the TFs of CTO are smooth, with a surface roughness of 0.602 nm and grain size of 59 nm.

The study of optical properties of CTO have recorded up to 90% optical transmittance and a 3.9 eV band gap (Ongwen et al., 2019), and of 85% (Mohammad & Ghafor, 1993). Other optical properties that have been studied include absorption coefficient, extinction coefficient, and refractive index. The TFs of CTO possess high absorption coefficient of up to$10^5$ $cm^{-1}$ (Agnihotri, Gupta, & Sharma, 1978). Diliegros-Godines et al. (2018), who studied the mechanical and tribological properties of CTO by Sol-gel, found a Young's modulus of 88.90 GPa. However, the Nanoindentation method that was applied in the study relies heavily on the direction of excitation of the sample and thus, a global Young's modulus determination is necessary as a confirmation of their result.

Electrical properties of $Cd_2SnO_4$ have been studied using several equipment, including the four-point probe (Sawat et al., 2009), sensitive electrometer and vacuum electric oven, Hall measurements, and direct current conductivity. The optical properties of the deposited TFs have been found to vary with the ratio of Cd to Sn in the starting solution, formation of an additional layer, spray time, film thickness, and deposition temperature. It has also been observed that TFs with a 2:1 ratio of Cd to Sn have very high sheet resistance in the range of 2.5-25 kΩ/ sq, depending on the thickness of the TFs, which decreases with an increase in the ratio of Cd to Sn (Krishna et al., 2010). Du, Liu, Zhang, & Zhu (2017) have obtained a low resistivity of CTO in the order of x $10^{-4}$ Ω-cm, with the lowest value being 1.73 x $10^{-4}$ Ω-cm upon annealing. The electrical conductivity of the deposited TFs has been found to increase with an increase in the film thicknesses. Hall measurements have shown that the TFs of CTO are n-type. The Carrier concentration of the TFs has been recorded to increase with increase in the film thickness (Nasir et al., 2013).

#### 2.2.1.4 Applications

TFs of CTO have been found to possess excellent optical and electrical properties, which are desirable for use as TCOs. TCOs generally require materials with: optical transmittance greater than 80% of incident light and absorbance of less than 10% (Andreas, 2012), absorption coefficient of greater than x $10^4$ $cm^{-1}$ in the UV-Vis wavelength range (Coutts, Yong, & Li, 2000), refractive indices in the range of 1.8-2.8, and wide band gaps whose energy values are greater than those of the visible light. As such, photon energies below the band gap value are not absorbed by the material, while those with energy larger than the band gap are absorbed. As a result, TCOs should have a band gap of greater than 3.2 eV (Minami, 2005).

The TFs of CTO have also been investigated for use in many devices such as in LCD screens as a matte coating (matte coating is a coating that is not smooth so as to enhance diffusion of ambient light (Yong, Xu, Liu, Xiao, & Wei, 2021)), where it is included as an outer polarizing layer, which has been coarsened by mechanical or chemical processes. The matte coating makes the LCD ani-glare and hence, minimize reflection on the screen. The TFs have also been utilized in coating the window layers of TF solar

cells, which require coating materials with high absorbance and transmittance, but low reflectance (antireflective) (Rauschenbach, 1980). Transparent electrodes is also an area of application of TFs of CTO, since it possesses high optical transmittance of 85% and above in the UV-Vis spectral range, and electrical conductivity of as high as 6,500 Ω/cm (Haacke, 1976). The TFs of CTO have also been investigated for use in ordinary thermal mirrors, and also in highly specialized filters (Alnaimi & Al-Dileamy, 2007).

### 2.2.2 Computational studies

CTO is an n-type semiconductor, which is made by doping the large band gap tin IV oxide ($SnO_2$) semiconductor with Cd. Most of the *ab initio* studies that have been conducted on CTO focus on doping the large band gap $SnO_2$ semiconductor with Cd to form the CTO semiconductor ($Cd_2SnO_4$), which has a lower band gap than that of $SnO_2$. Investigations of Cd-doped $SnO_2$ calculations have been done by many methods, including full-potential Linear Augmented Plane-Waves and local orbitals techniques (LAPW + lo) within the WIEN2K package (Zhang, Li, Liu, & Zhu, 2012), full-potential LAPW as implemented in the VASP package (Yang, Han, Yan, Du, Zhan, & Jin, 2012), Plane-wave pseudopotential (PP) total-energy approach with local density approximation (LDA) as implemented in the WIEN97 package (Zhang & Wei, 2002), and plane-wave-based (Plane Augmented Wave) PP method based on DFT within the GGA as implemented in the VASP package (Tang, Shang, & Zhang, 2018).

Zhang et al. (2012) used a 2 x 2 x 2 supercell of $SnO_2$ with a rutile structure, and substituted the Cd atoms at one or two Sn locations to obtain a structure with impurity concentrations of 6.25% or 12.5%. The Muffin-tin sphere diameters for Cd, Sn, and oxygen (O) were set to 1.10, 1.12, and 0.8 Bohr respectively. By using the Monkhorst-Pack method, a 4 x 4 x 6 k-point mesh was created for the Brillouin Zone (BZ) sampling. They used a kinetic energy cut-off (ecut) of 60 Ry to distinguish between the core states and the valence states. The atomic locations were fully relaxed, and the model states were optimized geometrically. Local orbitals were also introduced to include the Sn 4d & 5p, O 2p, and Cd 4p & 5d orbitals. In a study by Zhang & Wei (2002), the Sn and Cd 4d electrons were included in a 60 Ry plane-wave basis set.

A number of properties of Cd-doped $SnO_2$ have been investigated through computations, including ferromagnetism (Zhang et al., 2012), electric field gradient, band gap (Zhang & Wei, 2002), and electronic and optical (Tang et al., 2018). Zhang et al. (2012) who studied the ferromagnetic properties of Cd-doped $SnO_2$, found out that the doped systems favoured the ferromagnetism, which made them expect a higher Curie temperature in the systems. The result was that the doped system favoured the spin-polarized state. Tang et al. (2018), who studied the effect of O vacancy and lanthanum (La) doping on CTO, found out that with the introduction of O vacancy, the impurity energy level was observed in the band gap. Following the La doping, the fermi energy level reached the conduction band and occluded it, increasing the electrical conductivity. They found out that La doping led to a rise in the optical transmittance.

Computational studies of properties of Cd-doped $SnO_2$ have investigated its possible use in various applications such as in spintronics, and in TCOs (Zhang et al., 2012) (Tang et al., 2018). According to Zhang et al. (2012), dilute magnetic semiconductors are promising because they concurrently display spin and charge degrees of freedom for integration of data processing and storage. This applicability requires that the Curie temperature of the semiconductor be above room temperature, a property which CTO possesses. Tang et al. (2018) proposed the application of CTO in the TCOs, since it has good electrical conductivity, and high optical transmittance in the UV-Vis spectrum.

Substrate materials to be used for the fabrication of MEMS devices should have among other properties, good electrical, mechanical, and thermal. The electrical properties of CTO have been studied and found to be comparable with those of Si (tables 1.1 and 1.2), implying that based on the electrical properties alone, it can be used as a substitute for Si in the fabrication of most MEMS devices. However, the acoustical, mechanical, and thermal properties of the TFs of CTO have not been explored extensively. Moreover, CTO has not been utilized in the manufacture and design of MEMS devices. This study thus investigated for the first time, the acoustical, mechanical, and thermal properties of CTO to determine if it could find good use as a substrate in the fabrication of MEMS devices, and also as a laminate on window panes for noise control.

## 2.3 Structural studies of materials by X-Ray powder diffraction

The XRD powder diffraction studies helps in determining the structures of crystals, as well as the lattice constants. Exploration of structures of crystals requires that the waves which interact with atoms in the crystal have wavelengths that are comparable with the interatomic spacing/ interplanar distance in the crystal, that is, in the order of 1 Å. The interaction should be weak so that the waves can penetrate into the crystal in a coherent fashion (Kittel, 1953). The most convenient waves suitable for determination of crystal structure are those associated with X-rays. When a crystal is exposed to electromagnetic radiation (X-rays), the rays are reflected from various planes of the atoms in the crystal. The diffracted beams are formed for situations in which the reflections from parallel planes of atoms interfere constructively.

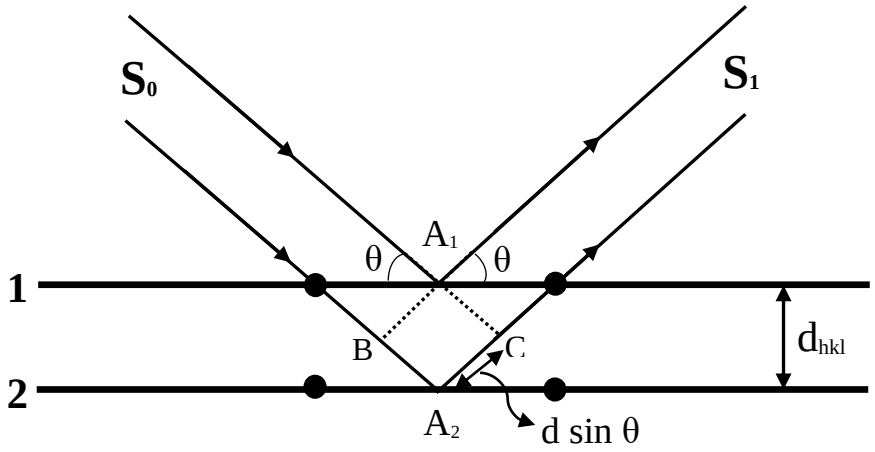


***Figure 2.1: X-Ray diffraction by crystals***

Consider a crystal of atomic planes that are partially reflecting X-ray light of wavelength $\lambda$ that are separated by equal distances $d$ (figure 2.1). The radiation is incident on the plane. Applying trigonometry gives the distance $BA_2$ as $d\,sin\,\theta$. The path difference for the X-rays reflected from the adjacent planes is $2d\,sin\,\theta$ (that is $2\,x\,d\,sin\,\theta$, the distance $BA_2C$). When the path difference is an integral number $n$ of wavelengths, then reinforcement of the radiation reflected from subsequent planes will take place. The condition for constructive reflection is that (Kittel, 1953):

$$n\lambda = 2d_{hkl}\sin\theta, \qquad (2.1)$$

where $\theta$ is the diffraction angle, $n$ is a positive integer, and $hkl$ are the Miller indices.

The value of $\lambda$ is taken as 1.540598 Å for the case of CuKα radiation. Equation 2.1 is known as the Bragg's diffraction law. Rearranging it gives the interplanar distance $d_{hkl}$ as:

$$d_{hkl} = \frac{n\lambda}{2 \sin \theta} \tag{2.2}$$

The equation connecting the cell parameters *a*, *b*, and *c* for an orthorhombic unit cell is:

$$\frac{1}{d_{hkl}^2} = \frac{h^2}{a^2} + \frac{k^2}{b^2} + \frac{l^2}{c^2} \tag{2.3}$$

The cell parameters *a*, *b*, and *c* are found by identifying three strongest indexed peaks, and then using the peaks to form three simultaneous equations with the use of equation 2.3. The values of the lattice parameters *a*, *b*, and *c* are then obtained by solving the simultaneous equations. The volume of the orthorhombic unit cell is given by:

$$V = abc \tag{2.4}$$

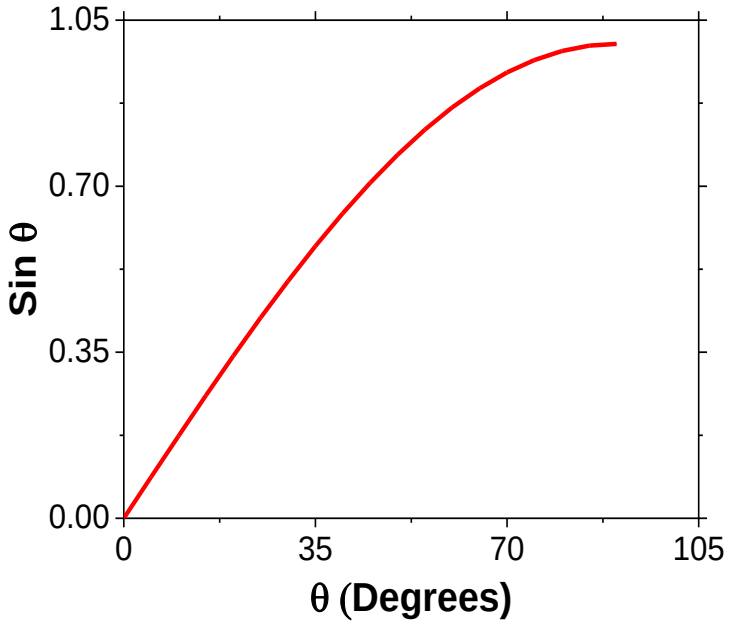


***Figure 2.2: Graph of sin θ against θ for the angles of X-ray diffraction data.***

When sin $\theta$ is plotted against $\theta$ (degrees), a curve similar to the one in figure 2.2 is obtained. As the angle ($\theta$) increases, the value of the slope of the graph reduces. The highest slope is therefore obtained at low values of θ, which means that even a little inaccuracy in the recorded angle of the diffraction peak at low values of $\theta$ will give rise to a considerable error in the value of the calculated unit cell parameters. But at high values of $\theta$, the slope is small, indicating that a little inaccuracy in the measured angle of the diffraction peak at high values of $\theta$ results into a small error in the calculated value of the unit cell parameter. This leads to a more accurate result of the lattice parameters.

The grain size of the crystals in a material can be determined using the formula (Khan, Ahmed, Ali, Igbal, Taboob, & Shafique, 2016):

$$D = \frac{K\lambda}{\beta\cos\theta}, \qquad (2.5)$$

in which equation 2.5 is called the Debye-Scherer's formula. In the formula, *K* is a constant known as the Scherrer's constant, *D* is the grain size of the crystal, $\lambda$ is the wavelength of the X-rays used, $\beta$ is the peak width, and $\theta$ is the diffraction angle. Both $\beta$ and $\theta$ are measured in radians. The peak width can be determined using two methods: full width at half maximum (FWHM), or integral breadth (IB).

FWHM is obtained by selecting the strongest peak, then dividing the peak length halfway. The width of the peak halfway gives the FWHM in radians (figure 2.3a). The FWHM is commonly used because it is easier to obtain. The peak width decreases as the crystallite size increases. The IB method on the other hand, involves finding the area under the peak, then dividing the area by the peak height (figure 2.3b). The background and peak's tails must be carefully evaluated for the case of the IB approach (Zhou & Switzer, 1996). For the calculation of the crystallite size using the IB, the symbol $\beta$ in equation 2.5 becomes *L*, where *L* is the IB.

Crystallites are usually irregular in shape. However, they can often be approximated as: spheres, cubes, tetrahedra or octahedra; prisms or cylinders; and parallelepiped (needles or plates) (Speakman, n.d). The value of *K* in equation 2.5 varies from 0.62 to 2.08. The most common values are 0.94 for FWHM of spherical crystals with cubic symmetry and 0.89 for IB of spherical crystals with cubic symmetry. The factors that affect the value of *K* and the crystallite size include: how the peak width is defined (FWHM or IB), shape of the crystal, how the crystallite size defined and the size distribution.

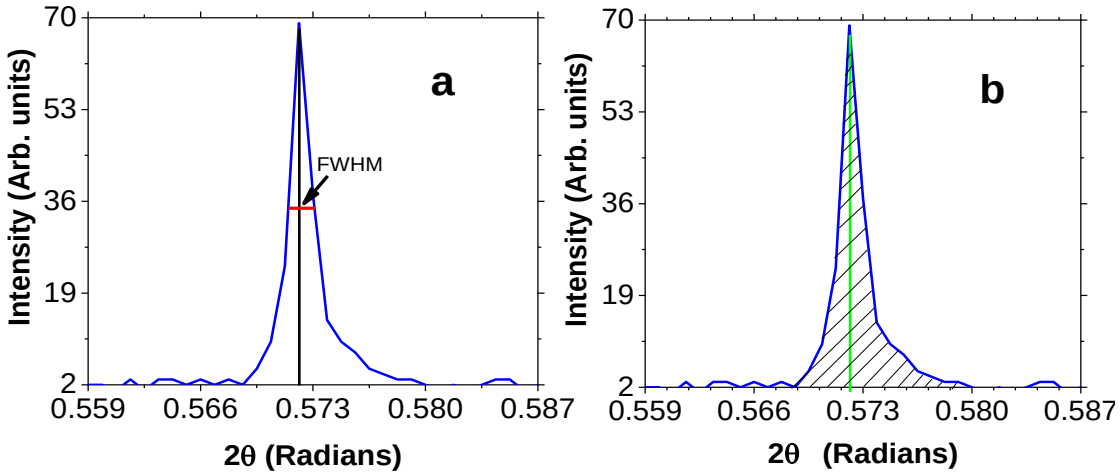


***Figure 2.3: Determination of (a) full width at half maximum, and (b) integral breadth of a peak***

## 2.4 Crystal physics and mechanical properties of materials

### 2.4.1 Crystal physics

Mechanical properties of materials are governed by the well-known Hooke's law, which can be given in terms of the stress-strain relationship as (Waters, 2008):

$$\sigma = c\varepsilon, \varepsilon = s\sigma, \tag{2.6a}$$

where $c$ the stiffness coefficient (which has the dimension of stress), $s$ is the compliance coefficient (which has the dimension of 1/stress), $\sigma$ is the second order stress tensor, and $\varepsilon$ is the second order deformation tensor. The law can also be expressed as:

$$\sigma_{ij} = c_{ijkl}\varepsilon_{kl};\ \varepsilon_{ij} = s_{ijkl}\sigma_{kl}, \tag{2.6b}$$

where *i*, *j*, *k*, & *l* have the values of 1, 2, or 3. As such, a 3 x 3 x 3 x 3 crystal has $3^4$ = 81 coefficients. However, due to the symmetry of the deformation and the stress tensors, the 81 coefficients are not independent. Single crystal elastic moduli are a 4th rank tensor with 3 to 21 independent, non-zero coefficients, which depend on the crystal system. In the Voigt notation, the $c_{ijkl}$ tensor can be written as a 6 x 6 symmetric tensor $c_{nm}$, with 21 independent values for a triclinic crystal, where $n$, $m$ can have values of 1, 2, 3, 4, 5, or 6 (Jaric, Kuzmanovic, & Golubovic, 2008). Figure 2.4 shows the seven crystal systems and their elastic tensors.

The elastic tensors are applied in classifying crystals into different geometries (systems). There are 7 crystal geometries, which result into 14 Bravais lattices. The 7 geometries are: cubic, hexagonal, trigonal, tetragonal, orthorhombic, monoclinic, and triclinic. The cubic system is the simplest, and is referred to as the one with the highest symmetry. The triclinic system, on the other hand, is the most complex, and is referred to as the lowest symmetric. Table 2.1 shows the 7 crystal systems and their properties in terms of their axial lengths (lattice parameters) and angles. The elastic tensor $c_{ij}$ can also be used to determine among other things, the: elastic wave velocity, elastic moduli (bulk modulus and Young's modulus), linear compressibility in any direction, mechanical stability analysis (softening of acoustic modes), isotropic elastic moduli and velocities, Debye temperature and the mean sound (phonon) velocity, and elastic energy (Weinberger & Cai, 2004).

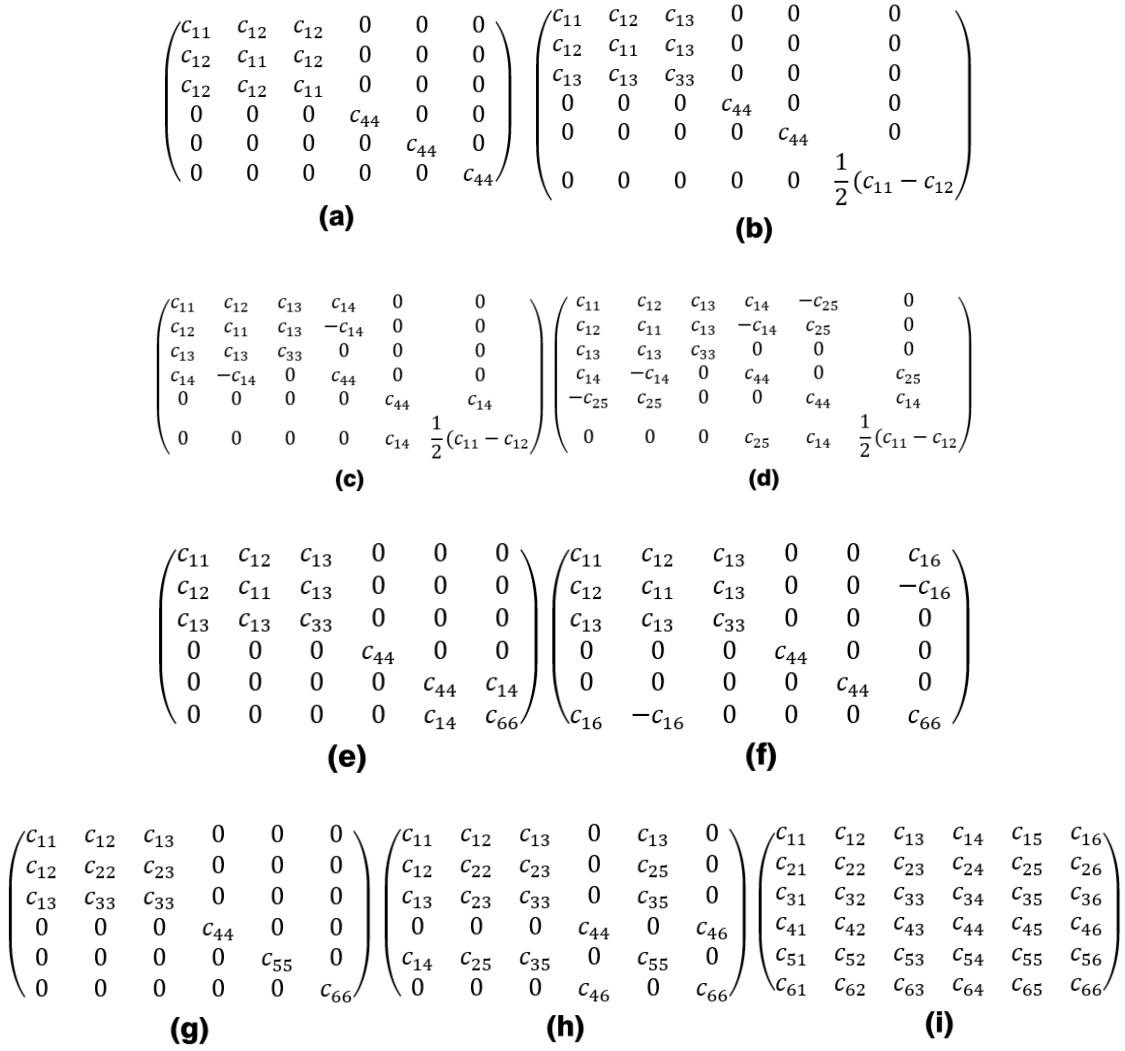


***Figure 2.4: The seven crystal systems: (a) cubic, (b) hexagonal, (c & d) trigonal, (e & f) tetragonal, (g) orthorhombic, (h) monoclinic, and (i) triclinic***

***Table 2.1: The seven crystal systems and their properties, together with the number of lattices in each crystal system***

| Crystal system | Axial lengths and angles | Number of lattices |
|---|---|---|
| Cubic | $a = b = c;\ \alpha = \beta = \gamma = 90^o$ | 3 |
| Hexagonal | $a = b \neq c;\ \alpha = \beta = 90^o, \gamma = 120^o$ | 1 |
| Trigonal | $a = b = c;\ \alpha = \beta = \gamma \neq 90^o$ | 1 |
| Tetragonal | $a = b \neq c;\ \alpha = \beta = \gamma = 90^o$ | 2 |
| Orthorhombic | $a \neq b \neq c;\ \alpha = \beta = \gamma = 90^o$ | 4 |
| Monoclinic | $a \neq b \neq c;\ \alpha = \gamma = 90^o \neq \beta$ | 2 |
| Triclinic | $a \neq b \neq c;\ \alpha \neq \beta \neq \gamma \neq 90^o$ | 1 |

The seven crystal systems are further classified according to: Laue class, crystal class, lattice centering, and space groups (table 2.2). The Laue classes are geometric crystal classes that contain centrosymmetric crystallographic types of point groups and their subgroups. When absorption is negligible and Friedel's law applies, it is impossible to distinguish by diffraction, between a centrosymmetric point group and one of its non-centrosymmetric subgroups; only point groups belonging to different Laue classes can then be distinguished. There are 32 crystal classes, each according to the possible combinations of symmetry elements possessed by the lattice. The number of permutations of Bravais lattices with rotation and screw axes, mirror and glide planes, and plus points of inversion, is finite. There are only 230 unique combinations for three-dimensional symmetry, and they are known as the 230 space groups (Hahn, Klapper, Muller, & Aroyo, 2016)

***Table 2.2: The seven crystal systems and their respective Laue classes, crystal classes, and lattice centering***

| Crystal system | Laue class | Crystal class | Lattice centering |
|---|---|---|---|
| Cubic | m-3 | 23, m-3 | P, F, I |
| | m-3m | 432, -43m, m-3m | P, F, I |
| Hexagonal | 6/m | 6, -6, 6/m | P |
| | 6/mmm | 622, 6mm, -6m2, 6/mmm | P |
| Trigonal | -3 | 3, -3 | P, R |
| | -3m | 312, 321, 31m, 3m1, -31m, -3m1 | P, R |
| Tetragonal | 4/m | 4, -4, 4/m | P, I |
| | 4/mmm | 422, 4mm, -42m, -42m2, 4/mmm | P, I |
| Orthorhombic | mmm | 222, m2, mmm | P, C, F, I, A |
| Monoclinic | 2/m | 2, m, 2/m | P, C |
| Triclinic | -1 | 1, -1 | P1, P-1 |

Lattice centering is concerned with the location of lattice points in the unit cell. They include: primitive unit cell (P), Body centred (I), face centred (F), and base centred (C). In the primitive unit cell (the simple unit cell), lattice points are found only on the corners of the cell. In the body centred unit cell, lattice points are found on the corners of the cell, with one additional lattice point at the centre of the cell. In the face centred unit cell, lattice points are found on the corners of the cell, with one additional lattice point at the centre of each face of the cell. In the base centred unit cell, lattice points are found on the corners of the cell, with one additional lattice point at the centre of each face of one pair of parallel faces of the cell. Table 2.2 shows the Laue classes and the crystal classes for the seven crystal systems (Pan, Han, & Lu, 2020) (Nelson, 2013).

### 2.4.2 Elastic constants and Vickers hardness

The ratio of the proportional decrease in the volume caused by an increase in the pressure to an infinitesimal rise in pressure, is known as the bulk modulus (p-wave modulus), which is used to gauge a body's resistance to compression (Cordill, Glushko, Kreith, Marx, & Kirchlechner, 2015). When the pressure is removed, the body returns to its original volume. A body with a higher value of bulk modulus is harder to compress than one with a lower value. The bulk modulus can be expressed as:

$$\mathrm{B} = -\mathrm{V_o}\frac{\mathrm{dP}}{\mathrm{dV}} = \rho\frac{\mathrm{dP}}{\mathrm{d\rho}}, \qquad (2.7a)$$

where $V_o$ is the equilibrium volume, $dV$ is the change in volume between the maximum and the minimum pressure, $dP$ is the change in pressure, and $\rho$ is the density of the material. It is worthwhile to note that expansion leads to a negative pressure, while contraction leads to a positive pressure.

The ratio of shear stress to shear strain is known as shear modulus (modulus of stiffness). A high shear modulus value indicates that a material is very rigid (a large amount of force is required to cause deformation). An example is diamond with a value of 514 GPA (Gray, 1992). A low shear modulus value on the other hand, indicates that the material is less rigid (a small amount of force is needed to deform it). Any amount of force could distort a material if it has a shear modulus of zero (Helmenstine, 2019).

The shear modulus can be calculated using the formula:

$$G = \frac{\tau_{xy}}{\gamma_{xy}} = \frac{F/A}{\Delta x/h} = \frac{Fl}{A\Delta x}, \quad (2.7b)$$

where $\tau_{xy} = F/A$ is the shear stress, $F$ is the force acting on the material, $A$ is the area that the force acts on, $\tau_{xy}$ is the shear strain, $x$ is the transverse displacement, and $h$ is the initial length of the material (figure 2.5).

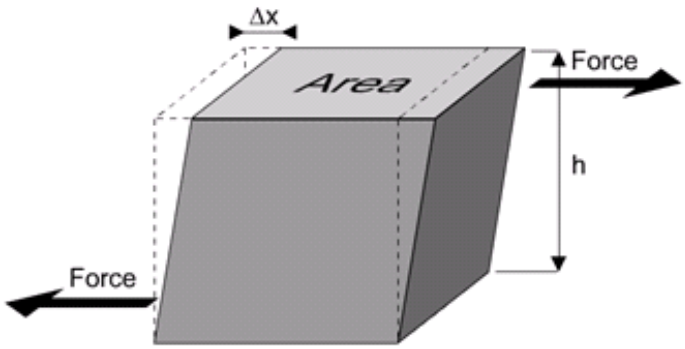


***Figure 2.5: Shear stress and shear transverse displacement for determination of shear modulus***

The elastic modulus, also referred to as the Young's modulus, is an indicator of a solid material's stiffness (Alexopoulos & O'Sullivan, 1990). Figure 2.6a shows the relationship between tensile stress and extensional strain, which gives the Young's modulus:

$$E = \frac{\sigma}{\varepsilon} = \frac{F/A}{\Delta L/L_i} = \frac{FL_i}{A\Delta L}, \quad (2.8)$$

where $\sigma$ is the mechanical stress $(force, F/area, A)$ and $\varepsilon$ is the strain (change in length, $\Delta L/$ original length, $L_i$). Solid materials undergo elastic deformation when loads are applied to them. When the stress applied to a material is small (before the elastic limit is reached), the curve of stress against strain is linear and passes through the origin (obeys Hooke's law). The Young's modulus is the proportionality coefficient of the curve. The Young's modulus is a measure of how much force is needed to expand or compress a material, and the greater the value, the more rigid the material is.

Poisson's ratio (μ), a property of materials which is a measure of the Poisson's effect, is the phenomenon in which a material tends to expand in directions perpendicular to the direction of compression. If a material is stretched rather than being compressed, it tends to contract in the direction transverse to the direction of stretching. On pulling the material, it stretches in the horizontal direction and becomes thinner in the vertical direction (figure 2.6b). The Poisson's ratio of the material is the ratio the contraction in the perpendicular direction (y-direction) to that of elongation in the direction of pull (x-direction). Poisson's ratio ranges from 0 to 0.5. Elastic materials elongate easily and therefore have higher values of Poisson's ratio than plastic or rigid materials, which have values close to zero (Grindrod et al., 2010).

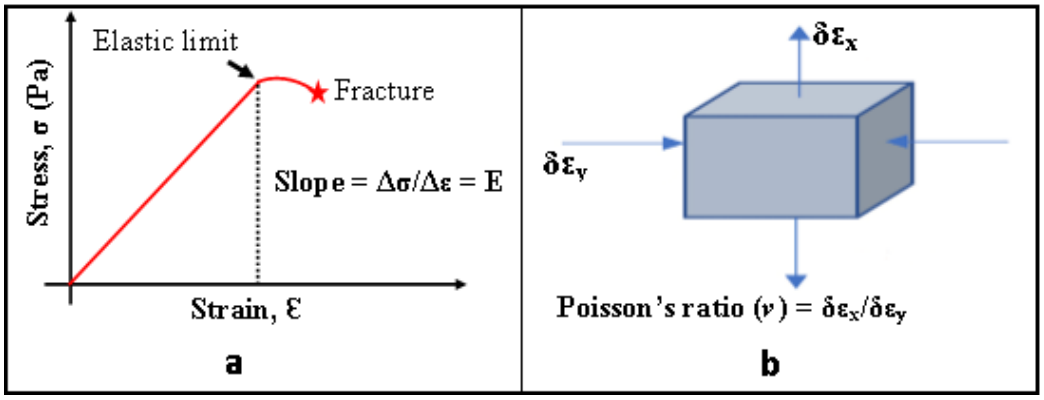


***Figure 2.6: Experimental determination of some elastic constants (a) stress-stain curve for obtaining the Young's modulus, and (b) demonstration of the Poisson's ratio***

The Young's modulus, Poisson's ratio, shear modulus, and bulk modulus, are all connected by (Ogam, E. Fellah, & Ogam, G., 2016) (Bouceta & Zegrar, 2001):

$$E = B\frac{(1+\mu)(1-2\mu)}{(1-\mu)} = 2G(1+\mu) = \frac{9BG}{3B+G}, \quad (2.9a)$$

$$G = B\frac{(1-2\mu)}{2(1-\mu)} = \frac{E}{2\mu+2}, \quad (2.9b)$$

$$B = \frac{E}{3(1-2\mu)}, \quad (2.9c)$$

$$\mu = \frac{3B-2G}{6B+2G} = \frac{E}{2B} - 1, \quad (2.9d)$$

Elastic properties of materials give vital information about their mechanical, anisotropic character of bonding, bonding characteristics between adjacent atomic planes, and structural stability. Understanding the curvature of the energy/stress curves as a function of strain for the chosen deformations is necessary for the calculation of elastic constants of materials (Munjal, Sharma, V., Sharma, G., Vyas, Sharma, B., & Lowther, 2011). The common and widely used method of calculating elastic stiffness constants (and hence, the mechanical properties of materials) is the energy-strain method, owing to its ease of use. The stress-strain method has not been reported in the literature.

An indicator of the resistance of a crystal to deformation when subjected to external strain is the elastic stiffness constant ($c_{ij}$). The total energy calculations for every crystal can be performed using the Full Potential Linearized Muffin-Tin Orbital technique. Small strains are allowed to the equilibrium lattice in order to determine the resulting change in the total energy. From the change in the total energy, the elastic constants can be deduced. In a polynomial fitting of the total energy as a function of the distortion parameter $\boldsymbol{\delta}$, the elastic constants are considered as being proportional to the second order coefficient. By stressing the lattice vector $\boldsymbol{R}$ in accordance with the formula $\boldsymbol{R'} = \boldsymbol{RD}$, where $\boldsymbol{R'}$ is a matrix containing the elements of the distorted lattice vectors and $\boldsymbol{D}$ is the symmetric distortion matrix containing the strain components, one can derive the linear combinations of the elastic constants.

With respect to the initial internal energy of the unstrained crystal, the internal energy of the crystal under strain can be Taylor-expanded in powers of the strain tensor as follows (Ravindran, Fast, Korzhavyi, & Johansson, 1998):

$$\mathrm{E}(\mathrm{V},\delta) = \mathrm{E}(\mathrm{V_o},0) \; + \; \mathrm{V_o}\left(\frac{1}{2!}\sum_{i,j=1}^{6} c_{ij}\,\eta_i\eta_j\right) + \mathrm{O}\delta^3, \qquad (2.10a)$$

where $E(V,\delta)$ is the total energy of the strained system, $E(V_o,0)$ is the total energy of the unstrained system, $V_o$ is the volume of the unstrained system, $\boldsymbol{\eta}$ is the Lagrangian coordinate, and $c_{ij}$ is the second-order elastic constants in the Voigt notation, where *ij* replaces the $xx$, $yy$, $zz$, $yz$, $xz$, and $xy$ by 1, 2, 3, 4, 5, and 6 respectively. Here, 1, 2, and 3 are associated with normal strains (stresses), while 4, 5, and 6 are associated with shear strains (stresses).

The Eulerian coordinates $\boldsymbol{\delta}$ are related to the Lagrangian coordinates $\boldsymbol{\eta}$ by the equation $\boldsymbol{\eta} = \boldsymbol{\delta} + \frac{1}{2}\boldsymbol{\delta}\boldsymbol{\delta}$ during the Taylor expansion of the total energy in terms of the Lagrangian coordinates. Since $\boldsymbol{\delta}$ is small, the approximation $\boldsymbol{\eta} = \boldsymbol{\delta}$ is valid. Rearranging equation 2.10a and replacing $\boldsymbol{\eta}$ with $\boldsymbol{\delta}$ gives (Søndenå, Stølen, & Ravindran):

$$\frac{\mathrm{E(V,\delta)-E(V_o,0)}}{\mathrm{V_o}} = \mathrm{E_\rho} = \left(\frac{1}{2!}\sum_{\mathrm{i,j=1}}^{6} \mathrm{c_{ij}}\,\delta_\mathrm{i}\delta_\mathrm{j}\right) + O\delta^3, \qquad (2.10b)$$

where the quantity $\frac{E(V,\delta)-E(V_o,0)}{V_o} = E_\rho$ is called the energy density. In the energy density, $V_o$ is the equilibrium (the optimized volume at zero GPa pressure) volume, and $E_o$ is the equilibrium total energy. The energy density obtained here (in equation 2.10b) is in the unit of Ry/a.u$^3$. To convert it to GPa, we multiply it by 14,710.5076.

For an orthorhombic crystal, Ravindran et al. (1998) developed a method that utilizes nine different strains and hence, nine distortion matrices in order to obtain all the nine independent elastic stiffness constants ($c_{11}, c_{22}, c_{33}, c_{44}, c_{55}, c_{66}, c_{12}, c_{13}$, and $c_{23}$). The first three elastic stiffness constants ($c_{11}, c_{22}$, and $c_{33}$) are obtained by the distortion matrices $D_1, D_2$, and $D_3$ respectively. The distortion matrices are written as:

$$\mathrm{D_1} = \begin{pmatrix} 1+\delta & 0 & 0 \\ 0 & 1 & 0 \\ 0 & 0 & 1 \end{pmatrix}, \mathrm{D_2} = \begin{pmatrix} 1 & 0 & 0 \\ 0 & 1+\delta & 0 \\ 0 & 0 & 1 \end{pmatrix}, \mathrm{D_3} = \begin{pmatrix} 1 & 0 & 0 \\ 0 & 1 & 0 \\ 0 & 0 & 1+\delta \end{pmatrix} \qquad (2.11)$$

The orthorhombic symmetry of the strained lattice is maintained despite all of the aforementioned distortions. However, the distortion modifies the volume of the cell. The straining of the lattice along the *x*, *y*, and *z* axes is represented by the distortions $D_1, D_2$, and $D_3$ respectively. The values of the strain matrices $D_1, D_2$, and $D_3$ are then inserted into equation 2.10b to determine the energy density associated with the distortions. Omitting the third order term ($O\delta^3$), we obtain:

$$\mathrm{E_{\rho(11)}} = \frac{1}{2}c_{11}\delta^2, \mathrm{E_{\rho(22)}} = \frac{1}{2}c_{22}\delta^2, \mathrm{E_{\rho(33)}} = \frac{1}{2}c_{33}\delta^2, \qquad (2.12)$$

from which the elastic stiffness constants ($c_{11}, c_{22}$, and $c_{33}$) are obtained from the coefficients of the quadratic function $\delta^2$.

The shear elastic stiffness constants *($c_{44}$, $c_{55}$,* and *$c_{66}$)* are calculated using the volume-conserving monoclinic shear distortions below (Ravindran et al, 1998):

$$D_4 = \begin{pmatrix} \frac{1}{(1-\delta^2)^{1/3}} & 0 & 0 \\ 0 & \frac{1}{(1-\delta^2)^{1/3}} & \frac{\delta}{(1-\delta^2)^{1/3}} \\ 0 & \frac{\delta}{(1-\delta^2)^{1/3}} & \frac{1}{(1-\delta^2)^{1/3}} \end{pmatrix}, \qquad (2.13a)$$

$$D_5 = \begin{pmatrix} \frac{1}{(1-\delta^2)^{1/3}} & 0 & \frac{\delta}{(1-\delta^2)^{1/3}} \\ 0 & \frac{1}{(1-\delta^2)^{1/3}} & 0 \\ \frac{\delta}{(1-\delta^2)^{1/3}} & 0 & \frac{1}{(1-\delta^2)^{1/3}} \end{pmatrix}, \qquad (2.13b)$$

$$D_6 = \begin{pmatrix} \frac{1}{(1-\delta^2)^{1/3}} & \frac{\delta}{(1-\delta^2)^{1/3}} & 0 \\ \frac{\delta}{(1-\delta^2)^{1/3}} & \frac{1}{(1-\delta^2)^{1/3}} & 0 \\ 0 & 0 & \frac{1}{(1-\delta^2)^{1/3}} \end{pmatrix}, \qquad (2.13c)$$

and the energy density corresponding to the distortions ($D_4, D_5$ , and $D_6$) are given as:

$$E_{\rho(44)} = 2c_{44}\delta^2,\ E_{\rho(55)} = 2c_{55}\delta^2, \qquad E_{\rho(66)} = 2c_{66}\delta^2, \qquad (2.14)$$

respectively, giving $c_{44}, c_{55,}$and $c_{66}$ directly.

In order to determine the last three elastic stiffness constants ($c_{12}$, $c_{13}$, and $c_{23}$), volume-conserving orthorhombic distortions of the following sorts are applied:

$$D_7 = \begin{pmatrix} \frac{1+\delta}{(1-\delta^2)^{1/3}} & 0 & 0 \\ 0 & \frac{1-\delta}{(1-\delta^2)^{1/3}} & 0 \\ 0 & 0 & \frac{1}{(1-\delta^2)^{1/3}} \end{pmatrix}, \qquad (2.15a)$$

$$D_8 = \begin{pmatrix} \frac{1+\delta}{(1-\delta^2)^{1/3}} & 0 & 0 \\ 0 & \frac{1}{(1-\delta^2)^{1/3}} & 0 \\ 0 & 0 & \frac{1-\delta}{(1-\delta^2)^{1/3}} \end{pmatrix}, \qquad (2.15b)$$

$$D_9 = \begin{pmatrix} \frac{1}{(1-\delta^2)^{1/3}} & 0 & 0 \\ 0 & \frac{1+\delta}{(1+\delta^2)^{1/3}} & 0 \\ 0 & 0 & \frac{1-\delta}{(1-\delta^2)^{1/3}} \end{pmatrix} \quad (2.15c)$$

Among the three distortions ($D_7, D_8$ and $D_9$), the $D_7$ distortion increases the value of *a* but decreases *b* by equal amount, while *c* remains constant. The $D_8$ distortion increases the value of *a* but decreases *c* by equal amount, while *b* remains constant. The distortion $D_9$ increases the value of *b* but decreases *c* by equal amount, while *a* remains constant. The resulting symmetry of the strained lattice from the three distortions is thus the same as that of the unstrained lattice. The volume of the cell is conserved in these distortions. The energy associated with the distortions ($D_7, D_8$ and $D_9$) are then obtained by inserting the values of the strain matrices into equation 2.10b to obtain:

$$E_{\rho(12)} = \frac{1}{2}(c_{11} + c_{22} - 2c_{12})\delta^2, \quad (2.16a)$$

$$E_{\rho(13)} = \frac{1}{2}(c_{11} + c_{33} - 2c_{13})\delta^2, \quad (2.16b)$$

$$E_{\rho(23)} = \frac{1}{2}(c_{22} + c_{33} - 2c_{23})\delta^2, \quad (2.16c)$$

respectively. The relations in equation 2.16a to c give the elastic constants $c_{12}, c_{13,}$ and $c_{23}$. For cubic crystals, the distortion matrices reduce to three ($D_1, D_4,$ and $D_7$), which are sufficient for determining the elastic stiffness constants $c_{11}, c_{44},$ and $c_{12}$, since $c_{11} = c_{22} = c_{33}, c_{44} = c_{55} = c_{66},$ and $c_{12} = c_{13} = c_{23}$ for the cubic crystals.

The energy-strain method of calculating elastic constants turns out to be complicated due to the complex matrices that are involved, which in turn becomes tedious, and may lead to wrong results as a result of wrong calculations. Thus, there is need for the modification of the matrices into simpler once that can be calculated easily. This study set out to provide a solution to this problem by developing a simpler method that applies stress and strain in calculating the elastic constants of materials. The focus was on the cubic and orthorhombic cells.

The ability of a material to withstand plastic deformation is known as hardness. Indentation hardness, scratch hardness, and rebound hardness, are the three types of hardness that are commonly assessed. One of the hardness tests, the Vickers test, determines the indentation hardness of thin metals, ceramics, or composite sections or small pieces. Shore, Mohs, Knoop, Brinell, and Rockwell are the other methods for determining hardness. The size of the impression left by a pyramid-shaped diamond indenter when it is loaded can be used to experimentally measure the Vickers hardness (Britannica, 2018). Engineers at Vickers Limited in the United Kingdom developed the approach in the 1920s, and it has since made it possible to create a continuous scale of comparable numbers that precisely reflect the enormous range of hardness found in steels. The indenter typically takes the shape of a square-based pyramid with opposite sides that meet at an angle of 136° at the top. A calibrated microscope is used to measure the size of the impression left by the indenter, which is typically not larger than 0.5 mm. The indenter is driven into the surface of the material being tested at loads of up to around 1.20 kg of force. The indentation set-up used to calculate the Vickers hardness is depicted in figure 2.7a for the indentation, and in figure 2.7b for the measurement of indent signals.

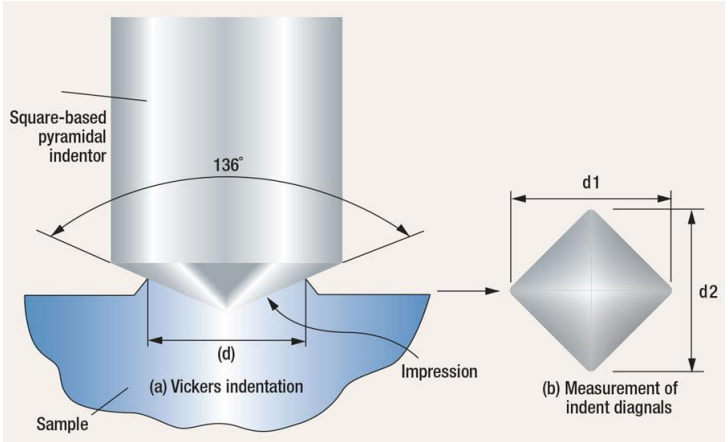


***Figure 2.7: Determination of the Vickers hardness using indentation method: (a) the Vickers indentation, and (b) measurement of the indent signals (image from: https://eprnews.com/whats-vickers-hardness-tester-492801/. 04/02/2021)***

Materials have a varied degree of hardness. The hardness is usually in the Vickers scale. 40 GPa is the boundary beyond which a material becomes super hard. The super hard materials are characterized by very high incompressibility, with high electron density and bond covalency (Wentorf, Devries, & Bundy, 1980) (Veprek, Zeer, & Riedel, 2000). Most of the hard and super hard materials are compounds of carbon, nitrogen, boron, osmium, and tungsten. However, the hardest naturally occurring substance, diamond, is an element, and not a compound. Some of the hard materials are presented in table 2.3. As the table depicts, diamond, cubic boron carbon nitride, carbon carbide, and cubic boron nitride are super hard; while osmium boride, boron carbide, silicon carbide, and tungsten boride are not.

***Table 2.3: Some selected hard and super hard materials and their values of Vickers hardness ($H_V$)***

| Material | $H_V$ (GPa |
|---|---|
| Diamond | 100[(a)], 115[(b)] |
| Cubic boron carbon nitride | 76[(c)] |
| Cubic boron carbide | 71[(d)] |
| Cubic boron nitride | 49[(e)] |
| Osmium boride | 37[(f)] |
| Boron carbide | 35, 38[(d)] |
| Silicon carbide | 32[(g)] |
| Tungsten boride | 30[(h)] |

[(a)] *Novikov, Dub, Mal'nev, & Beskrovanov (1994)*

[(b)] *Solozhenko, Oleksandr Denis, Yann, & Mohamed (2009)*

[(c)] *Vladimir, Solozhenko, Sergey, Dub, Nikolay, & Novikov (2001)*

[(d)] *Solozhenko, Oleksandr, Denis, Yann, & Mohamed (2009)*

[(e)] *Dub, Lytvyn, Strelchuk, Nikolenko, Stubrov et al. (2017)*

[(f)] *Ivanovskii (2012)*

[(g)] *Mehregany et al. (2000)*

[(h)] *Chrzanowska-Giżyńska, Denis, Woźniacka, & Kurpaska (2018)*

Equation 2.17 gives the formula used to determine the Vickers hardness (the Vickers number, $H_V$) (Essabir, Bouhfid, & Qaiss, 2019):

$$H_V = 1.854 \left(F/D^2\right), \quad (2.17)$$

where $D^2$ is the area of the indenter (in square millimetres), and $F$ is the applied load (in kilograms-force). When $H_V$ is noted, the applied load is typically specified. The Vickers test is a trustworthy method for determining the hardness of metals and ceramic materials. The harder the material under study is, the smaller the indentation. Depending on the force used to indent the test material, hardness testing can be divided into micro-indentation and macro-indentation tests. Typically, loads up to 200 gram-force are used in macro-indentation testing, whereas loads up to 1000 gram-force are used in micro-indentation tests. The most popular tests that can be used for both macro- and micro-indentation are the Vickers and Knoop hardness tests.

### 2.4.3 Elastic anisotropy

Isotropy is the property of a material which relates to the stresses and strains in the material. Anisotropy occurs when the orientation of a material affects the relationship between stress and strain in that material. If the applied stress is rotated, the response of the material to strain will differ. Elastic anisotropy in crystals can be viewed pictorially. This can be accomplished by employing a spherical coordinate system to plot the surface of the crystal in either three dimensions (3D) (figure 2.8a), or in two dimensions (2D) (figures 2.8b and c) in various orientations. For an isotropic crystal, the 2D diagram is a perfect circle (as in figure 2.8b and c), while the 3D structure is a perfect sphere (as in figure 2.8a). Any departure from the two structures shows that the crystal is anisotropic.

The relation in equation 2.18 can be used to determine how the Young's modulus for a cubic crystal depends on the direction:

$$\frac{1}{E} = l_1^4 s_{11} + l_2^4 s_{22} + l_3^4 s_{33} + 2l_1^2 l_2^2 s_{12} + 2l_1^2 l_3^2 s_{13} + 2l_2^2 l_3^2 s_{23} + l_1^2 l_2^2 s_{66} + l_1^2 l_3^2 s_{55} + l_2^2 l_3^2 s_{44}, \quad (2.18)$$

where, $l_1$, $l_2$, and $l_3$ are the directional cosines, and $s_{ij}$ are the elastic compliance constants. In the spherical coordinates, we have: $l_1 = sin\,\theta\, cos\,\varphi$, $l_2 = sin\,\theta\, sin\,\varphi$, and $l_3 = cos\,\theta$. The angles $\theta$ and $\varphi$ are defined on the horn in the spherical coordinates.

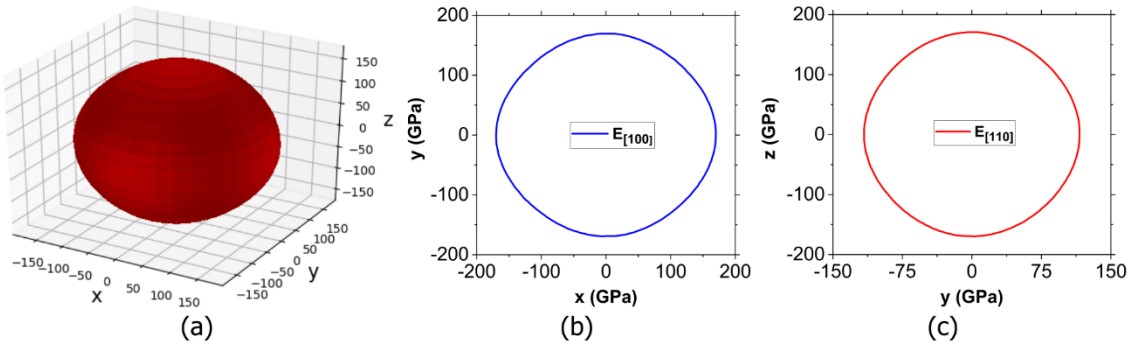


***Figure 2.8: Directional Young's moduli for Ti-Al (computational data obtained from a study by Ongwen et al., (2021)) in: (a) a 3-Dimension, (b) a 2-Dimension along the xy direction, and (c) a 2-Dimension along the yz direction***

The directional Young's moduli of other crystal structures are given by the relation (Teloff, 2014):

$$\frac{1}{E_{hkl}} = S_{11} - 2\left[(S_{11} - S_{12}) - \frac{1}{2}S_{44}\right](\alpha^2\beta^2 + \alpha^2\gamma^2 + \beta^2\gamma^2), \quad (2.19a)$$

where $\alpha$, $\beta$, and $\gamma$ are the directional cosines of the *hkl* direction and the (1 0 0), (0 1 0), and (0 0 1) directions respectively. The directional cosines are given by:

$$\alpha = \frac{h}{H}, \beta = \frac{k}{H}, \text{and } \gamma = \frac{l}{H}, \quad (2.19b)$$

where $H = \sqrt{h^2 + k^2 + l^2}$. For the (1 0 0) plane, $H = 1$ and $\alpha = 1$, while $\beta = \gamma = 0$. For the (1 1 0) plane, $H = \sqrt{2}$ and $\alpha = \beta = 0.7071$, while $\gamma = 0$. For the (1 1 1) plane, $H = \sqrt{3}$ and $\alpha = \beta = \gamma = 0.5774$.

In a multiphase alloy, the value of the Young's modulus is usually calculated using the specific direction of the individual phases that form the alloy, and by their volume fractions. However, this is only possible if the scanning electron microscopic images of the sample are available. With the help of the images, graphs of number of pixels against grey scale is plotted using a suitable programming language such as Julia. Figures 2.9a and b show such a plot, which investigated the elastic constants of a two-phase isotropic Ti-Al alloy (Ongwen et al., 2021).

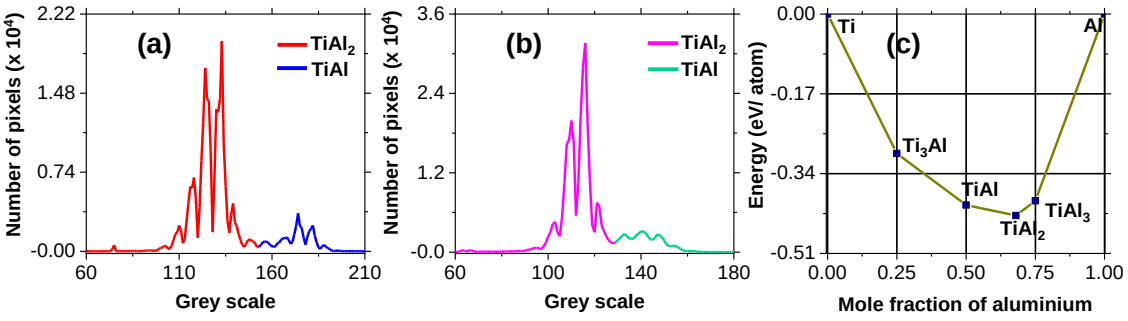


***Fig. 2.9: The requirements for the determination of the global Young's modulus: (a) curves enveloping the pixel histograms of Scanning Electron Microscopic images. They are representative of the fraction between TiAl and $TiAl_2$ for the $Ti_{32}Al_{68}$ alloy, (b) volume fractions between TiAl and $TiAl_2$ for the $Ti_{40}Al_{60}$ alloy, and (c) the computed phase diagram showing different stable phases of the Ti-Al binary alloy at different concentrations of aluminium (image obtained from the work by Ongwen et al., 2021)***

The approximate areas under the curves are then calculated through integration using the trapezoidal rule. In such multiphase alloys, a phase diagram is necessary (such as the one shown in figure 2.9c), as it will help in confirming the phases obtained from the experimental study, with the expected phases as per the concentrations of the reactants. For a two-phase alloy, a rule, called rule of mixtures, is applied. The rule can be written as (Zhou, Niinomi, & Akahori, 2004):

$$\mathrm{E} = \mathrm{V}_1\mathrm{E}_1 + (1 - \mathrm{V}_1)\mathrm{E}_2, \qquad (2.20)$$

where $E_1$ and $E_2$ are the Young's moduli of the two phases (1 and 2) respectively, and $V_1$ is the volume fraction of phase 1.

For a multiphase and anisotropic alloy, both the directional elastic moduli and the rule of mixtures are required (Ongwen, Ogam, Fellah, Otunga, Oduor, & Mageto, 2022). The elastic stiffness constants are first calculated, after which the calculation of directional Young's modulus follows. Finally, the global Young's modulus is performed through application of the rule of mixtures. This gives the effective Young's modulus value. The computed Young's modulus value obtained using this method then proves to match the value from the experimental studies fairly well. Figure 2.10 shows the 2D curves for the anisotropic Fe-Al binary alloys. As the figure depicts, Fe-Al is anisotropic, since all the 2D structures are not perfect circles.

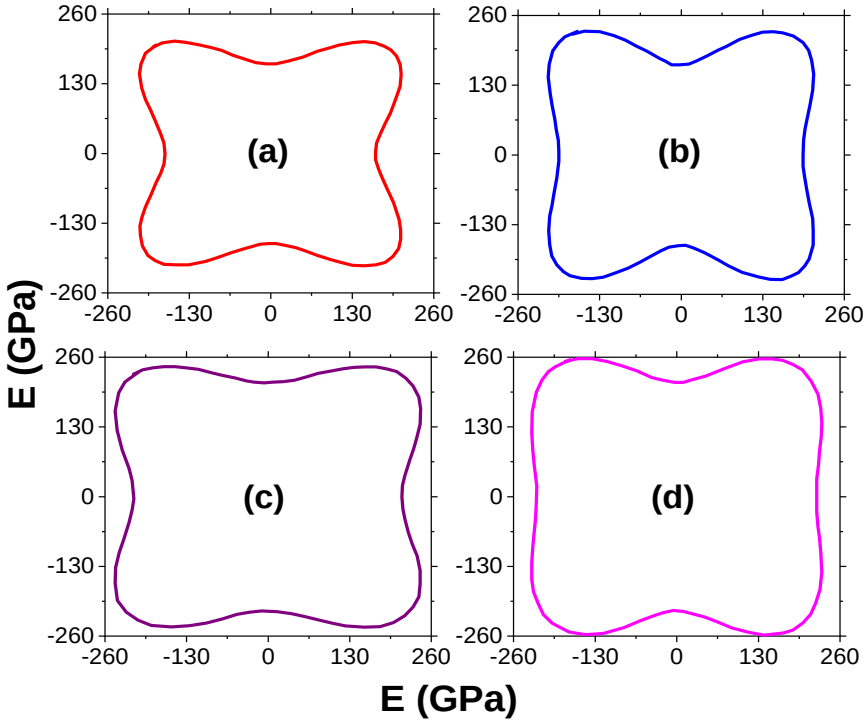


***Figure 2.10: The 2-Dimensional curves for the Young's moduli of $Fe_{42}Al_{58}$ and $Fe_{66}Al_{34}$ binary alloys along the (1 0 0) and (1 1 0) directions (data from the work by Ongwen et al., 2022): (a) $Fe_{42}Al_{58}$ along the [1 0 0] direction, (b) $Fe_{42}Al_{58}$ along the [1 1 0] direction, (c) $Fe_{66}Al_{34}$ along the [1 0 0] direction, and (d) $Fe_{66}Al_{34}$ along the [1 1 0] direction. The data was obtained using Perdew-Burke-Ernzerhof functional for SOLids functionals***

## 2.5 Thermal properties of materials

Thermal properties of a material are those that are associated with how well it conducts heat. They are the properties that a material demonstrates when heat is applied to it. The temperature at which a solid material transforms into a liquid at atmospheric pressure is known as the melting temperature ($T_m$). The solid and liquid phases in a material are in equilibrium at the melting point. The melting temperature depends on the strength of the bonds holding the atoms of the solid together, where stronger bonds result into higher values of the melting temperature.

Melting temperature and the elastic constant (Young's modulus) are related. Melting temperature is a measure of atomic bond strength. A greater melting temperature generally corresponds to a higher Young's modulus, and vice versa. Crystalline structures are typically more stable (thermally and chemically) than amorphous (glasses) ones because the crystalline lattice order is energetically favorable. Alumina is a suitable example, as its hexagonal, densely packed corundum structure is stable at high temperatures of up to 1925 °C in both oxidizing and reducing atmospheres. It also possesses excellent chemical stability. The alumina structure can only be attacked by wet fluorine gases, hydrofluoric acid, hot orthophosphoric acid, and alkali metal vapour (Hong, 2015).

The Lindemann melting criteria can be used to calculate the melting temperature using the relation (Lindemann, 1910):

$$T_m = cma^2\theta_D^2, \tag{2.21}$$

where *c* is a constant, *m* is the atomic mass, *a* is the length parameter chosen to be the cube root of volume per atom, and $\theta_D$ is the Debye temperature. The length parameter ($a$) is given by:

$$a = \sqrt[3]{\frac{V_{mol}}{N_A}}, \tag{2.22}$$

in which $N_A$ is the Avogadro's number, and $V_{mol}$ is the molar volume.

A periodic arrangement of atoms that make up a crystal lattice exists in almost all materials, with the exception of amorphous solids and glasses. A medium for distinctive vibrations is provided by the periodic crystal lattice that exists in solid materials. Phonons are quantized vibrational modes that exist between the lattice gaps. In order to understand how materials transport heat and electricity, the phonon theory is crucial. A particular kind of vibrational motion is also represented in quantum mechanics by phonons. Normal mode, a pattern of motion in which every component of the system moves sinusoidally and at the same frequency, is the name given to this kind of motion. Standing waves are an example of a continuous form of a normal mode, in which all spatial elements (*x*, *y*, and *z* coordinates) oscillate at the same frequency and phase, but with different amplitudes (Hassan, 2014).

Sound velocity, temperature characteristics, elastic properties, and optical properties of materials can all be explained by lattice vibrations. Lattice atoms in a solid oscillate in a process known as vibration around their equilibrium points. Due to the bonding between atoms, the equilibrium positions for crystals create a regular lattice. These nearby atomic vibrations are reliant on one another. Lattice waves are the usual modes of vibration in a regular lattice with harmonic forces between atoms. Lattice waves range in frequency up to 1,013 Hz or even higher. The wavelengths at very high frequencies, however, are on the order of the interatomic distance. Since these wavelengths are so short, there is no correlation between the motion of the nearby atoms. Instead, each atom moves around its average position in three dimensions with an average vibrational energy of $3k_BT$, where $k_B$ is the Boltzmann constant, and $T$ is the absolute temperature. Electrical resistance is created when lattice vibrations interact with free electrons in a conducting substance. The vibrational energy is the energy caused by the vibrating atoms in the lattice (Kosevich, 1999).

Gibbs free energy is one of the four thermodynamics potentials, the others being the internal energy, enthalpy, and the Helmholtz free energy. It is a quantity that is used to measure the maximum amount of work done in a thermodynamic system when the temperature and pressure are kept constant. It can be defined as the maximum amount of work that can be extracted from a closed system. This property was determined by American scientist Josiah Willard Gibbs in the year 1876 when he was conducting experiments to predict the behavior of systems when combined together or whether a process could occur simultaneously and spontaneously. The Gibbs free energy can be visualized as the amount of useful energy present in a thermodynamic system that can be utilized to perform some work (Shroeder, 2000).

Gibbs free energy is equal to the enthalpy (H) of the system minus the product of the temperature and entropy:

$$\mathrm{F} = \mathrm{H} - \mathrm{TS}, \tag{2.23}$$

which can also be expressed as:

$$\mathrm{F} = \mathrm{E} + \mathrm{pV} - \mathrm{TS}, \tag{2.24}$$

where $E$ is the internal energy (can also be given the symbol $U$), and $pV$ is the work done. The Gibbs free energy is also defined as the chemical potential that is minimized when a system reaches equilibrium at constant temperature and pressure. As soon as the system reaches thermal equilibrium, its derivative with respect to the response coordinate vanishes. Because of this, it serves as a useful criterion of spontaneity for processes that operate at constant temperature and pressure (Baierlein, 2012).

The temperature dependence of the Gibbs free energy for an ideal gas is given by the Gibbs-Helmholtz equation, and its pressure dependence is given by (Shroeder, 2000):

$$\frac{\mathrm{F}}{\mathrm{N}} = \frac{\mathrm{F^o}}{\mathrm{N}} + \mathrm{k_B T \ln}\frac{\mathrm{p}}{\mathrm{p_o}}, \tag{2.25}$$

where $p$ is the pressure applied to the system, and $p_o$ is the equilibrium pressure.

Equation 2.25 becomes, if the volume is known instead of the pressure:

$$\frac{F}{N} = \frac{F_o}{N} + k_B T \ln \frac{V_o}{V}, \tag{2.26}$$

where $F_o$ is the equilibrium Gibbs free energy, and $V_o$ is the equilibrium volume. More conveniently, the Gibbs free energy can be expressed as its chemical potential ($\mu$) as:

$$\frac{F}{N} = \mu = \mu_o + kT \ln \frac{p}{p^o}, \tag{2.27}$$

where $\mu_o$ is the equilibrium chemical potential.

Entropy, which is understood as a measure of the degree of disorder or unpredictability in a system, is a thermodynamic potential that expresses the inability of a system's thermal energy to be converted into mechanical work. As a result of a process that moves a system from its initial state $i$ to its final state $f$, the change in the entropy ($S_f - S_i$) of a system is expressed as:

$$\Delta S = S_f - S_i = \int_i^f \frac{dQ}{T}, \tag{2.28}$$

where *T* is the temperature of the system in kelvin, and *Q* is the amount of energy that is transported as heat to or from the system throughout the process. A change in entropy is therefore dependent on both the temperature at which the transfer occurs, and the amount of heat energy transmitted. Since *T* is always positive, the sign of $\Delta S$ is the same as that of *Q* (Shroeder, 2000).

Entropy is a state function. In other words, the entropy difference between states $i$ and $f$ must only be dependent on those states, and not at all on the process by which the system changed from one state to the next. Given that entropy measures how unpredictable a system is, a high value of entropy indicates that the system has a high degree of randomness. This implies that it is a challenge to anticipate the atomic or molecular state of the system. On the other hand, it is much simpler to anticipate the state of the system if the entropy is low. The minute characteristics of a system are not taken into account from a thermodynamic perspective on entropy. Entropy can also be used to describe how a system behaves in terms of the thermodynamic parameters such as temperature, pressure, and heat capacity.

The equilibrium state of the system takes into account the thermodynamic description (Baierlein, 2012). The term "specific heat at constant volume" is used to describe the amount of heat energy needed to raise the temperature of a unit quantity of a gas by 1 kelvin at constant volume. When the specific heat capacity is high, it allows for absorption of heat such as that released by a chemical reaction without significantly changing the temperature. This gives information as to how long the heating or cooling process will take under a given supply of heat.

$$c_v = \frac{\Delta Q}{n\Delta T}, \tag{2.29}$$

where $c_v$ is the specific heat capacity at constant volume.

Computational determination of thermal properties of materials can be determined within the scope of quasi-harmonic approximation (QHA) (Allen, 2020). In terms of the quantum statistical mechanics of an ensemble of harmonic oscillators, the Debye model for the heat capacity of solids describes the specific heat capacity of solids at low temperatures. At these temperatures, the solid is viewed as a gas of non-interacting quasi-particles, which perfectly conforms to the Bose-Einstein statistics, which relates to the phonons. The Debye temperature, also known as the characteristic temperature, is the temperature at which a pure cubic crystal's atomic heat is equal to 5.67 calories per gram of atoms per degree. It is a fundamental property of matter that governs a variety of solid properties, including specific heat, electric conductivity, thermal conductivity, X-ray spectral line widening, and elastic properties.

The internal energy of a harmonic oscillator with angular frequency in thermal equilibrium at temperature *T* is given by (Baroni, Giannozzi, & Isaev (2009):

$$E = \frac{h\omega}{4\pi} + \frac{h\omega}{2\pi e^{\frac{h\omega}{2\pi k_B T}} - 1}, \tag{2.30}$$

where $h$ is the Plank's constant, ω is the angular frequency, and $k_B$ is the Boltzmann constant. The specific heat capacity at constant volume of a solid is given by the derivative of equation 2.30 with regard to temperature of the sum over all possible values of the phonon momenta in the BZ as follows:

$$c_V = \frac{1}{V}\sum_{qv}\frac{h\omega}{2\pi}(\mathbf{b}, v)p'(\mathbf{b}, v), \quad (2.31)$$

where $\omega(\boldsymbol{b},v)$ is the angular frequency of the *v-th* mode (phonon) at point *q* in the BZ, and $p'(\boldsymbol{b},v)$ is given by the expression: $p'(\boldsymbol{b}, v) = \frac{\partial}{\partial T}\left[e^{\frac{\hbar\omega}{2\pi}(\boldsymbol{b},v)/k_B T} - 1\right]^{-1}$.

When the sum in equation (2.31) is transformed into an integral and three degenerate modes with frequencies of $\omega(\boldsymbol{b},v) = c|\boldsymbol{b}|$, where *c* is the sound velocity are assumed to exist at each point on the BZ, the resulting expression for the specific heat capacity at constant volume takes the form:

$$c_v(T) = \frac{1}{\phi}\,\frac{12\pi^4}{5}k_B\left(\frac{T}{\Theta_D}\right)^3, \quad (2.32)$$

where $\phi$ is the unit cell volume. The Debye temperature $\Theta_D$ is given by:

$$\Theta_D = \left(\frac{h}{k_B}\right)c\left(\frac{3}{4\pi\phi}\right)^3 \quad (2.33)$$

The Gibbs free energy of a crystal can be determined from the relation:

$$F(Z,T) = U(Z) + \frac{1}{2}\sum_{\mathbf{b}v}\frac{h(\mathbf{b},v|Z)}{2\pi} + k_B T\sum_{\mathbf{b}v}\log\left[1 - e^{\frac{h\omega(\mathbf{b},v|Z)}{2\pi k_B T}}\right], \quad (2.34)$$

in which *U(Z)* is the zero-temperature energy of the crystal as a function of *Z*, where *Z* represents any global static limitation on which vibrational frequencies may depend.

## 2.6 Acoustical properties of materials

Acoustic transmission through glass exhibits coincident and resonance effects. Monolithic glass has specific critical frequency at which the speed of incident sound in air matches that of the bending wave of the glass. Ordinary glass has poor sound insulation in the low frequency range (below 315 Hz), as has been asserted by Pigg and Weiss (1973). There is therefore need for modification of the ordinary glass so as to improve its acoustic insulation property. The appropriate design of facade with adequate sound insulation properties must consider the acoustic reduction index (R) value of the window panes (also referred to as the acoustic transmission loss, $\tau$), which depends on a number of factors, including: the type of glass, the dimensions of the glass, the type of joinery, the joints, and the seals in the window-opening system (Rasmussen, 2014).

Previous studies, including that by Miskinis, Dikavicius, Bliudzius, & Banionis (2015), have shown that laminated glass is a better acoustic insulator due to change of glass-air-glass resonant system. A study by Pickles, McCaig, Wood, Molyneux, & Makri (2017) also asserted that a medium between glass reduces transmission of noise into the house. In the study by Pigg and Weiss (1973), it was found out that optical coatings do not degrade the optical capability of the window panes. They also found out that a difference (higher) in the inner and outer layer thickness (for the case of a double layer window) gives better acoustic insulation.

Several methods have emerged, with the aim of reducing the transmission of sound between the inside and the outside of buildings. They can be put into three categories: double glazing, lamination, and using glass thickness. In double glazing, two glasses are used as the window pane, with air or a vacuum in between them. This arrangement significantly reduces noise and heat transmission ("Why double glazing", 2017). A space of 100-200 mm between the glasses is usually ideal. However, the disadvantage of such arrangement is that it may not be practical to be applied in a normal house, since thick walls will be required in order to accommodate the double-glazed window panes. In the laminated arrangement, one or both of the surfaces of the glass window pane is coated with a transparent material, usually a polymer such as polyvinyl butyral, thermoplastic polyurethane, or ethylene vinyl acetate (Schimmelpenningh, 2012).

The laminated window panes have an advantage over the double glazing in that besides reducing the noise, it also prevents the glass from shatter when it is hit. They are mainly used to prevent shatter of hurricane proof window panes. The laminated glass is more effective at reducing high frequency noise, such as those from aircrafts. A laminated glass with interlayer provides better acoustic insulation (Miskinis et al., 2015). Thicker glasses are better acoustic insulators compared to thinner ones, since the further the sound has to travel through the glass, the more the acoustic waves will drop off ("Thick glass windows, n.d."). Thicker glasses are good in reducing noise of low frequency such as those from common traffic. Usually, glass of thickness of above 4.8 mm are used for this purpose, and the value can go up to 20 mm. However, they fall short of the double-glazed window panes. Figure 2.11 shows the three technologies as applied in window panes.


***Figure 2.11: The three methods for noise control in window panes (a) double glazing (image from: https://www.priceyourjob.co.uk/double-glazed-window-cost/. 01/07/2020), (b) lamination (image from: https://www.cambridgedoors.com/windows/low-e-laminated-glass/. 21/05/2020), and (c) using glass thickness, a 20 mm glass as a window pane (image from: https://www.indiamart.com/proddetail/window-glass-17206597133.html. n.d)***

The ability to of a material to reduce noise as perceived by the human ear can be measured. The ability of a material to minimize the passage of sound through it is quantified using the sound transmission coefficient, which is defined as the ratio of the sound energy/ power transmitted through a material, to the sound energy/ power incident on the material. For a model of the acoustic transmission coefficient problem, consider two air spaces, one emitting and one receiving the sound, separated by a plate and surrounded by an infinite rigid baffle. The acoustic excitation is assumed to be of plane wave type in the emitting air space. The power transmitted into the receiving air space can then be represented in terms of the acoustic transmission loss, defined by the relation (Guyader & Lesueur, 1978):

$$\tau = \frac{P_T}{P_I}, \tag{2.35}$$

where $P_T$ and $P_I$ are, respectively, the acoustic power transmitted by the plate, and the incident acoustic power. The acoustic transmittance is related to the transmission loss $T$ by:

$$T = 10 \log\left(\frac{1}{\tau}\right) \tag{2.36}$$

Propagation of acoustic waves can be investigated using vibro-acoustic models, of which several have been employed in determining the acoustic transmission through plates (Arasan, Marchetti, Chevillotte, Tanner, Chronopoulos, & Gourdon, 2021). The common ones being the Kirchhoff-Love (Love, 1888) and the Resisner-Mindlin (Mindlin, 1951) (Resissner, 1945) (Henchy, 1947) theories, which are used to describe the vibro-acoustic behaviour of isotropic single-wall structures. Kirchhoff-Love theory applies to thin plates, while the Reissner-Mindlin theory applies to thick plates. Both models need modifications in order to explore complex structures such as those in double and triple glazing.

The basic equations for a rigid-frame medium (occupying $\Omega_1$) (figure 2.12) are the Euler equation and the law of mass conservation associated with the behaviour (or adiabatic) (Mansour, Fellah, Ogam, Cherif, Jelidi, & Jabrallah, 2016):

$$\rho_f \alpha(t) * \frac{\partial v}{\partial t} = -\nabla p; \frac{\beta(t)}{K_f} * \frac{\partial p}{\partial t} = -\nabla v \qquad (2.37a)$$

where $\rho$ is the density of the gas, $\alpha$ is the tortuosity, * represents the convolution operator, $v$ is the particle velocity , $p$ is the acoustic pressure, $\beta$ is the compressibility modulus of the fluid, $K_f = \gamma P_o$ is the compressibility of the gas saturating the pores, $P_o$ is the static pressure, and $\gamma$ is the specific heat ratio of the gas. Equation 2.37a comes from the fact that for two functions ($g$ and $f$) of class at least $C^1$ and $f'$ and $g'$ belong to $L^1$, then we have:

$$(f * g)' = f' * g = f * g' \qquad (2.37b)$$

Combining the two parts in equation (2.37a) gives the wave propagation equation in the time domain:

$$\frac{\partial^2 p(x,t)}{\partial x^2} - \left(\frac{\rho_f}{K_f}\right) \alpha(t) * \beta(t) * \frac{\partial^2 p(x,t)}{\partial t^2} = 0 \qquad (2.37c)$$

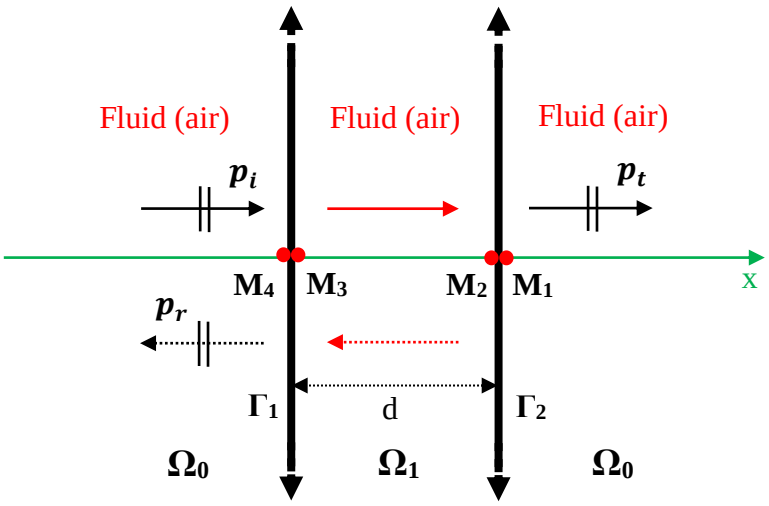


***Figure 2.12: Acoustic wave propagating in a medium (thin film) parallel to the x axis. $p_i$, $p_r$, and $p_t$ are the incident, reflected, and transmitted waves respectively. The red arrows (solid and dotted) represent the incident and reflected acoustic waves respectively in the fluid between the two window panes***

The solution to equation (2.37c) of the plane wave propagating along the *x* axis is sought in the frequency domain. This equation has a solution with time and space dependency of the form:

$$\mathrm{p(x,t)} = \tilde{\mathrm{A}}_{\mathrm{i}}\mathrm{e}^{\mathrm{i}(-\mathrm{k}_1\mathrm{x}+\,\omega\mathrm{t})} + \tilde{\mathrm{A}}_{\mathrm{r}}\mathrm{e}^{\mathrm{i}(\mathrm{k}_1\mathrm{x}+\,\omega\mathrm{t})}, \qquad (2.37\mathrm{d})$$

where $k_1(\omega) = \sqrt{p_f\alpha(\omega)\beta(\omega)\Big/K_f}$ is the wave number in the medium, and $\tilde{\mathrm{A}}_i$ & $\tilde{\mathrm{A}}_r$ are the complex amplitudes ($\tilde{\mathrm{A}}_i$ is the incident amplitude and $\tilde{\mathrm{A}}_r$ is the reflected amplitude). The coefficient $\alpha(\omega)\beta(\omega)$ is the refractive index of the medium that changes the wave velocity from $c_f = \left(p_f/K_f\right)$ in free space to $c_1(\omega) = c_f\Big/\sqrt{\alpha(\omega)\beta(\omega)}$ in the medium.

The specific acoustic impedance ($z$) characterizes the resistance of a medium to the passage of acoustic waves. It is the ratio between the sound pressure $p$ and the displacement speed $v$ of the particles in the medium $\left[z(x_2) = p(x_2)\Big/v(x_2)\right]$, where $x_2 = x(M_2)$. The pressure and velocity of the incident and reflected waves at the interface $\Gamma_2$ at the point $x_3 = x(M_3)$ (figure 2.12) in the medium are (Fellah, Z., Fellah, M., Ongwen, Ogam, & Depollier, 2021):

$$p(x_3) = \left(A_i^p e^{-ik_1x_3} + A_r^p e^{ik_1x_3}\right), \qquad (2.38\mathrm{a})$$

$$v(x_3) = \left(\frac{A_i^p}{z_c}e^{-ik_1x_3} - \frac{A_r^p}{z_c}e^{ik_1x_3}\right), \qquad (2.38\mathrm{b})$$

while the pressure and velocity of the incident and reflected waves at the interface $\Gamma_2$ at the point ($M_4$) in the fluid are:

$$p(x_4) = \left(A_i^f e^{-ik_fx_4} + A_r^f e^{ik_fx_4}\right), \qquad (2.38\mathrm{c})$$

$$v(x_4) = \left(\frac{A_i^f}{z_f}e^{-ik_fx_4} - \frac{A_r^f}{z_f}e^{ik_fx_4}\right), \qquad (2.38\mathrm{d})$$

where $x = x(M_4)$. The subscripts *i* and *r* denote the incident and reflected wave amplitude ($A$) respectively. The superscripts *f* and *p* are for the amplitudes in the fluid and the material medium respectively.

Solution of the acoustic wave problem usually involves boundary conditions. Continuity of pressure and velocity at $\Gamma_1$ & $\Gamma_2$ are: $p(x_1) = p(x_2)$, $\upsilon(x_1) = \phi\upsilon(x_2)$, $p(x_4) = p(x_3)$, and $\upsilon(x_4) = \phi\upsilon(x_3)$, where $x_1 = x(M_1)$. The velocity of the transmitted wave is $v(x_1) = {p(x_1)}/{Z_f}$. The thickness of the TF layer is $d = x_2 - x_3$. The origin $x = 0$ is chosen as the point at the beginning of the TF layer. The points $x_3 \approx x_4 \approx 0$. The resulting matrix equation is a linear system of the form **AX** = **B** (Mansour et al., 2016):

$$\begin{bmatrix} x_f^{-1} & \frac{\vartheta}{x_c} & -\frac{\vartheta}{x_c} & 0 \\ 1 & -1 & -1 & 0 \\ 0 & \frac{e^{-ik_1 d}}{x_f} - \frac{\vartheta e^{-ik_1 d}}{x_c} & \frac{e^{ik_1 d}}{x_f} + \frac{\vartheta e^{ik_1 d}}{x_c} & 0 \\ 0 & -e^{-ik_2 d} & -e^{ik_2 d} & e^{-ik_f d} \end{bmatrix} x \begin{bmatrix} A_r^f \\ A_i^P \\ A_r^P \\ A_t^f \end{bmatrix} = \begin{bmatrix} \frac{A_i^f}{x_f} \\ -A_i^f \\ 0 \\ 0 \end{bmatrix}, \qquad (2.39)$$

which is then solved to give the reflection and transmission coefficients ($R^{EFM}$ and $T^{EFM}$) respectively as:

$$R^{EFM}(\omega) = \frac{A_r^f}{A_i^f} = \frac{i(x_r^2 - \phi^2)\sin(k_1 d)}{i2(x_r^2 + \phi^2)\sin(k_1 d) + x_r \phi \cos(k_1 d)}, \qquad (2.40a)$$

$$T^{EFM}(\omega) = \frac{A_t^f}{A_i^f} = \frac{2\phi x_r e^{ik_f d}}{i2(x_r^2 + \phi^2)\sin(k_1 d) + x_r \phi \cos(k_1 d)}, \qquad (2.40b)$$

where the superscript *EFM* on *R* and *T* refer to "Equivalent Fluid Model".

## 2.7 Substrate materials used in the fabrication of MEMS devices

### 2.7.1 Silicon

Si is the most dominant substrate material for the manufacture of MEMS (Pratap & Arunkumar, 2006). This is because Si: is abundant; is relatively cheap and can be processed to unparalleled purity; is ideal for high levels of MEMS precision because it has high definition; and can accurately reproduce Si device forms via photolithography. Another factor that makes Si the most preferred substrate material for MEMS is the available and developed surface micromachining technology for its processing (Auciello, Birrell, Carlisle, Gerbi, & Xiao, 2004).

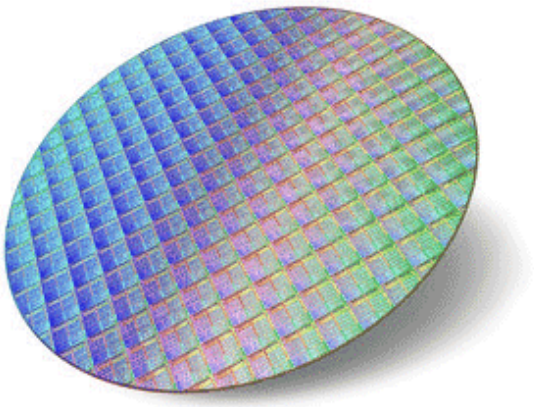

***Figure 2.13: A 60 mm silicon wafer used for manufacture of electronic devices (image from https://www.electronicsandyou.com/blog/top-silicon-wafer-manufacturing-companies-in-the-world.html. 06/11/2022)***

Figure 2.13 shows a 60 mm Si wafer, which is utilized in the manufacture of electronic devices. Si wafers are clean and free of impurities and microparticles. These qualities are ideal for manufacture of modern electronics. Depending on the intended specific purpose, the purity of the Si wafer can be doped appropriately so as to modify its electrical and electronic properties, a process which is very essential for specific applications. Among the possible dopants to Si are aluminium, gallium, indium, nitrogen, and boron (WaferPro, 2007). However, the existing demerits of Si, which include impurity, non-flexibility, brittleness, and non-piezoelectric nature, limit its commercial deployment. Table 1.1 displays some of the electrical, mechanical, and thermal properties of Si.

### 2.7.2 Silicon carbide

Si, the most dominant substrate material for MEMS fabrication, is unsuitable for MEMS that operate in demanding circumstances, including high temperatures of above 500 °C. For those severe environments, there is a significant demand for sensors and actuators. For example, the devices in combustion processes, gas turbine control, and oil industry require substrates that can operate under high-temperature conditions without having their properties compromised. SiC is suitable for these harsh environments, since it has higher hardness, better wear resistance, good thermal conductivity, and chemical inertness (Jiang & Cheung, 2009). Some of the properties of SiC include: density of 3.21 g/cm$^3$, bulk modulus of 220 GPa, shear modulus of 179 GPa, Young's modulus of 448 GPa, excellent physical stability, Poisson's ratio of 0.17, Vickers hardness of 32 GPa, Pugh's ratio of 1.23, Debye temperature of 1194.8 K, melting temperature of 3103 K, entropy of 213.02 J/mol/K, and specific heat capacity of 750 J/kg/K (Mehregany et al., 2000) (Mehregany, Zorman, Rajan, & Wu, 1998) (Shackelford, Han, Kim, & Kwon, 2015) (Munro, 1997) (Peng et al., 2012). A SiC wafer is shown in figure 2.14.

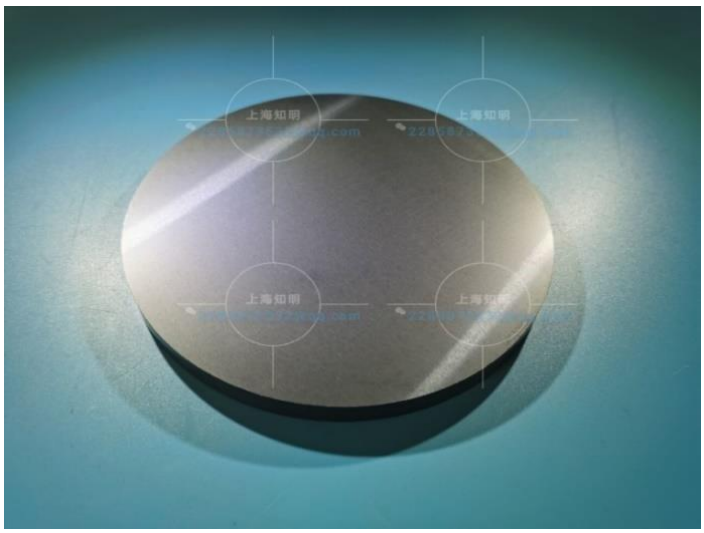

***Figure 2.14: A 6-inch Dia 153 mm single crystal silicon carbide wafer (image from: https://www.sapphire-substrate.com/sale-13130258-6-inch-dia-153mm-single-crystal-sic-silicon-carbide-wafer.html. n.d)***

Since SiC has a higher ratio of Young's modulus to density than Si and Ga-As, it is better than Si for fabrication of micromechanical oscillators, high-sensitivity sensors, and resonators for use as frequency filters in high-performance communication transceivers (Nguyen & Clark, 1997). Unwanted tear and adhesion is one of the Si MEMS reliability problems. SiC exhibits greater tribological qualities over Si, since it is a more durable material. Thus, it can be used as a micromotor as well as a coating material for Si MEMS, since it provides exceptional wear resistance (Yasseen, Wu, Zorman, & Mehregany, 2000).

Although SiC has a number of benefits over Si as a substrate for manufacture of MEMS devices due to its lower threshold voltage for low-voltage applications at lower frequency, investigations on SiC diodes demonstrate that Si-based MEMS devices are better than SiC-based devices in the steady-state zone. Due to its physical toughness, chemical inertness, and low diffusion coefficient of other contaminants, doping presents another challenge in the production of SiC devices. Moreover, its high production and processing costs, which are caused by the complex furnace procedures and processing needed to anneal the flaws, also pause a challenge to its use as a MEMS substrate. The methods for producing Si that are currently available may not be appropriate for SiC, since its thermal and electrical properties are very different from those of Si. Consequently, the inability to produce big wafers with few faults and the absence of appropriate production procedures lead to high SiC manufacturing costs (Kondrath & Kazimierczuk, 2010).

### 2.7.3 Gallium arsenide

Ga-As has emerged as a better MEMS substrate to Si, since it has a variety of technological and material benefits. These properties include strong electron mobility and direct band gap transition, resonant tunnelling, and fractional quantum Hall effect (Leclercq, Ribas, Karam, & Viktorovitch, 1998). The ability to alloy suitable ternary and quaternary compounds is a key characteristic of Ga-As. One of the disadvantages of Ga-As is that it has a narrow band gap. Because of this, it cannot do well in situations with high temperatures, high voltages, or high power (Kondrath & Kazimierczuk, 2010).

Some of the properties of Ga-As include: density of 5.36 g/cm$^3$, bulk modulus of 75 GPa, shear modulus of 33 GPa, Young's modulus of 303 GPa, Poisson's ratio of 0.36, Vickers hardness of 6.9 GPa, Pugh's ratio of 2.272, Debye temperature of 360 K, melting temperature of 1513 K, entropy of 63.36 J/mol/K, and specific heat capacity at constant volume of 46.23 J/mol/K (Diakite et al., 2017) (Hjort, Soderkvist, & Schweitz, 1994) (Mishra & Upadhyaya, 2012) (Guler, E. Guler, M. Aldirmaz, & Kara, 2016). A Ga-As wafer is shown in figure 2.15.

***Figure 2.15: A gallium arsenide wafer (image from: https://vitalchem.com/product/gallium-arsenide. n.d)***

MEMS based on Ga-As are currently being developed for microsensors and microactuators such as tuneable optoelectronic devices, as well as accelerometers (Hotovy et al., 2008). The main advantage of Ga-As over Si as a substrate for manufacture of MEMS is that it offers almost twice the efficiency of Si. Its other advantages include: insensitive to heat compared to silicon, high thermal stability, operates over a wide temperature range, and resistance to radiations. However, it has its drawbacks, which include: it does not have a natural oxide like that in Si, single Ga-As substrates are relatively expensive, and it has small size ingots of about 4 inches.

### 2.7.4 Silicon nitride

In MEMS devices such as the carrier of tuneable mirrors in Fabry-Perot filters, $Si_3N_4$ has been used as a structural material at relatively low temperatures (Winchester & Dell, 2001). With excellent properties, $Si_3N_4$ films are good at preventing the diffusion of ions like sodium and water. Due to its capacity to resist oxidation and corrosion, it can be utilized as a mask for ion implantation, deep etching, and electronic insulating layer (Zheng, Zhou, Wang, Chen, & Xue, 2013). The following are some of the properties of $Si_3N_4$: density of 2.37 g/cm$^3$, bulk modulus of 200 GPa, Shear modulus of 65.3 GPa, Young's modulus of 140-310 GPa, Poisson's ratio of 0.23, Vickers hardness of 43 GPa, Pugh's ratio of 3.1, melting temperature of 2173 K, and specific heat capacity of 673 J/kg/K (Tanakaa et al., 2002) (Huang, Suvorova, Winchester, Dell, & Faraone, 2006) (Ji & Yu, 2005) (Cerenius, 2004). Figure 2.16 shows a $Si_3N_4$ wafer.

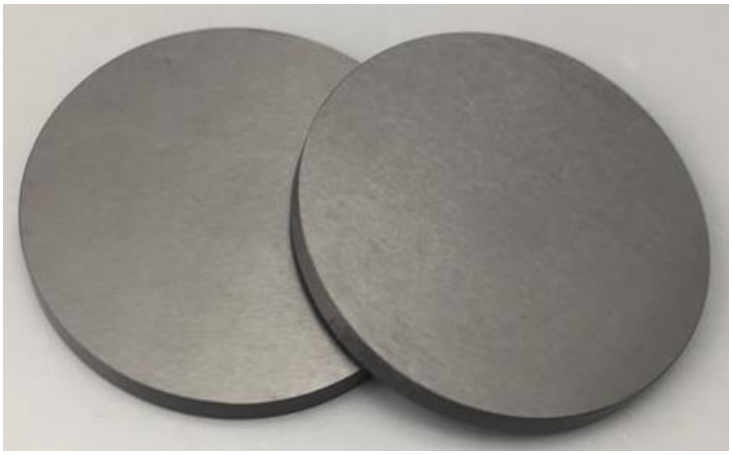

***Figure 2.16: A silicon nitride wafer-3X ceramic parts (image from: https://www.3xceramicparts.com/silicon-nitride-ceramic/silicon-nitride-wafer. N.d)***

$Si_3N_4$ membranes have been applied in a variety of MEMS applications. These include: optical beam steering and waveguides, microphones, and thermal isolation for gas detection in the chemical industry (Lazerand & Lishan, 2014). However, one major limitation that $Si_3N_4$ has is the high intrinsic film stress, which has limited both optical confinement and quality factor of ring resonators. Total or partial removal of $Si_3N_4$ on one of the sides of the wafer causes the wafer to bow or warp, and the magnitude of the warp depends on among other factors, the thickness of the $Si_3N_4$, and the thickness of the wafer (Luke, Dutt, Poitras, & Lipson, 2013).

### 2.7.5 Diamond

In contrast to Si, diamond has excellent tribological performance, outstanding thermal stability, much higher mechanical strength, and exceptional chemical inertness. These properties make it a potential MEMS material of choice (Auciello et al., 2004). Diamond also exhibits linear electromechanical response, low charge-trap dielectric, low temperature coefficient of frequency, and low heat dissipation. Furthermore, surface properties such as low adhesion energy and resistance to tribo-electrical foiling in active electrical contacts hold the possibility of making electronics that are less sensitive to environmental conditions (Auciello et al., 2008).

***Figure 2.17: A first-300 mm diamond wafer (image from: https://www.eenewseurope.com/en/first-300mm-cmos-diamond-wafer/. 27/07/2021)***

Diamond has been used in the fabrication of mechanical sensors, given that it has a very high Young's modulus of up to 1,145 GPa and a high fracture strength of up to 4.7 GPa; and in thermal actuators due to its high thermal conductivity (Luo, Fu, Le, Williams, Spearing, & Milne, 2007). Other properties of diamond include: density of 3.51 g/cm$^3$ bulk modulus of 449.8 GPa, shear modulus of 524.9 GPa, Poisson's ratio of 0.078, Vickers hardness of 82.4 Gpa, Pugh's ratio of 0.857, Debye temperature of 1880 K, melting temperature of 4200 K, entropy of 2.4 J/mol/K, and specific heat capacity of 6188.1 J/kg/K (Victor, 1962) (Spear & Dismukes, 1994). Presented in figure 2.17 is a diamond wafer.

The integration of diamond films with other materials is a significant obstacle for diamond MEMS. Because diamond films are created with big grains, high internal stress, poor and intergranular adhesion, and extremely rough surfaces, traditional chemical vapour deposition techniques are not suitable for diamond MEMS applications. Diamond-like films provide an alternative. However, they are created using physical vapour deposition techniques, which are inappropriate for conformal deposition on features with high aspect ratios. Moreover, they typically lack the exceptional mechanical properties of diamond (Auciello et al., 2004).

### 2.7.6 Polymers

Si substrates are rigid, opaque, and also have insufficient area for processing (Patil, Chu, & Conde, 2008). Thus, they are not ideal for the fabrication of transparent flexible MEMS devices. Polymers are generally plastics with low mechanical strength, low Young's modulus, low melting temperature, and poor electrical conductivity. The use of polymers in the fabrication of MEMS devices is a very fast-growing technology due to the need for flexible MEMS for use in areas such as in the medical field. For applications that require mechanical flexibility, durable integrated circuits, cheaper cost, and vast area flexibility, microelectronics on flexible substrates are of tremendous interest. The vast differences in the structure and characteristics of the polymers used for MEMS substrates allow for a wide range of uses. The polymers such as Langmuir-Blodgett (LB) films are conducting and are already being utilized in MEMS sound transducers in air and water, and also in tactile sensors (Kim & Meng, 2019).

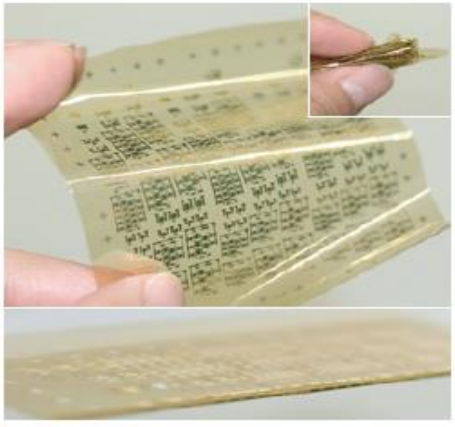

***Figure 2.18: Flexible organic thin film transistors having a functioning polyimide substrate that is 12.5 µm thick (image from the work by Sekitani et al., 2010)***

Polyimides are desirable for fabrication of microbolometers, position-sensing detectors, polysilicon strain gauge arrays, and MEMS temperature sensor arrays, owing to their exceptional mechanical strength, thermal and electrical insulation, excellent high-temperature stability, and good chemical inertness (Xiao, Che, Li, & Wang, 2008). Figure 2.18 shows organic thin film transistors fabricated on a foldable polyamide substrate (image from the work by Sekitani, Zschieschang, Klauk, & Someya, 2010). One of the main shortcomings of polymers as substrates for manufacture of MEMS is their poor electrical and thermal conductivities. They require structural modifications, which are not only tedious, but also costly. Additionally, across a certain temperature range (low glass transition temperature and melting temperature), their mechanical properties change significantly as well as being gas/ moisture permeable, which implies that they require hermetic packaging (Li, 2012).

Due to the diverse nature of polymers, there are a variety of their properties. Atomic force microscopic measurements of the mechanical characteristics of discogenic-DNA complex LB films reveal Young's moduli of 54 and 160 MPa for the PyTp and PyTp-DNA complex films respectively (Nayak & Sureh, 2009). Hess (2011) conducted research on the incorporation of materials that are incompatible with manufacturing processes for microfabricated polymer-based brain interfaces, and found an average Young’s modulus of 848 MPa. Finot et al. (2008) found a Young’s modulus of 250-300 MPa, and a Poisson ratio of 0.1 to 0.8.

## 2.8 MEMS applications

### 2.8.1 MEMS mechanical sensors

MEMS mechanical sensors are used to detect and also to measure external stimuli such as pressure and temperature. The sensor then responds to the stimuli with the help of some mechanical actions. Fabrication of MEMS integrated circuits is mainly done on a Si substrate. Here, light materials are placed onto the substrate. The common types of MEMS sensors in the market are: accelerometers, gyroscopes, magnetic field sensors, and pressure sensors. MEMS pressure sensors (circuit shown in figure 2.19a) are of two types: piezoresistive and capacitive. Both need the presence of a thin, flexible layer that deflects when under pressure, after which the displacement is measured.

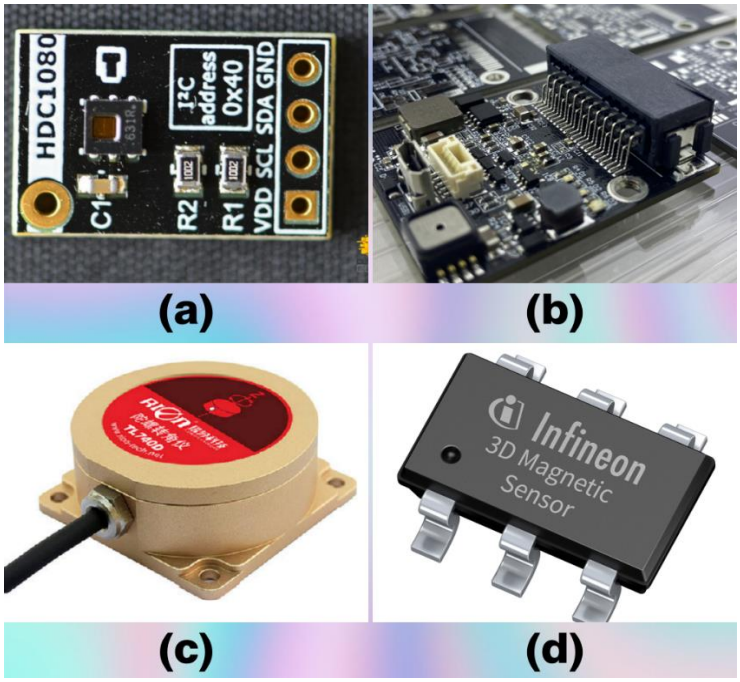


***Figure 2.19: Some types of Micro-Electromechanical Systems sensors: (a) humidity/ pressure sensor (image from: https://electronics.semaf.at/BME280-I2C-or-SPI-Temperature-Humidity-Pressure-Sensor. n.d), (b) accelerometer circuit (image from: https://www.twovolt.com/2016/11/29/dual-axis-accelerometers-signal-conditioned-voltage-outputs-using-adxl203-circuit-pcb-layout/dual-axis-accelerometers-with-signal-conditioned-voltage-outputs-using-adxl203-circuit-pcb-layout-sch/. 25/12/2016), (c) gyroscope (image from: MEMS gyroscope - TL740D - Shenzhen Rion Technology Co.,Ltd - single-axis / high-resolution / digital (directindustry.com.n.d), and (d) 3-Dimensional Micro-Electromechanical Systems magnetic field sensor (image from: https://rutronik-tec.com/infineon-3d-magnetic-sensor-tlv493d-a1b6/. 06/08/2016)***

Conductive layers are deposited on to the bottom of a cavity in a MEMS capacitive sensor to create a capacitor. When the diaphragm is deformed, the spacing between the conductive layers changes, which in turn, changes the capacitance. MEMS piezoresistive sensors are used in automotive, medical, and household appliances. In these sensors, the sensing elements are fabricated directly onto the diaphragm. Whenever there is a change in the resistance of the conductors, pressure is applied, which leads to a change in the length of the conductor (Bogue, 2007) (Shaikh & Shitole, 2012) (Reilly, Leach, Cuenat, & Awan, 2006).

Accelerometers are devices that measure proper acceleration (an object's rate of acceleration in its own instantaneous rest frame). They are used to monitor vibrations in rotating machines, in tablet computers, and in digital cameras for upright display of images. They are also used for stabilizing flight in drones, and in game controllers. In medicine, chest compression depth is measured using accelerometers and also in foot pods, which determines the speed and distance of the runners wearing the foot pods. Accelerometers are mainly fabricated on Si substrates (Tinder & Richard, 2007). Figure 2.19b shows a circuit of an accelerometer.

A gyroscope is a device that is used to measure or to maintain orientation and angular velocity. They are packaged in ways similar to the integrated circuits. They are used in automotive industry to detect errors in yaw sensors. Other applications include: entertainment, where they are used to detect rotational movement; in industry to control vibrations in robots; in photography to produce clear images; and in aviation to position spacecraft (Acar & Shkel, 2008). The main aim of the vibratory gyroscopes is to have a drive oscillator that should not only generate a constant momentum, but also maintain it. Moreover, the gyroscope should have a sense-mode accelerometer that measures the Coriolis force. The properties of interest in making gyroscopes are the: stiffness, Poisson’s ratio, shear modulus, and Young’s modulus. Si is impervious to fatigue, implying that it can withstand enormous cycles without failure, a property which is very essential for vibratory gyroscopes (Acar & Shkel, 2008). Figure 2.19c shows a MEMS gyroscope.

A MEMS magnetic field sensor (figure 2.19d) (also known as a magnetometer) is a device used for detecting and measuring magnetic fields. The principle of operation of most magnetometers is the detection of the Lorentz force. The three main types of MEMS magnetic field sensors are: resonance, fluxgate, and Hall sensors. When micromachined structures are activated at one of their resonating modes, the resonant sensors apply Lorentz force on those structures. The resonant sensors have a high sensitivity of up to 1 nT. The fluxgate sensors on the other hand, apply the principle of induction in their operation. They consist of excitation and sensing coils, which wrap round a ferromagnetic core. The fluxgate sensors mainly sense the static as well as the low frequency magnetic fields. They have a higher resolution of up to 100 pT. For the Hall sensors, they are based on the principle of transduction. They are used mainly to measure constant or varying magnetic fields. The sensitivity of the Hall sensors goes up to 1 μT (Todaro & Vittorio, 2012) (Marauska, Jahns, Greve, Quandt, Knochel, & Wagner, 2012) (Chen, Li, & Xu, 2019).

MEMS technology offers many advantages compared to the other printing technologies, which include accurately located and precisely defined jet nozzles, and creation of tightly packed and highly integrated jetting structures. Other advantages include: low power consumption; simplicity and ease of incorporation into systems; resistance to shock, radiation and vibrations; tolerance to shock; and low-cost mass production. The print heads are usually fabricated on Si wafers (Lau & Shrestha, 2017). The print heads need piezoelectric substrates. The desirable properties of the substrate should be: electrical charge, mechanical oscillation, and acoustic oscillation (Mawatari, Sameshima, Miyai, & Matsuda, 2005).


***Figure 2.20: Some industrial applications of MEMS: (a) industry's multi-output Micro-Electromechanical Systems clock generator (image from: https://www.5gtechnologyworld.com/industrys-smallest-multi-output-mems-clock-generator/. 06/11/2018), and (b) a Micro-Electromechanical Systems print head (image from: https://imieurope.com/inkjet-blog/2016/6/6/xaar-joins-the-si-mems-printhead-club. 06/06/2016)***

MEMS sensors have numerous applications such as in automotive, military, industrial (figure 2.20a), consumer, space exploration, as well as in biotechnology. Commercial applications of the sensors include accelerometers in modern cars, inkjet printers (figure 2.20b), consumer electronics, and in personal computers. MEMS printers are mechanically robust and chemically inert devices. Genomic, proteomic, drug delivery analysis, molecular assembly, tissue engineering, biosensor development, and nanoscale imaging, are all the areas where bioMEMS are applied in the medical industry. They are fabricated using the conventional micromachining techniques. The high material and processing costs make Si-based bioMEMS less attractive. Moreover, the brittle nature of Si is a serious issue for the fabrication of most of the bioMEMS (Grayson et al., 2004). Figure 2.21a and b show some applications of MEMS sensors in the medical field.

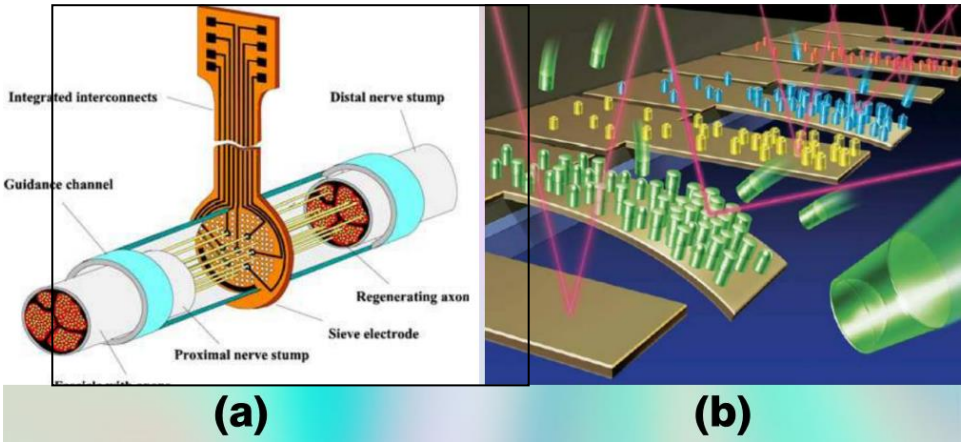


***Figure 2.21: Some applications of MEMS in the medical field: (a) a schematic diagram of the placement of a Micro-Electromechanical Systems sieve electrode in the guidance channel (image from: James, Mannoor, & Ivanov, 2008), and (b) a schematic illustration of a cantilever sensor array principle, which is functionalized with different sensing layers (image from: https://bmwtraderonline.info. n.d)***

### 2.8.2 MEMS Microactuators and resonators

A micro actuator is a servomechanism which supplies and transmits a given amount of energy for the operation of another mechanism or system. Among the conditions to be met by a micro actuator are: high precision, low power consumption, large travel, and fast switching. There are numerous classes of microactuators, including: electrostatic, electromagnetic, piezoelectric, fluid, and thermal (Li & Chew, 2014). Thermal microactuators are ideal as a bridge to the large and linear displacement, and low-power MEMS actuators (Seng, Dahari, Sidek, & Miskam, 2009). They are mainly used as micro-grippers, scanning probe arrays, and micro legs (Greminger, Sezen, & Nelson, 2005) (Zheng & Lu, 2007) (Bonvilain, Coudevylle, Blind, & Chaillet, 2001). Figure 2.22a shows a thermal actuator.

Resonators are mechanical structures that vibrate at their natural frequencies as a result of external excitations. The external excitations can be caused by laser, piezoelectric field, magnetic field, electrostatic field, or mechanical vibrations. They are used for real-time clocks in power management system chips, as well as in watches (Cioffi & Hsu, 2005). MEMS resonators usually have very low erythrocyte sedimentation rate properties that cannot be achieved with the conventional quartz crystal resonators. Without the requirement for active devices to rectify the starting frequency and temperature-related frequency shift, MEMS resonators offer outstanding frequency accuracy and stable temperature characteristics, a property that is very useful to consumers in reducing power consumption, weight, and mounting rate. These properties make them perfect for a variety of applications, including inclusion into integrated circuits, lighting, industrial equipment, and small, low-profile devices. Figure 2.22b shows a MEMS resonator that integrates a capacitor.

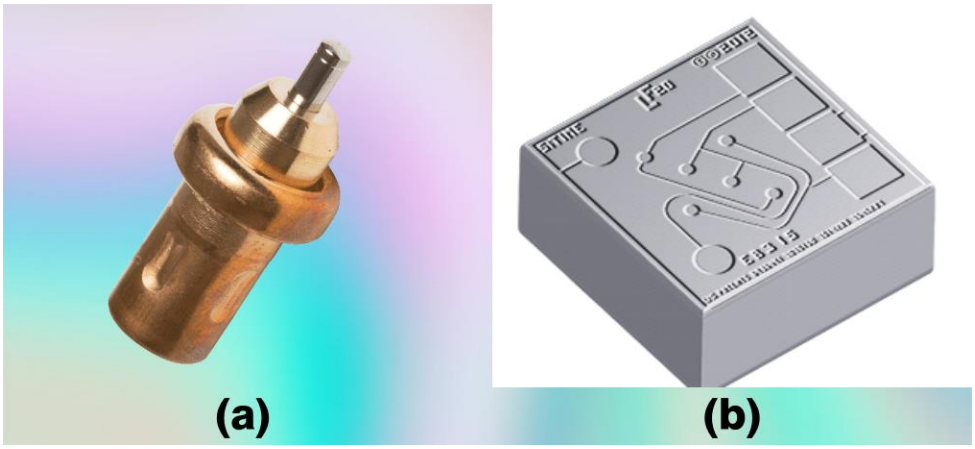


***Figure 2.22: Some MEMS actuators and sensors: (a) a Micro-Electromechanical Systems thermal micro actuator (image from: https://www.vernet-group.com. n.d), and (b) a tiny Micro-Electromechanical Systems integrating a capacitor (image from: https://www.electronics-lab.com. n.d)***

### 2.8.3 MEMS Micromotors and coating materials

A micromotor is a micrometre-sized particle that can move by itself autonomously in a specific direction. Three types of MEMS micromotors exist: electrostatic, piezoelectric, and electromagnetic. Of these, electrostatic ones are the most common (Merzaghi, Koechli, & Perriard, 2015), although the electromagnetic ones have emerged recently, and are proving to be better than both electrostatic and piezoelectric micromotors. Their main advantage is the larger torque capability compared to the other two (Ding, Liu, Du, Guo, Qian, & Gerada, 2015). Electromagnetic MEMS micromotor systems require ferromagnetic materials, which is not found in most microelectronics. The rotating parts of the micromotors require hard materials which do not wear out easily due to friction, as most MEMS operate in areas where there are high functional activities and stress.

For those MEMS that operate under harsh environmental conditions such as in extreme temperatures and abrasive liquids, there is need for hard materials that can withstand these conditions. Some circumstances also lead to degradation as well as malfunction of the MEMS devices. Moreover, most micro-components tend to experience stiction (friction which affects stationary surfaces that are being set into motion when they operate) (Chana et al., 2012). In these cases, the MEMS components are usually protected by depositing TFs of the materials to cover the substrate as the MEMS are being processed. The layer of the coating needs to be very thin (as thin as 5 nm) for most MEMS components so as to minimize stiction effectively, while at the same time, providing insulation to the components. If the coating layer exceeds 100 nm, it interferes with the performance of the MEMS components, which make them not effective for the intended purpose of the MEMS (Ashurst, Carraro, & Maboudian, 2004).

There are numerous methods of coating MEMS, including spraying, dipping, and vapour deposition. However, vapour deposition has proved to be more effective, since it does away with the wet deposition techniques required for coatings such as epoxy, silicone, or urethane, which have less applications in the MEMS manufacture. Other deposition methods for introducing layer coatings to MEMS include: physical vapour deposition, which has been utilized in coating diamond-like carbon; casting; electrodeposition; and thermal deposition.

Whereas physical vapour deposition results into coatings with low stiction levels and high micro-hardness, it produces low-quality adherence of the coating layer to the substrate, which is characterized by higher resistivity and more defects (Tamulevicius, 1998). Casting on the other hand, produces coatings with thick layers in the range of 100 nm, which are not good for most MEMS. Electrodeposition method is only applicable to materials that are electrically conductive. Thus, the substrates on which this method is applied usually need an already electrically-conducting layer prior to deposition. Usually, chromium, tungsten, gold, and nickel are used for this purpose (Korlyakov, Mikhailova, & Serkov, 2018) (Luchinin et al., 1999).

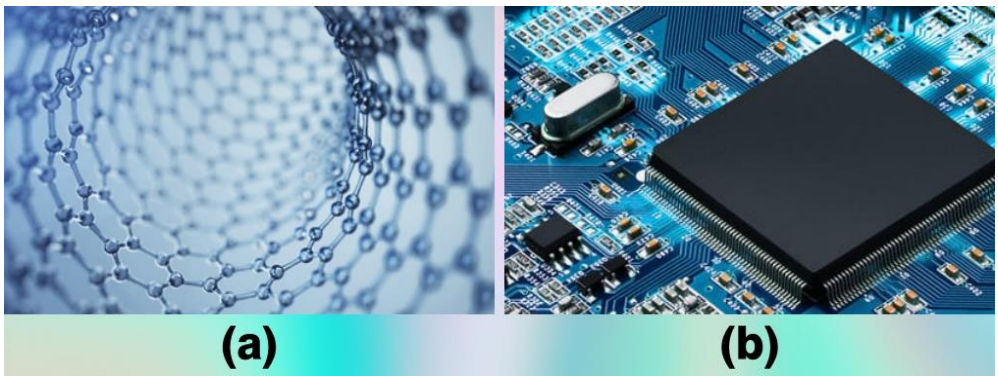


***Figure 2.23: MEMS coating materials: (a) a 2-Dimensional structure of a parylene molecule (image from: https://www.paryleneconformalcoating.com/industries/mems/#. 10/03/2019), (b) a Micro-Electromechanical Systems chip coated with parylene (images from: https://www.paryleneconformalcoating.com/conformal-coating-education-center/parylene-removal/. 02/10/2020)***

The most common coating material for MEMS is parylene, which is preferred because: it can be made thin (up to 5 nm), which is ideal for reduction of stiction; it shields the MEMS from elements that are a part of it yet could destroy it, such as acids, salt and chemicals; it provides a uniform layer of the coating, which conforms to the topography of the MEMS and gives total protection; it is resistant to ultraviolet light, which can damage the components of the MEMS; and it offers electrical insulation. Because parylene has a good dielectric strength, and low dielectric constant and loss, it prevents these elements from getting into contact with MEMS (Diepgen et al., 2019). Figure 2.23a shows a 2D structure of parylene, while figure 2.23b is an electronic MEMS chip that has been coated with parylene to protect it against stiction.

# CHAPTER THREE
# MATERIALS AND METHODS

## 3.1 Introduction

This chapter is divided into two major sections. The first section deals with the experimental study, while the second section deals with the computational study. In the first section, the process of cleaning the glass substrates that were used in depositing the TFs, the preparation of the precursor solutions at different concentrations of Cd and Sn, and the deposition of the TFs at the different concentrations are discussed. The measurements taken, including those of the thicknesses of the deposited TFs, the chemical composition, and those of the XRD are also discussed. In the second section, the convergence criteria, the optimization of the lattice parameters as well as the atomic coordinates, the development of the stress-strain method for determining elastic stiffness constants of materials, and the calculation of the acoustical, mechanical, and thermal properties of CTO are explained.

## 3.2 Experimental study

### 3.2.1 Substrate cleaning

Aqua Regia was used as the method of cleaning the substrates in this study. This method was chosen because it produces very clean surfaces, which are free from solvents or traces of metals (Shugar & Ballinger, 1996). Ordinary microscope glass slides of dimensions 25.4 mm by 76.2 mm by 2 mm were used as the substrates. The scheme in figure 3.1 shows a summary of the process of cleaning the glass substrates. While wearing acid-proof gloves, safety googles and a lab coat, the Aqua Regia was prepared by mixing stock solutions of HCl and nitric (V) acid ($HNO_3$) at a ratio of 3:1 by volume, that is: 600 ml of stock slution of HCl and 200 ml of stock solution of $HNO_3$ in a polypropylene container, giving a total volume of 800 ml of the solution mixture. This was done in the open air so as to avoid poisoning by chlorine and nitrosyl chloride gases that fume from the solution mixture.

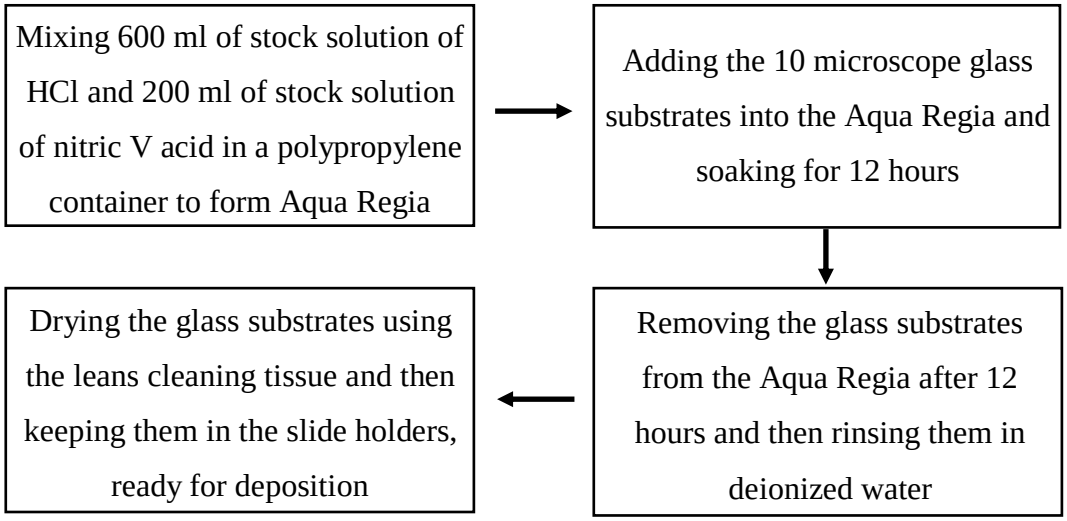


***Figure 3.1: The process of cleaning the microscope glass substrates***

The microscope glass slides were then immersed into the Aqua Regia in the polypropylene container to soak for 12 hours, after which they were removed from the Aqua Regia solution and then rinsed in deionized water. During the rinsing process, latex gloves were worn so as to eliminate direct contact with the slides, which would otherwise have contaminated the slides. Since Aqua Regia is slow acting, it was necessary to leave the slides soaked for such a long time so as to ensure that there no contaminants remaining on their surfaces. To dry the glass slides, Whatman lens cleaning tissue, model number 105 (100 x 150 mm), was employed, after which the dry glass substrates were kept in the slide holders, ready for use.

### 3.2.2 Preparation of solutions

The masses of the solids (cadmium chloride monohydrate ($CdCl_2 \cdot H_2O$) and tin II chloride dihydrate ($SnCl_2 \cdot 2H_2O$)) that were dissolved in the solvent (water) to form the solutions for spraying were determined using the following procedure (Ongwen, 2019):

$$\text{Moles} = \text{molarity x volume}$$

Since the total volumes of the two solutions that were sprayed were 250 ml at a concentration of 0.4 M, the number of moles was calculated using the formula:

$$\text{Moles} = 0.4 \text{ x } \left(\frac{250}{1000}\right) = 0.1 \text{ moles}$$

The masses of the individual solids that were weighed were then found by:

$$\text{Mass} = \text{moles x molar mass}$$

For $CdCl_2 \cdot H_2O$, the molar mass is 201.32, which gave the mass as:

$$\text{Mass} = 0.1 \text{ x } 201.32 = 20.132\text{g}$$

Figure 3.2a and b show the mass being weighed using a weighing balance. For $SnCl_2 \cdot 2H_2O$, the molar mass is 225.63, which gave the mass as:

$$\text{Mass} = 0.1 \text{ x } 225.63 = 22.56 \text{ g}$$

Figure 3.2 c and d show the mass being weighed using a weighing balance.

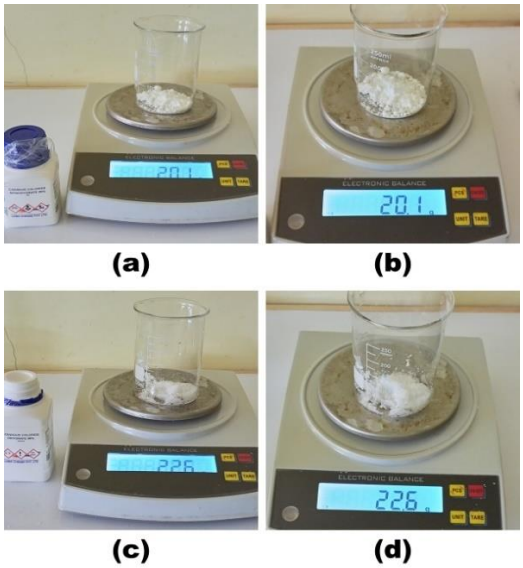


***Figure 3.2: Weighing the masses of (a and b) cadmium chloride monohydrate, and (c and d) tin II chloride dihydrate that were later dissolved in deionized water for preparing the precursor solutions***

The aqueous solution of $CdCl_2 \cdot H_2O$ was thus prepared by dissolving the 20.1 g (99% pure) of the compound in 250 ml of deionized water in a 250 ml glass volumetric flask, making a 0.4 M solution. The aqueous solution of $SnCl_2 \cdot 2H_2O$ was prepared by dissolving 22.6 g (98% pure) of the compound in 250 ml of deionized water in a 250 ml glass volumetric flask. This also made a 0.4 M solution (Ongwen, 2019) (figure 3.3). The masses of $CdCl_2 \cdot H_2O$ and $SnCl_2 \cdot 2H_2O$ were weighed using the MOCCO (SF-400C, United States of America) analytical weighing balance of accuracy 0.1g, and a maximum weighing capacity of 500 g.


***Figure 3.3: The prepared precursor solutions of cadmium chloride monohytrate and tin II chloride dihydrate***

***Table 3.1: Different concentrations (molarity) of cadmium chloride monohydrate and tin II chloride dihydrate, and the volume of 2 molar hydrochloric acid required to completely dissolve the white precipitates in order to form colourless solutions***

| Sample ID | Ratio | Volume ($cm^3$) | | |
|---|---|---|---|---|
| | $CdCl_2$: $SnCl_2$ | $CdCl_2$ | $SnCl_2$ | HCl |
| CTO 1 | 1:5 | 15 | 75 | 8.5 |
| CTO 2 | 2:4 | 30 | 60 | 7.6 |
| CTO 3 | 3:3 | 45 | 45 | 7.1 |
| CTO 4 | 4:2 | 60 | 30 | 4.4 |
| CTO 5 | 5:1 | 75 | 15 | 3.1 |

The two precursor solutions ($CdCl_2 \cdot H_2O$ and $SnCl_2 \cdot 2H_2O$) were then mixed at different ratios by volume in 250 ml glass beakers as shown in table 3.1 (a total volume of 90 $cm^3$), giving white precipitates (figure 3.4a). The ratios of Cd to Sn in table 3.1 were chosen, since they correspond to a consistent increase in the number of Cd atoms by 1 from CTO 1 to CTO 5. The total number of the Cd and Sn atoms was kept at 6. Thus, an increase in the number of Cd atoms led to a corresponding decrease in the number of Sn atoms. The total volume of 90 cm3 was sufficient for the total duration of deposition (2 minutes) that was required in this study. HCl was then added to the white precipitates in the volumes shown in table 3.1 in order to dissolve them to form colourless solutions of CTO (figure 3.4b). The samples were given sample identities: CTO 1, CTO 2, CTO 3, CTO 4, and CTO 5.

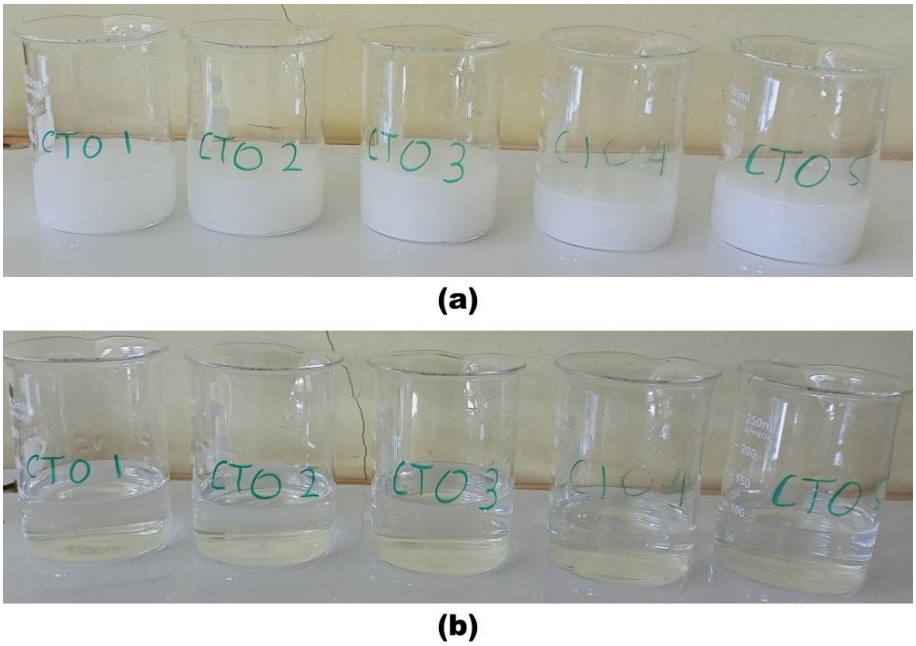


***Figure 3.4: Mixing the precursor solutions to form cadmium-tin-oxide: (a) The white precipitates formed after mixing the two precursor solutions of cadmium chloride monohydrate and tin II chloride dihydrate; (b) The colourless solutions formed after adding 2 molar hydrochloric acid to the white precipitates***

### 3.2.3 Optimization of deposition parameters

Before depositing the TFs of CTO, the optimization was done on the deposition parameters. The temperature was varied from 300 $^{o}$C to 500 $^{o}$C. At the lower temperature, the TFs turned out to be wet. Beyond 450 $^{o}$C, the TFs got burnt. A value of 450 $^{o}$C was thus chosen. For the spray pressure, it was found out that high pressure of above 3.5 bars led to the substrates being blown away and thus, making it difficult to spray, while very low pressures of below 3 bars led to production of TFs that were not evenly distributed. A value of 3.5 bars was thus chosen. The spray duration of less than 2 minutes led to formation of TFs that were not evenly distributed, while a spray duration of more than 2 minutes led to very thick films that were almost opaque. Thus, a spray duration of 2 minutes was chosen. A spray speed of 200, 4 was found to be the ideal, since at those values, the nozzle of the pyrolysis was concentrated at the substrate, and there was thus little wastage of the spray solution. A distance of 11.0c cm was taken, since at that distance, the solution was sprayed at a moderate pressure that was ideal for the formation of evenly spread TFs. Table 3.3 shows the optimized spray parameters.

***Table 3.2: The optimized parameters that were kept constant during spray deposition***

| Parameter | Value |
|---|---|
| Substrate temperature | 450 $^{o}$C |
| Spray pressure | 3.5 bars |
| Spray duration | 2 minutes |
| Spray speed | 200, 4 |
| Flow rate | 1 ml/ min |
| Distance between the nozzle and the substrate | 11.0 cm |

### 3.2.4 Deposition

The spray pyrolysis equipment (model number HO-TH-04) was used for spraying in this study. The microscope glass slides that were used as the substrates were held on both sides by two iron tubes, each of length 15 cm, gauge 12. This was done to prevent the slides from being blown away by the high pressure from the nozzle of the spray pyrolyis. The tubes were wrapped with aluminium foil so as to prevent them from contaminating the samples during spraying (figure 3.5a), while the plate of the pyrolysis was cleaned in advance using absolute ethanol, followed by deionized water.

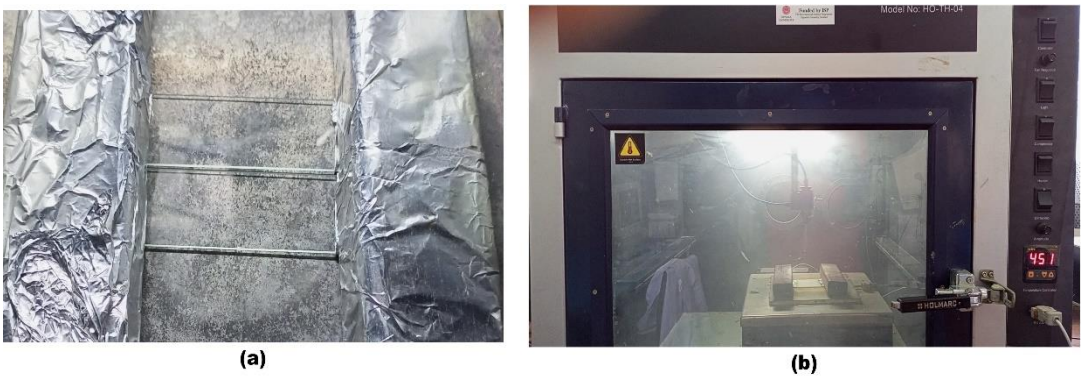


***Figure 3.5: The process of depositing the thin films of cadmium-tin-oxide: (a) the clean microscope glass slides placed on top of the plate of the spray pyrolysis equipment. The slides are supported by iron tubes, each of length 15 cm, gauge 12. The tubes are wrapped in aluminium foil; and (b) the process of depositing the thin films at a temperature of 450 ± 5 $^{o}$C***

The final solutions were then poured into the syringe pump of the spray pyrolysis equipment at a time, then sprayed onto the hot glass substrates at the optimum conditions in order to obtain the TFs of CTO (figure 3.5b). For each deposition, two glass slides were sprayed at once. Thus, a total of 10 glass slides were sprayed. The slide holder was the kept airtight so as to prevent the TF from affected by the presence of ambient adsorption of air. After each deposition, the channel of the pyrolysis was cleaned using absolute ethanol, followed by deionized water. Figure 3.6 shows the TFs deposited on the microscope glass slides (substrates), placed in a slide holder.

***Figure 3.6: The deposited thin films of cadmium-tin-oxide in a slide holder***

### 3.2.5 Measurements

After deposition, the TFs formed were taken for measurements. The film thickness was measured using the computerized KLA-tensor alpha-step IQ surface profiler with a thickness range of 8-2000 nm, with an accuracy of 0.75 nm. A resolution of 1 μm was used, with a scan time of 40 s. A stylus force of 11.7 mg was applied to the samples. The surface profiler was used in this study because it measures the thicknesses of thin films effectively, up to the nanometre scale (Kitagawa, 2007). Table 3.3 shows the measured thicknesses. Niton XL2 X-Ray Fluorescence Spectroscope (XRF) Analyzer from Thermo-Fisher Scientific was used to determine the chemical compositions of the TFs, with a precision of 1000 ppm. The excitation was carried out using monochromatic Al-K radiation with an energy of 1486.6 eV. Since the XRF used in this study detects only heavy elements (it does not detect light elements such as O), the percentage of O was determined by subtracting those of Cd and Sn from 100%.

***Table 3.3 The measured thicknesses of the thin film samples (in micrometers)***

| | Sample ID | | | | |
|---|---|---|---|---|---|
| Trial | CTO 1 | CTO 2 | CTO 3 | CTO 4 | CTO 5 |
| Trial 1 | 2.08 | 2.11 | 1.94 | 2.14 | 2.05 |
| Trial 2 | 2.07 | 2.15 | 2.10 | 2.01 | 1.98 |
| Trial 3 | 2.04 | 2.09 | 2.13 | 1.99 | 2.17 |
| Average | 2.06 | 2.12 | 2.06 | 2.05 | 2.07 |

The XRD analysis of the TF samples was done using Malvern Panalytical X'Pert Pro diffractometer system (Engineering Business Park, Grovewood Road, Malvern, United Kingdom) with $CuK_\alpha$ source of wavelength of 1.5418 Å. The diffractometer was equiped with a repid detector X'Celerator. The measurement was made through an angle of 2θ ranging from $10^o$ to $70^o$ in steps of $0.02^o$. The operating power of the diffractometer was set at 45 kV, 40 mA. The equipment had a goniometer of θ-θ geometry, with an angular precision of $0.001^o$.

## 3.3 Computational study

The computational study in this work was done within the framework of DFT as implemented in the QE package (QE 6.5) (Giannozzi et al., 2017), which uses plane waves for the expansion of atomic wave functions. The GGA of PBESOL (Perdew, Burkes, & Ernzerhof, 1996) was used for all the calculations on all the crystal structures that were studied. GGA was chosen over LDA, since previous computational studies have shown that LDA highly overestimates the elastic constants of materials. Moreover, LDA highly underestimates the lattice parameters (Ongwen, Ogam, & Otunga, 2021). The choice of the PBESOL exchange correlation (XC) functional over other XC functionals such as PAW and the Perdew-Burke-Ernzerhof (PBE) functional, was based on previous computational studies which have demonstrated that PBESOL produces values of elastic constants that replicate the experimental values compared to the other functionals (Rasander & Moram, 2015).

### 3.3.1 Crystal structures for input

The crystal structures of all the three materials considered in this study were obtained from the crystallographic open database (*crystallography.net*). For Si, we used an Fd-3m cubic cell with a space group number 227, consisting of 8 atoms (Hui et al., 2007). The crystal structure of the Si cell is shown in Appendix 1a. For SiC, we used an F-43m cubic cell (space group number 216), consisting of 8 atoms (Burdick & Owen, 1918). The crystal structure of the SiC cell is shown in Appendix 1b. For CTO, a 14-atom simple orthorhombic unit cell with a *pbam* space group (number 55) (Troemel, 1969) was used. The orthorhombic structure of CTO 4 ($Cd_2SnO_4$) is shown in figure 3.7, while the crystal structures of the other four CTO samples (CTO 1, CTO 2, CTO 3, and CTO 5) that were generated from CTO 4 are shown in Appendix 2.

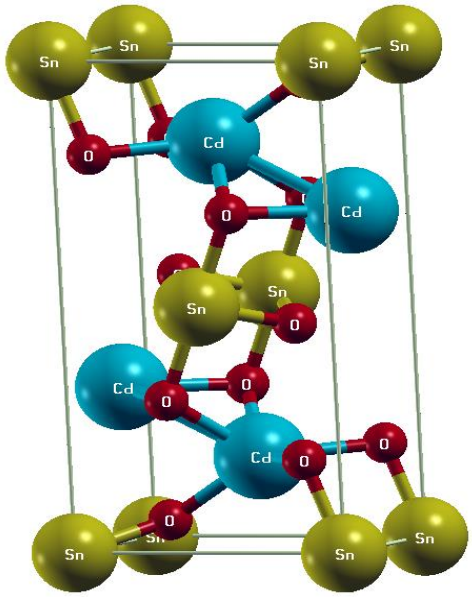


***Figure 3.7: A 3-Dimensional structure of the orthorhombic cadmium-tin-oxide (CTO 4) as viewed in X-window Crystalline Structures and Densities, a crystalline and molecular structure visualization program***

The experimental lattice parameter for Si was $a$ = 10.259 a.u, with a unit cell volume of 1,079.730 a.u$^3$. For the SiC cell, the experimental lattice parameter was $a$ = 8.2401 a.u, with a unit cell volume of 559.4966 a.u$^3$. For CTO, the experimental lattice parameters were: $a$ = 10.484 a.u, $b$ = 18.693 a.u, and $c$ = 6.039 a.u, with a unit cell volume of 1,183.508 a.u$^3$. The original input file as well as the optimized input file for CTO 4 are shown in figure 3.8a and b. The optimized input files for CTO 1, CTO 2, CTO 3, and CTO 5 are shown in Appendix 3. The celldm (2) and (3) for CTO 4 were obtained by dividing the values of the lattice parameters $b$ and $c$ respectively by $a$. The initial values of ecut and density energy cut-off (ecutrho) were set at 20 Ry and 160 Ry respectively for all the three materials (Si, SiC, and CTO).

```
&control
calculation='scf'
prefix='CTO4'
pseudo_dir ='./'
outdir='./tmp'
/
&system
ibrav=8
celldm(1)=10.484
celldm(2)=1.783
celldm(3)=0.576
nat=14
ntyp=3
degauss     = 0.02
ecutwfc=20
ecutrho=160
occupations = "smearing"
smearing    = "gaussian"
/
&electrons
electron_maxstep=1000
conv_thr=1.d-6
    mixing_beta      =  7.00000e-01
    startingpot      = "atomic"
    startingwfc      = "atomic+random"
/
ATOMIC_SPECIES
O  15.99940  O.pbesol-n-rrkjus_psl.0.1.UPF
Cd 112.40000 Cd.pbesol-dn-rrkjus_psl.0.2.UPF
Sn 118.69000 Sn.pbesol-dn-rrkjus_psl.0.2.UPF

K_POINTS {automatic}
2 2 2 0 0 0

ATOMIC_POSITIONS {angstrom}
Cd     0.321668    3.164160    1.596500
Cd     5.224332    6.723840    1.596500
Cd     3.094668    1.779840    1.596500
Cd     2.451332    8.108160    1.596500
Sn     0.000000    0.000000    0.000000
Sn     2.773000    4.944000    0.000000
O      2.052020    3.065280    0.000000
O      3.493980    6.822720    0.000000
O      4.825020    1.878720    0.000000
O      0.720980    8.009280    0.000000
O      1.164660    0.494400    1.596500
O      4.381340    9.393600    1.596500
O      3.937660    4.449600    1.596500
O      1.608340    5.438400    1.596500
```

a

```
&control
calculation='scf'
prefix='CTO4'
pseudo_dir ='./'
outdir='./tmp'
/
&system
Ibrav     = 8
celldm(1) = 10.5325440
celldm(2) = 1.78050065
celldm(3) = 0.57529941
nat         = 14
ntyp        = 3
degauss     = 0.02
ecutrho     = 400
ecutwfc     = 50
occupations = "smearing"
smearing    = "gaussian"
/
&electrons
    conv_thr         =  1.00000e-06
    electron_maxstep = 200
    mixing_beta      =  7.00000e-01
    startingpot      = "atomic"
    startingwfc      = "atomic+random"
/
K_POINTS {automatic}
 5 3 9  0 0 0

ATOMIC_SPECIES
O      15.99940  O.pbesol-n-rrkjus_psl.0.1.UPF
Cd    112.40000  Cd.pbesol-dn-rrkjus_psl.0.2.UPF
Sn    118.69000  Sn.pbesol-dn-rrkjus_psl.0.2.UPF

ATOMIC_POSITIONS {angstrom}
Cd        0.338916424   3.209833027   1.603239520
Cd        5.234667602   6.713938388   1.603239520
Cd        3.125707945   1.752053170   1.603239520
Cd        2.447876081   8.171718245   1.603239520
Sn        0.000000000   0.000000000   0.000000000
Sn        2.786791521   4.961886198   0.000000000
O         0.754081919   7.993219083  -0.000000000
O         4.819502108   1.930552333  -0.000000000
O         3.540873440   6.892437551   0.000000000
O         2.032710587   3.031333865   0.000000000
O         1.332412637   0.383731403   1.603239520
O         4.241170406   9.540040012   1.603239520
O         4.119205142   4.578153815   1.603239520
O         1.454378884   5.345617601   1.603239520
```

b

***Figure 3.8: Contents of (a) the original input file for CTO 4, and (b) the optimized input file of CTO 4***

The original input file for CTO 4 consisted of 4 atoms of Cd, 2 atoms of Sn, and 8 atoms of O (figure 3.7). The input file was then doped (substitutional doping) by replacing some of the Cd atoms with those of Sn according to table 3.4 (which corresponds to the ratios of $CdCl_2 \cdot H_2O$ to $SnCl_2 \cdot 2H_2O$ shown in table 3.1). The table also shows the percentage of Cd atoms that replaced the Sn atoms. Doping was done in such a way that the crystal structures of the doped cells remained orthorhombic. The crystal structures of the doped cells were checked upon their relaxation. The doping was done using Burai, a graphical user interface for QE software, which enabled the visualization of the crystal structures as well as the atoms in the structures.

***Table 3.4: The number of atoms and the ratios of cadmium to tin in the doped cadmium-tin-oxide samples, as well as the percentage of cadmium atoms that replaced tin atoms***

| Sample ID | No. of atoms | | Ratio | % Cd |
|---|---|---|---|---|
| | Cd | Sn | Cd:Sn | |
| CTO 1 | 1 | 5 | 1:5 | 16.67 |
| CTO 2 | 2 | 4 | 2:4 | 33.33 |
| CTO 3 | 3 | 3 | 3:3 | 50.00 |
| CTO 4 | 4 | 2 | 4:2 | 66.67 |
| CTO 5 | 5 | 1 | 5:1 | 83.33 |

### 3.3.2 Choice of pseudopotentials

The DFT, which was applied in the computational study of the properties of Si, SiC, and CTO in this work, is based on solving the Kohn-Sham equation, which is basically a one-electron Schrödinger equation of a fictitious system of non-interacting particles, which generates the same density as any given system of interacting particles (Kohn & Sham, 1965). The equation can be given as:

$$\left[-\frac{\hbar^2}{2m}\nabla^2 + V_{eff}(\boldsymbol{r})\right]\varphi_i(r) = \varepsilon_i\varphi_i(\boldsymbol{r}), \qquad (3.1)$$

where $\varepsilon_i$ is the total orbital energy of the corresponding Kohn-Sham orbital $\varphi_i$. The density of states for a system consisting of N-particles is given as:

$$\rho(\boldsymbol{r}) = \sum_i^N |\varphi_i(\boldsymbol{r})|^2 \qquad (3.2)$$

Solving the Kohn-Sham equation is done by DFT in an iterative way as outlined in Appendix 4. Equations 3.1 and 3.2 are also known as the Self-Consistent Field (SCF) equations, and the process of solving them is known as an SCF calculation. The number of SCF cycles run before reaching convergence (self-consistency) depends on the material under study (such as the number of atoms, the crystal structure, and the molecular masses of the atoms) and the conditions set (such as convergence threshold).

Computation of properties of materials requires PPs as inputs. A PP is an attempt to substitute the complex effects of the motion of the core electrons and the nuclei with effective potential, so that the Schrödinger equation now contains a modified effective potential term in place of the Coulombic potential term for core electrons that is typically present in the Schrödinger equation (figure 3.9). The PP is a replacement for the atomic all-electron potential (full potential) that eliminates the core states, and describes the valence electrons using pseudo-wave functions with fewer nodes. As a result, the plane-wave basis sets can be effectively used to represent the pseudo-wave functions using fewer Fourier modes. It is necessary for the pseudo and all-electron valence eigenstates to have the same energies, amplitudes, and densities outside a selected core with cut-off radius $r_c$ in order for first principle PPs to be derived from an atomic reference state. Larger cut-off radii are supposed to make PPs softer (to converge more quickly), but they also make the PPs less transferrable (Schwerdtfeger, 2011).

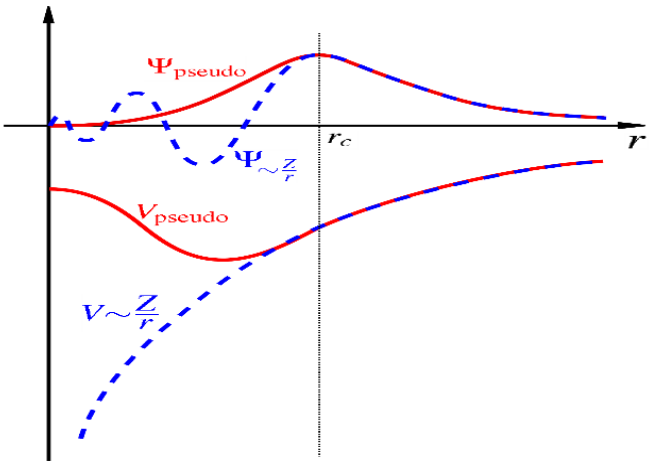


***Figure 3.9: A wave function in the nucleus's Coulomb potential (blue), and in the pseudopotential (red). Above the cut-off radius $r_c$, the Coulomb and pseudo wave function potentials coincide***

The electron-ion interactions in this study were described by scalar-relativistic, norm-conserving ultrasoft PPs. This is because apart from allowing a basis-set with a significantly lower ecut to be used to describe the electron wave functions and allowing numerical convergence with reasonable computing resources, ultrasoft PPs also relax the norm-conserving constraint to reduce the necessary basis-set size further at the expense of introducing a generalized eigenvalue problem (Vanderbilt, 1990). In the calculation of elastic constants, we employed the GGA (Perdew at al., 1996).

The valence configurations considered for the calculations were $3s^2$ and $3p^2$ for Si; while for SiC, the valence configurations were: $3s^2$, $3p^2$ for Si, and $2s^2$, $2p^2$ for C. The valence configurations considered for the calculations for CTO were: *Cd* $5s^2$, *Sn* $5s^2$ $5p^2$, and *O* $2s^2$ $2p^4$, with the semi-core *Cd 4d* and *Sn 4d* orbitals being considered, since they are crucial for the computation of the lattice constants and the bulk moduli, despite having little impact on the cohesive energy (Albrecht, Paulus, & Stoll, 1997). Moreover, they play a significant role in the spin-orbit coupling (relativistic effect) in heavy metals for the case of relativistic PPs (Lenthe, Leeuwen, Baerends, & Snijders, 1996). It is worthwhile noting that Si and C atoms are light elements and therefore, do not have *d* orbitals. The PPs used in the calculations for Si was *Si.pbesol-n-rrkjus_psl.1.0.0.UPF*; while for SiC, the PPs used were: *Si.pbesol-n-rrkjus_psl.1.0.0.UPF* for Si, and *C.pbesol-n-rrkjus_psl.1.0.0.UPF* for C. For CTO, we used: *Cd.pbesol-dn-rrkjus_psl.0.2.UPF* for Cd, *Sn.pbesol-dn-rrkjus_psl.0.2.UPF* for Sn, and *O.pbesol-n-rrkjus_psl.0.1.UPF* for O. All the PPs used were ultrasoft, generated by Adllan & Corso (2011).

### 3.3.3 Convergence criteria

Convergence of the ecut was performed by varying the ecut values of all the three materials from 20 to 90 Ry in steps of 10 Ry (8 data points). The values of ecutrho were obtained by multiplying the values of ecut by 8, since the calculations involved ultrasoft PPs. For each variation of the ecut and the corresponding ecutrho, the total energy was calculated using the *pw.x* command as implemented in the *QE* package. The calculated total energies and the corresponding ecuts were then collected into files, and graphs of total energy against ecut plotted for each structure. The convergence of the total energy with respect to the ecut was obtained when the change in the total energy for two consecutive calculations was within x $10^{-3}$ Ry. This was done for all the three materials separately. The convergence threshold was set at 1 x $10^{-6}$ Ry for CTO and 1 x $10^{-8}$ Ry for both Si and SiC. The higher convergence threshold for CTO was informed by its large size, which means that a lower threshold would have meant more SCF cycles and consequently, longer computational time, which in turn would have demanded for more computing resources.

Convergence of the k-points was done by varying the k-points from 2 to 9 in steps of 1 (2 2 2 to 9 9 9, 8 data points) for all the three structures. For each variation of the k-point, the total energy was calculated. Upon collecting the k-point values against the total energy data, graphs of total energy against k-points for each material were then plotted. The convergence of the total energy was attained when the change in the total energy for two consecutive calculations of the total energy with respect to k-point was within x $10^{-3}$ Ry for all the three materials. The converged values of ecut and ecutrho for all the three materials were then inserted into their respective input files for structural optimization.

### 3.3.4 Structural optimization

Before proceeding with the calculations for finding the acoustical, mechanical and thermal properties, the optimization of the lattice parameters as well as the atomic coordinates were performed. This was very crucial, especially for the CTO samples, since doping led to distortion of the cells. The main aim of the optimization was to obtain the minimum total energy, the minimum forces acting on the atoms in each cell, as well as the optimum lattice parameters of each cell. The structural optimization as done on all the three materials.

#### 3.3.4.1 Optimization of the lattice parameters

To determine the equilibrium lattice parameters of the crystals, calculations on the total energy were done for a range of unit cell volumes (15 different volumes) by varying the lattice parameters *a*, *b*, and *c*, each at a time. The resulting total energies and volumes data were then fitted into the third-order Birch-Murnaghan isothermal equation of state, given by (Birch, 1947):

$$\mathrm{p(V)} = \frac{3\mathrm{B_0}}{2}\left[\left(\frac{\mathrm{V_o}}{\mathrm{V}}\right)^{\frac{7}{3}} - \left(\frac{\mathrm{V_o}}{\mathrm{V}}\right)^{\frac{5}{3}}\right]\left[1 + \frac{3}{4}(\mathrm{B_o'} - 4)\left\{\left(\frac{\mathrm{V_o}}{\mathrm{V}}\right)^{\frac{2}{3}} - 1\right\}\right], \quad (3.3)$$

where *p* is the pressure, $V_o$ is the reference volume, *V* is the deformed volume, $B_o$ is the bulk modulus, and $B_o'$ is the derivative of the bulk modulus with respect to pressure. From equation 3.3, the minimum volumes were obtained. The values of the volumes were then fitted into the equation for finding the volume of orthorhombic unit cell as well as the cubic cell, which are given respectively by:

$$\mathrm{V} = \mathrm{abc} \quad (3.4a)$$

$$\mathrm{V} = a^3 \quad (3.4b)$$

From equation 3.4a and b, the optimized (equilibrium) lattice parameters *a*, *b* and *c* for all the three materials were obtained. The total energies were calculated for various unit cell volumes using the SCF procedure. For CTO, parameter *a* was varied from 9.5 a.u to 14.0 a.u in steps of 0.3 a.u while keeping the values of *b* and *c* constant. Parameter *b* was varied from 17.0 a.u to 20.0 a.u in steps of 0.2 a.u while keeping the values of *a* and *c* constant, while parameter *c* was varied from 5.0 a.u to 7.1 a.u in steps of 0.14 a.u

while keeping the values of *a* and *b* constant. The large steps for parameter *a* (0.3 a.u) was necessary so as to take care of the value for CTO 1 that underwent a large elongation upon doping. For Si, parameter *a* was varied from 9.23 a.u to 11.27 a.u in steps of 0.136 a.u, while that for SiC was varied from 7.4 a.u to 9.2 a.u in steps of 0.12 a.u. These values of variation of the lattice parameters correspond to 10% below and above the values of the experimental values, except the value of parameter *a* for CTO, which was extended in order to accommodate the large elongation for CTO 1.

#### 3.3.4.2 Optimization of atomic coordinates

Both the atomic positions and the lattice parameters contribute to the total energy of a system. For simple (cubic) crystals such as Si and SiC, the equilibrium atomic positions are known and fixed. However, this is not the case for complex crystals such as the orthorhombic CTO. The equilibrium atomic positions for such complex crystals are not known, and have to be determined. The Kohn-Sham wave functions in this study were expanded on a plane-wave basis set up to an ecut of 80 Ry for the optimization of the atomic coordinates for both Si and SiC, with a total energy accuracy of 2.14 x $10^{-4}$ Ry for Si, and 6.58 x $10^{-4}$ Ry for SiC. The BZ integration for both Si and SiC was performed over an unshifted 8 x 8 x 8 Monkhorst-Pack mesh (Monkhorst & Pack, 1976). For CTO, 50 Ry was set as the ecut, with a total energy accuracy of 1.55 x $10^{-3}$ Ry, while the BZ integration was performed over an unshifted 5×3×9 k-point mesh, with a total energy accuracy of 1.67 x $10^{-3}$ Ry for all the five CTO samples so as to obtain the ground-state configurations for the systems.

The optimization of atomic coordinates was done by performing variable-cell relax (vc-relax) calculations on all the input files with the optimized ecut, optimized k-point mesh, and optimized lattice parameters in order to optimize the lattice points, the minimum stresses, and the minimum forces acting on the atoms in each cell. The input script for the vc-relax calculation is shown in Appendix 5. The vc-relax calculation was done using the Brodyden-Fletcher-Goldfarb-Shanno (BFGS) algorithm. At the end of the vc-relax calculations, the forces acting on the atoms were less x $10^{-4}$ Ry/a.u for both Si and SiC, and less than x $10^{-3}$ Ry/a.u for CTO. The total pressure was less than 0.1 GPa for Si and SiC, and less than 0.2 GPa for all the five CTO samples that were considered.

### 3.3.5 Calculation of mechanical properties

#### 3.3.5.1 The stress-strain method

In this study, we developed an easier method that applies stress instead of energy in calculating elastic stiffness constants. According to Landau and Lifshitz (1970), the elastic energy should have a quadratic dependence on the deformation tensor for small deformations, whereas the stress should exhibit a linear relationship (Hooke's law). According to Hooke's law, stresses $\sigma_i$ in a crystal are directly proportional to the corresponding strains $\boldsymbol{\eta_i}$ within the linear regime (Waters, 2008):

$$\sigma_i = \sum_{i=1}^{6} c_{ij}\, \eta_i \qquad (3.5)$$

The stress-strain method is based on the modification of the distortion matrices for the energy-strain relationship by Ravindran et al. (1998). However, unlike the energy-strain relationship that requires 9 independent distortion matrices, only 6 are required when using the stress-strain relationship to calculate the 9 independent elastic stiffness constants of orthorhombic crystals. For the cubic crystal, only two distortion matrices are required instead of the three matrices that are required for the energy-strain method. SCF calculations are then performed on the distorted cells in order to obtain output files.

For the orthorhombic crystal, the first three distortion matrices are similar to those of the energy-strain relationship (equation 2.11). From the distortion matrix $D_1$, three elastic stiffness constants ($c_{11}$, $c_{12}$, and $c_{13}$) are obtained from the stress matrix of the output file of the SCF calculation. $c_{11}$ is obtained from the $xx$ element of the matrix, $c_{12}$ is obtained from the $yy$ element, while $c_{13}$ is obtained from the $zz$ element. $c_{22}$ and $c_{23}$ are obtained from the distortion matrix $D_2$. $c_{22}$ is obtained from the $yy$ element, while $c_{23}$ is obtained from the $zz$ element of the stress matrix of $D_2$. Finally, $c_{33}$ is obtained from the $zz$ element of the stress matrix of $D_3$ (Ongwen et al., 2021). The distortion matrices ($D_4$, $D_5$, and $D_6$) in equations 2.13a-c are however modified to:

$$D_4 = \begin{pmatrix} 1 & 0 & 0 \\ 0 & 1 & \delta \\ 0 & \delta & 1 \end{pmatrix}, D_5 = \begin{pmatrix} 1 & 0 & \delta \\ 0 & 1 & 0 \\ \delta & 0 & 1 \end{pmatrix}, D_6 = \begin{pmatrix} 1 & \delta & 0 \\ \delta & 1 & 0 \\ 0 & 0 & 1 \end{pmatrix}, \qquad (3.6)$$

since the expression $\frac{1}{(1-\delta^2)^{1/3}}$ can be taken as 1 if the value of the strain $\delta$ is small (less than 0.008). From the distortion matrices, $c_{44}$ is then obtained from the $yz$ or $zy$ element of the stress matrix of the output file of $D_4$, $c_{55}$ is obtained from the $xz$ or $zx$ element of $D_5$, while $c_{66}$ is obtained from the $xy$ or $yx$ element of the stress matrix of $D_6$. For the cubic cell, $c_{11}$ and $c_{12}$ are obtained from $D_1$, while $c_{44}$ is obtained from $D_4$ using the same procedure for the orthorhombic cell. Figure 3.10 shows how to obtain the stresses for $c_{11}$, $c_{12}$, and $c_{13}$ for the distortion $D_1$. The values of the stresses presented here were obtained for the strain value of -0.0075. The stress matrices for $D_2$, $D_3$, $D_4$, $D_5$, and $D_6$ at the -0.0075 strain are presented in Appendix 6.

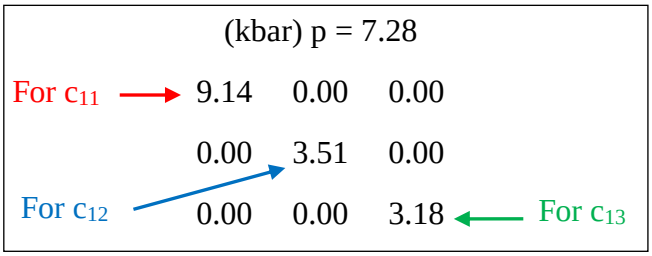


***Figure 3.10: A section of the output of Self Consistent Function calculation, showing the stresses on CTO 4 for $D_1$. The stresses for elastic stiffness constants $c_{11}$, $c_{12}$, and $c_{13}$ are read from the matrix as shown***

The strains applied to the crystals in this study were changed for each strain mode from -0.0075 to 0.0075 in steps of 0.0025 (7 data points). The resulting data was then fitted into a linear curve, from which the values of the elastic stiffness constants were obtained. Elastic stiffness constants and elastic compliance constants ($s_{ij}$) for orthorhombic crystals are related by (Li, Ju, & Wan, 2014):

$$s_{11} = \frac{c_{22}c_{33} - c_{23}^2}{\Sigma}, \; s_{22} = \frac{c_{11}c_{33} - c_{13}^2}{\Sigma}, \; s_{33} = \frac{c_{11}c_{22} - c_{12}^2}{\Sigma}, \qquad (3.7a)$$

$$s_{44} = \frac{1}{c_{44}}, \; s_{55} = \frac{1}{c_{55}}, \; s_{66} = \frac{1}{c_{66}}, \qquad (3.7b)$$

$$s_{12} = \frac{c_{13}c_{23} - c_{12}c_{33}}{\Sigma}, \; s_{13} = \frac{c_{12}c_{23} - c_{13}c_{22}}{\Sigma}, \; s_{23} = \frac{c_{12}c_{13} - c_{23}c_{11}}{\Sigma}, \qquad (3.7c)$$

where the constant $\Sigma$ is given by:

$$\Sigma = c_{13}(c_{12}c_{23} - c_{13}c_{22}) + c_{23}(c_{12}c_{13} - c_{23}c_{11}) + c_{33}(c_{11}c_{22} - c_{12}^2) \qquad (3.7d)$$

For the cubic crystals, the elastic stiffness constants and the corresponding elastic compliance constants are related by (Muslov, Lotkov, & Arutyunov, 2019):

$$s_{11} = \frac{c_{11}+c_{12}}{(c_{11}-c_{12})(c_{11}+2c_{12})}, \quad (3.8a)$$

$$s_{12} = \frac{-c_{12}}{(c_{11}-c_{12})(c_{11}+2c_{12})}, \quad (3.8b)$$

$$s_{44} = \frac{1}{c_{44}} \quad (3.8c)$$

From the elastic stiffness and elastic compliance data, the polycrystalline bulk modulus, shear modulus, Young's modulus, and Poisson's ratio were calculated by applying the Voigt approximation (which describes the upper bound), and the Reuss approximation (which describes the lower bound). The average of the two approximations is called the Hill's approximation (Hill, 1952). For orthorhombic crystals, the Voigt moduli (Bulk modulus ($B_v$), shear modulus ($G_v$), Poisson's ratio ($\mu_v$), and Young's modulus ($E_v$)) are given by:

$$\mathrm{B_v} = {}^{1}\!/_{9}\,(\mathrm{c_{11}} + \mathrm{c_{22}} + \mathrm{c_{33}}) + {}^{2}\!/_{9}\,(\mathrm{c_{12}} + \mathrm{c_{13}} + \mathrm{c_{23}}), \quad (3.9a)$$

$$\mathrm{G_v} = {}^{1}\!/_{15}\,(\mathrm{c_{11}} + \mathrm{c_{22}} + \mathrm{c_{33}} - \mathrm{c_{12}} - \mathrm{c_{13}} - \mathrm{c_{23}}) + {}^{1}\!/_{5}\,(\mathrm{c_{44}} + \mathrm{c_{55}} + \mathrm{c_{66}}), \quad (3.9b)$$

$$\mu_\mathrm{v} = \frac{3\mathrm{B_v}-2\mathrm{G_v}}{6\mathrm{B_v}+2\mathrm{G_v}}, \quad (3.9c)$$

$$\mathrm{E_v} = 2\mathrm{G_v}(1+\mu_\mathrm{v}) \quad (3.9d)$$

The Reuss Bulk modulus ($B_R$), shear modulus ($G_R$), Poisson's ratio ($\mu_R$), and Young's modulus ($E_R$) are given by:

$$\mathrm{B_R} = \frac{1}{(\mathrm{s_{11}}+\mathrm{s_{22}}+\mathrm{s_{33}})+2(\mathrm{s_{12}}+\mathrm{s_{13}}+\mathrm{s_{23}})}, \quad (3.10a)$$

$$\mathrm{G_R} = \frac{15}{4(\mathrm{s_{11}}+\mathrm{s_{22}}+\mathrm{s_{33}})-4(\mathrm{s_{12}}+\mathrm{s_{13}}+\mathrm{s_{23}})+3(\mathrm{s_{44}}+\mathrm{s_{55}}+\mathrm{s_{66}})}, \quad (3.10b)$$

$$\mu_\mathrm{R} = \frac{3\mathrm{B_R}-2\mathrm{G_R}}{6\mathrm{B_R}+2\mathrm{G_R}}, \quad (3.10c)$$

$$\mathrm{E_R} = 2\mathrm{G_R}(1+\mu_\mathrm{R}) \quad (3.10d)$$

For the cubic crystal, the two approximations become:

$$B_v = B_R = {}^{1}/_{3}\,(c_{11} + 2c_{12}), \tag{3.11a}$$

$$G_v = {}^{1}/_{5}\,(c_{11} - c_{12} + 3c_{44}), G_R = \frac{5(c_{11} - c_{12})c_{44}}{4c_{44} + 3(c_{11} - c_{12})} \tag{3.11b}$$

The Hill's averages for the elastic moduli (for all the crystal structures, including the both the orthorhombic and cubic) are given as:

$$B = \frac{B_v + B_R}{2} \text{ and } G = \frac{G_v + G_R}{2}, \tag{3.12a}$$

$$\mu = \frac{\mu_v + \mu_R}{2} \text{ and } E = \frac{E_v + E_R}{2} \tag{3.12b}$$

The bulk moduli of the orthorhombic cell can also be determined along the axes *a*, *b*, and *c* (axial bulk moduli) by the equations (Wen, Wang, Liu, & Song, 2017):

$$B_a = \frac{\Sigma}{3(1 + \tau + \gamma)}, B_b = \frac{B_a}{\tau}, B_c = \frac{B_a}{\gamma}, \tag{3.13}$$

where $\tau = \frac{(c_{11} - c_{12})(c_{33} - c_{13}) - (c_{23} - c_{13})(c_{11} - c_{13})}{(c_{33} - c_{13})(c_{22} - c_{12}) - (c_{13} - c_{23})(c_{12} - c_{23})}$, $\gamma = \frac{(c_{22} - c_{12})(c_{11} - c_{13}) - (c_{11} - c_{12})(c_{23} - c_{12})}{(c_{22} - c_{12})(c_{33} - c_{13}) - (c_{12} - c_{23})(c_{13} - c_{23})}$.

The following necessary and sufficient mechanical stability conditions must be met by the elastic constants of an orthorhombic crystal if it has to be mechanically stable (Mouhat & Coudert, 2014):

$$c_{11} > 0, c_{11}c_{22} - c_{12}^2 > 0,$$

$$c_{11}c_{22}c_{33} + 2c_{12}c_{13}c_{23} - c_{11}c_{23}^2 - c_{22}c_{13}^2 - c_{33}c_{12}^2 > 0,$$

$$c_{44} > 0, c_{55} > 0, c_{66} > 0, \tag{3.14}$$

while the mechamical stability condition for the cubic crystals is given by (Boucetta & Zegrar, 2013):

$$c_{11} - c_{12} > 0, c_{11} + 2c_{12} > 0, c_{44} > 0, c_{11} > B > c_{12} \tag{3.15}$$

The brittle and ductile nature of a material can be determined using equation 3.16 (Wen et al., 2017). The material is ductile if n > 1.75. If not, then the material is brittle:

$$\frac{\mathrm{B}}{\mathrm{G}} = \mathrm{n}, \tag{3.16}$$

where *n* is a constant called the Pugh's modulus ratio. Furthermore, the ductility or brittleness of a material can be quantitatively described using the Cauchy pressure. The following are the three Cauchy pressures for the orthorhombic cell:

$$\mathrm{p}_{\mathrm{a}}^{\mathrm{C}} = \mathrm{c}_{23} - \mathrm{c}_{44}, \mathrm{p}_{\mathrm{b}}^{\mathrm{C}} = \mathrm{c}_{13} - \mathrm{c}_{55}, \mathrm{p}_{\mathrm{c}}^{\mathrm{C}} = \mathrm{c}_{12} - \mathrm{c}_{66} \tag{3.17}$$

while for the cubic cell, we have:

$$\mathrm{p}_{\mathrm{a}}^{\mathrm{C}} = \mathrm{p}_{\mathrm{b}}^{\mathrm{C}} = \mathrm{p}_{\mathrm{c}}^{\mathrm{C}} = \mathrm{c}_{12} - \mathrm{c}_{44} \tag{3.18}$$

If the answer to each of the parts in equations 3.17 and 3.18 turns out to be negative, then the material is brittle. The material can only be ductile if all the three values of Cauchy pressure are positive (Chen, Yu, Chiang, & Cheng, 2015). Another important mechanical property of materials that determines many of the technological applications is the hardness. The Vickers hardness in this study was determined using the Chen model (Chen, Niu, Li, D., & Li, Y., 2011), which predicts the Vickers hadness of materials, ranging from metals, semiconductors, to insulators:

$$\mathrm{H}_{\mathrm{v}} = 2\left[\left(\frac{1}{\mathrm{n}}\right)^{2}.\mathrm{G}\right]^{0.585} - 3, \tag{3.19}$$

where $n = {}^{B}/_{G}$, the Pugh's modulus ratio.

### 3.3.5.2 Elastic anisotropy

Materials crack as a result of elastic anisotropy. Essentially, elastic anisotropy is present in all known crystals, which has a significant impact on engineering applications. The degree of anisotropy in the bonding between atoms in various planes is quantified by the shear anisotropic factor (A) (Fan, Wei, Chai, & Yu, 2005). For the {100} shear planes between the ⟨011⟩ and ⟨010⟩ directions, the shear anisotropic factor ($A_1$) is given by:

$$A_1 = \frac{4c_{44}}{c_{11}+(c_{33}-2c_{13})}, \tag{3.20a}$$

For the shear plane {010} between the ⟨101⟩ and ⟨001⟩ directions, the shear anisotropic factor ($A_2$) is given by:

$$A_2 = \frac{4c_{55}}{c_{22}+(c_{33}-2c_{23})}, \tag{3.20b}$$

while for the {001} shear planes between the ⟨110⟩ and the ⟨010⟩ directions, we have the shear anisotropic factor ($A_3$) as:

$$A_3 = \frac{4c_{66}}{c_{11}+(c_{22}-2c_{12})} \tag{3.20c}$$

The anisotropic factors ($A_1$, $A_2$, and $A_3$) must all be equal to one for an isotropic crystal. Any departure from one is a measure of the crystal's elastic anisotropy to some extent. The higher the degree of deviation of the factor from unity, the higher the degree of anisotropy (Breidi, Fries, Palumbo, & Ruban, 2016). The linear bulk modulus can also be used to indicate elastic anisotropy. The anisotropy along the unit cell axes *a* and *c* can be expressed with respect to the *b* axis as:

$$A_{B_a} = \frac{B_a}{B_b}, A_{B_c} = \frac{B_c}{B_b} \tag{3.21}$$

where $B_a$, $B_b$, and $B_c$ are the directional bulk moduli. To assess anisotropy in crystals, Chung & Buessem (2010) developed the percentage anisotropy factors of the bulk ($A_B$) and shear ($A_G$) moduli. The definitions of the percentage anisotropy factors are:

$$A_B = \frac{B_V - B_R}{B_V + B_R} \text{ x } 100\%, A_G = \frac{G_V - G_R}{G_V + G_R} \text{ x } 100\% \tag{3.22a}$$

A universal anisotropic factor ($A^U$), introduced by Ranganathan & Ostoja-Starzewski (2008) to measure crystal anisotropy, is given by:

$$\mathrm{A^U} = \frac{\mathrm{B_V}}{\mathrm{B_R}} + 5\frac{\mathrm{G_V}}{\mathrm{G_R}} - 6 \qquad (3.22b)$$

The $A_B$, $A_G$, and $A^U$ values for an isotropic crystal must all be equal to zero. The amount of anisotropy is determined by the deviation of the three factors from zero. For the orthorhombic crystal, the directional Young's moduli (2D and 3D) are given by the relation (Zhang, J-M. Zhang, Y. Xu, & Ji, 2008):

$$\frac{1}{\mathrm{E_{hkl}}} = \frac{\mathrm{S_{11}}H^4+\mathrm{S_{22}}K^4+\mathrm{S_{33}}L^4+(2\mathrm{S_{12}}+\mathrm{S_{66}})H^2K^2+(2\mathrm{S_{13}}+\mathrm{S_{55}})H^2L^2+(2\mathrm{S_{23}}+\mathrm{S_{44}})K^2L^2}{(H^2+K^2+L^2)^2}, \qquad (3.23)$$

where the constants *H*, *K*, and *L* are related by the miller indices (*hkl*) as: $H = h, K = \frac{a}{b}k, L = \frac{a}{c}l$, and $a, b, \& \ c$ are the lattice parameters.

### 3.3.6 Calculation of thermal properties

The calculation of thermal properties in this work was done within the QHA. The melting temperature, thermal conductivity, thermal expansion, lattice vibrations, and specific heats are all correlated with the Debye temperature, which is a characteristic temperature of crystalline materials. The Debye temperature can be schemed using a variety of techniques, including the Anderson approach (the one that was used in this study), which is accurate and rigorous, and relies on the average elastic wave (sound) velocity ($v_a$) via the following expression (Anderson, 1963):

$$\theta_\mathrm{D} = \frac{\mathrm{h}}{\mathrm{k_B}}\left[\left(\frac{3\mathrm{n}}{4\pi}\right)\frac{\mathrm{N_A}\rho}{\mathrm{M}}\right]^{1/3} v_a, \qquad (3.24)$$

where $h$ is the Planks constant, $k_B$ is the Boltzmann constant, $N_A$ is the Avogadro's number, $\rho$ is the density, $n$ is the number of atoms in the molecule (n = 14 atoms for CTO, and 8 for Si and SiC in this study), and $M$ is the molecular weight of the crystal. The value of $v_a$ was approximated from the expression:

$$v_a = \left[\frac{1}{3}\left(\frac{1}{v_l^3} + \frac{2}{v_t^3}\right)\right]^{-1/3} \qquad (3.25)$$

The longitudinal and transverse sound velocities of a crystal are represented by $v_l$ and $v_t$ respectively in equation 3.25. The two sound velocities were calculated using the Navier's equation (Schreiber, Anderson, & Soga, 1973):

$$v_l = \left(\frac{3B_V+4G_V}{3\rho}\right)^{1/2} \text{and } v_t = \left(\frac{G_V}{\rho}\right)^{1/2}, \qquad (3.26)$$

where $B_V$ and $G_V$ are the Voigt bulk and shear moduli respectively, which were obtained from the elastic stiffness constants.

Using the relation in equation 3.27, the specific heat capacity at a constant volume ($c_V$) was determined from the Debye temperature:

$$c_v(T) = \frac{1}{\phi}\frac{12\pi^4}{5}k_B\left(\frac{T}{\Theta_D}\right)^3, \qquad (3.27)$$

where $T$ is the absolute temperature, and $\phi$ is the volume of the unit cell. The melting temperature can be determined from the relationship (Fine, Brown, & Marcus, 1984):

$$T_m = 607 + 9.31B, \qquad (3.28)$$

where 607 is a constant and $B$ is the bulk modulus. An uncertainty value of 300 K was then added to the equation so as to obtain a good match between the computed values of the melting temperatures of Si and SiC and those that are available in the literature. We carried out phonon simulations to assess the temperature dependence of the Gibbs free energy, entropy, and the specific heat capacity at constant volume of the materials using QHA.

### 3.3.7 Calculation of acoustical properties

In the calculation of acoustic transmission loss, we adopted the Kirchoff-Love theory of plates, which is a two-dimensional mathematical model used to detemine the stresses and deformations that occur in single thin plates subjected to forces and moments (Love, 1888). This theory is an extension of the Euler-Bernoulli beam theory. The equations of motion to solve the problem of plate movement is a moving formulation. The bending equation of motion of a thin plate surrounded by air along the x-direction is given by:

$$p_1(x,t) - p_2(x + h_1, t) = \mathfrak{D}_1 \frac{\partial^4}{\partial x^4} w_1(x,t) + \rho_1 h_1 \frac{\partial^2}{\partial t^2} w_1(x,t), \qquad (3.29)$$

where $p_1$ is the pressure acting on one side of the plate, while $p_2$ is the pressure acting on the other side of the plate. $h_1$ is the thickness of the plate, $\rho_1$ is the density of the plate, $\rho_1 h_1$ is the mass ($m_p$) of the plate, and $w_1$ is the displacement of the wave from the mean position as a function of the bending of the plate. Thus, the density and thickness of the plate play a crucial role in the propagation of acoustic waves through the plate, as they are the ones that determine the mass of the plate. Figure 3.11 shows the arrangement for the acoustic wave transmission through a single plate.

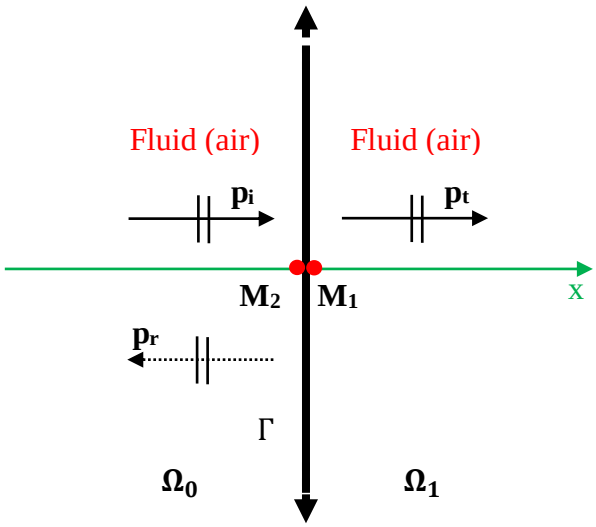


***Figure 3.11: Acoustic wave transmission through a single plate***

The quantity $(\mathfrak{D}_1)$, the rigidity of the plate, is given by: $\mathfrak{D}_1 = \frac{h_1^3 E}{12(1-\mu^2)}$, where $E$ is the Young's modulus, and $\mu$ is the Poisson's ratio of the plate. The solution of the plate movement equation in the harmonic regime takes the form:

$$w_1(x,t) = A_1 e^{ikp_1 . x\sin(\theta)} e^{-i\omega t}, \tag{3.30}$$

where $kp_1$ is the wave number of the plate. The acoustic transmission loss $\tau = \left({}^{1}/_{T}\right)$ of the wave as it propagates through the plate is given by:

$$\tau(\theta, f) = 1 + \frac{ik_o m_p}{2\rho_f}\left(1 - \frac{f^2}{f_c^2}\right)\cos(\theta) \tag{3.31}$$

where $f_c$ is the critical frequency, given by: $f_c = \frac{1}{2\pi}\sqrt{\frac{m_p c_1^4}{\mathfrak{D}\,(\sin(\theta)^4}}$, where $c$ is the speed of light in vacuum.

For two thin plates separated by air, the equations of motion become (Putra, Ismail, Ramlan, Ayob, & Py, 2013):

$$p_1(x,t) - p_2(x + h_1, t) = \mathfrak{D}_1 \frac{\partial^4}{\partial x^4} w_1(x,t) + m_{p1} \frac{\partial^2}{\partial t^2} w_1(x,t), \tag{3.32a}$$

$$p_2(x,t) - p_{t2}(x + h_2, t) = \mathfrak{D}_2 \frac{\partial^4}{\partial x^4} w_2(x,t) + m_{p2} \frac{\partial^2}{\partial t^2} w_2(x,t), \tag{3.32b}$$

where $p_{t2}$ is the sound transmitted by the second plate. Such arrangement is shown in figure 2.12, and is commonly called double glazing.

The solutions of the equations of the movement of the plates in the harmonic regime are then given by:

$$w_1(x,t) = A_1 e^{ikp_1 . x\sin(\theta)} e^{-i\omega t}, \tag{3.33a}$$

$$w_2(x,t) = A_2 e^{ikp_2 . x\sin(\theta)} e^{-i\omega t}, \tag{3.33b}$$

where the wave numbers of the two plates are $kp_1$ and $kp_2$. Their accelerations are:

$$\frac{\partial^2}{\partial t^2} w_1(x,t) = -\omega^2 A_1 e^{ikp_1 . \sin(\theta)} e^{-i\omega t} \tag{3.34a}$$

$$\frac{\partial^2}{\partial t^2} w_2(x,t) = -\omega^2 A_2 e^{ikp_2 . \sin(\theta)} e^{-i\omega t} \tag{3.34b}$$

The pressures acting on the plates and their corresponding derivatives with respect to the *x* direction are given by:

$$p_1(x,t) = p_i\left(e^{-ik_0(x\cos(\theta)-x\sin(\theta))} + R_1 e^{ik_0(x\cos(\theta)+x\sin(\theta))}\right)e^{-i\omega t},\ x \le 0 \quad (3.35a)$$

$$\frac{\partial p_1(x)}{\partial x} = p_i\left(-ik_0\cos(\theta)e^{-ik_0(x\cos(\theta)-x\sin(\theta))} + iR_1k_o\cos(\theta)e^{ik_0(x\cos(\theta)+x\sin(\theta))}\right), \quad (3.35b)$$

$$p_2(x,t) = p_i\left(T_1e^{-ik_0(x\cos(\theta)-x\sin(\theta))} + R_2T_1e^{-ik_0\left(-(x-(d+h_1))\cos(\theta)-x\sin(\theta)\right)}\right)e^{-i\omega t},$$
$$h_1 \le x \le d, \quad (3.35c)$$

$$\frac{\partial p_2(x)}{\partial x} = p_i\left(-iT_1k_0\cos(\theta)e^{-ik_0(x\cos(\theta)-x\sin(\theta))} + iR_2T_1k_0\cos(\theta)e^{-ik_0\left(-(x-(d+h_1))\cos(\theta)-x\sin(\theta)\right)}\right), \quad (3.35d)$$

$$p_{t2}(x,t) = p_i\left(T_1T_2e^{-ik_0(x\cos(\theta)-x\sin(\theta))}\right)e^{-i\omega t},\ x \ge h_1 + h_2 + d, \quad (3.35e)$$

$$\frac{\partial p_{t2}(x)}{\partial x} = p_i\left(-iT_1T_2k_0\cos(\theta)e^{-ik_0(x\cos(\theta)-x\sin(\theta))}\right), \quad (3.35f)$$

where $p_i$ is the pressure of the incident sound signal, $R_1$ is the reflection coefficient of the first plate, $T_1$ is the transmission coefficient of the first plate, $R_2$ is the reflection coefficient of the second plate, *d* is the thickness of the air layer, and $h_2$ is the thickness of the second plate. $T_2$ is the transmission coefficient of the second plate and $p_{t2}$ is the pressure on the second plate.

The following boundary conditions were applied:

$$\frac{\partial p_1}{\partial x}(x,t)\Big|_{x=0} = -\rho_f\frac{\partial^2}{\partial t^2}w_1 \quad (3.36a)$$

$$\frac{\partial p_1}{\partial x}(x,t)\Big|_{x=h_1} = -\rho_f\frac{\partial^2}{\partial t^2}w_1 \quad (3.36b)$$

$$\frac{\partial p_2}{\partial x}(x,t)\Big|_{x=d+h_1} = -\rho_f\frac{\partial^2}{\partial t^2}w_2 \quad (3.36c)$$

$$\frac{\partial p_2}{\partial x}(x,t)\Big|_{x=d+h_1+h_2} = -\rho_f\frac{\partial^2}{\partial t^2}w_2 \quad (3.36d)$$

Letting $\mathbb{A}_1 = \mathfrak{D}_1 kp_1{}^4 (\sin(\theta))^4 - m_1\omega_1^2$ and $\mathbb{A}_2 = \mathfrak{D}_2 kp_2{}^4 (\sin(\theta))^4 - m_2\omega_2^2$, the last two boundary conditions become:

$$p_1(x,t) - p_2(x + h_1, t) = \mathbb{A}_1, z = 0 \qquad (3.37a)$$

$$p_2(x,t) - p_2(x + h_2, t) = \mathbb{A}_2, x = d + h_1 \qquad (3.37b)$$

The resulting transmission loss is given by:

$$\tau(\theta, f) = e^{-ik_0(h_1+h_2)\cos\theta}\left[1 - \frac{ik_0}{2pf}\left(m_1\left(\frac{f^2}{f_{c1}^2} - 1\right) + m_2\left(\frac{f^2}{f_{c2}^2} - 1\right)\right)\cos\theta - \frac{k_0^2 m_1 m_2}{4pf}\left(\frac{f^2}{f_{c1}^2} - 1\right)\left(\frac{f^2}{f_{c2}^2} - 1\right)\left(1 - e^{-2ik_0 d\cos\theta}\right)(\cos\theta)^2\right] \qquad (3.38)$$

For three plates, the equations of motion and the boundary conditions are the same as those of the two plates. The arrangement for the three plates is shown in figure 3.12. This arrangement is called triple glazing. The resulting transmission loss is given in equation 3.39.

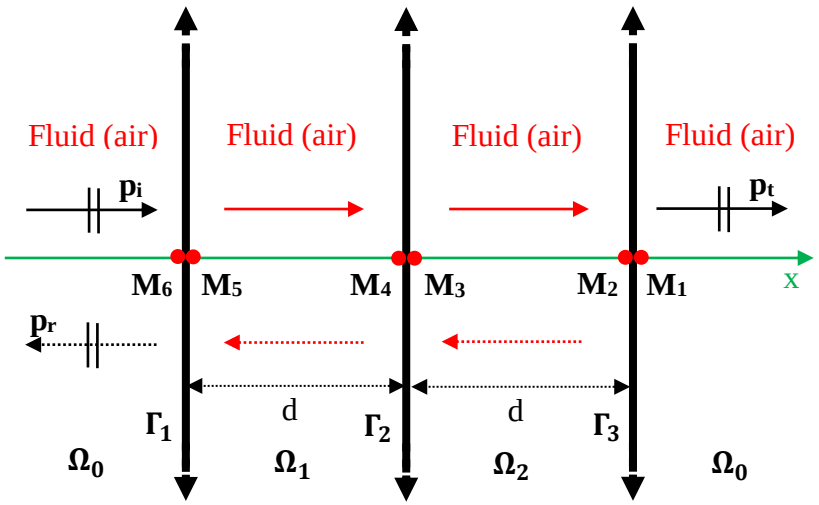


***Figure 3.12: Acoustic wave transmission through a series of three plates ($\Gamma_1$, $\Gamma_2$, and $\Gamma_3$), all separated by air***

$$\tau(\theta, f) = e^{-i\cos\theta k_0(h_1+h_2+h_3)}\left[1+\left(\frac{i\cos\theta k_0}{2pf}\right)m_1\left(\frac{f^2}{f_{c1}^2}-1\right)+m_2\left(\frac{f^2}{f_{c2}^2}-1\right)+m_3\left(\frac{f^2}{f_{c3}^2}-1\right)\right]-\frac{(\cos\theta)^2k_0^2}{4pf^2}\left[m_1m_2\left(\frac{f^2}{f_{c1}^2}-1\right)\left(\frac{f^2}{f_{c2}^2}-1\right)\left(1-e^{-2ik_0\cos(\theta)d_1}\right)+m_1m_3\left(\frac{f^2}{f_{c1}^2}-1\right)\left(\frac{f^2}{f_{c3}^2}-1\right)\left(1-e^{-2ik_0\cos(\theta)(d_1+d_2)}\right)+m_2m_3\left(\frac{f^2}{f_{c2}^2}-1\right)\left(\frac{f^2}{f_{c3}^2}-1\right)x\left(1-e^{-2ik_0\cos(\theta)d_2}\right)+\frac{im_1m_2m_3(\cos\theta)^3k_0^3}{8pf^3}\left(\frac{f^2}{f_{c1}^2}-1\right)\left(\frac{f^2}{f_{c2}^2}-1\right)\left(\frac{f^2}{f_{c3}^2}-1\right)x\left(e^{-2ik_0\cos(\theta)(d_1+d_2)}-e^{-2ik_0\cos(\theta)d_2}-e^{-2ik_0\cos(\theta)d_1}+1\right)\right] \quad (3.39)$$

In this study, we used glass as the plate, then determined the value of transmission loss without and with the TF of CTO laminated on one side of the glass. The following properties of glass were used in the calculations: Young's modulus of 72 GPa, Poisson's ratio of 0.208, and density of 2500 kg/m$^3$. These are the parameters of the ordinary glass that is usually used on window panes ("Thick glass windows, n.d."). The thickness of the glass was kept constant at 3 mm, that of the air space between the glass panes at 5 mm, while that of the TF was kept at 200 nm, after which it was later varied to 400, 600, and 800 nm. Although a thicker glass and a larger air space between them is better for acoustic attenuation, they require very thick walls. The choice of the thickness of the TF was informed by the fact that larger values reduce the optical transparency of the TF in the UV-Vis range. The simulation of the acoustical properties was done using Maple software from Maplesoft (version 2021.0, x64). The Maple codes and the corresponding matrices are shown in Appendices 7, 8, and 9.

# CHAPTER FOUR
# RESULTS AND DISCUSSION

## 4.1 Introduction

In this chapter, the results of the experimental and computational studies are presented and discussed. The experimental study captures the crystal structures from XRD as well as the chemical compositions of the deposited CTO samples. The computational study on the other hand, captures the convergence of both the ecut and the k-point grid, the optimization of both the lattice parameters and the atomic coordinates, as well as the mechanical properties of the CTO samples at zero GPa pressure. The results for structural and elastic constants of both Si and SiC are also presented in this chapter, which was used to prove the success of the stress-strain method of calculating elastic constants that was developed in this study. The pressure-dependent mechanical properties of CTO are also discussed. The chapter concludes with the discussion of the computed thermal properties (at zero pressure and as a function of the applied pressure), and the acoustic transmission loss of the CTO samples.

## 4.2 Structural properties

Figure 4.1 shows the XRD curves of all the five CTO samples. As figure 4.1a depicts, all the CTO samples show crystalline nature due to the presence of the diffraction peaks. However, all the other samples except CTO 4, were found to be polycrystalline. Since analysis of polycrystals is complex, the polycrystals were not analysed. Sample CTO 4 was found to crystalize in the orthorhombic structure, with *Pbam* (number 55) space group (Reference code number 00-031-0242). The reference chemical formula of CTO 4 is $Cd_2SnO_4$. The CTO 4 sample was observed to have a growth orientation along the (1 3 0) direction in the orthorhombic structure (figure 4.1b), which is consistent with the result by Krishna et al. (2010), which showed that $Cd_2SnO_4$ TFs are orthorhombic with growth orientation along the (1 1 1) direction. Chopra, Major, & Pandya (1983) also reported the orthorhombic structure of $Cd_2SnO_4$.

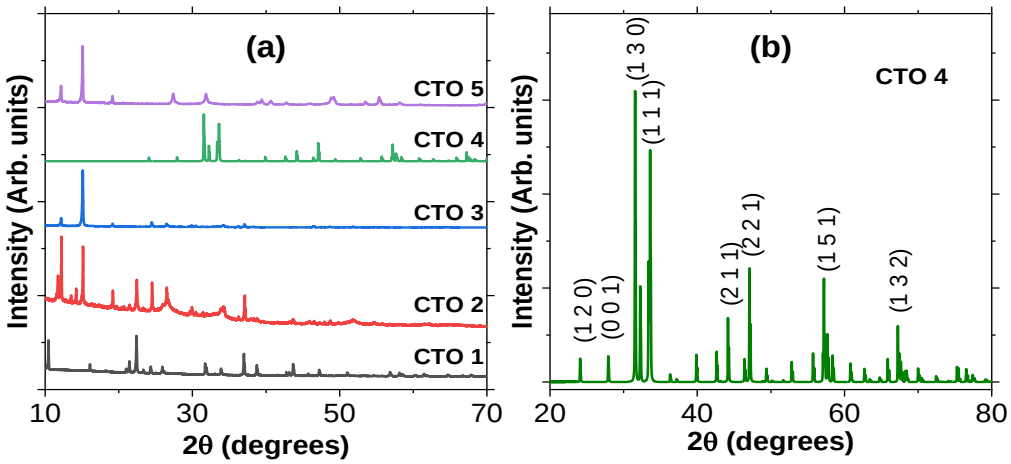


***Figure 4.1: The X-ray diffraction curves of (a) all the five cadmium-tin-oxide samples, and (b) sample CTO 4***

Table 4.1 shows the $2\theta$ and the *hkl* values obtained from the XRD curve of the CTO 4 sample. With the help of equations 2.1 and 2.2, the interplanar distances ($d_{hkl}$) were calculated, which are also presented in table 4.1. Using equation 2.3 and the data in table 4.1, we calculated the values of the lattice parameters for sample CTO 4, which are presented in table 4.2. Compared with those of the other studies, the lattice parameters of CTO 4 obtained in this work have very good agreement, with a deviation of less than 1% from the other two experimental results for all the three lattice parameters. For the unit cell volumes, the result in this study presents a +0.2847% and a +0.5296% deviation from the results of Troemel (1969), and Jeyadheepan & Sanjeeviraja (2014) respectively. A study by Setty & Sinha (1986) obtained the lattice parameters of $Cd_2SnO_4$ as $a$ = 10.480 – 10.741 a.u, $b$ = 18.649 – 18.685 a.u, and $c$ = 6.026 – 6.033 a.u, with a unit cell volume of 1,177.73 – 1210.79 a.u$^3$.

***Table 4.1: The diffraction angles (2θ), the miller indices (hkl), and the interplanar spacing ($d_{hkl}$) for the first four peaks for sample CTO 4***

| 2θ (°) | hkl | $d_{hkl}$ (Å) |
|---|---|---|
| 24.0953 | (1 2 0) | 3.6905 |
| 27.9202 | (0 0 1) | 3.1900 |
| 31.5505 | (1 3 0) | 2.8333 |
| 33.6042 | (1 1 1) | 2.6647 |

***Table 4.2: A comparison between the experimental lattice parameters (a.u) and the unit cell volume (a.u$^3$) for CTO 4 obtained in this study, with some previous experimental results. Also presented are the ratios b/a and c/a)***

| | *a* | *b* | *c* | *b/a* | *c/a* | $V_o$ |
|---|---|---|---|---|---|---|
| This work | 10.467 | 18.686 | 6.034 | 1.785 | 0.576 | 1180.15 |
| Ref (1) | 10.484 | 18.693 | 6.039 | 1.873 | 0.573 | 1183.51 |
| Ref (2) | 10.524 | 18.686 | 6.033 | 1.776 | 0.573 | 1186.40 |

*Ref (1), Experimental data from [Troemel, 1969].*

*Ref (2), Experimental data from [Jeyadheepan & Sanjeeviraja, 2014].*

Table 4.3 shows the calculated crystallite sizes of all the five CTO samples, applying both the FWHM and the IB methods. As the table depicts, the average crystallite sizes of the CTO samples range from 3.01 nm to 60.75 nm. Sample CTO 1 was found to have the largest crystallite size, while CTO 2 was found to have the smallest. The FWHM method was found to have slightly larger values of the crystallite size compared to the IB method. Many researchers tend to use the FWHM method because it is easier compared to the IB method. However, better results have been obtained with the IB method. The difference in the values of crystallite size between FWHM and IB in this study is within 6%. A previous study by Sidorak, Ivanov, & Shubin (2011), who synthesized CTO ($Cd_2SnO_4$, which corresponds to sample CTO 4 in this study) via thermal treatment of coprecipitated salts, found out a crystallite size of 30-50 nm. Their result is quite in the range of 42.225-44.946 nm that was obtained in this study for FWHM and IB methods respectively for CTO 4.

***Table 4.3: The calculated interplanar spacing (d), the full width at half maximum, the integral breadth, and the crystallite size for all the five cadmium-tin-oxide samples, using both the full width at half maximum and the integral breadth***

| Sample | 2 θ (°) | θ (rad) | d spacing (Å) | FWHM (rad) | IB (rad) | Crystallite size (nm) | |
|---|---|---|---|---|---|---|---|
| | | | | | | FWHM | IB |
| CTO 1 | 10.4497 | 0.09119 | 8.45880 | 0.0016659 | 0.001773 | 83.5771 | 78.5164 |
| | 22.4057 | 0.19552 | 3.96483 | 0.0024358 | 0.002592 | 58.0296 | 54.5167 |
| | 37.0116 | 0.32298 | 2.42690 | 0.0028896 | 0.003075 | 50.6009 | 47.5369 |
| | 61.6053 | 0.53760 | 1.50425 | 0.0031786 | 0.003153 | 50.7851 | 51.1883 |
| **Average** | | | | | | **60.7482** | **57.9396** |
| CTO 2 | 12.2259 | 0.10669 | 7.23361 | 0.0426358 | 0.045384 | 3.27066 | 3.07257 |
| | 15.1553 | 0.13225 | 5.84138 | 0.0444253 | 0.047289 | 3.14856 | 2.95788 |
| | 22.4786 | 0.19616 | 3.95213 | 0.0444261 | 0.047290 | 3.18203 | 2.98931 |
| | 24.5077 | 0.21387 | 3.62932 | 0.0444265 | 0.047290 | 3.1937 | 3.00032 |
| **Average** | | | | | | **3.19875** | **3.00502** |
| CTO 3 | 12.1587 | 0.10610 | 7.27343 | 0.0098199 | 0.010452 | 14.1995 | 13.3397 |
| | 15.1284 | 0.13202 | 5.85170 | 0.0098198 | 0.010452 | 14.2439 | 13.3813 |
| | 24.4674 | 0.21351 | 3.63521 | 0.0098191 | 0.010452 | 14.4490 | 13.5740 |
| | 26.5233 | 0.23145 | 3.35791 | 0.0098201 | 0.010453 | 14.5063 | 13.6277 |
| **Average** | | | | | | **14.3497** | **13.4807** |
| CTO 4 | 31.5711 | 0.27551 | 2.83159 | 0.0023363 | 0.002486 | 61.6737 | 57.9402 |
| | 33.5868 | 0.29310 | 2.66611 | 0.0050192 | 0.005342 | 28.8552 | 27.1079 |
| | 47.1248 | 0.41124 | 1.92696 | 0.0030389 | 0.003234 | 49.7754 | 46.7620 |
| | 57.2233 | 0.49936 | 1.60857 | 0.0040006 | 0.004258 | 39.4789 | 37.0884 |
| **Average** | | | | | | **44.9458** | **42.2247** |
| CTO 5 | 12.1049 | 0.10563 | 7.30561 | 0.0157657 | 0.016782 | 8.84394 | 8.30837 |
| | 15.1418 | 0.13213 | 5.84653 | 0.0157650 | 0.016781 | 8.87238 | 8.33499 |
| | 24.4405 | 0.21328 | 3.63915 | 0.0157650 | 0.016781 | 8.998938 | 8.45392 |
| | 26.4696 | 0.23099 | 3.36461 | 0.0157659 | 0.016782 | 9.034501 | 8.48739 |
| **Average** | | | | | | **8.937439** | **8.39617** |

***Table 4.4: X-Ray Fluorescence analysis data for CTO 4***

| Atom | Atomic concentration (%) | Weight concentration (%) |
|---|---|---|
| Cd | 28.54 | 55.21 |
| Sn | 14.32 | 28.95 |
| O | 100 - (28.54 + 14.32) | 100 - (55.21 + 28.95) |
| | =57.14 | =15.84 |

The size of crystallites in a material are known to have a significant influence on its properties, especially the mechanical. At room temperature, the mechanical properties such as yield strength, hardness, tensile strength, and fatigue increase with a decrease in the crystallite size. Typically, the impact of crystallite size is greatest on properties associated with early deformation such as yield stress, and has less impact on the tensile strength (Dieter, 1961). In a previous study, Yuan, Chen, Zhao, Di, & Zhu (2014) investigated the effect of grain size on the mechanical properties and microstructures of high manganese austenitic steel, and discovered that the yield and ultimate strengths of the steel decreased with increase in the grain size from 22 to 287 nm when the ultimate strength increased from 410 to 232.5 MPa, and from 725 to 517 MPa respectively. Table 4.4 shows the XRF chemical analysis data for CTO 4. The empirical formula of the compound, which is provided in table 4.5, was determined using the weight concentration values in table 4.4. Table 4.5 shows that the ratio of Cd:Sn:O is 2:1:4. Thus, the chemical formula of CTO 4 was found to be $Cd_2SnO_4$.

*Table 4.5: Determination of the empirical formula of the deposited CTO 4*

| Atom | Cd | Sn | O |
|---|---|---|---|
| % by mass | 55.21 | 28.95 | 15.84 |
| Molecular mass | 112.411 | 118.710 | 15.999 |
| Moles | $\frac{55.21}{112.411}$ | $\frac{28.95}{118.710}$ | $\frac{15.84}{15.999}$ |
| | =0.4911 | =0.2439 | =0.9901 |
| Mole ratio | $\frac{0.4911}{0.2439}$ | $\frac{0.2439}{0.2439}$ | $\frac{0.9901}{0.2439}$ |
| | =2.014 | =1.000 | =4.059 |
| | =2 | =1 | =4 |

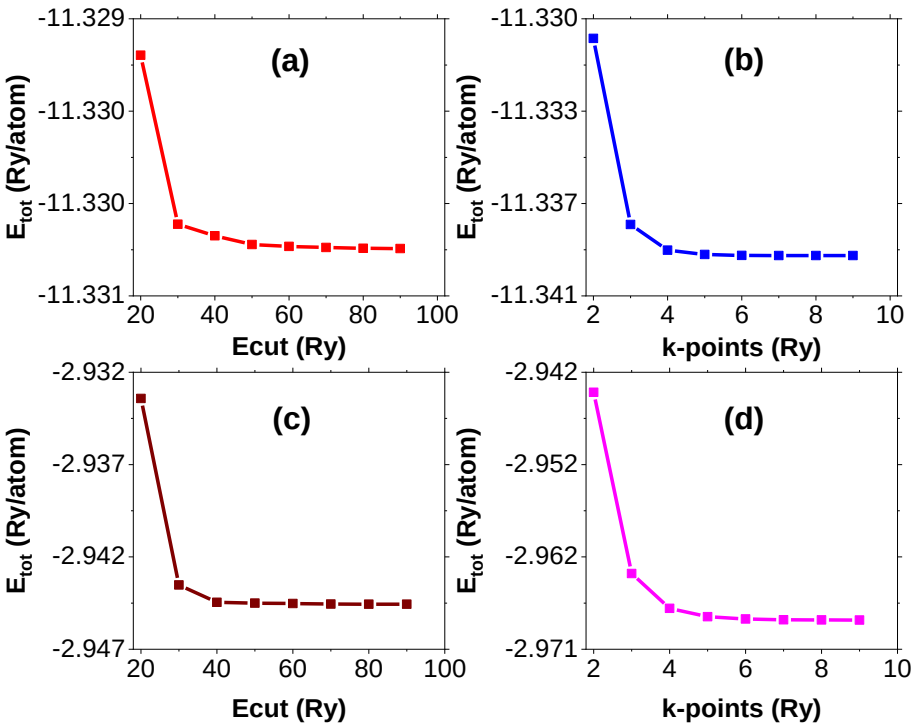


*Figure 4.2: The variation of: (a and b) the total energy against kinetic energy cut-off and k-points respectively for silicon, and (c and d) the total energy against kinetic energy cut-off and k-points respectively for silicon carbide*

The computed equilibrium lattice constants and atomic positions in all the three materials at the ground state were determined through structural optimization of each material. In Figure 4.2, the total energy per atom for Si and SiC is presented against ecut and k-points. As the figure depicts, a good convergence of ecut was achieved at a total energy of above 60 Ry/atom for Si (figure 4.2a), while for SiC, the convergence was achieved at a lower ecut of above 40 Ry/atom (figure 4.2c). For the k-points (figures 4.2b and d), the convergence was achieved at total energies of above 50 Ry/atom and above 60 Ry/atom for Si and SiC respectively.

Since both Si and SiC are light crystals (due to the high cubic symmetry as well as low molecular-weight atoms of Si and C), they do not require a lot of computing resources. We therefore chose a high ecut value of 80 Ry and a k-point mesh of 8 x 8 x 8 for subsequent calculations for both materials. The corresponding value of ecutrho was taken as 640 Ry (80 Ry x 8). Presented in figure 4.3 is the variation of total energy against the normalized unit cell volume for both Si and SiC, which show that Si has a lower total energy compared to SiC.

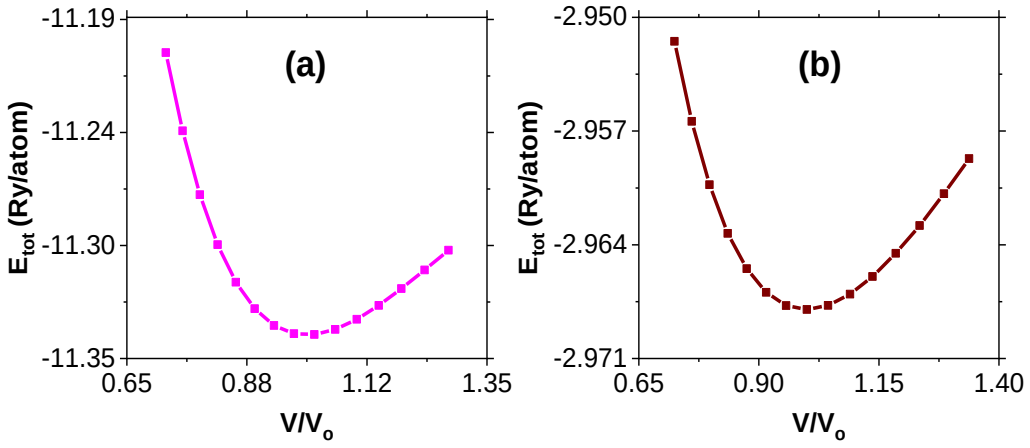


***Figure 4.3: The variation of the total energy against the normalized unit cell volume for (a) silicon, and (b) silicon carbide***

The calculated physical properties, the bulk moduli, and the derivative of the bulk moduli with respect to pressure that were obtained for both Si and SiC from figure 4.3 are presented in table 4.6, which show a perfect agreement with those from the reference experimental values as well as other data that are available in the literature. However, the slightly higher value of the calculated lattice parameter for Si shows that the unit cell underwent an expansion (of 0.07371%) upon full cell relaxation. The calculated value of the density of Si in this study and the value recorded by both Tilli & Haapalinna (2020) and Hopcroft et al. (2010) are in perfect accord (representing 0.1204% and 0.1634% respectively). The bulk modulus was found to be slightly lower (1.368% lower) than that obtained by Utkin & Fomin (2020). For SiC, the cell underwent a contraction of 0.0459% upon full cell relaxation. The bulk modulus was also found to be very much in agreement with those that are available in the literature (within 2%).

***Table 4.6: Physical properties as well as the bulk moduli, and the derivative of the bulk moduli of both silicon and silicon carbide***

| | a (Å) | ρ (Kg/m$^3$) | B (GPa) | B’ |
|---|---|---|---|---|
| Si | 5.431 | 2326.2 | 93.7 | 4.249 |
| | 5.427[(1)], 5.431[(2)], 5.402[(3)] | 2329.0[(3)], 2330[(4)] | 95.0[(5)] | |
| SiC | 4.357 | 3215.9 | 221.8 | 4.030 |
| | 4.359[(6)], 4.360[(7)] | 3210.0[(7)] | 222.0[(8)], | |

[(1)]*Reference experimental data from Hui et al. (2007)*

[(2)]*Data from Tilli & Haapalinna (2020)*

[(3)]*Data from Kim, Chuo, Ekerdt, & Hwang (2011)*

[(4)]*Data from Hopcroft et al. (2010)*

[(5)]*Data from Utkin & Fomin (2020)*

[(6)]*Reference experimental data from Burdick & Owen (1918)*

[(7)]*Data from Jiang & Cheung (2009)*

[(8)]*Data from Clayton (2010)*

[(9)]*Data from Dinesh, Shriya, Varshney, Singh, & Khenata (2015)*

Figure 4.4 shows the convergence of the total energy against ecuts for the five CTO samples, in which the total energy is observed to stabilize above the ecut of 40 Ry for all the samples. An ecut of 50 Ry was therefore taken for use in the subsequent calculations. The corresponding value of ecutrho was taken as 400 Ry. Although a higher value than 50 Ry for ecut could have been taken so as to improve the accuracy of the calculations, it was noted that higher values required more computing resources. However, the convergence was achieved with an energy difference of within x $10^{-3}$ Ry, which is good enough for accurate calculations of both mechanical and thermal properties. Figure 4.4f shows a comparison of the total energy against ecut for all the five CTO samples. A consistent increase in the total energy with increase in the number of Cd atoms is observed, which implies a decrease in the stability of the samples with increase in the number of Cd atoms. This shows that CTO 1 is the most stable of all the five samples, since it has the lowest total energy. CTO 5 was found to be the least stable.

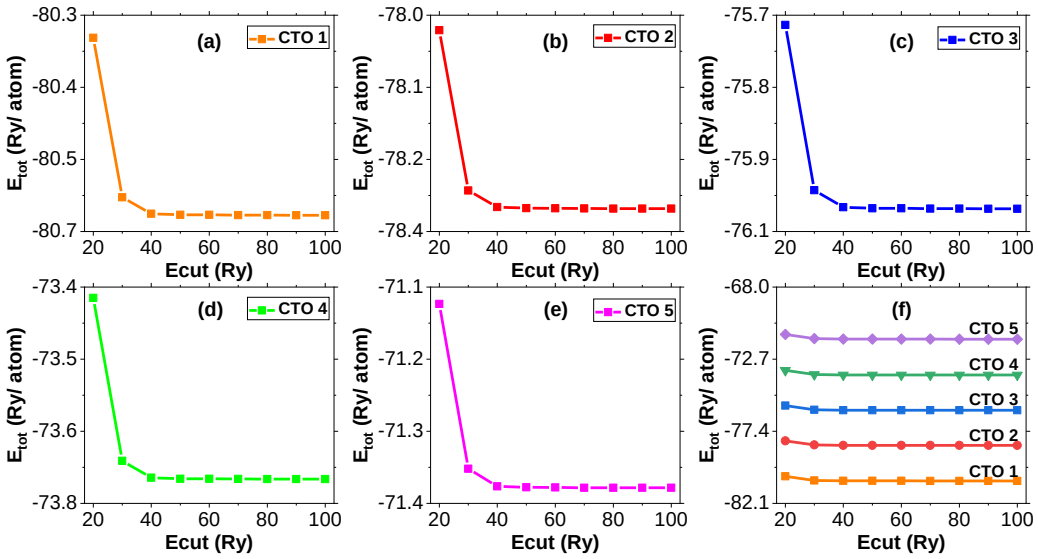


***Figure 4.4: Total energy against kinetic energy cut-off for samples: (a) CTO 1, (b) CTO 2, (c) CTO 3, (d) CTO 4, (e) CTO 5, and (f) all the five CTO samples combined***

Figure 4.5 shows the variation of the total energy of the CTO samples with k-points. The k-point was observed to stabilize at the 5 x 5 x 5 grid. Thus, a k-point grid of 5 3 9 (5, 5/celldm(2), 5/celldm(3)) was used in the subsequent calculations of the lattice parameters, acoustical, mechanical as well as thermal properties of CTO. Just like in figure 4.4f for total energy against ecut, figure 4.5f, which is a plot of the total energy against k-points for all the five samples, also shows a consistent increase in the total energy with increase in the number of Cd atoms. This confirms that sample CTO 1 is the most stable of all the five samples, while CTO 5 is the least stable, since CTO 5 has the highest total energy.

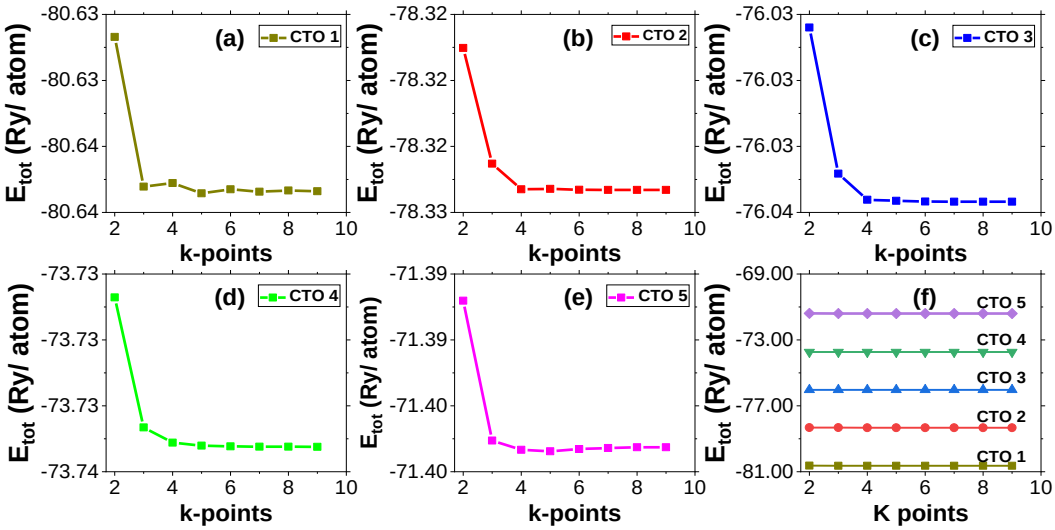


***Figure 4.5: Total energy against k-points for samples: (a) CTO 1, (b) CTO 2, (c) CTO 3, (d) CTO 4, (e) CTO 5, and (f) all the five CTO samples combined***

Evolution of the total energy with the normalized unit cell volumes for the three lattice parameters of the unit cells of the five CTO samples are shown in figures 4.6 (parameter *a*), 4.7 (parameter *b*), and 4.8 (parameter *c*). The equilibrium volumes for obtaining each of the lattice parameters were obtained at the minimum total energy. Just like in figures 4.4f and 4.5f, figures 4.6f, 4.7f, and 4.8f also show that sample CTO 1 is the most stable of all the five CTO samples. The optimized lattice parameters extracted from figures 4.6, 4.7, and 4.8, together with their optimized unit cell volume as well as comparisons with some previous experimental and computational data, are presented in table 4.7.

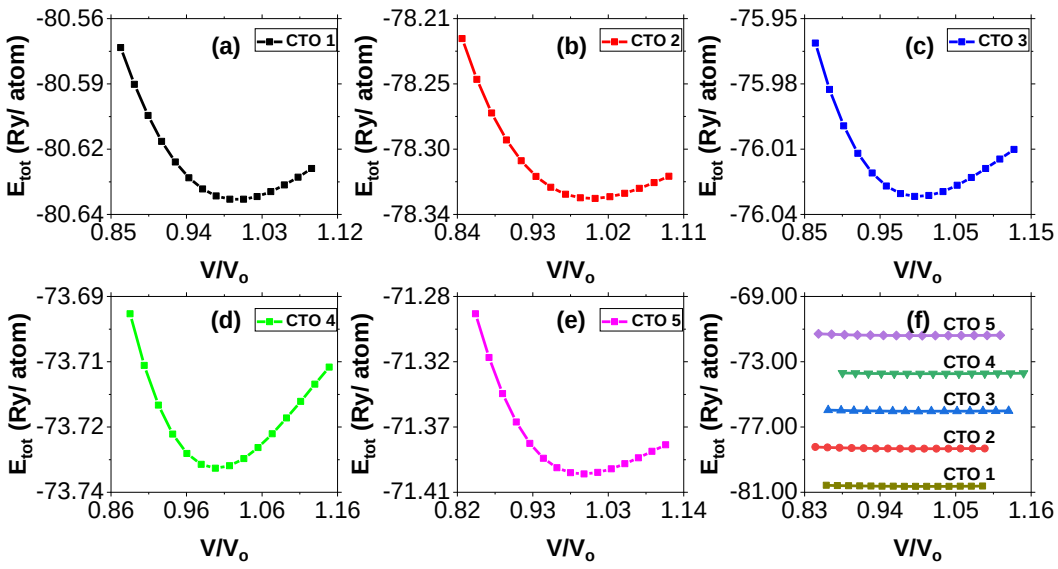


***Figure 4.6: Total energy against normalized unit cell volume for parameter a for samples: (a) CTO 1, (b) CTO 2, (c) CTO 3, (d) CTO 4, (e) CTO 5, and (f) all the five CTO samples combined***

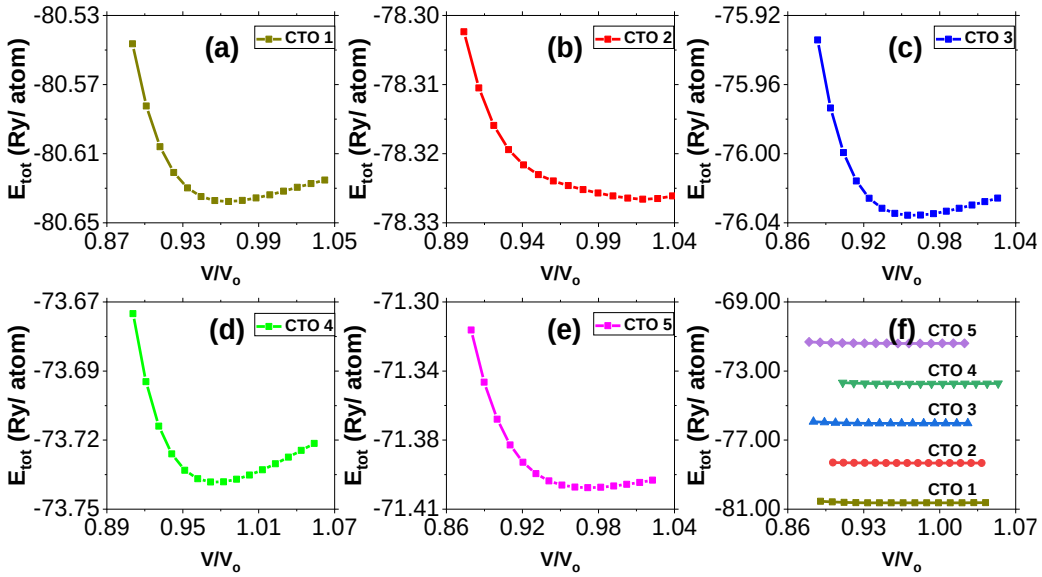


***Figure 4.7: Total energy against normalized unit cell volume for parameter b for samples: (a) CTO 1, (b) CTO 2, (c) CTO 3, (d) CTO 4, (e) CTO 5, and (f) all the five CTO samples combined***

With a variation of less than 2% for all the lattice parameters and less than 5% for the unit cell volumes, it can be seen that the optimized lattice parameter values for sample CTO 4 in this study are in very good agreement with those of the previous investigations presented on table 4.7. The values of the ratios b/a and c/a obtained in this study are also consistent with those that are available in the literature (table 4.7). It is also noted from table 4.7 that CTO 1 recorded the highest increase in parameters *a* and *c* (along the *x* and *z* axes respectively) compared to CTO 4, while CTO 5 recorded the lowest increase along the *c* direction. CTO 2 underwent the longest elongation along the *z* direction (parameter *c*), while CTO 5 underwent a contraction along the *z* direction compared to CTO 4.

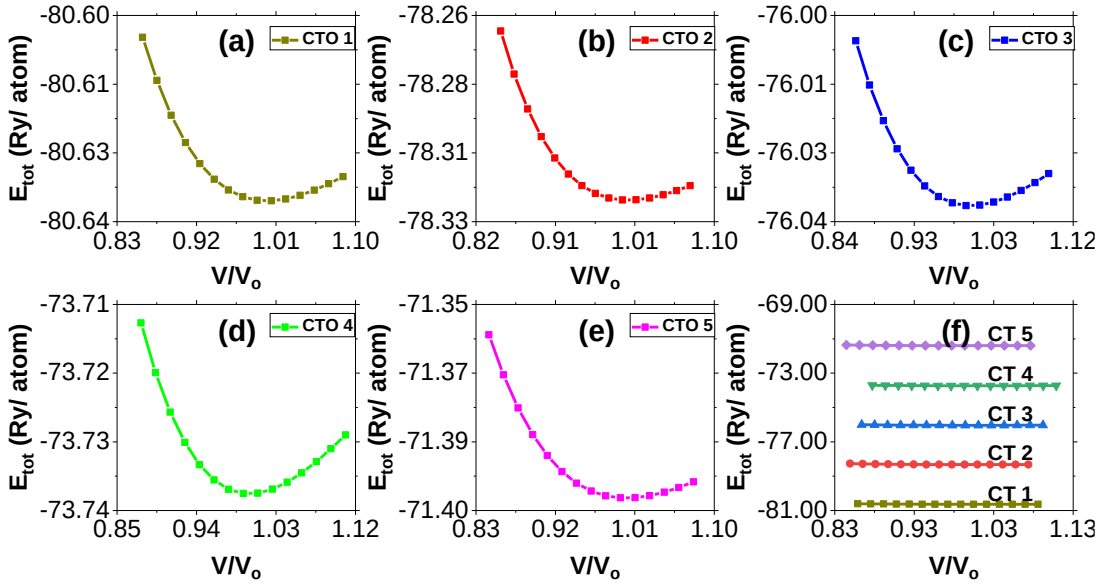


***Figure 4.8: Total energy against normalized unit cell volume for parameter c for samples: (a) CTO 1, (b) CTO 2, (c) CTO 3, (d) CTO 4, (e) CTO 5, and (f) all the five CTO samples combined***

Comparing the experimental and computed values in this study (tables 4.2 and 4.7), the computed values for sample CTO 4 are higher than the experimental values by + 0.4872, + 0.5035 and + 0.3812 for cell parameters *a*, *b* and *c* respectively. The higher values of the lattice parameters for CT 4 in this study compared to the values in the experimental studies (both tables 4.2 and 4.7) can be attributed to the overestimation of the lattice parameters and hence, the underestimation of the bulk moduli effect of the GGA that was employed in the DFT calculations in this study (Sousa, Fernandes, & Ramos, 2007).

The calculated unit cell volume is 0.993% larger than the experimental volume by Troemel, (1969), and 1.387% larger than the experimental volume obtained in this study (table 4.2), which are quite in agreement with the known trend of the GGA in overestimating the lattice parameters and hence, the unit cell volumes. However, a study by Yu, Fang, Zhao, & Zheng, 2014) who investigated the thermodynamic properties of wurtzite zinc sulphide by both GGA and LDA, obtained the value of the lattice parameter (*a*) to be within 2% for both functions compared to the experimental values.

***Table 4.7: A comparison between the computational study of the optimized lattice parameters (a.u) and equilibrium unit cell volume (a.u$^3$) of all the five cadmium-tin-oxide samples obtained in this study, together with some previous computational and experimental results. Also presented are the ratios b/a and c/a, and the densities (in g/cm$^3$)***

| | a | b | c | b/a | c/a | $V_o$ | ρ |
|---|---|---|---|---|---|---|---|
| This work (comp) | | | | | | | |
| CTO 1 | 12.585 | 18.038 | 6.147 | 1.433 | 0.488 | 1395.35 | 6.6995 |
| CTO 2 | 11.021 | 19.888 | 6.134 | 1.805 | 0.557 | 1344.51 | 6.9070 |
| CTO 3 | 10.697 | 19.034 | 6.116 | 1.779 | 0.572 | 1245.29 | 7.3903 |
| CTO 4 | 10.518 | 18.780 | 6.057 | 1.786 | 0.576 | 1196.52 | 7.6326 |
| CTO 5 | 10.585 | 19.136 | 6.002 | 1.808 | 0.567 | 1215.81 | 7.4535 |
| Ref (1) (CTO 4) | 10.484 | 18.693 | 6.039 | 1.873 | 0.573 | 1183.51 | ……. |
| Ref (2) (CTO 4) | 10.524 | 18.686 | 6.033 | 1.776 | 0.573 | 1186.40 | ……. |
| Ref (3) (CTO 4) | 10.705 | 19.137 | 6.140 | 1.788 | 0.674 | 1257.85 | ……. |
| Ref (4) (CTO 4) | 10.359 | 18.507 | 5.955 | 1.787 | 0.575 | 1141.66 | ……. |

*Ref (1), Experimental data from Troemel (1969)*

*Ref (2), Experimental data from Jeyadheepan & Sanjeeviraja (2014)*

*Ref (3), Computational data from Persson (2014)*

*Ref (4), Computational data from Wei & Segev (2004)*

In their study of the structural, electrical, and optical properties of orthorhombic calcium germanate, Henriques, Caetano, Freire, da Costa, & Albuquerque (2007) also noted higher values of the lattice parameters and the unit cell volume compared to the experimental values, which they attributed to the underestimation of the strength of the inter-atomic forces. The values of the lattice parameters and the unit cell volume of the computational study by Persson (2014) are however slightly higher than the values obtained in this study (CTO 4), although the differences in the values of the lattice parameters are within the acceptable range of 2%. The differences observed can be attributed to the different computational techniques as well as the types of PPs that were employed in the calculations. In her calculation, she used the VASP code, with PAW PPs, while in this study, QE code with PBESOL PPs were employed. A computational study by Wei & Segev (2004) on the other hand, recorded values of the lattice parameters that are slightly lower than those obtained in this study. In their study, they employed PAW PPs within the VASP package.

The density of 6.6995 - 7.6326 g/cm$^3$ obtained in this study shows that CTO is a heavy material, much heavier than Si at 2.33 g/cm$^3$. However, it compares very well with the value obtained by Persson (2014), who got 7.26 g/cm$^3$, representing a 5.1322% deviation from that of CTO 4 at 7.6326 g/ cm$^3$. As can be noted in table 4.7, the density of CTO increases consistently with increase in the number of Cd atoms from CTO 1 to CTO 4, then drops at CTO 5. This is caused by the decrease in the unit cell volumes from CTO 1 to CTO 4, followed by the increase at CTO 5, which implies a contraction of the unit cells from CTO 1 to CTO 4, followed by an expansion at CTO 5. The slightly lower value of the density obtained by Persson, (2014) is attributed to the relatively higher value of the unit cell volume, since the two are inversely related. Density is one of the simplest, but most important of the material properties. It is related to the arrangement of the atoms in the crystal as well as the corresponding electron density (Daoud, Loucif, Bioud, & Lebgaa, 2012). Thus, the relatively high density of CTO obtained in this study is an indication of the closeness of the atoms, as well as the high electron density in its structure. At the time of carrying out this study, there was no information in the literature about the density of CTO. This study thus forms the basis for future reference.

Structural properties of materials cannot be complete without the discussion of the bond angles and bond lengths. Bond length/ distance is the average distance of two bonded atoms in a compound. It is a transferable property of bonds between atoms of fixed types. Bond lengths are related to bond orders in that when more electrons in a compound participate in the formation of a bond, the bond becomes shorter. Since bond lengths are inversely related to bond strength and bond dissociation energy, a stronger bond will be shorter. The bond angle, on the other hand, is the angle between two bonds (angle between three atoms) in a structure. Bond angles are usually measured in degrees. The bond angles give information about the distribution of the bonded electron pairs around the atoms, which in turn, helps in the determination of the shapes of molecules.

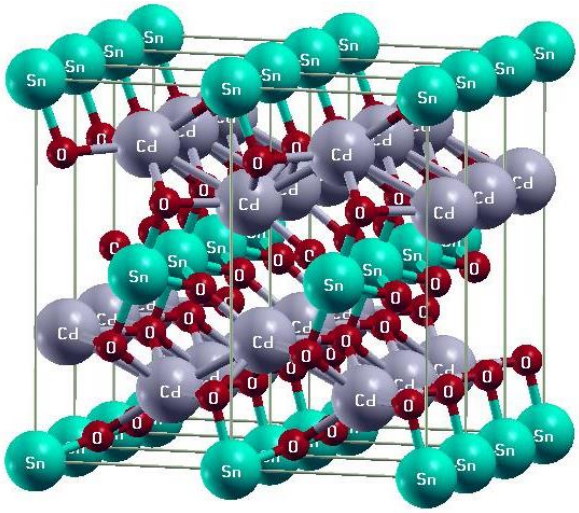


***Figure 4.9: A 3-Dimensional structure of CTO 4 showing a 2 x 1 x 3 supercell as viewed in X-window Crystalline Structures and Densities software, both showing the bonds between the atoms in the crystal***

Figure 4.9 shows the bonding between the atoms in the CTO 4 sample. In the structure, Sn is bonded to 6 O atoms, with no direct bonding with Cd. The O atom is in turn bonded to 4 Cd atoms and 1 Sn atom, while the Cd atom is bonded to 4 other Cd atoms and 5 O atoms. An experimental study of the orthorhombic CTO (which corresponds to CTO 4 in this study) by Bowden & Cardile (1990) obtained bond lengths of 2.336 Å and 2.087 Å for the Cd – O and Sn – O bonds respectively. Their findings are in very good agreement with those obtained in this study, as can be observed in table 4.8, which shows the bond lengths in the structure of CTO 4.

***Table 4.8: The computed bond lengths (in angstrom, Å) between the atoms in the CTO 4 crystal, and the bond length splitting ($\Delta_b$)***

| Bond | Bond length (Å) | Average (Å) | Δb (Å) |
|---|---|---|---|
| Cd — O | 2.2557, 2.3241, 2.3391 | 2.3063 | 0.0834 |
| Sn — O | 2.0726, 2.1197 | 2.0962 | 0.0471 |
| Cd — Cd | 3.1450, 3.2065 | 3.1758 | 0.0615 |

As can be observed in table 4.8, more than one type of bond length exists for the Cd – O, Sn – O, and Cd – Cd bonds. This phenomenon in which two atoms in a unit cell have two or more bond lengths is referred to as bond length splitting, denoted by $\Delta_b$, whose value (shown in table 4.8) is the difference between the largest and the smallest values of the bond lengths. It was noted that the Cd – Sn and O – O bonds do not exist for the CTO (CTO 4), since there is no direct bonding between the stated atoms, as can be observed in figure 4.9. Table 4.9 shows the bond angles between the atoms that make up the CTO 4 crystal. The calculated bond angles are between 79.963$^o$ and 180$^o$. The Sn – Cd – Sn and O – Cd – Sn bonds were not detected in the crystal. A previous study by Bowden & Cardile (1990) observed bond angles subtended at the Sn to be in the range of 81$^o$ to 180$^o$, while those subtended at the Cd to be in the range of 72$^o$ to 142$^o$. Their findings and those from this study are in excellent accord.

***Table 4.9: The calculated bond angles (in degrees) between the atoms in the CTO 4 crystal***

| Bond | Bond angle ($^o$) |
|---|---|
| Cd — O — Cd | 84.821, 86.538, 87.232, 148.801 |
| O — Cd — O | 79.963, 86.538, 87.709, 128.461 |
| Cd — O — Sn | 101.092, 127.557 |
| O — Cd — O | 79.1980, 128.286 |
| O — Sn — O | 86.556, 93.444, 98.290, 180.000 |

## 4.3 Mechanical properties

### 4.3.1 Zero-pressure mechanical properties

To reduce errors caused by higher-order terms, small strains were applied to the optimized unit cells in the calculation of elastic constants. Moreover, the small distortions were applied so as to remain within the elastic (linear) domain of the crystals. The stress-strain relationship was implemented using two distortion matrices ( $D_1$ and $D_4$) for both Si and SiC in order to determine the three elastic stiffness constants ( $c_{11}$, $c_{12}$, and $c_{44}$). For CTO, six distortion matrices ( $D_1 - D_6$) were used in order to determine the nine independent elastic stiffness constants ( $c_{11}$ to $c_{23}$). The first three elastic stiffness constants ( $c_{11}$, $c_{22}$, and $c_{33}$) are related to elasticity of the length (linear resistance to compression along the axes *a*, *b*, and *c* directions respectively), while the rest ( $c_{44}$, $c_{55}$, $c_{66}$, $c_{12}$, $c_{13}$, and $c_{23}$) are related to the shape of the crystal. Figure 4.10 shows the curves of the stresses as functions of the applied strains for the three independent elastic stiffness constants for both Si and SiC.

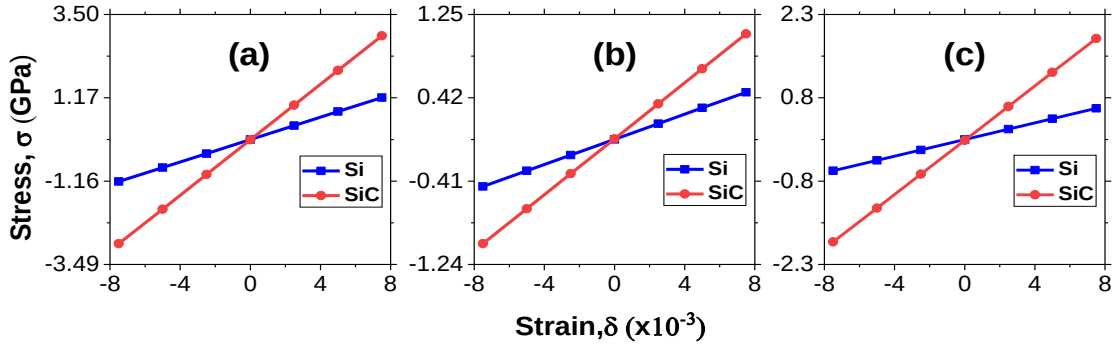


***Figure 4.10: Stress-strain curves for determining the elastic stiffness constants: (a) $c_{11}$, (b) $c_{12}$, and (c) $c_{44}$ of both silicon and silicon carbide***

As figure 4.10 depicts, the elastic stiffness constants of SiC are higher than those of Si, owing to the steeper slopes of the SiC curves. Through linear fitting of the curves, the elastic stiffness constants of the two materials were obtained. The values of the elastic stiffness constants were used to compute the mechanical properties, which are presented in table 4.10, which shows that the mechanical properties of both Si and SiC obtained in this study agree very well with those that are available in the literature. For reference 9 (table 4.10), only the elastic stiffness constants ($c_{11}, c_{12}, \text{and } c_{44}$) are available. The corresponding mechanical properties were then calculated. For Si, the bulk modulus obtained in this study is 4.154% and 3.301% lower than those reported by Hopcroft et al. (2010) and Moon, Cho, K., & Cho, M. (2012) respectively. The shear modulus calculated in this study is 4.823% and 1.601% lower than those obtained from the works by Hopcroft et al. (2010) and Moon et al. (2012) respectively. The Young's modulus calculated in this work was found to be 2.030% lower than that by Moon et al. (2012).

For SiC, the calculated bulk modulus was found to be 2.252% and 0.1351% lower than those by Dinesh et al. (2015) and Pizzagalli (2021) respectively. The shear modulus was found to be 0.269% higher than that by Dinesh et al. (2015), but 0.807% lower than that by Pizzagalli (2021). The Youngs modulus was found to be 2.776% and 0.574% lower than those by Mehregany (1998, 2000) and Pizzagalli (2021) respectively. Thus, the mechanical properties of SiC in this study were found to in better agreement with those that are available in the literature compared to those of Si. The stress-strain method that was developed in this study proved to be effective and suitable for calculating mechanical properties of materials. The method was then applied in calculating the mechanical properties of CTO.

***Table 4.10: Mechanical properties of silicon and silicon carbide. $c_{11}$, $c_{12}$, $c_{44}$, B, G, and $H_V$ are in GPa, while μ and n have no units***

| | $c_{11}$ | $c_{12}$ | $c_{44}$ | B | G | E | μ | n | $H_V$ |
|---|---|---|---|---|---|---|---|---|---|
| Si | 156.6 ± .4 | 62.5 ± .8 | 74.9 ± .5 | 93.9 | 62.2 | 152.7 | 0.23 | 1.510 | 10.84 |
| | 165.6[3] | 63.9[3] | 79.5[3] | 97.8[3] | 65.2[3] | 130-169[3] | 0.26[4] | 1.500[3] | 11.33[3] |
| | 161.0[5] | 65.0[5] | 76.0[5] | 97.0[5] | 63.2[5] | 155.8[5] | 0.23[5] | 1.535[5] | 10.70[5] |
| SiC | 387.5 ± 1 | 139.3 ± .8 | 243.9± 1 | 222.0 | 185.9 | 435.9 | 0.17 | 1.194 | 31.56 |
| | 371.1[6] | 142[6] | 256[6] | 227[6] | 185.4[6] | 448[7,8] | 0.17[6] | 1.178[6] | 32.05[6] |
| | 390.9[9] | 138.0[9] | 243.4[9] | 222.3[9] | 187.4[9] | 438.4[9] | 0.17[9] | 1.188[9] | 31.92[9] |

[3]*Data from Hopcroft et al. (2010)*

[4]*Data from Hull (1999)*

[5]*Data from Moon et al. (2012)*

[6]*Da ta from Dinesh et al. (2015)*

[7]*Data from Mehregany et al. (1998)*

[8]*Data from Mehregany et al. (2000)*

[9]*Data from Pizzagalli (2021)*

Figure 4.11 shows the stress-strain curves for all the nine independent elastic stiffness constants for all the five CTO samples. By linearly fitting the stress-strain data, the resulting elastic stiffness constants presented in table 4.11 were obtained. As can be observed, $c_{11}$ is larger than $c_{22}$, but smaller than $c_{33}$ for all the CTO samples. This implies that all the five crystals are anisotropic. The elastic constants of a crystal serve as the foundation for the determination of the mechanical stability. Using the stability conditions in equations 3.14 and 3.15, we concluded that all the five CTO samples in this study are mechanically stable under ambient conditions. As can be observed in table 4.11, the calculated elastic stiffness constants increase with increase in the number of atoms of Cd up to CTO 4, then decrease at CTO 5. The elastic stiffness constants $c_{11}$ and $c_{33}$ are higher than the rest. This demonstrates that under uniaxial force in the *a* and *c* directions, CTO is exceedingly incompressible (Parvin & Naqib, 2019). $c_{33}$ is the highest, which is an indication that the incompressibility of the crystal along the *c* direction is the highest, and suggests that the crystal is anisotropic.

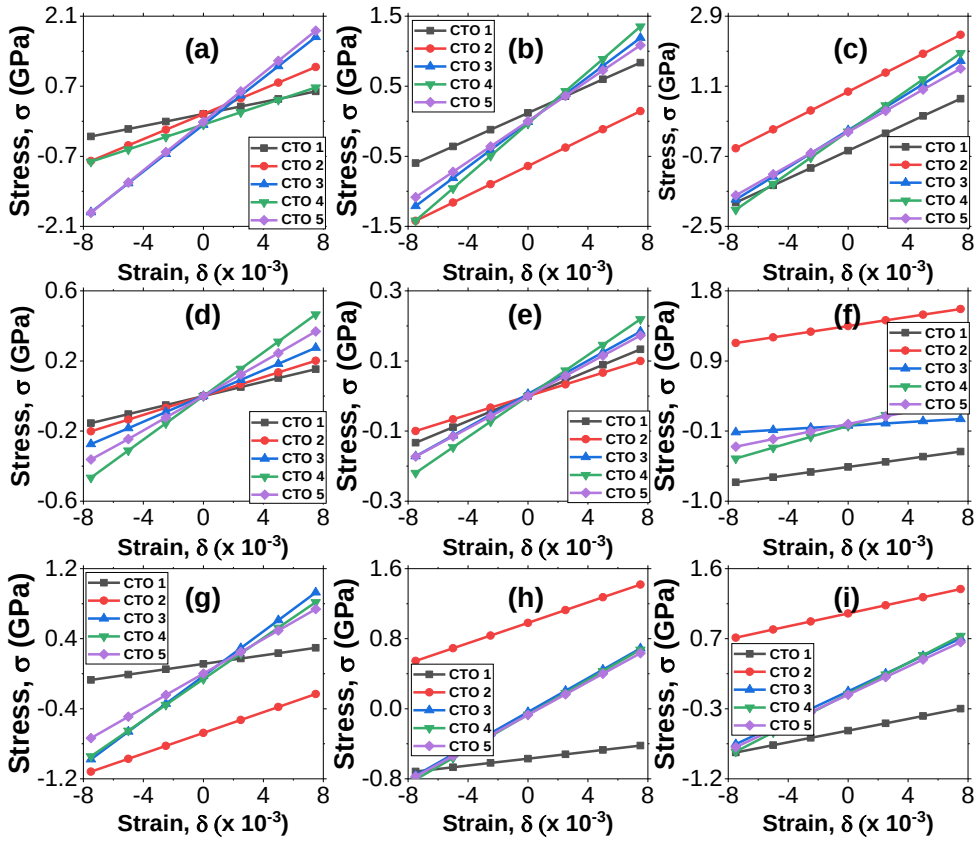


***Figure 4.11: Stress-strain curves for determining the elastic stiffness constants: (a) $c_{11}$, (b) $c_{22}$, (c) $c_{33}$, (d) $c_{44}$, (e) $c_{55}$, (f) $c_{66}$, (g) $c_{12}$, (h) $c_{13}$, and (i) $c_{23}$ of all the five CTO samples***

The shear elastic constants $c_{12}$ and $c_{13}$ together lead to a functional stress component in the crystallographic *a*-axis with a uniaxial strain along the crystallographic *b*- and *c*-axes, respectively. The comparatively small values of these two stiffness constants of the CTO samples make them less capable of resisting the shear deformation along the crystallographic *b*- and *c*-axes under a large stress along the crystallographic *a*-axis. The ability of the CTO samples to resist shear deformation increases with increase in the number of Cd atoms up to CTO 4, then drops at CTO 5. The elastic stiffness constants $c_{44}$, $c_{55}$ and $c_{66}$ indirectly lead to the indentation hardness of materials. Due to comparatively low values of these three elastic stiffness constants, the hardness of all the CTO samples is expected to be low. The low values of $c_{44}$, $c_{55}$ and $c_{66}$ are indicative of high shearability and high machinability of the CTO samples, since they are the ones contributing to the shear (Ching, Rulis, & Misra, 2009). Thus, the all the CTO samples are relatively soft materials.

***Table 4.11: The computed elastic stiffness constants (in GPa) and the corresponding compliance constants (in $GPa^{-1}$) obtained from the stress-strain relationship for all the five cadmium-tin-oxide samples***

| | | $c_{11}$ | $c_{22}$ | $c_{33}$ | $c_{44}$ | $c_{55}$ | $c_{66}$ | $c_{12}$ | $c_{13}$ | $c_{13}$ |
|---|---|---|---|---|---|---|---|---|---|---|
| $c_{ij}$ | CTO 1 | 60.017 | 95.66 | 177.99 | 20.53 | 17.79 | 27.45 | 24.384 | 19.74 | 39.129 |
| | CTO 2 | 125.32 | 104.5 | 194.47 | 26.89 | 13.31 | 30.34 | 59.126 | 58.13 | 43.413 |
| | CTO 3 | 233.44 | 160.0 | 237.52 | 36.68 | 23.70 | 53.68 | 127.09 | 96.79 | 94.638 |
| | CTO 4 | 267.19 | 184.6 | 268.33 | 62.11 | 29.21 | 58.44 | 117.32 | 98.91 | 103.56 |
| | CTO 5 | 242.70 | 144.5 | 217.09 | 49.09 | 23.0 | 40.6 | 98.247 | 93.92 | 93.936 |
| | | $s_{11}$ | $s_{22}$ | $s_{33}$ | $s_{44}$ | $s_{55}$ | $s_{66}$ | $s_{12}$ | $s_{13}$ | $s_{13}$ |
| $s_{ij}$ ($x10^{-3}$) | CTO 1 | 18.79 | 12.48 | 6.242 | 48.71 | 56.11 | 36.42 | -4.233 | -1.133 | -2.264 |
| | CTO 2 | 11.70 | 13.33 | 6.091 | 37.19 | 75.13 | 32.96 | -5.698 | -2.226 | -1.271 |
| | CTO 3 | 7.697 | 12.21 | 5.618 | 27.26 | 42.19 | 18.63 | -5.572 | -0.917 | -2.594 |
| | CTO 4 | 5.335 | 8.512 | 4.889 | 16.10 | 34.25 | 17.11 | -2.919 | -0.839 | -2.209 |
| | CTO 5 | 5.878 | 11.43 | 6.627 | 20.37 | 43.44 | 24.60 | -3.260 | -1.133 | -3.537 |

Elastic constants control how a crystal reacts to external pressure. The crystalline elastic constants that can be described in form of the bulk modulus, shear modulus, Young's modulus, and Poisson's ratio, are used to characterize most engineering materials, and are useful parameters in the engineering design. Table 4.12 shows the mechanical properties of all the five CTO samples. All the properties increase from CTO 1 to CTO 4 (with the number of Cd atoms) before dropping at CTO 5. The drop at CTO 5 can be attributed to the increase in its unit cell volume, as can be observed in table 4.7.

The bulk modulus is a measure of resistance of a material to fracture, which is also referred to as the incompressibility. It also has to do with a material's typical bonding strength. The strength of the bond increases with increase in the bulk modulus. The Hill's average bulk modulus of 149.1 GPa obtained in this study for CTO 4 shows that it is much less compressible compared to that of Si at 80 GPa (Auciello et al., 2008), at 97 GPa (Moon et al., 2012), and at 93.9 GPa (the computational value obtained in this study). The bulk modulus of SiC at 222 GPa obtained in this study is however much higher than that of CTO. Sample CTO 1 recorded the lowest value of the Hill's average bulk modulus among all the CTO samples (at 50.44 GPa).

The ratio of shear stress to shear strain, which is also known as the shear modulus or modulus of stiffness, was also calculated for the CTO samples in this study. As the name suggests, a large value of shear modulus indicates that a material is highly rigid. It was found out that the bulk modulus was consistently greater than the shear modulus, indicating that the shear modulus is what restricts the mechanical stability of the CTO samples. Super hard materials have very high microhardness values as well as high thermal conductivity and compressional strength (Teter, 1998).

***Table 4.12: The computed mechanical properties of the five cadmium-tin-oxide samples. The bulk modulus (B), shear modulus (G), Young's modulus (E), and Vickers hardness ( $H_V$) are in GPa, while the Poisson ratio ($\mu$) and the Pugh's ratio (n) have no units***

| | $B_V$ | $B_R$ | B | $G_V$ | $G_R$ | G | $E_V$ | $E_R$ | E | $\mu$ | $H_V$ | n |
|---|---|---|---|---|---|---|---|---|---|---|---|---|
| CTO 1 | 55.57 | 45.31 | 50.44 | 29.9 | 24.8 | 27.3 | 75.95 | 62.90 | 69.42 | 0.270 | 3.757 | 1.846 |
| CTO 2 | 82.84 | 78.57 | 80.71 | 31.7 | 25.1 | 28.4 | 84.29 | 68.11 | 76.20 | 0.343 | 1.174 | 2.841 |
| CTO 3 | 140.9 | 135.9 | 138.4 | 43.6 | 37.3 | 40.4 | 118.7 | 102.4 | 110.5 | 0.367 | 1.131 | 3.422 |
| CTO 4 | 151.1 | 147.1 | 149.1 | 56.6 | 49.8 | 53.2 | 151.0 | 134.3 | 142.7 | 0.340 | 3.130 | 2.801 |
| CTO 5 | 130.7 | 123.8 | 127.2 | 43.8 | 38.2 | 41.0 | 118.1 | 103.9 | 111.0 | 0.355 | 1.663 | 3.105 |

Diamond, the hardest known naturally occurring substance, has a shear modulus value of 535 GPa (McSkimin & Andreatch, 1972), while the value for SiC obtained in this study is 185.9 GPa. Si, which widely used in the manufacture of MEMS, has a value of 66 GPa (Ding, Zhou, & Zhao, 2004) and 62.2 GPa (the computational value obtained in this study). The result in this study produced values of shear modulus of 27.3-53.2 GPa for CTO. However, since the difference between 53.2 (for CTO 4) and that of Si is not very large, it can be used as a substitute to Si in the manufacture of MEMS mechanical sensors. All the samples have bulk moduli that are significantly greater than shear moduli, suggesting that CTO is more resistant to volume change than to shape change.

Young's modulus is one of the mechanical properties of materials that has the greatest impact on technological applications. A material's resistance to longitudinal tension is gauged by the Young's modulus. A higher value of the Young's modulus indicates high stiffness. Additionally, the Young's modulus affects the ability of a material to withstand thermal shock, because it is inversely correlated with the critical thermal shock coefficient, which is good for the fabrication of MEMS mechanical sensors as well as high-speed contact-mode microactuators, which are consequently used in the fabrication of a wide range of MEMS devices such as gears, micro engine rotors, and accelerometers (Luo et al., 2007).

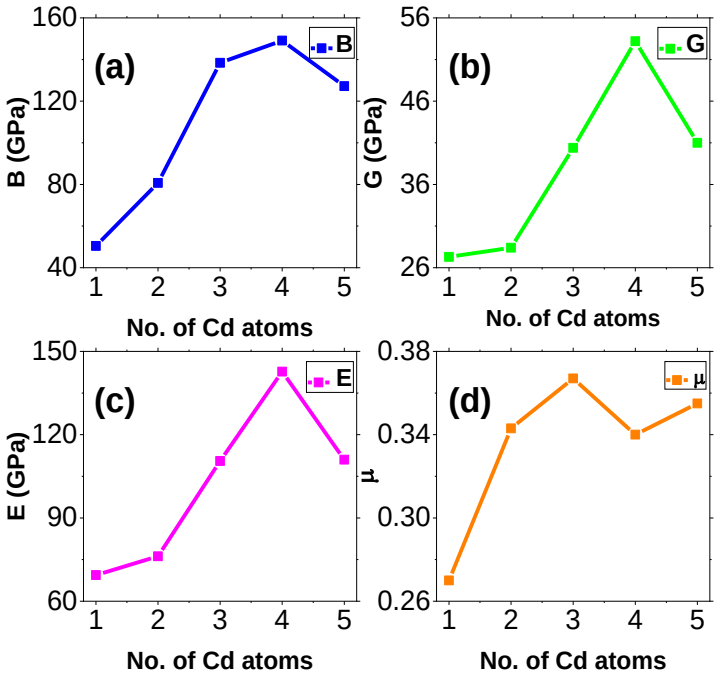


***Figure 4.12: The variation of the calculated elastic constants of cadmium-tin-oxide samples with the number of cadmium atoms***

The computed value of the Young's modulus of CTO of 69.42-142.7 GPa in this study, and more so, the value of 142.7 for CTO 4, is comparable to that of Si at 130-169 GPa (Hopcroft et al., 2010). Thus, CTO can be used as a substitute to Si in the fabrication of mechanical sensors. The Young's modulus of SiC is much larger at 435.9 (computed in this study), which are good for MEMS that operate under harsh environmental conditions such as microactuators. However, Si has a larger ratio of Young's modulus to density (67.04, from table 4.6) compared to that of CTO 4 (18.70, from table 4.7),

which causes greater resonance frequencies with better beam structure quality factors (Coakley et al., 2003). This property makes micromechanical resonators particularly advantageous for frequency filtering in high-speed communication transceivers. Si thus outperforms CTO in this regard. The graphical variation of the elastic constants of CTO as a function of the number of Cd atoms is depicted in figure 4.12, which clearly shows that all the four elastic constants increase consistently with increase in the number of Cd atoms up to CTO 4, then drop at CTO 5.

A significant property that affects many of the technological applications of materials, is the hardness. It is generally the resistance that a material offers to external mechanical actions that tend to scratch, abrade, indent, or in other way, permanently affect its surface. Hard materials such as diamond have low compressibility and high wear resistance (Manyali & Sifuna, 2019), a property that is highly desired for the substrates used in the manufacture of MEMS devices such as micromotors and coating materials that work under harsh environmental conditions (Jiang & Cheung, 2009). Materials with Vickers hardness of more than 40 GPa are said to be super hard (Teter, 1998).

The Vickers hardness of 1.131-3.757 GPa obtained in this study shows that CTO is a softer material compared to Si at 10 GPa (Teter, 1998) (10.84 GPa obtained in this study), and much softer compared to SiC at 31.56 GPa. This shows that it cannot be a better substrate to Si in the manufacture of some MEMS. Harder MEMS materials like SiC are needed for devices that operate in hostile environments, such as those used in combustion processes, gas turbine control, and the oil sector. These harsh-environment MEMS devices include microsensors and microactuators. However, CTO can be a better substrate in the fabrication of MEMS devices for use in the medical field such as microbridges, image sensors, and microbolometers, which require soft substrates. These MEMS devices have been fabricated on polymer substrates, which are preferred to Si since they are flexible, transparent, and have a large area for processing. However, the main drawback of polymers is that they are poor conductors of both heat and electricity. CTO being a better conductor of electricity compared to polymers, which is comparable to that of Si as well as being transparent in the UV-Vis spectrum, can be a better alternative to both Si and polymers in the manufacture of these MEMS.

Poisson's ratio can be used to assess many physical properties of solids, including prediction of stability against shear (Hadi, Rayhan, Naqib, Chroneos, & Islam, 2019). A lower value of the Poisson's ratio leads to stability of a material against shear. The Poisson's ratio is relatively large for CTO at 0.270-0.367 in this study, since it ranges from 0.0 to 0.5 for most materials. This demonstrates that, in contrast to Si whose Poisson's ratio is 0.23 (in this study), CTO exhibits substantial elastic deformation even when subjected to small amounts of strain. The lower value of Poisson's ratio for Si means that it is not easily deformed as compared to CTO. SiC is much harder to deform, since its value of the Poisson's ratio is much lower at 0.17.

The Pugh's ratio (Pugh, 1954) as well as the Poisson's ratio can be used to determine the ductile or brittle nature of materials. Materials which fracture when subjected to stress, but have little tendency to deform before rupture, are said to be brittle; while those that can easily be distorted are said to be ductile. Super hard materials such as diamond are excellent examples of brittle materials. The value of the Pugh's ratio obtained in this study of 1.846-3.422 shows that CTO is a ductile material, with CTO 3 being the most ductile, while CTO 1 is the least. Since hard materials such as diamond and carbon nitride are characterized by brittleness, the combination of soft and ductile nature of CTO in this study is justified, and so, is the combination of hard and brittle nature of both Si and SiC. Going by the proposal of Haines, Leger, & Bocquillon (2001), the calculated Poisson's ratio in this study of 0.270-0.367 confirms the ductile nature of CTO. Sample CTO 1 was found to be the least ductile, while sample CTO 3 is the most ductile, which agrees with the trend for the Pugh's ratio. The brittleness of both Si and SiC was also confirmed from a combination of their Poisson's and Pugh's ratios.

Further confirmation of the ductile/ brittle nature of materials can be assessed using the Cauchy pressures. Table 4.13 shows the computed values of the Cauchy pressures in this study. The Cauchy pressure helps in determining the nature of bonding in materials. According to Pettifor (1992), and Eberhart & Jones (2012), a material with more positive Cauchy pressures has more metallic bonds, and is consequently more ductile; whereas a material with more negative Cauchy pressures has more dihedral/angular bonds, and is consequently more brittle. As can be observed in table 4.13, the Cauchy

pressures $P_a^C$, $P_b^C$, and $P_c^C$, which are for the {100}, {010}, and {001} planes respectively, are all negative for both Si and SiC. This further confirms their brittle nature. The table shows that SiC is more brittle than Si, since its values of Cauchy pressure are more negative than those of Si. This is consistent with the Poisson ratios and the Pugh's ratios in table 4.10, which shows that the values for SiC are lower than those of Si and thus, more brittle.

***Table 4.13: The calculated Cauchy pressures for determination of the ductile or brittle nature of silicon and silicon carbide***

| | $P_a^C$ | $P_b^C$ | $P_c^C$ |
|---|---|---|---|
| Si | -12.4 | -12.4 | -12.4 |
| SiC | -104.6 | -104.6 | -104.6 |

Table 4.14 shows the calculated Cauchy pressures for all the five CTO samples. As the table depicts, all the values are positive except $P_c^C$ for CTO 1, which is negative. This implies that CTO has metallic bonds and thus, further confirms its ductile nature. The less ductile nature of CTO 1 can be confirmed from the Poisson's ratio (where it has a value of 0.270, just at the boundary between brittleness and ductility), and from the Pugh's ratio (where it has a value of 1.846, just slightly above the boundary of 1.75). From table 4.14 it can also be observed that CTO 3 is the most metallic of all the samples, with the {001} plane having the most metallic bonds, since the higher the positive values of the Cauchy pressure, the more the metallic bonds.

***Table 4.14: The calculated Cauchy pressures for determination of the ductile or brittle nature of cadmium-tin-oxide samples***

| | $P_a^C$ | $P_a^C$ | $P_c^C$ |
|---|---|---|---|
| CTO 1 | 18.597 | 1.950 | -3.065 |
| CTO 2 | 16.520 | 44.817 | 28.787 |
| CTO 3 | 57.962 | 73.087 | 73.406 |
| CTO 4 | 41.448 | 69.698 | 58.876 |
| CTO 5 | 44.844 | 70.902 | 57.599 |

Si, the most widely utilized material in the fabrication of MEMS devices, is brittle and so, are the other MEMS substrate materials like SiC (confirmed in this study) and diamond. The combination of the ductility obtained in this study, and the transparent and electrically conducting nature of CTO that are available in the literature, makes it a unique material as a substrate for the manufacture of most MEMS. Thus, it can find good use in the fabrication of flexible MEMS for non-planar and non-rigid applications such as sound transducers in air and water; and also, in biomedical applications such as bioMEMS, tissue compatible implants, cardiopulmonary sensors, microbolometers, temperature and pressure sensors, flexible displays, and accelerometers (Kim & Meng, 2019).

The physical properties of materials such as anisotropic plastic deformation, elastic instability, and crack behaviour, are significantly influenced by elastic anisotropy in crystals (Chen et al., 2015). As indicated in table 4.15, the shear anisotropy factors ($A_1$, $A_2$, and $A_3$) indicate the degree of anisotropy in the bonding between atoms in the {100}, {010}, and {001} planes respectively for both Si and SiC. The shear anisotropic factors ($A_1$, $A_2$, and $A_3$) must all be equal to unity for an isotropic crystal. Any departure of the values from unity indicates some degree of anisotropy.

***Table 4.15: Anisotropy factors: ($A_1$), ($A_2$), and ($A_3$) for the shear planes along the x, y, and z directions (representing the a, b, and c axes respectively) for both silicon and silicon carbide. $A_B$ and $A_G$ are the anisotropy factors of bulk and shear moduli respectively, while $A^U$ is the universal anisotropy factor. $A_{Ba}$ and $A_{Bc}$ are the axial anisotropic factors with respect to the b axis***

| | $A_1$ | $A_2$ | $A_3$ | $A_{Ba}$ | $A_{Bc}$ | $A^U$ | $A_B$ | $A_G$ |
|---|---|---|---|---|---|---|---|---|
| Si | 1.592 | 1.592 | 1.592 | 1.00 | 1.00 | 0.264 | 0.000 | 0.026 |
| SiC | 1.965 | 1.965 | 1.965 | 1.00 | 1.00 | 0.569 | 0.000 | 0.054 |

The value of shear anisotropic factors $A_1$, $A_2$, and $A_3$ in table 4.15 for both Si and SiC, are much larger than unity. This implies that both materials are anisotropic. Si is more anisotropic than SiC, since it has a larger deviation from unity. A further condition for isotropy requires that the values of $A_B$, $A_G$, and $A^U$ must be equal to zero for an isotropic material. Anisotropy is represented by any deviation of the three parameters from zero. Using the values in table 4.15, it can be observed that $A_B$ indicates that both materials are isotropic, whereas $A^U$ indicates that they are anisotropic. The computed values of $A_G$ show that both materials are anisotropic. Thus, it can be concluded that both Si and SiC have isotropic bulk moduli and anisotropic shear moduli. The anisotropic shear moduli, which when combined with the anisotropic shear planes ($A_1$, $A_2$ and $A_3$), leads to the universal anisotropy ($A^U$), which show that both materials are universally anisotropic.

Table 4.16 shows the computed values of the elastic anisotropic factors for CTO, which show that the value of shear anisotropic factor $A_2$ is much less than unity for all the five CTO samples, followed closely by $A_1$. This implies that the *b* axis which $A_2$ represents, is the most anisotropic. The {001} plane, which is represented by the *c* axis, is more isotropic compared to the other planes, with CTO 5 being the least anisotropic, while CTO 3 is the most anisotropic. The values of $A_B$, $A_G$, and $A^U$ confirm the anisotropic nature of CTO. All the $A_B$, $A_G$, and $A^U$ factors have non-zero values, and the values for $A_G$ are generally larger than those for $A_B$, implying that CTO exhibits a larger anisotropy of the bulk modulus, but a lower anisotropic degree of the shear modulus. CTO 4 has the lowest degree of universal anisotropy of all the five samples of CTO in this study, since it is the one whose value is closest to zero. On the other hand, CTO 2 has the highest degree of universal anisotropy.

Pure normal stress would only cause normal stains in isotropic materials. Similarly, only shear strains would result from a pure shear stress. However, for anisotropic materials, pure normal stress would result into both normal and shear strains, and likewise to the shear stress. Anisotropy makes stress analysis of structures to be tedious. It affects surface stability by weakening it. A value of anisotropy factor close to unity is acceptable. However, large deviations from unity should not be ignored, especially if the substrate is thin (in the range of micrometres and nanometres) (Li, Khounsary, & Gosz, 2004). Thus, CTO 4 makes the best substrate for MEMS of all the five CTO samples in this study, since it has the lowest value of universal anisotropy.

***Table 4.16: Anisotropy factors: ($A_1$), ($A_2$), and ($A_3$) for the shear planes along the x, y, and z directions (representing the a, b, and c axes respectively) for cadmium-tin-oxide. $A_B$ and $A_G$ are the anisotropy factors of bulk and shear moduli respectively, while $A^U$ is the universal anisotropy factor. $A_{Ba}$ and $A_{Bc}$ are the axial anisotropic factors with respect to the b axis***

| | $A_1$ | $A_2$ | $A_3$ | $A_{Ba}$ | $A_{Bc}$ | $A^U$ | $A_B$ | $A_G$ |
|---|---|---|---|---|---|---|---|---|
| CTO 1 | 0.414 | 0.364 | 1.027 | 0.442 | 2.071 | 1.246 | 0.1020 | 0.0925 |
| CTO 2 | 0.529 | 0.251 | 1.088 | 1.683 | 2.450 | 1.359 | 0.0265 | 0.1154 |
| CTO 3 | 0.529 | 0.455 | 1.542 | 3.345 | 1.920 | 0.895 | 0.0181 | 0.0709 |
| CTO 4 | 0.736 | 0.475 | 1.077 | 2.147 | 1.839 | 0.713 | 0.0134 | 0.0612 |
| CTO 5 | 0.722 | 0.530 | 0.852 | 3.120 | 2.369 | 0.785 | 0.0273 | 0.0680 |

Figure 4.13 shows the 2D directional Young's moduli of both Si and SiC, while figure 4.14 shows the 3D structures of their corresponding directional Young's moduli. Since the curves in figure 4.13 are not perfectly circular, and the 3D structures in figure 4.14 are not perfectly spherical, we confirm the anisotropy in both Si and SiC. Figure 4.15 shows the directional Young's moduli for CTO 4. The 2D and 3D curves for the other CTO samples (CTO 1, CTO 2, CTO 3, and CTO 5) are presented in Appendix 10a to c. The figure (figure 4.15) confirms that CTO is equally anisotropic. The anisotropy along the {1 1 0} direction (figure 4.15b) is more than that along the {1 0 0} direction (figure 4.15a), since the curve for the {1 0 0} direction is closer to being circular than that along the {1 1 0} direction. The 3D structure (figure 4.15c) shows a very large deviation from being perfectly spherical.

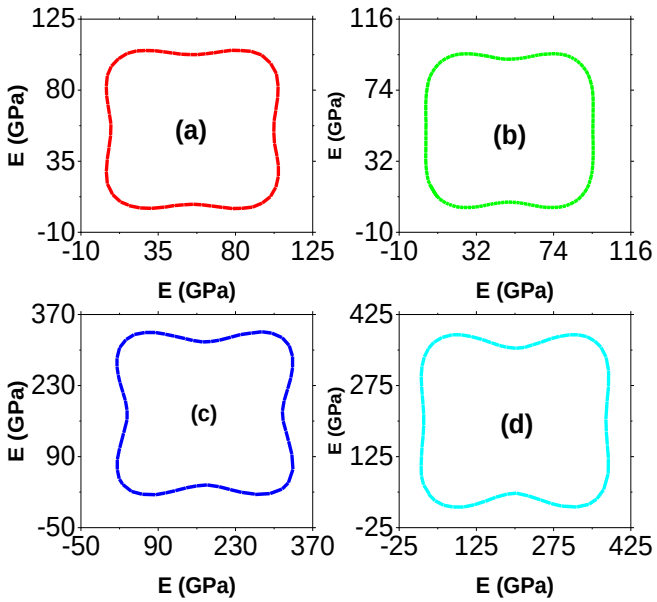


***Figure 4.13: The 2-Dimensional curves for directional Young's moduli of: (a) silicon along the {1 0 0} direction, (b) silicon along the {1 1 0} direction, (c) silicon carbide along the {1 0 0} direction, and (d) silicon carbide along the {1 1 0} direction***

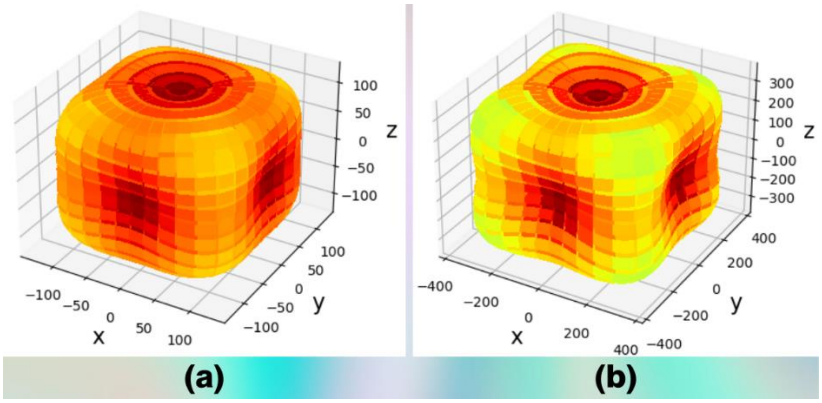


***Figure 4.14: The 3D curves for the directional Young's moduli of: (a) silicon, and (b) silicon carbide***

A recent study on the effect of anisotropy of single crystal Si on the frequency split of vibrating MEMS ring gyroscope by Qin, Gao, Jia, Ding, Huang, & Li (2019) showed that anisotropy causes the elastic properties of the gyroscopes to vary, depending on the direction and thus, affecting their frequency characteristics. From this study, we have found out that CTO is anisotropic, both axially ($A_{Ba}$ and $A_{Bc}$) and universally ($A^U$). Thus, it is not ideal for the manufacture of MEMS such as the ring gyroscopes, whose elastic properties are greatly influenced by the elastic anisotropy.

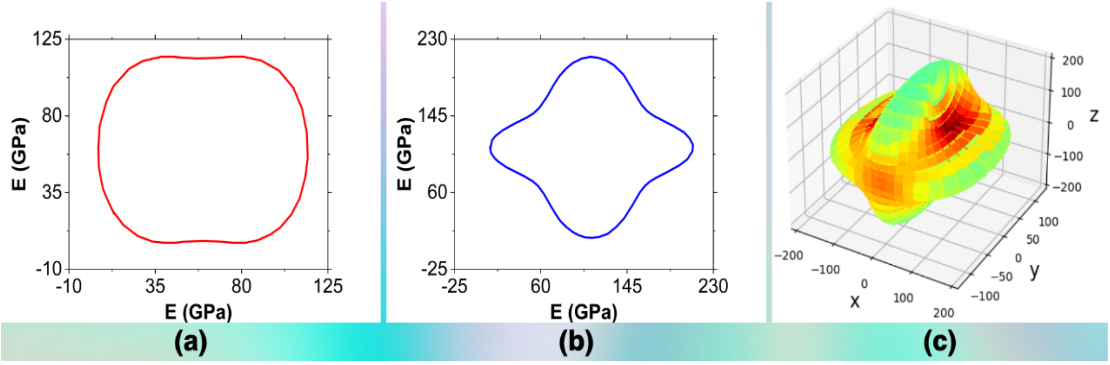


***Figure 4.15: (a) a 2-Dimensional structure for the Young's modulus of CTO 4 along the {1 0 0} direction, (b) a 2-Dimensional structure for the Young's modulus of CTO 4 along the {1 1 0} direction, and (c) a 3-Dimensional structure of the Young's modulus for CTO 4***

### 4.3.2 Pressure-dependent mechanical properties

The elastic stiffness constants of the three materials as a function of the applied pressure are displayed in Table 4.17. With an increase in the applied pressure, the elastic stiffness constants of all three materials increased. This implies that as the applied pressure increases, the bonds between the atoms become shorter, a phenomenon that leads to resistance to the change in their volumes, which consequently leads to an increase in the elastic stiffness constants.

***Table 4.17: The calculated elastic stiffness constants (in GPa) of silicon, silicon carbide, and cadmium-tin-oxide as a function of the applied pressure (in GPa).***

| Silicon | | | | Silicon carbide | | | |
|---|---|---|---|---|---|---|---|
| p | $c_{11}$ | $c_{44}$ | $c_{12}$ | p | $c_{11}$ | $c_{44}$ | $c_{12}$ |
| 00 | 156.6 | 74.9 | 62.5 | 00 | 387.5 | 139.3 | 243.9 |
| 10 | 183.0 | 75.3 | 90.7 | 10 | 426.5 | 177.0 | 260.0 |
| 20 | 185.2 | 75.4 | 93.2 | 20 | 461.7 | 212.4 | 271.9 |
| 30 | 185.7 | 75.5 | 93.9 | 30 | 494.3 | 246.9 | 281.3 |
| 40 | 186.0 | 75.6 | 94.1 | 40 | 516.7 | 271.3 | 286.9 |
| 50 | 186.1 | 75.7 | 94.2 | 50 | 525.7 | 281.1 | 289.0 |

***Table 4.18: The calculated elastic stiffness constants (in GPa) of cadmium-tin-oxide as a function of the applied pressure (in GPa).***

| p | $c_{11}$ | $c_{22}$ | $c_{33}$ | $c_{44}$ | $c_{55}$ | $c_{66}$ | $c_{12}$ | $c_{13}$ | $c_{23}$ |
|---|---|---|---|---|---|---|---|---|---|
| 00 | 268.6 | 186.1 | 272.4 | 62.9 | 29.2 | 58.5 | 117.8 | 99.3 | 104.2 |
| 10 | 322.3 | 206.9 | 312.8 | 67.5 | 32.3 | 70.0 | 171.1 | 141.9 | 148.9 |
| 20 | 331.7 | 214.0 | 322.2 | 68.0 | 33.3 | 71.7 | 176.3 | 150.1 | 158.7 |
| 30 | 334.7 | 213.0 | 324.0 | 68.1 | 33.6 | 72.3 | 178.3 | 152.5 | 158.8 |
| 40 | 336.0 | 216.0 | 324.2 | 68.2 | 33.5 | 72.4 | 179.0 | 153.5 | 159.0 |
| 50 | 336.7 | 217.0 | 324.4 | 68.4 | 33.6 | 72.5 | 179.7 | 154.1 | 159.7 |

The calculated mechanical properties derived from the elastic stiffness constants in tables 4.17 and 4.18 are presented in table 4.19. All the four elastic constants (the bulk modulus, the shear modulus, the Young's modulus, and the Poisson ratio) increase as the applied pressure increases. All the three materials become more incompressible as the applied pressure increases, owing to increase in their bulk moduli. The bulk modulus of Si increased by 32.81%, that of SiC increased by 63. 38%, while that of CTO increased by 34.91% when the applied pressure was increased from 0 to 50 GPa. This indicates that SiC becomes much more incompressible with increase in the applied pressure.

Except for Si, the shear moduli of the other two materials increased with increase in the applied pressure, indicating that the materials become more resistant to shape change (except Si). The shear modulus of Si decreased by 0.81%, that of SiC increased by 10.06%, while that of CTO increased by 4.81% when the applied pressure was increased from 0 to 50 GPa, implying that SiC becomes much more resistant to shape change compared to CTO. The decrease in the shear modulus of Si indicates that it becomes less resistant to shape change, though the change is small.

The Young's modulus increased by 4.39% for Si, 18.44% for SiC, and 5.76% for CTO, which implies that SiC becomes more resistant to longitudinal tension with increase in the applied pressure compared to both Si and CTO. The ductility of the three materials was tested using both the Poisson's ratio as well as the Pugh's ratio, where we observed from table 4.19 that the ductility increased with increase in the applied pressure. CTO is far much ductile even at 0 GPa pressure. Si becomes ductile as from 10 GPa, while SiC just reaches the boundary of ductility/ brittles (1.771) at 50 GPa pressure. The Poisson's ratios of the three materials increased by 27.95%, 51.74%, and 9.71 % for Si, SiC and CTO respectively, while the Pugh's ratios increased by 3.44%, 48.32 %, and 29.50 % for Si, SiC and CTO respectively.

Although all the three materials become more ductile as the applied pressure increases, there is a corresponding drop in their Vickers hardness, which implies that they become less hard, with lower wear resistance and hence, more vulnerable to scratch and abrasion, a property that is not desirable for MEMS such as micromotors and coating materials (Jiang & Cheung, 2009). The values of the Vickers hardness decreased by 58.83%, 57.41%, and 89.60% for Si, SiC and CTO respectively as the applied pressure was increased from 0 to 50 GPa. Figure 4.16 shows the graphs of the calculated mechanical properties of the three materials as a function of the applied pressure. As the figure depicts, the mechanical properties rise sharply from 0 to 10 GPa, except the shear modulus of Si. Upon increasing the applied pressure, the change becomes small.

***Table 4.19: The calculated mechanical properties*** of ***silicon, silicon carbide, and cadmium-tin-oxide as a function of the applied pressure (in GPa)***

| Silicon | | | | | | |
|---|---|---|---|---|---|---|
| P (GPa) | B (GPa) | G (GPa) | E (GPa) | μ | n | $H_V$ (GPa) |
| 00 | 93.9 | 62.2 | 152.7 | 0.229 | 1.510 | 10.84 |
| 10 | 121.5 | 62.1 | 158.9 | 0.281 | 1.963 | 7.169 |
| 20 | 123.8 | 62.0 | 159.1 | 0.286 | 2.003 | 6.922 |
| 30 | 124.5 | 61.9 | 159.2 | 0.289 | 2.013 | 6.855 |
| 40 | 124.6 | 61.8 | 159.3 | 0.292 | 2.014 | 6.840 |
| 50 | 124.7 | 61.7 | 159.4 | 0.293 | 2.015 | 6.825 |
| Silicon carbide | | | | | | |
| P (GPa) | B (GPa) | G (GPa) | E (GPa) | μ | n | $H_V$ (GPa) |
| 00 | 222.0 | 185.9 | 435.9 | 0.172 | 1.194 | 31.56 |
| 10 | 260.0 | 193.6 | 465.1 | 0.201 | 1.344 | 27.82 |
| 20 | 295.5 | 198.8 | 486.8 | 0.224 | 1.486 | 24.82 |
| 30 | 329.4 | 202.2 | 503.3 | 0.244 | 1.628 | 22.26 |
| 40 | 353.1 | 204.1 | 512.9 | 0.256 | 1.731 | 20.64 |
| 50 | 362.7 | 204.6 | 516.3 | 0.261 | 1.771 | 20.05 |
| Cadmium-tin-oxide | | | | | | |
| P (GPa) | B (GPa) | G (GPa) | E (GPa) | μ | n | $H_V$ (GPa) |
| 00 | 149.1 | 53.7 | 143.7 | 0.340 | 2.780 | 3.216 |
| 10 | 191.7 | 54.9 | 150.5 | 0.369 | 3.488 | 1.829 |
| 20 | 199.7 | 55.8 | 153.2 | 0.372 | 3.581 | 1.727 |
| 30 | 200.5 | 56.1 | 153.8 | 0.372 | 3.588 | 1.747 |
| 40 | 201.7 | 56.2 | 154.2 | 0.372 | 3.590 | 1.733 |
| 50 | 202.5 | 56.3 | 154.4 | 0.373 | 3.600 | 1.723 |

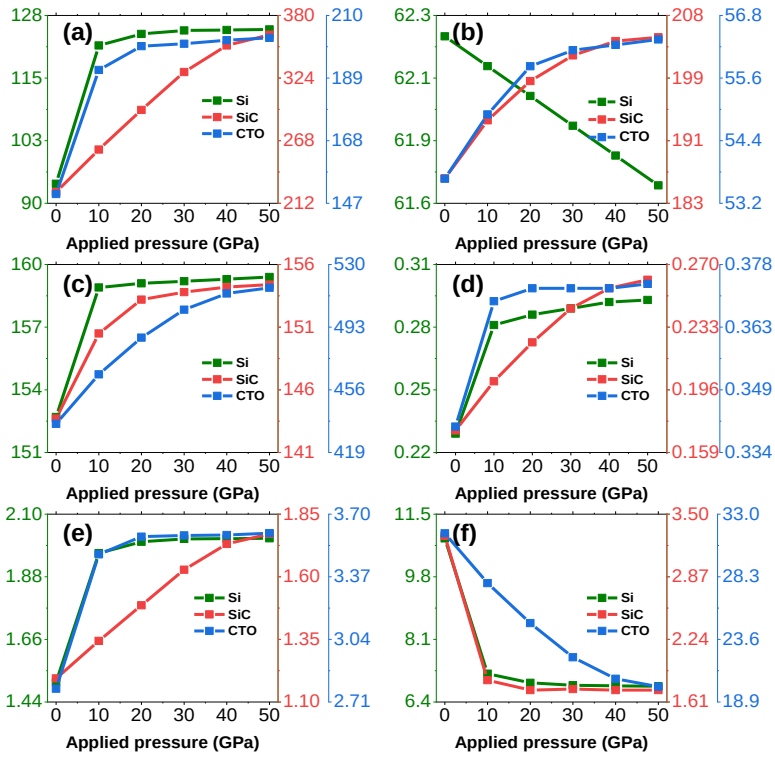


***Figure 4.16: The computed mechanical properties of silicon, silicon carbide, and cadmium-tin-oxide as a function of the applied pressure: (a) Bulk modulus, (b) Shear modulus, (c) Young's modulus, (d) Poisson's ratio, (e) Pugh's ratio, and (f) Vickers hardness***

SiC in this study has shown to be mechanically unstable with increase in the applied pressure compared to both Si and CTO. It undergoes a significant change in the mechanical properties with change in the applied pressure. CTO on the other hand, undergoes a much lower change in its mechanical properties as the applied pressure increases. All the three materials become ductile with increase in the applied pressure. Since CTO is mechanically more stable than SiC, it can form a better substrate for manufacture of downhole pressure sensors and diesel engines. The large drop in the Vickers hardness of CTO with increase in the applied pressure implies that it is not suitable for manufacture of MEMS micromotors and coating materials, which require super hard substrates. Both bulk and Young's moduli of Si and CTO undergo comparable increase with increase in the applied pressure. The decrease in the shear modulus for Si is not good for manufacture of MEMS such as mechanical sensors. The Pugh's ratio of Si undergoes a much lower change with increase in the applied pressure compared to that of CTO.

## 4.4 Thermal properties

### 4.4.1 Zero-pressure thermal properties

Table 4.20 shows the calculated thermal properties of the three materials at zero GPa pressure. SiC has the highest value of the Debye temperature, which indicates that the optical phonons in SiC have the highest frequency compared to those of Si and CTO, which implies that they require greatest energy to activate as compared to the other two. This further confirms the highest stiffness of SiC compared to both Si and CTO. The calculated Debye temperature of SiC obtained in this study is 3.742% lower than the value that has been reported by Peng et al. (2012). The value of the Debye temperature for Si from a study by Keesom & Seidel (1959) is within 1% of the result obtained in this study, showing an excellent agreement (table 4.20).

***Table 4.20. The calculated Debye temperature ($\theta_D$) and melting temperature ($T_m$) of silicon, silicon carbide, and cadmium-tin-oxide***

| Material | $\theta_D$ (K) | $T_m$ (K) |
|---|---|---|
| Si | 624.6 (636[a]) | 1781.1(1687[c]), (1688[d]) |
| SiC | 1152 (1194.8[b]) | 2974.4 (3103[e]) |
| CTO 1 | 261.5 | 1377.8 |
| CTO 2 | 294.6 | 1658.2 |
| CTO 3 | 323.4 | 2168.1 |
| CTO 4 | 377.7 | 2295.5 |
| CTO 5 | 316.9 | 2091.3 |

[a]*Experimental data from [Keesom & Seidel, 1959]*

[b]*Experimental data from [Peng et al, 2012]*

[c]*Experimental data from [Yang & Jiang, 2005]*

[d]*Computational data from [Talyzin, Samsonov, Samsonov, Pushkar, & Dronnikov, 2019]*

[e]*Experimental data from [Munro, 1997]*

As table 4.20 depicts, the Debye temperatures of CTO increase consistently up to CTO 4, then drops at CTO 5. This shows that that it increases with increase in the number of Cd atoms up to 4, then drops at 5. The highest value of the Debye temperature for CTO 4 indicates that the optical phonons in CTO 4 have the highest frequency, which implies that the optical phonons in CTO 4 require greater energy to activate as compared to those of the other four CTO samples, and thus, CTO 4 is the stiffest, as can be observed in table 4.11 for the elastic stiffness constants. As far as we are aware, there is currently no information about the Debye temperature of CTO in the literature. Thus, this work serves as a foundation for future reference.

The melting temperatures of the three materials was calculated from their bulk moduli using equation 3.28, where we added the uncertainty of 300 K to the calculated values so as to obtain a good match between the experimental values that already exist in the literature and the computed values of Si and SiC obtained in this study. As table 4.20 shows, the calculated melting temperature of Si in this study is 5.572% higher than the one obtained by Yang & Jiang (2005), and by (Talyzin, Samsonov, Samsonov, Pushkar, & Dronnikov, 2019). For SiC, the calculated melting temperature is 4.338% lower than that reported by Munro (1997) (table 4.20). We therefore calculated the melting temperature of CTO using the same formula, which shows that it increases consistently with increase in the number of Cd atoms up to CTO 4, then drops at CTO 5. The highest melting temperature of CTO 4 shows that it has greatest intermolecular forces and therefore, least vapour pressure compared to the other four CTO samples.

The results of the melting temperature in this study show that CTO (especially CTO 4) is a suitable replacement to Si for high-temperature applications, since its melting temperature is higher than that of Si and therefore, can perform better than Si in high-temperature conditions. However, the values obtained in this study can be treated as estimates, since the formula used in calculating them has a large uncertainty of 300 K. Unfortunately, there is no data in the literature on the melting temperature of CTO for comparison.

The thermal properties investigated in this study were estimated within the temperature range of 0 to 800 K, because the quasi-harmonic Debye model is completely relevant within the same range. Figure 4.17a shows the Debye vibrational energies for Si and SiC, which increase non-linearly with increase in temperature below 200 K. The trend is the same for both materials, except that the curve for SiC becomes flat at slightly higher temperatures of above 300 K. The trend for the Debye vibrational energy in figure 4.17a is in contrast to the Gibb's free energy (figure 4.17b), which decreases non-linearly with temperature within the whole temperature range. The entropy (figure 4.17c) tends to zero at 0 K, which implies that there is very little or no lattice disorder at 0 K temperature, which is in agreement with the third law of thermodynamics (the law states that the entropy of perfect crystals tends to zero at the absolute zero temperature).

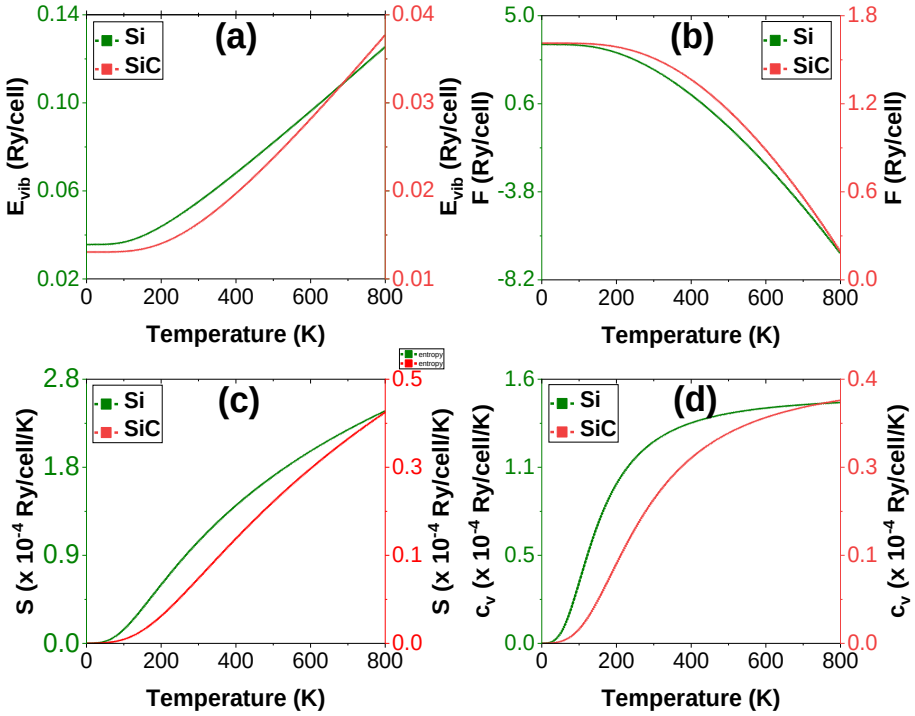


***Figure 4.17: Thermal properties of silicon and silicon carbide at zero pressure. $E_{vib}$ is the vibrational energy, F is the Gibbs free energy, S is the entropy, and $c_V$ is the specific heat capacity at constant volume***

With increase in temperature, the system deviates from the perfect order and thus, the entropy increases. Specific heat capacity of a material relates to the absorption of heat. The specific heat capacities at constant volume of the two materials (figure 4.17d) tends to zero as the absolute temperature tends to zero. This is quite in agreement with the Debye model (Kittel, 1996). The specific heat capacity of Si exhibits a cubic dependence of temperature as the temperature tends to zero. This implies that the phonon contribution is predominant here. The sharp increase in the specific heat capacity with increase in temperature up to about 300 K is due to phonon thermal vibrations. As the temperature rises to above 500 K, the anharmonic effect is suppressed and thus, the specific heat capacity approaches the Dulong-Petit classical limit (Dulong & Petit, 1819). At the intermediate temperatures between 200 to 400 K, the atomic lattice vibrations are the main contributors to the specific heat capacity.

Figure 4.18 shows the thermal properties of CTO as function of temperature. The trend for the Debye vibrational energy is the same as those of Si and SiC for all the CTO samples, except that the curve for CTO 2 becomes linear at a much lower temperature (below 50 K) as compared to those of the other samples that become linear beyond 200 K temperature. Unlike elastic constants that showed specific trends with increase in the number of Cd atoms, the Debye vibrational energies of the CTO samples do not show a specific trend. CTO 4 recorded the highest value, while CTO 2 recorded the least (table 4.21). The trend for the Debye vibrational energy in figure 4.18a is also in contrast to the Gibb's free energy (figure 4.18b), which decreases non-linearly with temperature within the whole temperature range. CTO 2 recorded the lowest value, while CTO 4 recorded the highest (table 4.21). The curves for Gibbs free energy do not follow a specific trend, just like those for the Debye vibrational energy.

Figure 4.18c shows that sample CTO 2 has the highest specific heat capacity at constant volume, while CTO 4 has the lowest. Sample CTO 2 was found to have thermal properties that very different from the other CTO samples, except the Gibbs vibrational energy. Its Gibbs free energy, entropy as well as the specific heat capacity at constant volume, were significantly higher than those of the other samples. Thus, it is the most disorderly system, while CTO 4 is the least disorderly. Unlike for Si and SiC in figure 4.17d where the specific heat capacity exhibits a cubic dependence with temperature, the specific heat capacity at constant volume of CTO in figure 4.18d does not seem to exhibit the same trend, as can be observed from the zoomed section of figure 4.18d. However, the specific heat capacity also tends to zero as the absolute temperature tends to zero, just like for Si and SiC (figure 4.17d).

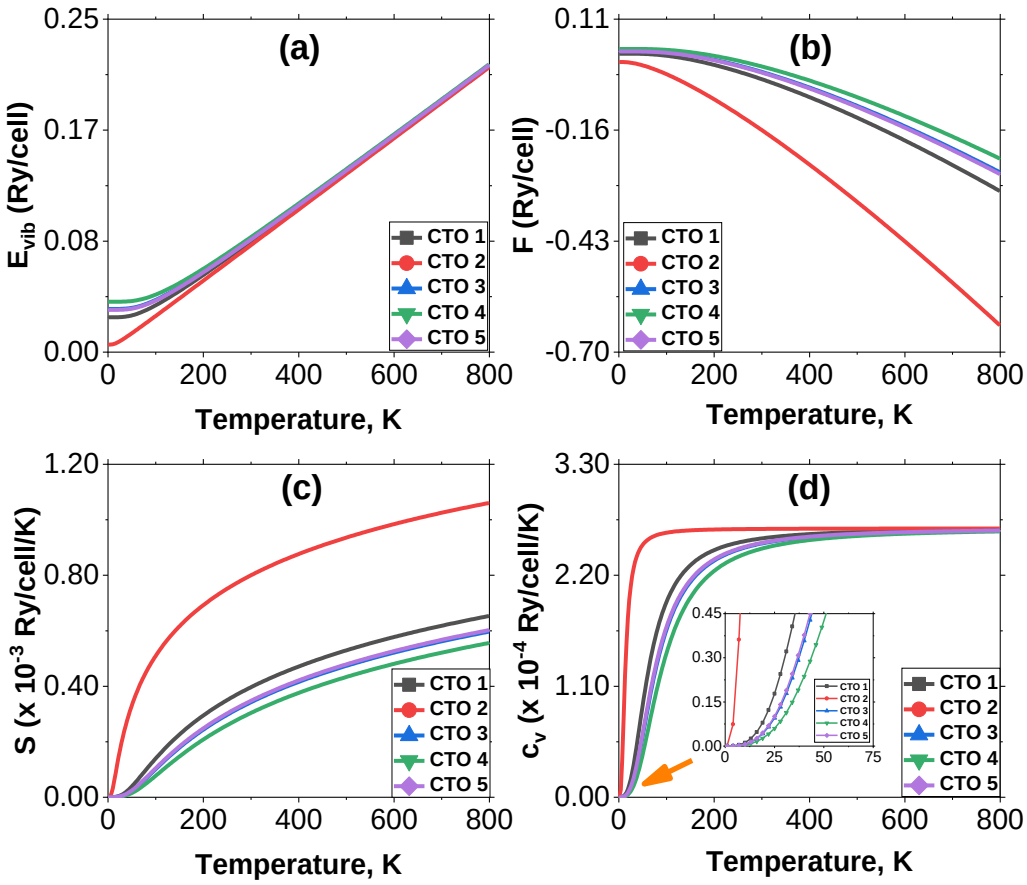


***Figure 4.18: Thermal properties of the five cadmium-tin-oxide samples. $E_{vib}$ is the vibrational energy, F is the Gibbs free energy, S is the entropy, and $c_V$ is the specific heat capacity at constant volume***

***Table 4.21. The calculated thermal properties of silicon, silicon carbide, and cadmium-tin-oxide. $E_{vib}$ is the Debye vibrational energy, F is the Gibbs free energy, S is the entropy, and $c_V$ is the specific heat capacity at constant volume. $E_{vib}$ and F are in Ry/cell, while S and $c_V$ are in Ry/cell/K***

| Material | $E_{vib}(x\ 10^{-2})$ | F $(x\ 10^{-2})$ | S $(x\ 10^{-4})$ | $c_v$ $(x\ 10^{-4})$ |
|---|---|---|---|---|
| Si | 5.479 | 2.327 | 1.057 | 1.234 |
| SiC | 1.838 | 1.512 | 1.094 | 0.203 |
| CTO 1 | 8.234 | -3.536 | 3.951 | 2.564 |
| CTO 2 | 7.952 | -15.84 | 7.984 | 2.659 |
| CTO 3 | 8.394 | -1.764 | 3.409 | 2.513 |
| CTO 4 | 8.557 | -0.454 | 3.024 | 2.462 |
| CTO 5 | 8.376 | -1.938 | 3.461 | 2.519 |

### 4.4.2 Pressure-dependent thermal properties

Table 4.22 shows the variation of the Debye temperature and melting temperature of CTO 4 with the applied pressure. The table shows that both the two thermal properties are sensitive to the applied pressure. When compared to the Debye temperature, the melting temperature exhibits a significantly greater sensitivity to the applied pressure. The value of the Debye temperature increases by 1.43% with increase in the applied pressure from 0 to 50 GPa, while the melting temperature increases by 21.66% for the same change in the applied pressure. When the applied pressure increased from 0 to 10 GPa, there was a noticeable increase in both properties. However, the increase becomes less pronounced at higher values of the applied pressure.

***Table 4.22: The calculated Debye temperature and melting temperature of CTO 4 as functions of the applied pressure***

| p (Gpa) | $\theta_D$ (K) | $T_m$ (K) |
|---|---|---|
| 00 | 377.7 | 2295.1 |
| 10 | 379.0 | 2691.7 |
| 20 | 381.8 | 2766.2 |
| 30 | 382.3 | 2773.7 |
| 40 | 382.9 | 2784.8 |
| 50 | 383.1 | 2792.3 |

Figures 4.19, 4.20, and 4.21 show the dependence of thermal properties of Si, SiC, and CTO (CTO 4) respectively on the applied pressure. The trends for the curves are the same as those of the zero-pressure thermal properties. However, unlike for both Si (figure 4.19) and CTO (figure 4.21) where the pressure seems not to have significant effect on the thermal properties, an increase in the applied pressure has a significant impact on the thermal properties of SiC (figure 4.20). The entropy of SiC is the most affected by the applied pressure, especially at high temperature (figure 4.20c). The specific heat capacity of SiC also tends to zero as the temperature tends to zero (figure 4.20d), although the effect of pressure is not prominent in this case. Thus, both elastic and thermal properties of SiC have been found to be more sensitive to the applied pressure compared to those of Si and CTO.

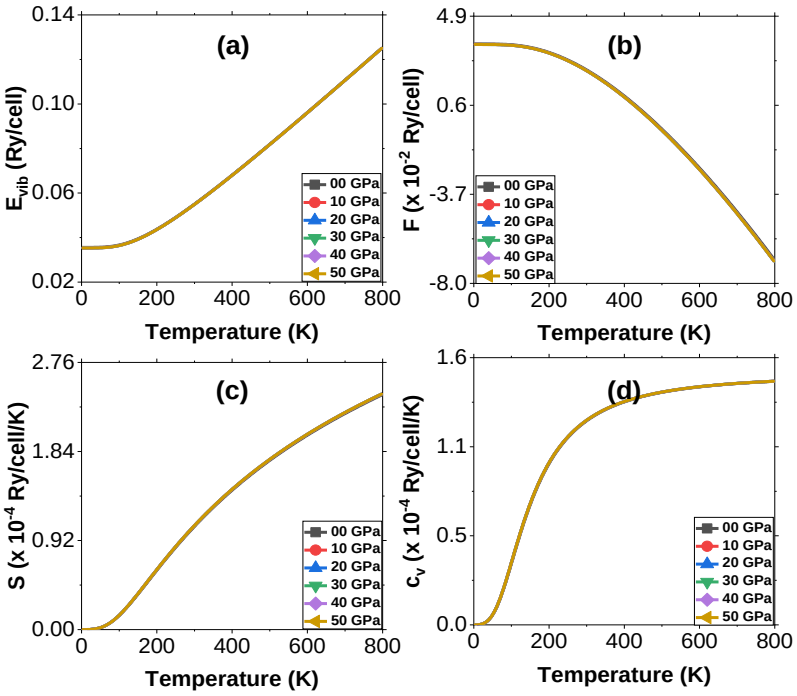


***Figure 4.19: Thermal properties of silicon at different values of the applied pressure. $E_{vib}$ is the vibrational energy, $F$ is the Gibbs free energy, $S$ is the entropy, and $c_V$ is the specific heat capacity at constant volume***

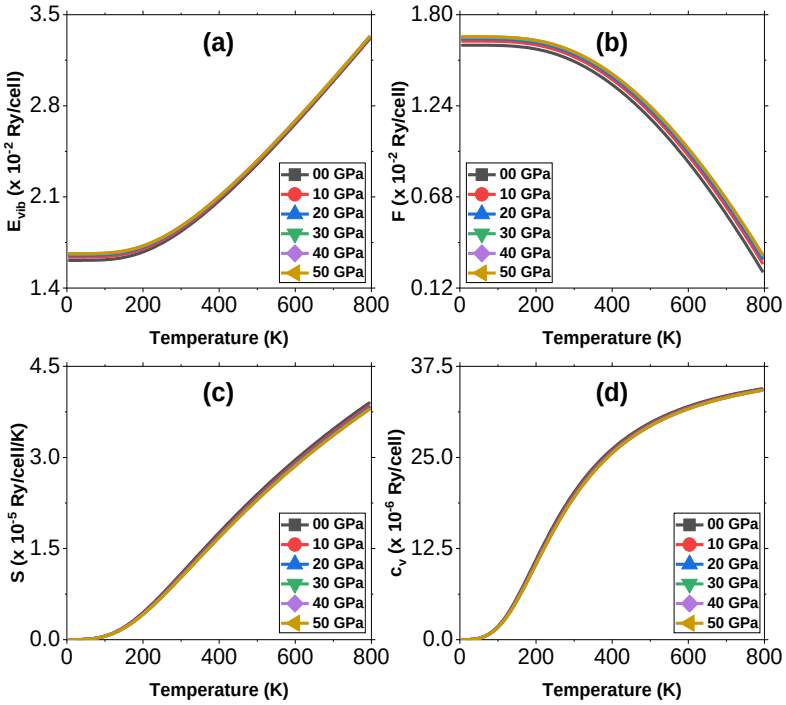


***Figure 4.20: Thermal properties of silicon carbide at different values of the applied pressure. $E_{vib}$ is the vibrational energy, $F$ is the Gibbs free energy, $S$ is the entropy, and $c_V$ is the specific heat capacity at constant volume***

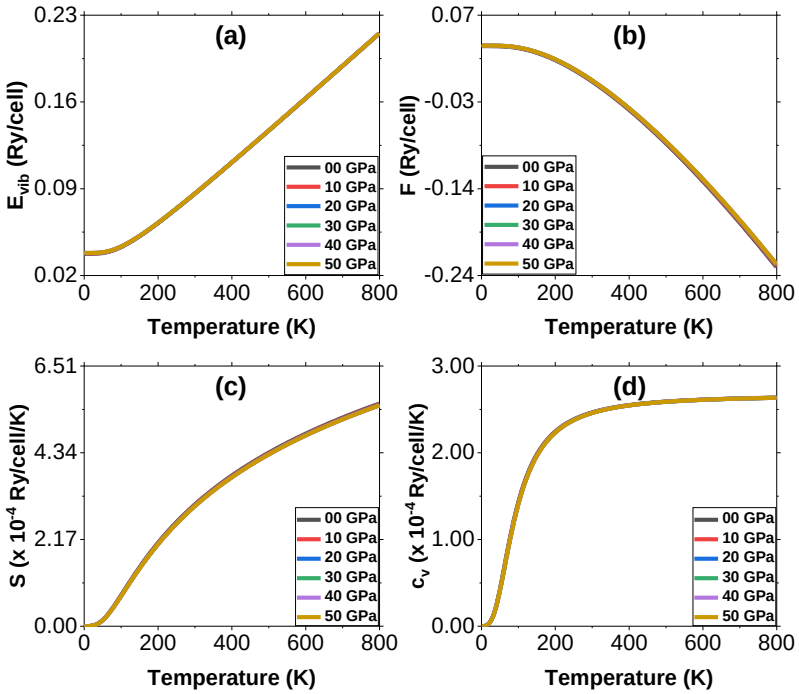


***Figure 4.21: Thermal properties of cadmium-tin-oxide (CTO 4) at different values of the applied pressure. $E_{vib}$ is the vibrational energy, $F$ is the Gibbs free energy, $S$ is the entropy, and $c_V$ is the specific heat capacity at constant volume***

## 4.5 Acoustical properties

Figure 4.22 shows the curves of the acoustic transmission loss as a function of the frequency for the bear glass, and for the glass laminated with CTO for single glazing. As the figure depicts, the value of the transmission loss did not show a significant change with addition of the CTO layer on to the glass. The values of the transmission loss were obtained at the first peak on the figure (between 0 and 7 MHz). Moreover, the transmission loss did not show a significant change with increase in the number of Cd atoms, since all the peaks remained fairly at the same height. However, addition of Cd to the glass lead to a drastic shift in the cut-off frequency towards lower values, with CTO 2 recording the lowest cut-off frequency, while CTO 4 recorded the highest value. Thus, a consistent trend in the cut-off frequency values with CTO numbers was not observed.

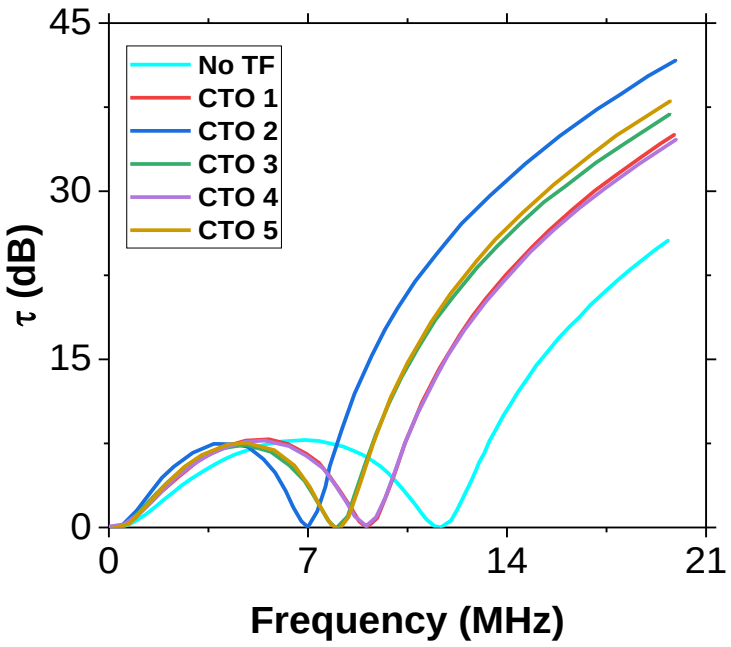


***Figure 4.22: Transmission loss against frequency for single glazing for the glass alone (no thin film), and for the glass laminated with the thin film of cadmium-tin-oxide***

Although the exact cut-off frequency occurs at a single point, the dip associated with this frequency is a valley (as depicted in figure 4.22), allowing transmission of noise around the critical frequency, which unfortunately, is where human hearing and conversation are concentrated. Resonances inherent to the glass at natural frequencies also permit acoustic transmission and thus, affect the low frequency performance of the glass. This cut-off frequency changes with the glass thickness. The thicker the glass, the better the low frequency performance, and the shallower the cut-off frequency valley is. However, the use of very thick glass is not always possible or desirable due to availability, weight, and cost (Schimmelpenningh, 2012).

The single glazed glass provided acoustic attenuation at very high frequencies, which implies that they are not good for sound reduction at low frequencies. This is because they will allow most of the low-frequency sound to penetrate into the buildings, a property that is not desirable for most buildings, since most of the ambient noise comes from low-frequency sources such as vehicles in highways, trains in railways, and aeroplanes in airports. Noise from aeroplanes, which usually have the highest frequency, are in the range of 315 to 6300 Hz. Noise from diesel locomotives on the other hand, range from 125 to 1000 Hz. Thus, the single-glazed glass simulated in this study is not suitable for such low frequency applications. Noise from aeroplanes can be quite high, which can reach values of up to 140 dB during flight, while those from trains range between 80 and 93 dB. This high noise level is detrimental to human health, since long exposure to noise of above 85 dB can lead to hearing loss, especially if one is exposed it for long (Zhu, Yu, Rajamani, & Stelson, 2004) (Liu, C-Y. Wang, Bo, & Liu, J-L., 2014).

The variation of the acoustic transmission loss against frequency for the double-glazed glass is shown in figure 4.23, which shows that the double glazing is better in acoustic attenuation than the single glazing, since the transmission loss is much higher. This is quite in agreement with previous studies, including that by Pickles et al. (2017), who asserted that a medium between glass reduces transmission of noise into the house. Pigg & Weiss (1973), also found out that a difference (higher) in the inner and outer layer thickness (for the case of a double-glazed window) gives better acoustic insulation. The spikes/ glitches in the region 8-9 kHz represent the coincident frequency. At this frequency, the plate acts as if it is acoustically transparent.

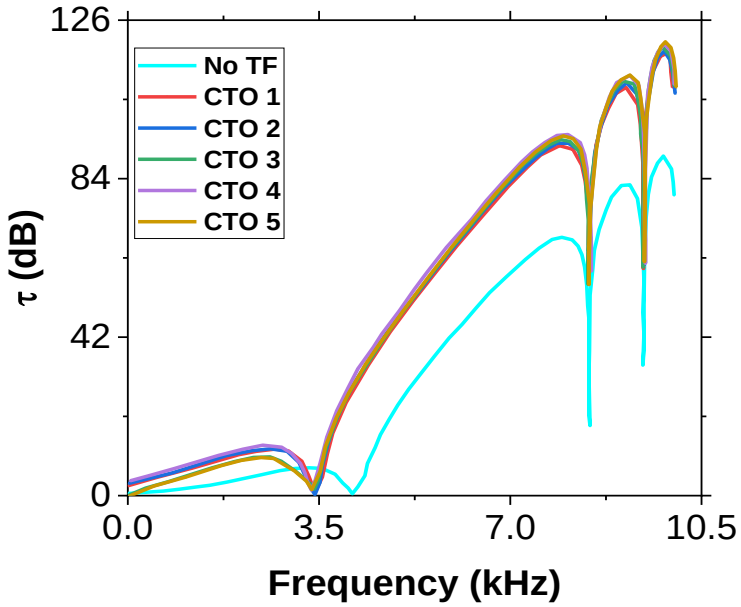


***Figure 4.23: Transmission loss against frequency for double glazing for the glass alone (no thin film), and for the glass laminated with the thin film of cadmium-tin-oxide***

Moreover, addition of CTO on the glass increased the transmission loss to a large extent, which increased with increase in the number of Cd atoms up to CTO 4, then dropped at CTO 5. The increase in the transmission loss with increase in the number of Cd atoms can be attributed to the increase in the mass of the glass as a result of the increase in the density as well as the Young's moduli of the CTO samples with Cd atoms. This finding agrees well with that by Miskinis et al. (2015), which has shown that laminated glass is a better acoustic insulator due to change of glass-air-glass resonant system. The more the mass, the more the sound-proofing ability of the glass (Clarke, 2019).

The variation of the transmission loss with frequency for the triple-glazed glass is shown in figure 4.24, which shows that triple glazing provides much higher sound-proofing ability compared to both the single and double-glazed glasses. The acoustic transmission loss for the unlaminated glass is much lower than for the laminated glass. The increase in the acoustic transmission loss with increase in the number of Cd atoms is due to the increase in the density as well as the Young's moduli of the CTO samples.

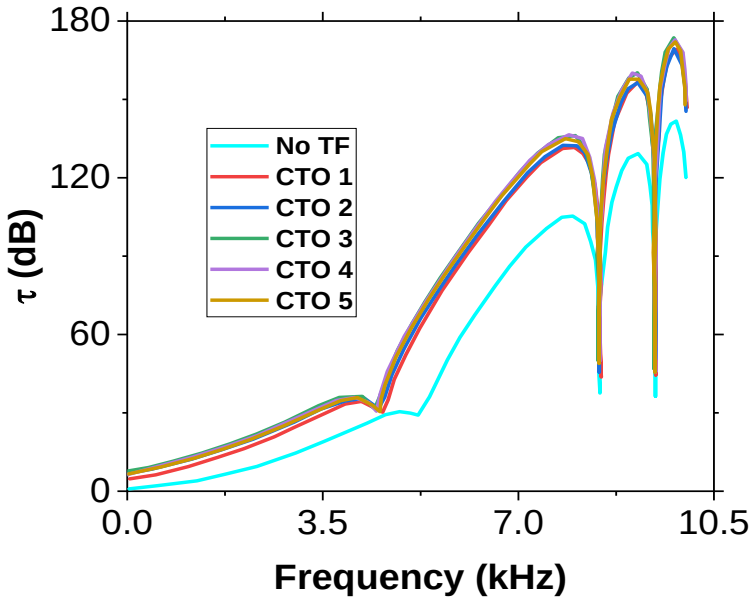


***Figure 4.24: Transmission loss against frequency for triple glazing for the glass alone (no thin film), and for the glass laminated with the thin film of cadmium-tin-oxide***

Figure 4.25 is a comparison of the acoustic transmission loss against frequency for all the three types of glazing. As can be observed, the triple glazing arrangement is much better at acoustic transmission loss compared to the other two. The curve for the single-glazed glass does not have a minimum, owing to its high frequency. Its cut-off frequency is found beyond the 10.5 kHz value that is presented in figure 4.25. The increase in the acoustic transmission loss for the triple-glazed glass is due the larger mass of CTO on the glass, well the more air space between the glasses.

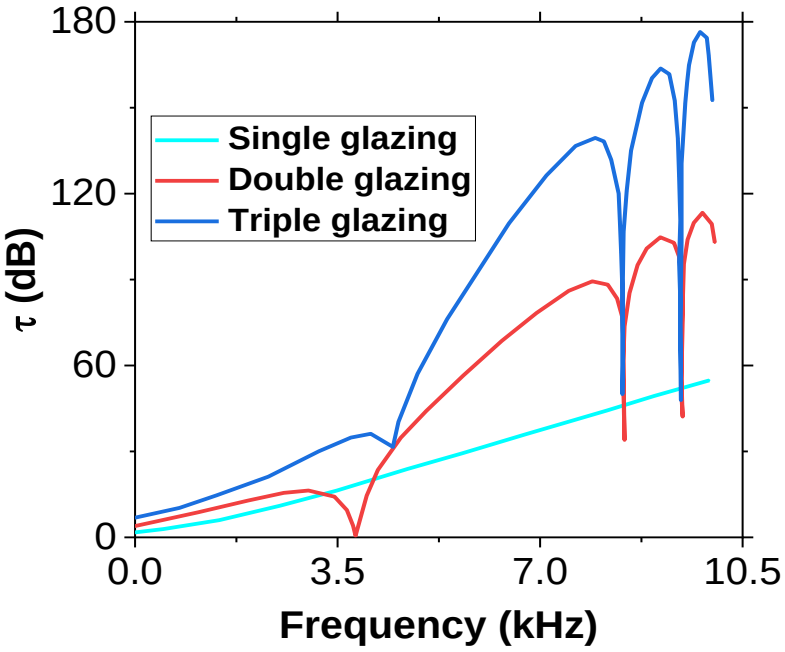


***Figure 4.25: Transmission loss against frequency for the three types of glazing laminated with CTO 4, all at the same film thickness of 200 nm***

Hao, Liu, Zhang, & Zhong (2015) asserted that it is not the thickness of the glass that blocks sound as much as the air between the layers, which distorts and reduces the intensity of sound as it travels from one barrier to the next. This assertion comes out to be consistent with the outcome of this study, which showed that the thickness of the layer does not have a significant effect on the acoustic transmission loss, as is evident in figure 4.26, which is for the tripled-glazed glass laminated with CTO 4 at different thicknesses of the CTO 4 layer.

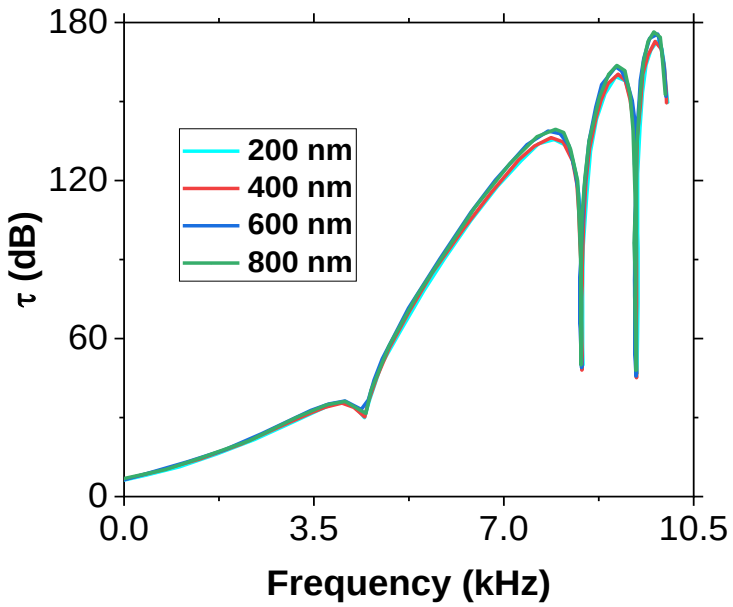


***Figure 4.26: Transmission loss against frequency for the triple-glazed window pane laminated with CTO 4 at different thicknesses of cadmium-tin-oxide***

Although increasing the thickness of the layer beyond 800 nm could have improved the acoustic transmission loss by increasing the value of the quantity $m_p = \rho h$, a thicker layer of CTO leads to a reduction in its optical transparency in the UV-Vis spectrum, which in turn leads to a reduction in the transparency of the glass, a property which is not desired in window panes. The calculated values of the acoustic transmission loss for the three types of glazing with Cd content is shown in table 4.23. A maximum acoustic transmission loss of 136.444 dB is reported for the triple-glazed glass laminated with sample CTO 4, while the single-glazed glass laminated with sample CTO 3 recorded the lowest value of 7.383 dB.

***Table 4.23: The calculated transmission loss (in dB) for the three types of glazing for the five cadmium-tin-oxide samples***

| Glazing type | No TF | CTO 1 | CTO 2 | CTO 3 | CTO 4 | CTO 5 |
|---|---|---|---|---|---|---|
| Single | 7.801 | 7.753 | 7.466 | 7.383 | 7.752 | 7.385 |
| Double | 68.44 | 92.74 | 93.85 | 94.35 | 95.35 | 95.34 |
| Triple | 104.9 | 131.6 | 132.4 | 132.5 | 136.4 | 135.0 |

Apart from reducing the noise that enters into buildings, window glazing also serves as a means of reducing the shatter when the window pane is hit. Thus, the CTO in this study also serves the purpose of reducing (and even eliminating) the shattering of the window panes when they are hit. Moreover, the glazing serves as a barrier that minimizes heat transfer between the inside and the outside of the house, thereby maintaining a fairly constant temperature inside the houses. The double and triple glazing are thus ideal in regions that experience winter season, since they lead to a reduction in the electricity bills that would have otherwise been used in heating the houses. This is because the inside temperature will remain relatively higher than that of the outside.

# CHAPTER FIVE
# CONCLUSION AND RECOMMENDATIONS

## 5.1 Conclusion

The experimental and computational studies of CTO were successfully carried out in this work. The structural properties showed that all the five CTO samples are crystalline. CTO 4 was found to be monocrystalline, while the other four samples were found to be polycrystalline. CTO 4 was found to exhibit an orthorhombic structure with strong peak along the (1 3 0) direction. Both the experimental and computed lattice parameters obtained in this study were found to be in accord with those that have been published. The values of the lattice parameters obtained were: $a$ = 10.467 & 10.518 a.u, $b$ = 18.686 & 18.780 a.u, and $c$ = 6.034 & 6.057 a.u for the experimental and computational studies respectively. From the chemical analysis by XRF, sample CTO 4 was found to have the chemical formula of $Cd_2SnO_4$. The crystallite sizes obtained were found to be in very good agreement with the values that are available in the literature. However, the crystallite sizes calculated using FWHM were found to be up to 6% higher than those calculated using IB. There was no consistent effect of the concentration of Cd atoms on the crystallite size. CTO 1 recorded the largest crystallite size of 60.75 nm and 57.94 nm for FWHM and IB respectively, while CTO 2 recorded the smallest value at 3.20 nm and 3.01 nm for FWHM and IB respectively. CTO 4 recorded values of 44.95 nm and 42.22 nm for FWHM and IB respectively. The high density of 6.6995-7.6366 g/cm$^3$ obtained in this study shows that CTO is a heavy material, much heavier than Si. The density increased consistently with increase in the number of Cd atoms up to CTO 4, then dropped at CTO 5. CTO 4 recorded the highest density of 7.6366 g/cm$^3$, while CTO 1 was found to be the least dense at 6.6995 g/cm$^3$. In the bond structure analysis, direct bonds between Sn & Cd, O & O, and Sn & Sn were not detected. The Sn – Cd – Sn and O – Cd – Sn bond angles were not detected either. The bond angles were found to be in perfect agreement with the data that is available in the literature. More than one type of bond length (bond splitting) was detected for Cd – O, Sn – O, and Cd – Cd bonds.

All the CTO samples turned out to be mechanically stable. A consistent increase in mechanical stability was observed with increase in the number of Cd atoms, with CTO 1 being the most mechanically stable against ecut, k-points, and lattice parameters of all the five CTO samples, since it had the lowest total energy, while CTO 5 was found to be the least stable. The stress-strain method developed in this study for the calculation of elastic constants, which was tested using both Si and SiC, was found to be accurate. The calculated elastic constants for Si and SiC using the method was found to be in very good agreement with the data that is available in the literature. For Si, the bulk modulus calculated in this study was found to be within 3.301-4.154% compared to those that have been reported. The shear modulus was found to be within 1.601-4.823% compared to those that were obtained from previous studies. The calculated Young's modulus in this work was found to be 2.030% larger than that from a previous study. For SiC, the values obtained were: bulk modulus at 0.1351-2.252%, shear modulus at 0.267-0.807, and Young's modulus at 0.574-2.776% compared to some data that is available in the literature. Thus, the method was adopted in calculating the mechanical properties of CTO. The elastic constants of the CTO samples were found to be greatly affected by the number of Cd atoms. All the elastic constants increased with increase in the number of Cd atoms up to CTO 4, then dropped at CTO 5. The bulk modulus increased from 50.44 GPa for CTO 1 to 149.1 GPa for CTO 4. The much higher bulk modulus obtained in this study for CTO 4 shows that CTO is much less compressible compared to Si. The shear modulus values increased from 27.3 GPa for CTO 1 to 53.2 GPa for CTO 4, then dropped at CTO 5. Since the bulk modulus values are much larger than the shear modulus values, it shows that CTO is more resistant to volume change than to shape change. The Young's modulus increased from 69.62 GPa for CTO 1 to 142.7 GPa for CTO 4, then dropped at CTO 5. The value for CTO 4 is comparable to that of Si at 130-169 GPa. The Vickers hardness increased from 1.131 GPa for CTO 1 to 3.757 GPa for CTO 4, then dropped at CTO 5. The low value of the Vickers hardness of CTO shows that it is a much softer material compared to Si at 10 GPa. The Poisson ratio, the Pugh's ratio as well as the Cauchy pressure were used to determine the ductile/ brittle nature of CTO in this study. All the three parameters proved that CTO is ductile. This is unlike both Si and SiC, which are brittle. CTO 3 recorded the highest value of the Poisson ratio

of 0.367, while CTO 1 recorded the lowest value of 0.270. CTO 4 recorded a value of 0.340. The large value of the Poisson ratio in this study shows that CTO exhibits a large elastic deformation when exposed to small amounts of strain compared to Si at 0.26. For the Pugh's ratio, CTO 3 also recorded the highest value of 3.422, while CTO 1 recorded the lowest at 1.846. CTO 4 recorded a value of 2.801. Thus, there was no consistent change in the ductility of CTO with the number of Cd atoms. All the CTO samples turned out to be anisotropic, with the highest degree of anisotropy along the {0 1 0} plane. The {0 0 1} plane was found to be the least anisotropic of all the five CTO samples. All the CTO samples showed a larger anisotropy of the bulk modulus, but a smaller degree of anisotropy of the shear modulus. CTO 4 was found to have the lowest degree of universal anisotropy of all the five CTO samples, while CTO 2 had the highest. Thus, there was no consistent change in the anisotropy of CTO with the number of Cd atoms.

The Debye temperature increased consistently with increase in the number of Cd atoms from CTO 1 at 261.46 K to CTO 4 at 377.68 K, then dropped at CTO 5. The melting temperature also increased consistently from CTO 1 at 1781.1 K to CTO 4 at 2295.5 K, then dropped at CTO 5. The entropy tended to zero at 0 K for all the CTO samples, implying that there was very little or no disorder at the 0 K temperature. The specific heat capacity at constant volume tended to zero as the absolute temperature tended to zero, which is quite in agreement with the Debye model. As the temperature increased to above 500 K, the anharmonic effect was suppressed and thus, the specific heat capacity approached the Dulong-Petit classical limit.

The study of acoustical properties of CTO showed that addition of CTO to glass greatly increased the acoustic transmission loss for both the double and triple-glazed glass. The single-glazed glass did not show a significant impact on addition of CTO, except that the cut-off frequency shifted towards lower values with addition of the TF layer. However, the acoustic transmission did not show a significant change in the transmission loss with a change in the film thickness. There was a small effect on the acoustic transmission loss with increase in the number of Cd atoms. A maximum acoustic transmission loss of 136.4 dB was recorded for the triple-glazed laminated glass.

The mechanical properties of CTO were found to be affected by the applied pressure. The applied pressure led to an increase in each of CTO 4's nine independent elastic stiffness constants. When the applied pressure increased from 0 to 10 GPa, there was a noticeable increase in the elastic stiffness constants. However, the increase diminished for pressures beyond 10 GPa. The bulk modulus increased by 34.91%, the shear modulus by 4.81%, the Young's modulus by 5.76%, the Poisson's ratio by 9.71%, and the Pugh ratio by 29.51% when the applied pressure was increased from 0 to 50 GPa. The Vickers hardness however decreased by 89.60%. Thus, the bulk modus experienced the largest increase, while the Vickers hardness experienced the largest reduction. With an increase in the applied pressure, both the Debye temperature and the melting temperature of CTO 4 increased. Since the melting temperature was derived from the bulk modulus, which increased with an increase in the applied pressure, the increase in the melting temperature with increase in the applied pressure was anticipated. The Debye temperature experienced a 1.43% increase, while the melting temperature experienced a 21.66% increase when the applied pressure was increased from 0 to 50 GPa. Thus, the melting temperature was the one most affected by the applied pressure. The other thermal properties (Debye vibrational energy, Gibbs free energy, entropy, and specific heat capacity at constant volume) did not show a significant change with an increase in the applied pressure.

The outcome of this study (mechanical and thermal properties) shows that TFs of CTO form a suitable candidate as a substitute to Si in the manufacture of most MEMS, especially the flexible ones such as bioMEMS, microbolometers, image sensors, and drug delivery MEMS, owing to its ductile nature. Due to it high acoustic transmission loss on the double and triple-glazed window panes (which is contributed by its much higher density compared to that of Si) and its transparent nature in the UV-Vis spectrum, it is a suitable candidate as a substitute to polymers as a laminate on window panes for noise control in buildings that are situated close to places where there is a lot of noise such as those close to airports, railway lines or highways.

***Summary of the desirable properties of cadmium-tin-oxide obtained in this study over those of silicon***

| Property | Comparison with that of Si |
|---|---|
| Density | Much heavier (at 7.6366 g/cm$^3$) compared to that of Si at 2.33 g/cm$^3$ |
| Mechanical and thermal stability | Better than Si |
| Bulk modulus | Much higher (149.1 GPa) than that of Si at 90-97 GPa |
| Young's modulus | Comparable (at 142.7 GPa) to that of Si at 130-169 GPa |
| Hardness | Much softer (at 3.757 GPa) than that of Si at 10 GPa, good flexible MEMS |
| Ductility | Ductile, unlike Si which is brittle |

## 5.2 Recommendations

### 5.2.1 Possible applications

Among the desirable properties of MEMS devices is a wide, direct band gap. Previous experimental studies have shown that CTO is better than Si, since it has a wider and direct band gap of 3.5 and above compared to the indirect band gap of 1.1 for Si. It can thus be utilized as a substrate in the fabrication of MEMS devices that are used in high temperature, high voltage, and high-power environmental conditions. Such devices include microsensors and microactuators.

The Vickers hardness in this study showed that CTO is a much softer material compared to Si. Thus, it is not suitable as a substitute to Si in the manufacture of MEMS devices that operate under harsh environmental conditions such as in combustion process, gas turbine control, and in oil industry such as microsensors and microactuators. However, it is suitable for fabrication of MEMS devices for medical field such as bioMEMS, microbridges, image sensors, and microbolometers that require soft substrates.

The ductile nature of CTO is a property that is highly sought-after for the manufacture of flexible MEMS. The common MEMS substrates such as Si, diamond and SiC, are all brittle. The ductile nature of CTO obtained in this study is ideal for the manufacture of flexible MEMS such as bioMEMS, sound transducers, flexible displays, and accelerometers.

The results of this study show that CTO (especially CTO 4) is a suitable replacement to Si for high-temperature applications, since its melting temperature is higher than that of Si. It can therefore be used in MEMS that operate under high temperatures of above 500. These harsh-environment MEMS include microsensors and microactuators.

The result of this study has also shown that CTO is a heavy material. Materials with high density are ideal for acoustic attenuation. The calculated acoustic transmission loss showed that TFs of CTO are good at reducing sound transmission through the glass. It can therefore find good use as a laminate on the window panes for the reduction of noise inside houses, especially in places where there is a lot of noise, such as those near airports or railway lines. This is because in addition to high density, it is also optically transparent in the UV-Vis wavelength region.

### 5.2.2 Further research

A wide band gap and piezoelectric property are ideal for MEMS substrates that are used for sensing applications in harsh environmental conditions that involve high radiation and high temperature, which can be used in various sensors like temperature detectors, and pressure detectors. Previous studies have shown that CTO is a wide band gap semiconductor with a band gap value of up to 3.9 eV, which is ideal for this application. However, its piezoelectric property is not available, and thus needs to be investigated.

Determination of mechanical properties of CTO in this study was done using DFT. For comparison, an experimental study needs to be conducted. Since TFs are involved, acoustical reflection coefficient of the TFs can be taken by an acoustic transducer of very high frequency (in the Gigahertz range). From the acoustic reflection coefficient, the mechanical properties can be calculated by solving an inverse acoustic problem.

In the study of the mechanical properties, we only explored the bulk modulus, shear modulus, Young's modulus, Poisson's ratio, Vickers hardness, Pugh's ratio, Cauchy pressure, and elastic anisotropy. The other mechanical properties such as ultimate strength, creep, and resilience were not considered, although these properties also play a curial role in the working of MEMS. Thus, they also need to be investigated.

In the study of the thermal properties of CTO, we only investigated the Debye temperature, melting temperature, Debye vibrational energy, Gibb's free energy, entropy, and specific heat capacity at constant volume. Other thermal properties such as thermal conductivity, thermal diffusivity, and thermal expansion were not explored. Thus, studies need to be carried out on these properties, since they also play a very significant role in the working of MEMS.

In the study of the acoustical properties, the acoustic transmission loss was calculated with the laminate on one side of the glass. However, laminating the glass on both sides can possibly increase the transmission loss. Thus, studies on the transmission loss on both sides of the glass needs to be conducted so as to compare its effect with that of the glass laminated on only one side. Moreover, the acoustic transmission loss was done through simulation. An experimental study needs to be conducted so as to ascertain the feasibility of practical use of CTO as a window layer.

## REFERENCES


1. Acar, C. & Shkel, A. M. (2008). *MEMS vibratory gyroscopes: Structural approaches to improve robustness*. London: Springer.
2. Adllan, A. A. & Corso, A. D. (2011). Ultrasoft pseudopotentials and projector augmented-wave data sets: Application to diatomic molecules. *Journal of Physics: Condensed Matter*, **23**(42), 425501. https://doi.org/10.1088/0953-8984/23/42/425501.
3. Agnihotri, O. P. & Gupta, B. K. (1980). Cadmium stannate selective coatings prepared by spray pyrolysis. *Solar Energy International Progress*, 540-548. https://doi.org/10.1016/B978-1-4832-8437-8.50043-0.
4. Agnihotri, O. P. Gupta, B. K., & Sharma, A. K. (1978). Optical-absorption edge in cadmium stannate selective coatings. *Journal of Applied Physics*, **49**, 4540. https://doi.org/10.1063/1.325463.
5. Albrecht, M. Paulus, B., & Stoll, H. (1997). Correlated ab initio calculations for ground-state properties of II-VI semiconductors. *Physical Review B*, **56**(12), 7339-7347. https://doi.org/10.1103/PhysRevB.56.7339.
6. Alexopoulos, P. S. & O'Sullivan, T. C. (1990). Mechanical properties of thin films. *Annual Review of Materials Science*, **20**, 391-420. https://doi.org/10.1146/annurev.ms.20.080190.002135.
7. Ali, H. M. H. A. Mohamed, Wakkad, M. M., & Hasaneen, M. F. (2009). Optical and electrical properties of tin-doped cadmium oxide films prepared by electron beam technique. *Japanese Journal of Applied Physics*, **480**, 41101(1-7). https://doi.org/10.1143/JJAP.48.041101.
8. Allen, P. B. (2020). Theory of thermal expansion: Quasi-harmonic approximation and corrections from quasi-particle renormalization. *Modern Physics Letters B,* **34**(2), 2050025. https://doi.org/10.1142/S0217984920500256.
9. Alnaimi, S. M. & Al-Dileamy, M. N. (2007). *Determination of optical constants of cadmium stannate films*. Doha: University of Qatar.
10. Anderson, O. L. (1963). A simplified method for calculating the Debye temperature from elastic constants. *Journal of Physical Chemistry of Solids*, **24**(7), 909-917. https://doi.org/10.1016/0022-3697(63)90067-2.

11. Andreas, S. (2012). Transparent conducting oxides: An up-to-date overview. *Materials (Basel)*, **5**(4), 661-683. https://doi.org/10.3390/ma5040661.
12. Arasan, U. Marchetti, F. Chevillotte, F. Tanner, G. Chronopoulos, D., & Gourdon, E. (2021). On the accuracy limits of plate theories for vibro-acoustic predictions. *Journal of Sound and Vibration*, **493**, 115848(1-33). https://doi.org/10.1016/j.jsv.2020.115848.
13. Ashurst, W. R. Carraro, C., & Maboudian, R. (2004). Vapor phase anti-stiction coatings for MEMS. *IEEE Transactions on Device and Materials Reliability*, **3**(4), 173-178. https://doi.org/10.1109/TDMR.2003.821540.
14. Auciello, O. Birrell, J. Carlisle, J. A. Gerbi, J. E., & Xiao, X. (2004). Materials science and fabrication processes for a new MEMS technology based on ultra-nanocrystalline diamond thin films. *Journal of Physics: Condensed Matter*, **16**(16), 1-15. https://doi.org/10.1088/0953-8984/16/16/R02.
15. Auciello, O. Pacheco, S. Sumant, A. V. Gudeman, C. Sampath, S. Datta, A. et al. (2008, January). Are diamonds a MEMS' best friend? *IEEE Microwave Magazine* **8**(6), 61-75. https://doi.org/10.1109/MMM.2007.907816.
16. Baierlein, R. (2012). *Thermal Physics*. Cambridge: Cambridge University Press.
17. Baratto, C. Ponzoni, A. Ferroni, M. Borgese, L. Bontempi, E., & Sberveglieri, G. (2012). Sputtering deposition of amorphous cadmium stannate as transparent conducting oxide. *Thin Solid Films*, **520**(7), 2739-2744. https://doi.org/10.1016/j.tsf.2011.11.079.
18. Barbara, F. Castanedo, P., & Zelaya-Angel, O. (2016). Influence of vacuum and Ar/ CdS atmospheres-rapid thermal annealing on the properties of cadmium stannate thin films obtained by sol-gel technique. *Materials Science in Semiconductor Processing*, **56**, 302-306. https://doi.org/10.1016/j.mssp.2016.09.017.
19. Baroni, S. Giannozzi, P., & Isaev, E. (2009). Thermal properties of materials from ab initio quasi-harmonic phonons. *Reviews in Mineralogy & Geochemistry*, **71**, 39-57. https://doi.org/10.48550/arXiv.1112.4977.

20. Bhuvaneswari, P. & Velusamy, M. A. (2013). Effect of fluorine doping on the structural, optical and electrical properties of spray deposited cadmium stannate thin films. *Materials Science in Semiconductor Processing*, **16**, 1964-1970. http://doi.org/10.1016/J.MSSP.2013.07.025.
21. Birch, F. (1947). Finite elastic strain of cubic crystals. *Physical Review*, **71**(11), 809-824. https://doi.org/10.1103/PhysRev.71.809.
22. Blackmore, J. M. & Cattell, A. F. (1990). Properties of two-phase cadmium stannate thin films. *Thin Solid Films*, **185**(1), 97-110. https://doi.org/10.1016/0040-6090(90)90010-B.
23. Bogue, R. (2007). MEMS sensors: Past, present and future. *Sensor Review*, **27**(1), 7-13. https://doi.org/10.1108/02602280710729068.
24. Bonvilain, A. Coudevylle, J-R. Blind, P., & Chaillet, N. (2001). Micromachined thermal actuated microlegs for an insect-like microrobot. *Proceedings of the SPIE: Micromachining and Microfabrication Process Technology VII*, **4557**, 403-414. https://doi.org/10.1117/12.442972.
25. Boucetta, S. & Zegrar, F. (2013). Density functional study of elastic, mechanical and thermodynamic properties of MgCu with a CsCl-type structure. *Journal of Magnesium and Alloys*, **1**(2), 128-133. https://doi.org/10.1016/j.jma.2013.05.001.
26. Bowden, M. F. & Cardile, C. M. (1990). Structures of orthorhombic and cubic dicadmium stannate by Rietveld refinement. *Powder Diffraction*, **5**(1), 36-40. https://doi.org/10.1017/S0885715600015190.
27. Breidi, A. Fries, S. G. Palumbo, M., & Ruban, A. V. (2016). First-principles modelling of energetic and mechanical properties of Ni-Cr, Ni-Re and Cr-Re random alloys. *Computational Materials Science*, **117**, 1-16. https://doi.org/10.1016/j.commatsci.2016.01.020.
28. Britannica, T. (2018). *Vickers hardness. Encyclopedia Britannica*. https://www.britannica.com/science/Vickers-hardness.
29. Burdick, C. L. & Owen, E. A. (1918). The atomic structure of carborundum determined by X-rays. *Journal of the American Chemical Society*, **40**, 1749-1759. https://doi.org/0.1021/JA02245A001.

30. Cerenius, Y. (2004). Melting-temperature measurements on α-silicon nitride to a pressure of 37 GPa. *Journal of American Ceramic Society*, **82**(2), 380-386. https://doi.org/10.1111/j.1551-2916.1999.tb20073.x.
31. Chana, M. L. Yoxall, B. Parka, H. Kang, Z. Izyuminb, I. Choub, J. et al. (2012). Design and characterization of MEMS micromotor supported on low friction liquid bearing. *Sensors and Actuators A: Physical*, **177**, 1-9. https://doi.org/10.1016/j.sna.2011.08.003.
32. Chen, J. Li, J., & Xu, L. (2019). Highly integrated MEMS magnetic sensor based on GMI effect of amorphous wire. *Micromachines (Basel)*, **10**(4), 237(1-11). https://doi.org/10.3390/mi10040237.
33. Chen, W-H. Yu, C-F. Chiang, K-N., & Cheng, H-C. (2015). First-principles density functional calculations of physical properties of orthorhombic $Au_2Al$ crystal. *Intermetallics*, **62**, 60-68. https://doi.org/10.1016/J.INTERMET.2015.03.009.
34. Chen, X. Q. Niu, H. Li, D., & Li, Y. (2011). Modelling hardness of polycrystalline materials and bulk metallic glasses. *Intermetallics*, **19**(19), 1275-1281. http://dx.doi.org/10.1016/j.intermet.2011.03.026.
35. Ching, W. Y. Rulis, P., & Misra, A. (2009). Ab initio elastic properties and tensile strength of crystalline hydroxyapatite. *Acta Biomaterialia*, **5**, 3067-3075. https://doi.org/10.1016/j.actbio.2009.04.030.
36. Chopra, K. L. Major, S., & Pandya, D. K. (1983). Transparent conductors-A status review. *Thin Solid Films*, **102**, 1-46. https://doi.org/10.1016/0040-6090(83)90256-0.
37. Chrzanowska-Giżyńska, J. Denis, P. Woźniacka, S. & Kurpaska, L. (2018). Mechanical properties and thermal stability of tungsten boride films deposited by radio frequency magnetron sputtering. *Ceramics International*, **44**(16), 19603-19611. https://doi.org/10.1016/j.ceramint.2018.07.208.
38. Chung, D. H. & Buessem, W. R. (2010). The elastic anisotropy of crystals. *Journal of Applied Physics*, **38**(5), 2010-2012. https://doi.org/10.1063/1.1709819.

39. Cimalla, V. Pezoldt, J., & Ambacher, O. (2007). Group III nitride and SiC based MEMS and NEMS: Materials properties, technology and applications. *Journal of Physics D: Applied Physics*, **40**(20), 6386-6434. https://doi.org/10.1088/0022-3727/40/20/S19.
40. Cioffi, K. & Hsu, W. (2005). 32KHz MEMS-based oscillator for low-power applications. *Proceedings of the 2005 IEEE International Frequency Control Symposium and Exposition*, 551-558. https://doi.org/10.1109/FREQ.2005.1573992.
41. Clarke, G. (2019, June 25). *6 facts about laminated glass soundproofing*. Retrieved from: https://www.thermawood.co.nz/laminated-glass-soundproofing/.
42. Clayton, J. D. (2010). *A geometrically non-linear model of ceramic crystals with defects applied to silicon carbide (SiC)*. Maryland: U.S. Army Research Laboratory.
43. Coakley, K. J. Splett, J. D., & Janezic, M. D. (2003). Estimation of Q-factors and resonant frequencies. *IEEE Transactions on Microwave Theory and Techniques*, **51**(3), 862-868. https://doi.org/10.1109/TMTT.2003.808578.
44. Cordill, J. M. Glushko, O. Kreith, J. Marx, V. M., & Kirchlechner, C. (2015). Measuring electro-mechanical properties of thin films on polymer substrates. *Microelectronic Engineering*, **137**(1), 96-100. https://doi.org/10.1016/j.mee.2014.08.002.
45. Coutts, T. J. Yong, D. L., & Li, X. N. (2000). Characterization of transparent conducting oxides. *MRS BULLETIN*, **25**(8), 58-65. https://doi.org/10.1557/mrs2000.152.
46. Cristaldi, D. A. Impellizzeri, G. Priolo, F. Gupta, T., & Gulino, A. (2012). Structural, electronic and electrical properties of yttrium-doped cadmium stannate. *Journal of Physical Chemistry C*, **116**(5), 3363-3368. https://doi.org/10.1021/JP2103676.
47. Crystallography.net home page. *http://www.crystallography.net/cod/*.

48. Daoud, S. Loucif, K. Bioud, N., & Lebgaa, N. (2012). First-principles study of structural, elastic and mechanical properties of zinc-blende boron nitride (B3_BN). *Acta Physica Polonica A*, **122**(1), 109-115. https://doi.org/10.12693/APHYSPOLA.122.109.

49. Diakite, Y. I. Traore, S. D. Malozovsky, Y. Khamala, B. Franklin, L. et al. (2017). Accurate electronic, transport, and bulk properties of gallium arsenide (GaAs). *Journal of Modern Physics*, **8**, 531-546. https://doi.org/10.4236/jmp.2017.84035.

50. Diepgen, A. Zimmermann, V. Bayer, C. F. Zhou, Y. Forster, C. Leib, J. et al. (2019). Parylene coatings in power electronic modules. In Fraunhofer IISB (Eds.), *Proceedings of the 2019 ISAPP*. Heidelberg, DE. http://cris.fau.de/bibtex/publication/235367228.bib.

51. Dieter, G. E. (1961). *Mechanical Metallurgy*. New York: McGraw-Hill.

52. Diliegros-Godines, C. J. Flores-Ruiz, F. J. Castanedo-Pérez, R. Torres-Delgado, G., & Broitman E. (2018). Mechanical and tribological properties of CdO + $SnO_2$ thin films prepared by sol-gel. *Journal of Sol-Gel Science and Technology*, **74**, 114-120. https://doi.org/10.1007/978-3-319-32101-1_115.

53. Dinesh, V. Shriya, S. Varshney, M. Singh, N., & Khenata, R. (2015). Elastic and thermodynamical properties of cubic (3C) silicon carbide under high pressure and high temperature, *Journal of Theoretical and Applied Physics*, **9**, 221-249. https://doi.org/10.1007/s40094-015-0183-7.

54. Ding, X. Liu, G. Du, M. Guo, H. Qian, H., & Gerada, C. (2015). Development of an axial flux MEMS BLDC micromotor with increased efficiency and power density. *Energies*, **8**, 6608-6626. https://doi.org/10.3390/en8076608.

55. Ding, Z. Zhou, S., & Zhao, Y. (2004). Hardness and fracture toughness of brittle materials: A density functional theory study. *Physical Review B*, **70**, (1-6). https://doi.org/10.1103/PHYSREVB.70.184117.

56. Du, Z. Liu, X. Zhang, Y., & Zhu, Z. (2017). High-quality cadmium stannate annealed in $N_2$ atmosphere for low-cost thin film solar cells. *RSC advances*, **7**, 18545-18552. https://doi.org/10.1039/C7RA00394C.

57. Dub, S. Lytvyn, P. Strelchuk, V. Nikolenko, A. Stubrov, Y. et al. (2017). Vickers hardness of diamond and cBN single crystals: AFM approach. *Crystals*, **7**(12), 369. https://doi.org/10.3390/cryst7120369.
58. Dulong, P. L. & Petit, A. T. (1819). Researches on some important points of the heat theories. *Annals of Chemistry and Physics*, **10**, 395-413.
59. Dutta S. & Datta, P. (2010). *Silicon-A versatile material*. New Delhi: Solid State Physics Laboratory.
60. Eberhart, M. E. & Jones, T. E. (2012). Cauchy pressure and the generalized bonding model for nonmagnetic bcc transition metals. *Physical Review B*, **86**, 134106(1-7). https://doi.org/10.1103/PhysRevB.86.134106.
61. Essabir, H. Bouhfid, R., & Qaiss, A. K. (2019). Fracture surface morphologies in understanding of composite structural behaviour. *Structural Health Monitoring of Bio composites, Fibre-Reinforced Composites and Hybrid Composites*, 277-293. https://doi.org/10.1016/B978-0-08-102291-7.00014-9.
62. Fan, Q. Wei, Q. Chai, C., & Yu, X. (2015). First-principles study of structural, elastic, anisotropic, and thermodynamic properties of R3-$B_2C$. *Chinese Journal of Physics*, **53**(5), 100601(1-14). http://PSROC.phys.ntu.edu.tw/cjp.
63. Fellah, Z. E. A. Fella, M. Ongwen, N. O. Ogam, E., & Depollier, C. (2021). Acoustics of fractal porous material and fractal calculus. *Mathematics*, **1774**(9), (1-16). https://doi.org/10.3390/math9151774.
64. Fine, M. E. Brown, L. D., & Marcus, H. L. (1984). Elastic constants versus melting temperature in metals. *Scripta Metallurgica*, **18**(9), 951-956. https://doi.org/10.1016/0036-9748(84)90267-9.
65. Finot, E. Passion, A., & Thundat, T. (2008). Measurement of mechanical properties of cantilever shaped materials. *Sensors*, **8**(5), 3497-3541. https://doi.org/10.3390/s8053497.
66. Gerberich, W. W. Stauffer, D. D. Beaber, A. R., & Tymiak, N. I. (2012). A brittleness transition in silicon due to scale. *Journal of Materials Research*, **27**(3), 552-561. https://doi.org/10.1557/jmr.2011.348.

67. Giannozzi, P. Andreussi, O. Brumme, T. Bunau, O. Buongiorno, M. Calandra, M. et al. (2017). Quantum Espresso: A modular and open-source software project for quantum simulations of materials. *Journal of Physics: Condensed Matter*, **29**(46). https://doi.org/10.1088/0953-8984/21/39/395502.

68. Golestani-Fard, F. Hashemi, T. Mackenzie, K. J. D., & Hogarth, C. A. (1983). Formation of cadmium stannate studied by electron spectroscopy. *Journal of Materials Science*, **18**(12), 3679-3685. https://doi.org/10.1007/BF00540740.

69. Gray, K. J. (1992, November 20). Electromagnetic window properties of CVD diamond. *Proceedings of the SPIE 1759, Diamond Optics V*. https://doiorg/10.1117/12.130773.

70. Grayson, A. C. R. Shawgo, R. S. Johnson, A. M. Flynn, N. T. Li, Y. et al. (2004). A BioMEMS review: MEMS technology for physiologically integrated devices. *Proceedings of the IEEE*, **92**(1), 6-21. https://doi.org/10.1109/JPROC.2003.820534.

71. Greminger, M. A. Sezen, A. S., & Nelson, B. J. (2005). A four degree of freedom MEMS microgripper with novel bi-directional thermal actuators. *Proceedings of International Conference on Intelligent Robots and Systems (IROS)*, 2814-2819. https://doi.org/10.1109/IROS.2005.1545137.

72. Grindrod, P. M. Heap, M. J. Fortes, A. D. Meredith, P. G. Wood, I. G. et al. (2010). Experimental investigation of the mechanical properties of synthetic magnesium sulphate hydrates: Implications for the strength of hydrated deposits on Mars. *Journal of Geophysical Research*, **115**, 1-15. https://doi.org/10.1029/2009JE003552.

73. Guler, E. Guler, M. Aldirmaz, E., & Kara, M. (2016). Some vibrational and thermodynamic properties of gallium arsenide. *Journal of Engineering and Fundamentals*, **3**(1), 9-16. https://doi.org/10.17530/jef.16.02.3.1.

74. Guyader, J. L. & Lesueur, C. (1978). Acoustic transmission through orthotropic multi-layered plates, part II: transmission loss. *Journal of Sound and Vibration*, **58**(1), 69-86. https://doi.org/10.1016/S0022-460X(78)80061-3.

75. Haacke, G. (1976). Transparent electrode properties of cadmium stannate. *Applied Physics Letters*, **28**(10), 622-623. https://doi.org/10.1063/1.88589.

76. Haacke, G. Ando, H., & Mealmake, W. E. (1977). Spray deposition of cadmium stannate films. *Journal of the Electrochemical Society*, **124**(12), 1923. https://doi.org/10.1149/1.2133196.

77. Hadi, M. A. Rayhan, M. A. Naqib, S. H. Chroneos, A., & Islam, A. K. M. A. (2019). Structural, elastic, thermal and lattice dynamic properties of new 321 MAX phases. *Computational Materials Science*, **170**, 109144(1-9). https://doi.org/10.1016/j.commatsci.2019.109144.

78. Hahn, T. Klapper, H. Muller, U., & Aroyo, M. I. (2016). Point groups and crystal classes. *International Tables for Crystallography*, A (3.2.1), 720-737. https://doi.org/10.1107/97809553602060000930.

79. Haines, J. Leger, J. M., & Bocquillon, G. (2001). Synthesis and design of super hard materials. *Annual Review of Materials Research*, **31**(1), 1-23. http://dx.doi.org/10.1146/annurev.matsci.31.1.1.

80. Hao, Y. Liu, Y. Zhang, X., & Zhong, Z. (2015). Study of characteristics of noise of diesel locomotive. *MATEC Web Conferences*, **31**, 02001. https://doi.org/10.1051/matecconf/20153102001.

81. Hassan, F. (2014). *Electronic and vibrational theory of crystals: Vibrations of lattice*. Beirut: Lebanese University Faculty of sciences 1.

82. Helmenstine, A. M. (2019, January 30). *The shear modulus and rigidity*. Retrieved from: http://www.thoughtCo.com/shear-modulus.

83. Hencky, H. (1947). On the consideration of shear distortion in flat plates. *Engineer Archive*, **16**, 72-76. https://doi.org/10.1007/BF00534518.

84. Henriques, J. M. Caetano, E. W. S. Freire, V. N. da Costa, J. A. P., & Albuquerque, E. L. (2007). Ab initio structural, electronic and optical properties of orthorhombic $CaGeO_3$. *Journal of Solid-State Chemistry*, **180**(3), 974-980. https://doi.org/10.1016/j.jssc.2006.12.029.

85. Hess, A. E. (2011). Integration of process-incompatible materials for microfabricated polymer-based neural interfaces [PhD dissertation, Case Western Reserve University]. Retrieved from https://www.researchgate.net/publication/268340054.

86. Hill, R. W. (1952). The elastic behaviour of a crystalline aggregate. *Proceedings of Physical Society. Section A*, **65**(5), 349. https://doi.org/10.1088/0370-1298/65/5/307.

87. Hjort, K. Soderkvist, J., & Schweitz, J-A. (1994). Gallium arsenide as a mechanical material. *Journal of Microtechnology and Microengineering*, **4**(1), 1-13. https://doi.org/10.1088/0960-1317/4/1/001.

88. Hong, Q-J. (2015). Methods for melting temperature calculation [Unpublished PhD thesis, California Institute of Technology].

89. Hopcroft, M. A. Nix, W. D., & Kenny, T. W. (2010). What is the Young's modulus of silicon? *Journal of Microelectromechanical Systems*, **19**(2), 229-238. https://doi.org/10.1109/JMEMS.2009.2039697.

90. Hotovy, I. Rehacek, V. Mika, F. Lalinsky, T. Hascik, S. et al. (2008). Gallium arsenide suspended microheater for MEMS sensor arrays. *Microsystems Technology*, **14**, 629-635. https://doi.org/10.1007/s00542-007-0470-6.

91. Huang, H. Suvorova, A. Winchester, K. J. Dell, J. M., & Faraone, L. (2006). Characteristics of low temperature pecvd silicon nitride for mems structural materials. *International Journal of Modern Physics B*, **20**(25, 26 & 27), 3799-3804. https://doi.org/10.1142/S0217979206040398.

92. Hull, R. (1999). *Properties of crystalline silicon*. London: INSPEC.

93. Ivanovskii, A. L. (2012). Microhardness of osmium borides, carbides, and nitrides. *Inorganic Materials: Applied Research*, **3**(4), 319-322.

94. James, T. Mannoor, M. S., & Ivanov, D. V. (2008). BioMEMS-Advancing the frontiers of medicine. *Sensors*, **8**, 6077-6107. https://doi.org/10.3390/s8096077.

95. Jaric, J. P. Kuzmanovic, D., & Golubovic, Z. (2008). On tensors of elasticity. *Theoretical and Applied Mechanics*, **35**(1-3), 119-136. https://doi.org/10.2298/TAM0803119J.

96. Jeyadheepan, K. & Sanjeeviraja, C. (2014). Preparation and crystal structures of some $A^{IV}B_2^{II}O_4$ compounds: Powder X-ray diffraction and Rietveld analysis. *Journal of Chemistry*, **2014**(1), 1-6. https://doi.org/10.1155/2014/245918.

97. Ji, H. & Yu, D. (2005). Study of the bending modulus of individual silicon nitride nanobelts via atomic force microscopy. *Applied Physics A*, **82**(3), 475-478. https://doi.org/10.1007/s00339-005-3335-9.

98. Jiang, L. & Cheung, R. (2009). A review of silicon carbide development in MEMS applications. *International Journal of Computational Materials Science and Surface Engineering*, **2**(3/4), 225-240. https://doi.org/10.1504/ijcmsse.2009.027484.

99. Keesom, P. H. & Seidel, G. (1959). Specific heat of germanium and silicon at low temperatures. *Physical Review*, **113**(1), 33-39. https://doi.org/10.1103/PhysRev.113.33.

100. Khan, M. A. Ahmed, A. Ali, N. Igbal, T. Maboob, U., & Shafique, M. (2016). Improved optical properties of tin-antimony sulphide thin films for photovoltaics. *American Journal of Materials Science and Engineering*, **4**(1), 1-6. https://doi.org/10.12691/AJMSE-4-1-1.

101. Kim, B. & Meng, E. (2019). Review of polymer MEMS micromachining. *Journal of Micromachines and Microengineering*, **26**, 1-42. https://doi.org/10.1088/0960-1317/26/1/013001.

102. Kim, H. Chuo, C. Y. Ekerdt, J. G., & Hwang, G. S. (2011). Structure and properties of Li-Si phases: A first principles study. *Journal of Physical Chemistry C*, **115**(5), 2514-2521. https://doi.org/10.1021/JP1083899.

103. Kitagawa, K. (2007, October 10). Thin film thickness profile measurement using an interferometric surface profiler. *Proceedings of SPIE, Optomechatronic Sensors and Instrumentation III*, **6716**, 671607(1-12). https://doi.org/10.1117/12.754178.

104. Kittel, C. (1996). *Introduction to solid state physics*. New York: John Wiley & Sons Inc.

105. Kittel, C. (1953). *Introduction to solid state physics*. New York: John Wiley & Sons Inc.

106. Kohn, W. & Sham, L. J. (1965). Self-consistent equations including exchange and correlation effects. *Physical review*, **140**(4A), 1133-1138. https://doi.org/10.1103/PhysRev.140.A1133.

107. Kondrath, N. & Kazimierczuk, M. K. (2010). Characteristics and applications of silicon carbide power devices in power electronics. *International Journal of Electronics and Telecommunications*, **56**(3), 231-236. https://doi.org/10.2478/V10177-010-0030-3.
108. Korlyakov, A. V. Mikhailova, O. N., & Serkov, A. V. (2018). Metallic coatings for MEMS structures. *Materials Science and Engineering*, **387**, 012040(1-4). https://doi.org/10.1088/1757-899X/387/1/012040.
109. Kosevich, A. M. (1999). *The crystal lattice*. Berlin: Wiley-VCH.
110. Koutsoureli, M. Xavier, S. Michalas, M. Lioutas, C. Bansropun, S. et al. (2017). Electrical properties of nanostructured SiN films for MEMS capacitive switches. *Journal of Micromechanics and Microengineering*, **27**, 1-11. https://doi.org/10.1088/0960-1317/27/1/014001.
111. Krishna, K. Kamamurthi, K., & Elangovan, E. (2010). *Novel procedure to prepare cadmium stannate films using spray pyrolysis technique for solar cell applications.* Caparica: New University of Lisbon.
112. Kurbanov, T. K. Amirdzhanova, T. B. Movsum-zade A. M., & Panakh-zade, S. A. (1986). ChemInform abstract: Synthesis and properties of cadmium stannate. *Inorganic Materials*, **22**(2), 1-11. https://doi.org/10.1002/CHIN.198618036.
113. Landau, L. D. & Lifshitz, E. M. (1970). *Theory of elasticity course of theoretical physics. 3rd edition, vol. 7*. Oxford: Butterworth-Heinemann.
114. Lau, G. & Shrestha, M. (2017). Ink-jet printing of micro-electromechanical systems (MEMS). *Micromachines*, **8**(94), 1-19. https://hdl.handle.net/10356/86520.
115. Lazerand, T. & Lishan, D. (2014). *Silicon nitride for MEMS applications: LPCVD and PECVD process comparison*. St. Petersburg: Plasma-Thermo.
116. Leclercq, J. L. Ribas, R. P. Karam, J. M., & Viktorovitch, P. (1998). Micromachined devices for microsystems, *Microelectronics Journal*, **29**(9), 613-619. https://doi.org/10.1016/S0026-2692(98)00024-X.

117. Lenthe, E. Leeuwen, R. Baerends, E. J., & Snijders, J. G. (1996). Relativistic regular two-component Hamiltonians. *International Journal of Quantum Chemistry*, **57**(3), 281-293. https://doi.org/10.1002/(SICI)1097-461X(1996)57:3<281::AID-QUA2>3.0.CO;2-U.

118. Li, L. & Chew, Z. J. (2014). 11-Microactuators: design and technology. *Smart Sensors and MEMS*, 305-348. https://doi.org/10.1533/9780857099297.2.305.

119. Li, S. Ju, X., & Wan, C. (2014). Theoretical studies of elastic properties of orthorhombic $LiBH_4$. *Computational Materials Science*, **81**, 379-385. https://doi.org/10.1016/j.commatsci.2013.08.044.

120. Li, W. (2012). *MEMS for biomedical applications*. Microtechnology laboratory, Michigan: Michigan State Univeristy.

121. Li, Y. Khounsary, A., & Gosz, M. (2004). Effect of silicon anisotropy on mirror substrate design. *Proceedings of the SPIE-The International Society for Optical Engineering*, **5533**, 124-130. https://doi.org/10.1117/12.561438.

122. Lindemann, F. A. (1910). About the calculation of own molecular frequencies. *Physical Papers*, **11**, 609-612.

123. Liu, C-Y. Wang, T-H. Bo, Z-Z., & Liu, J-L. (2014). Internal low-frequency noise analysis of high-speed train under mechanical excitation. *JVE International LTD. Journal of Vibroengineering*, **16**(6), 3086-3094.

124. Love, A. E. H. (1888). The small free vibrations and deformation of a thin elastic shell. *Philosophical Transactions of the Royal Society of London A*, **179**, 491-546. https://www.jstor.org/stable/90527.

125. Luchinin, V. Korlyakov, A. V. Jandjgava, G. I. Prosorov, S. V. Solomatin, A. K. Sorokin, V. et al. (1999). Microtechnology for fabrication of surface micro mechanic devices based on a novel SiC-AlN composition: Design, test, integration, and packaging of MEMS/ MOEMS. *SPIE*, **3680**, 897-905. https://doi.org/10.1117/12.341156.

126. Luke, K. Dutt, A. Poitras, C. B., & Lipson, M. (2013). Overcoming $Si_3N_4$ film stress limitations for high quality factor ring resonators. *Optics Express*, **21**(19), 22829-22833. https://doi.org/10.1364/OE.21.022829.

127. Luo, J. K. Fu, Y. Q. Le, H. R. Williams, J. A. Spearing, S. M., & Milne, W. I. (2007). Diamond and diamond-like carbon MEMS. *Journal of Microtechnology and Microengineering*, **17**(7), S147- S163. http://eprints.soton.ac.uk/id/eprint/48537.

128. Mansour, M. B. Ogam, E. Fellah, Z. E. A. Cherif, A. S. Jelidi, A., & Jabrallah, S. B. (2016). Characterization of compressed earth blocks using low frequency guided acoustic waves. *Journal of Acoustical Society of America*, **139**(5), 2551-2560. http://dx.doi.org/10.1121/1.4948573.

129. Manyali, G. S. & Sifuna, J. (2019). Low compressible β-$BP_3N_6$. *AIP Advances*, **9**, 125929(1-5). https://doi.org/10.1063/1.5129268.

130. Marauska, S. Jahns, R. Greve, H. Quandt, E. Knöchel, R., & Wagner, B. (2012). MEMS magnetic field sensor based on magnetoelectric composites. *Journal of Micromechanics and Microengineering*, **22**(6), 065024(1-6). http://iopscience.iop.org/0960-1317/22/6/065024.

131. Mariana, A. F. Rodrigo, S. P. Marcos, M., & Homero, S. M. (2012). *Applications of SiC-based thin films in electronic and MEMS devices*. Vale do Paraiba: University of Vale do Paraiba. http://doi.org/10.5772/50998.

132. Mawatari, K. Sameshima, K. Miyai, M., & Matsuda, S. (2005). Development of new inkjet head applying MEMS technology and thin film actuator. *Konica Minolta Technology Report*, **12**, 23-27.

133. McSkimin, H. J. & Andreatch, P. (1972). Elastic moduli of diamond as a function of pressure and temperature. *Journal of Applied Physics*, **43**, 2944. https://doi.org/10.1063/1.1661636.

134. Mehregany, M. Zorman, C. A. Rajan, N., & Wu, C. H. (1998). Silicon carbide MEMS for harsh environments. *Proceedings of the IEEE*, **86** (8), 1594-1610. https://doi.org/10.1109/5.704265.

135. Mehregany, M. Zorman, C. A. Roy, S. Fleischman, A. J. Wu, C. H., & Rajan, N. (2000). Silicon carbide for microelectromechanical systems. *International Materials Reviews*, **45**(3), 85-108. https://doi.org/10.1179/095066000101528322.

136. Meng, T. McCandless, B. E. Buchanan, W. A. Birkmire, R. W. Hamilton, C. T. et al. (2012). Effect of annealing atmosphere and temperature on the properties of cadmium stannate thin films. *Conference Record of the 38th IEEE Photovoltaic Specialists Conference.*1803-1806. Chicago: IEEE. https://doi.org/10.1109/PVSC.2012.6317943.

137. Merzaghi, S. Koechli, C., & Perriard, Y. (2015). Development of a hybrid MEMS BLDC micromotor. *IEEE Transactions on Industry Applications*, **47**, 3-11. https://doi.org/10.1109/TIA.2010.2090841.

138. Messaoud, J. B. Michaud, J-F. Certon, D. Camarda, M. Piluso, N. Colin, L. Barcella, F., & Alquier, D. (2019). Investigation of the Young's modulus and the residual stress of 4H-SiC circular membranes on 4H-SiC substrates. *Micromachines (Basel)*, **10**(12), 1-12. https://doi.org/10.3390/mi10120801.

139. Minami, T. (2005). Transparent conducting oxide semiconductors for transparent electrodes. *Semiconductor Science and Technology*, **20**(4), 35-44. https://doi.org/10.1088/0268-1242/20/4/004.

140. Mindlin, R. D. (1951). Influence of rotatory inertia and shear on flexural motions of isotropic, elastic plates. *Journal of Applied Mechanics*, **18**(1), 31-38. https://doi.org/10.1115/1.4010217.

141. Mishra, K. K. & Upadhyaya, K. S. (2012). A theoretical study of Debye temperature variations of gallium pnictides. *International Journal of Engineering Research & Technology (IJERT)*, **1**(5), 1-3. https://doi.org/10.17577/IJERTV1IS5176.

142. Miskinis, K. Dikavicius, V. Bliudzius, R., & Banionis, K. (2015). Comparison of sound insulation of windows with double glass units. *Applied Acoustics*, **92**, 42-46. https://doi.org/10.1016/j.apacoust.2015.01.007.

143. Mohammad, M. T. & Ghafor, W. A. S. A. (1993). Cadmium stannate thin film as a solar energy utilizing element. *Solid State Communications*, **88**(3), 227-230. https://doi.org/10.1016/0038-1098(93)90747-B.

144. Monkhorst, H. J. & Pack, J. D. (1976). Special points for Brillouin zone integration. *Physical Review B*, **13**, 5188-1592. http://dx.doi.org/10.1103/PhysRevB.13.5188.

145. Moon, J. Cho, K., & Cho, M. (2012). Ab-initio study of silicon and tin as negative electrode materials for lithium-ion batteries. *International Journal of Precision Engineering and Manufacturing*, **13**(7), 1191-1197. https://doi.org/10.1007/s12541-012-0158-4.
146. Mouhat, F. & Coudert, F-X. (2014). Necessary and sufficient elastic stability conditions in various crystal systems. *Physical Review B*, **90**(22), 224104(1-4). https://doi.org/10.1103/PhysRevB.90.224104.
147. Munjal, N. Sharma, V. Sharma, G. Vyas, V. Sharma, B. K., & Lowther, J. E. (2011). Ab-initio study of the electronic and elastic properties of beryllium chalcogenides BeX (X = S, Se and Te). *Physica Scripta*, **84**(3), 035704 (10). https://doi.org/10.1088/0031-8949/84/03/035704.
148. Munro, R. G. (1997). Material properties of a sintered α-SiC. *Journal of Physical and Chemical Reference Data*, **26**(5), 1195-1203. https://doi.org/10.1063/1.556000.
149. Muslov, S. A. Lotkov, A. I., & Arutyunov, S. D. (2019). Extrema of elastic properties of cubic crystals. *Russian Physics Journal*, **62**, 1417-1427. https://doi.org/10.1007/s11182-019-01859-w.
150. Nasir, E. M. Naji, I. S., & Alias, M. F. A. (2013). Characterization of cadmium tin oxide thin films as a window layer for solar cell. *International Journal of Application and Innovation in Engineering and Management*, **2**(9), 189-194.
151. Nayak, A. & Suresh, K. A. (2009). Mechanical properties of Langmuir-Blodgett films of a discogen-DNA complex by atomic force microscopy. *Journal of Physical Chemistry B*, **113**(12), 3669-3675. https://doi.org/10.1021/jp806600g.
152. Nelson, S. A. (2013). *External Symmetry of Crystals, 32 Crystal Classes*. New Orleans: Tulane University
153. Nguyen, C. & Clark, T. (1997). High-Q micromechanical oscillators and filters for communications. *Proceedings of the 1997 IEEE: International Symposium on Circuits and Systems*, (2825-2828). Michigan: University of Michigan.
154. Novikov, N. V. Dub, S. N. Mal'nev, V. I., & Beskrovanov, V. V. (1994). Mechanical properties of diamond at 1200 °C. *Diamond and Related Materials*, **3**(3), 198-204. https://doi.org/10.1016/0925-9635(94)90080-9.

155. Ogam, E. Fellah, Z. E. A., & Ogam, G. (2016). Identification of mechanical moduli of closed-cell porous foams using transmitted acoustic waves in air and the transfer matrix method. *Composite structures*, **135**, 205-216. https://doi.org/10.1016/j.compstruct.2015.09.029.
156. Ongwen, N. O. (2019). *Optical properties of iron-doped cadmium stannate thin films*. Beaun Bassin: Lambert Academic Publishing.
157. Ongwen, N. O. Chanbi, D. Ogam, E. Otunga, H. Oduor, A., & Fellah, Z. E. A. (2021). Microstructural and elastic properties of stable aluminium-rich TiAl and $TiAl_2$ formed phase intermetallics. *Materials Letters*, **287**, 129295(1-4). https://doi.org/10.1016/j.matlet.2020.129295.
158. Ongwen, N. O. Oduor, A. O., & Ayieta, E. O. (2019). Effect of deposition temperature on the optical properties of iron-doped cadmium stannate thin films deposited by spray pyrolysis. *International Journal of Scientific and Technical Research in Engineering (IJSTRE)*, **4**(3), 38-48.
159. Ongwen, N. O. Ogam, E. Fellah, Z. E. A. Otunga, H. Oduor, A., & Mageto, M. (2022). Accurate Ab-initio calculation of elastic constants of anisotropic binary alloys: A case of Fe-Al. *Solid State Communications*, **353**, 114879(1-6). https://doi.org/10.1016/j.ssc.2022.114879.
160. Ongwen, N. O. Ogam, E., & Otunga, H. (2021). Ab initio study of elastic properties of orthorhombic cadmium stannate as a substrate for the manufacture of MEMS devices. *Materials Today Communications*, **26**, 101822. https://doi.org/10.1016/j.mtcomm.2020.101822.
161. Ortiz, A. R. (1982). Spray deposition and characterization of cadmium stannate films for solar cells. *Journal of Vacuum Science and Technology*, **20**(7), 7-12. https://doi.org/10.1116/1.571312.
162. Pan, C. Han, Y., & Lu, J. (2020). Design and optimization of lattice structures: A review. *Applied Sciences*, **10**(18), 6374. https://doi.org/10.3390/app10186374.
163. Parvin, F. & Naqib, S. H. (2019). Structural, elastic, electronic, thermodynamic, and optical properties of layered $BaPd_2As_2$ pnictide superconductor: A first principles investigation. *Journal of Alloys and Compounds*, **780**, 452-460. https://doi.org/10.1016/j.jallcom.2018.12.021.

164. Patil, L. A. Dea, V. V., & Kaushik, M. P. (2012). Modified cadmium stannate nanostructured thin films prepared by spraying technique for detection of chemical warfares. *Pratibha: International Journal of Science, Spirituality, Business and Technology*, **1**, 2261-2277.
165. Patil, S. B. Chu, V., & Conde, J. P. (2008). Performance of thin film silicon MEMS on flexible plastic substrates, *Sensors and Actuators A: Physical*, **144**(1), 201-206. https://doi.org/10.1016/j.sna.2007.12.022.
166. Peng, T. H. Lou, Y. F. Jin, S. F. Wang, W. Y. Wang, W. J. et al. (2012). Debye temperature of 4H-SiC determined by X-ray powder diffraction. *Powder Diffraction*, **24**(4), 311-314. https://doi.org/10.1154/1.3257905.
167. Perdew, J. P. Burkes, K., & Ernzerhof, M. (1996). Generalized gradient approximation made simple. *Physical Review Letters*, **77**(18), 3865-3868. https://doi.org/10.1103/PhysRevLett.78.1396.
168. Perednis, D. & Gauckler, L. J. (2005). Thin film deposition using spray pyrolysis. *Journal of Electroceramics*, **14**, 103-111. http://dx.doi.org/10.1007/s10832-005-0870-x.
169. Persson, K. (2014, July). Materials data on $Cd_2SnO_4$ (SG:55) by materials project. https://doi.org/10.17188/1277205.
170. Pettifor, D. G. (1992). Theoretical predictions of structure and related properties of intermetallics. *Materials Science and Technology*, **8**(4), 345-349. https://doi.org/10.1179/mst.1992.8.4.345.
171. Pickles, D. McCaig, I. Wood, C. Molyneux, N., & Makri, E. (2017). *Traditional windows: Their care, repair and upgrading*. London: Historic England.
172. Pigg, O. E. & Weiss, S. P. (1973). Apollo experience report-Spacecraft structural windows. (Report No. NASA TN D-7439). National Aeronautics and Space Administration.
173. Pizzagalli, L. (2021). Accurate values of 3C, 2H, 4H, and 6H SiC elastic constants using DFT calculations and heuristic error corrections. *Philosophical Magazine Letters*, **101**(6), 242-252. https://doi.org/10.1080/09500839.2021.1909167.
174. Pratap, R. & Arunkumar, A. (2006). Material selection for MEMS devices. *Indian Journal of Pure and Applied Physics*, **45**(4), 358-367.

175. Prime, F. P. (2002). *An Introduction to MEMS (Micro-electromechanical Systems)*. Loughborough: Loughborough University.
176. Pugh, S. F. (1954). XCII. Relations between the elastic moduli and the plastic properties of polycrystalline pure metals. *The London, Edinburgh, and Dublin Philosophical Journal of Science*, **45**(367), 823-843. https://doi.org/10.1080/14786440808520496.
177. Putra, A. Ismail, A. Y. Ramlan, R. Ayob, R., & Py, S. M. (2013). Normal incidence of sound transmission loss of a double-leaf partition inserted with a microperforated panel. *Advances in Acoustics and Vibration*, **2013**, 1-8. https://doi.org/10.1155/2013/216493.
178. Qin, Z. Gao, Y. Jia, J. Ding, X. Huang, L., & Li, H. (2019). The effect of the anisotropy of single crystal silicon on the frequency split of vibrating ring gyroscopes, *Micromachines*, **10**(26), 1-13. https://doi.org/10.3390/mi10020126.
179. Ranganathan, S. I. & Ostoja-Starzewski, M. (2008). Universal elastic anisotropy index. *Physical Review Letters*, **101**(5), 055504(1-4). https://doi.org/10.1103/PhysRevLett.101.055504.
180. Rasander, M. & Moram, M. A. (2015). On the accuracy of commonly used density functional approximations in determining the elastic constants of insulators and semiconductors. *Journal of Chemical Physics*, **143**, 144104(1-10). https://doi.org/10.1063/1.4932334.
181. Rasmussen, B. (2012). *Sound classification of dwellings-quality class ranges and class intervals in national schemes in Europe*. Prague: EuroNoise 2012. http://vbn.aau.dk/en/persons/birgit-rasmussen(c0e774a9-8cdf410f-8727-6a2cc11a4f14)/publications.html.
182. Rauschenbach, H. S. (1980). *Solar cell array design*. New York: Van Nostrand Reinhold Co.
183. Ravindran, P. Fast, L. Korzhavyi, P. A. & Johansson, B. (1998). Density functional theory for calculation of elastic properties of orthorhombic crystals: Application to $TiSi_2$. *Journal of Applied Physics*, **84**(9), 4891-4904. http://dx.doi.org/10.1063/1.368733.

184. Reddy, J. D. (2007). *Mechanical properties of silicon carbide (SiC) thin films* [Graduate thesis and dissertations]. https://pscholarcommons.usf.edu/edt/210.
185. Reilly, S. Leach, R. Cuenat, A., & Awan, S. (2006). *Overview of MEMS sensors and the metrology requirements for their manufacture*. Middlesex: National Physical Laboratory.
186. Reissner, E. (1945). The effect of transverse shear deformation on the bending of elastic plates. *Journal of Applied Mechanics*, **12**(2), A69-A77. https://doi.org/10.1115/1.4009435.
187. Sawat, V. S. Shinde, S. S. Deokate, R. J. Bhosale, C. H. Chougule, H. K., & Rajpure, K. Y. (2009). Effect of calcining temperature on electrical and dielectric properties of cadmium stannate. *Applied Surface Science*, **255**(13-14), 6675-6678. https://doi.org/10.1016/j.apsusc.2009.02.070.
188. Schimmelpenningh, J. (2012). *Acoustic interlayers for laminated glass-what make them different and how to estimate performance*. Advanced Interlayers-Solutia Inc: Glass Performance Days.
189. Schreiber, E. Anderson, O. L., & Soga, N. (1973). *Elastic constants and their measurements*. New York: McGraw-Hill.
190. Schwerdtfeger, P. (2011). The Pseudopotential approximation in electronic structure theory. *Physical Chemistry*, **12**(17), 1-9. https://doi.org/10.1002/cphc.201100387.
191. Sekitani, T. Zschieschang, U. Klauk, H., & Someya, T. (2010). Flexible organic transistors and circuits with extreme bending stability. *Nature Materials*, **9**, 1015-1022. http://dx.doi.org/10.1038/nmat2896.
192. Seng, A. B. Dahari, Z. Sidek, O., & Miskam, M. A. (2009). Design and analysis of thermal microactuator. *European Journal of Scientific Research*, **35**(2), 281-292.
193. Setty, M. S. & Sinha, A. P. B. (1986). Characterization of highly conducting Pb-doped $Cd_2SnO_4$ thick films. *Thin Solid Films*, **144**, 7-19. https://doi.org/10.1016/0040-6090(86)90065-9.
194. Shaikh, A. A., & Shitole, D. S. (2012). Micro-electromechanical system (MEMS) sensor. *International Journal of Scientific & Engineering Research*, **3**(11), 1-8.

195. Shackelford, J. F. Han, Y-H. Kim, S., & Kwon, S-H. (2015). *CRC materials science and engineering handbook*, **262**. https://doi.org/10.1201/b18971.
196. Shroeder, D. V. (2000). *An introduction to thermal physics*. San Francisco: Addison-Wesley.
197. Shugar, G. & Ballinger, J. (1996). *Chemical technicians' ready reference handbook.* New York: McGraw-Hill.
198. Sidorak, A. V. Ivanov, V. V., & Shubin, A. A. (2011). Cadmium stannate synthesis via thermal treatment of coprecipitated salts. *Materials Sciences and Applications*, **2**, 1219-1224. https://doi.org/10.4236/MSA.2011.29165.
199. Solozhenko, V. L. Oleksandr O. Denis, A. Yann, L. G., & Mohamed, M. (2009). Ultimate metastable solubility of boron in diamond: Synthesis of superhard diamondlike $BC_5$. *Physical Review Letters*, **102** (1), 015506. https://doiorg/10.1103/PhysRevLett.102.015506.
200. Sondena, R. Stolen, S., & Ravindran, P. (2016). *Ab initio calculation of elastic constants and derived mechanical properties of cubic and hexagonal* $SrMnO_3$. Oslo: Department of Chemistry and Centre for Materials Science and Nanotechnology, University of Oslo.
201. Sousa, S. F. Fernandes, P. F., & Ramos, M. J. (2007). General performance of density functionals. *Journal of Physical Chemistry*, **111**(42), 10439-10452. http://dx.doi.org/10.1021/jp0734474.
202. Speakman, S. A. (n.d). *Estimating crystallite size using XRD*. Cambridge: MIT Centre for Materials Science and Engineering.
203. Spear, K. E. & Dismukes, J. P. (1994). *Synthetic diamond: Emerging CVD science and technology*. London: John Wiley and Sons Inc.
204. Srinivasa, R. K. Girija, K. Sravani, D. S. Sailaja, J. Vijay, S. Srinivasa, Y. et al. (2012). Micro-Electro-Mechanical-Systems (MEMS) Technology. *Archives of Applied Science Research*, **4**(1), 307-314.
205. Talyzin, I. V. Samsonov, M. V. Samsonov, V. M, Pushkar, M. Y., & Dronnikov, V. V. (2019). Size dependence of the melting point of silicon nanoparticles: Molecular dynamics and thermodynamic simulation. *Semiconductors*, **53**, 947-953. https://doi.org/10.1134/S1063782619070236.

206. Tamulevicius, S. (1998). Stress and strain in the vacuum deposited thin films. *Vacuum*, **51**(2), 127-139. https://doi.org/10.1016/S0042-207X(98)00145-6.
207. Tanakaa, I. Oba, F. Sekine, T. Ito, E. Kubo, A. Tatsumi, K. et al. (2002). Hardness of cubic silicon nitride. *Journal of Materials Research*, **17**, 731-733. https://doi.org/10.1557/JMR.2002.0105.
208. Tang, M. Shang, J., & Zhang, Y. (2018). Oxygen vacancy and doping atom effect on electronic structure and optical properties of $Cd_2SnO_4$. *RSC Advances*, **8**, 640-646. https://doi.org/10.1039/c7ra10641f.
209. Teloff, E. M. (2014). *Elastic modulus calculation tutorial: Moduli in particular crystallographic directions*. Austin: The University of Texas at Austin.
210. Teter, D. M. (1998). Computational alchemy: The search for new super hard materials. *MRS Bulletin*, **23**(1), 22-27. https://doi.org/10.1557/S0883769400031420.
211. "Thick glass windows". (n.d.). Retrieved from http://www.ringerwindows.com/.
212. Tilli, M. & Haapalinna, A. (2020). Chapter 1-Properties of silicon. In Tilli, M. Paulasto-Krockel, M. Petzold, M. Theuss, H. Motooka, T., & Lindroos, V. (eds). Micro and Nano Technologies, Handbook of silicon-based MEMS materials and technologies (third edition) (3-17). https://doi.org/10.1016/B978-0-12-817786-0.00001-3.
213. Tinder, S. & Richard, F. (2007). *Relativistic flight mechanics and space travel: A prime for students, engineers and scientists*. London: Morgan and Claypool Publishers.
214. Todaro, M. T. Sileo, L., & Vittorio, M. (2012). Magnetic field sensors based on microelectromechanical systems (MEMS) technology, magnetic sensors-Principles and applications. Available from: http://www.intechopen.com/books/magnetic-sensors-principles-and-applications/magnetic-field-sensorsbased-on-microelectromechanical-systems-mems-technology.
215. Troemel, M. (1969). The crystal structure of the compounds of the $Sr_2PbO_4$ type. *Zetschrift for Inorganic and General Chemistry*, **371**(5-6), 237-247. https://doi.org/10.1002/zaac.19693710504.

216. Tu, H. (2007). *Flexible MEMS: A novel technology to fabricate flexible sensors and electronics*. Michigan: Wayne State University.
217. Utkin, A. & Fomin, V. M. (2020). Molecular dynamic calculation of the bulk modulus for silicon and silicon carbide. *Doklady Physics*, **65**(5), 174-177. https://doi.org/10.1134/S1028335820050122.
218. Vanderbilt, D. (1990). Soft self-consistent pseudopotentials in generalized eigenvalue formalism. *Physical Review B: American Physical Society*. **41**(11), 7892-7895. https://doi.org/10.1103/PhysRevB.41.7892.
219. Varadan, V. K. (2003). Nanotechnology: MEMS and NEMS and their applications to smart systems and devices. *Proceedings of the SPIE*, **5062**, 20-43. https://doi.org/10.1117/12.514830.
220. Velásquez, C. Campero, A., & Ortiz, A. (2003). Cadmium stannate thin films prepared by sol-gel process. In: López, T. M. Avnir, D., & Aegerter, M. (eds). Emerging Fields in Sol-Gel Science and Technology. Boston, MA: Springer. https://doi.org/10.1007/978-1-4615-0449-8_33.
221. Veprek, S. Zeer, A., & Riedel, R. (2000). *Handbook of ceramic hard materials*, R. Riedel (ed.). Weinheim: Wiley & Sons Inc.
222. Victor, A. (1962). Heat capacity of diamond at high temperatures. *The Journal of Chemical Physics*, **36**(7), 1903-1911. https://doi.org/10.1063/1.1701288.
223. Vladimir L. Solozhenko, A. Sergey, N. Dub, S. Nikolay, V., & Novikov, N. (2001). Mechanical properties of cubic BC N, a new superhard phase. *Diamond and Related Materials*, **10**, 2228-2231.
224. WaferPro (2017, May 28). What is a silicon wafer? What is it used for? Retrieved from: https://waferpro.com/what-is-a-silicon-wafer.
225. Waters, P. (2008). *Stress analysis and mechanical characterization of thin films for microelectronics and MEMS applications* [PhD dissertation, University of South Florida, South Florida]. Retrieved from: https://scholarcommons.usf.edu.
226. Weast, R. (1984). *CRC, Handbook of Chemistry and Physics*. Boca Raton, Florida: Chemical Rubber Company Publishing.

227. Wei, S. H. & Segev, D. (2005, January 01). Electronic and optical properties of spinel TCOs: $Cd_2SnO_4$, $Zn_2SnO_4$, and $CdIn_2O_4$ [Conference presentation]. *DOE Solar Energy Technologies Program Review Meeting*. Oak Ridge, United States.
228. Weinberger, C. & Cai, W. (2004). *ME340B-Elasticity of Microscopic Structures: Introduction to elasticity*. Stanford: Stanford University.
229. Wen, Y. Wang, L. Liu, H., & Song, L. (2017). Ab initio study of the elastic and mechanical properties of B19 TiAl. *Crystals*, **7**(39), 1-11. https://doi.org/10.3390/cryst7020039.
230. Wentorf, R. H. Devries, R. C., & Bundy, F. P. (1980). Sintered Super hard Materials. *Science*. **208** (4446), 873-380. https://doi.org/10.1126/science.208.4446.873.
231. "Why double glazing". (2007, March) Why double glazing is so important when it comes to glass selection. Retrieved from http://www.glassonweb.com/.
232. Winchester, K. J. & Dell, J. M. (2001). Tuneable Fabry-Perot cavities fabricated from PECVD silicon nitride employing zinc sulphides as the sacrificial layer. *Journal of Microtechnology and Microengineering*, **11**, 589-594. https://doi.org/10.1088/0960-1317/11/5/323.
233. Wu, H. Hartman, M. R. Udovic, T. J. Rush, J. J. Zhou, W. Bowman, R. C., & Vajo, J. J. (2007). Structure of the novel ternary hydrides $Li_4Tt_2D$ (Tt = Si and Ge). *Acta Crystallographica Section B*, **63**, 63-68. https://doi.org/10.1107/S0108768106046465.
234. Xiao, S. Y. Che, L. F. Li, X. X., & Wang, X. L. (2008). A novel fabrication process of MEMS devices on polyimide flexible substrates, *Microelectronic Engineering*, **85**, 452-457. https://doi.org/10.1016/J.MEE.2007.08.004.
235. Yang, C. & Jiang, Q. (2005). Effect of pressure on melting temperature of silicon and germanium. *Materials Science Forum*, **475-479**, 1893-1896. https://doi.org/10.4028/www.scientific.net/MSF.475-479.1893.
236. Yang, H. Han, R. Yan, Y. Du, X. Zhan, Q., & Jin, H. (2012). First-principles study of ferromagnetism in Zn- and Cd-doped $SnO_2$. *Journal of Magnetism and Magnetic Materials*, **324**(10), 1764-1769. https://doi.org/10.1016/j.jmmm.2011.12.034.

237. Yasseen, A. A. Wu, C. H. Zorman, C. A., & Mehregany, M. (2000). Fabrication and testing of surface micromachined polycrystalline SiC micromotors. *IEEE Electron Device Letters*, **21**(4), 164-166. https://doi.org/10.1109/MEMSYS.1999.746903.
238. Yong, Q. Xu, D. Liu, Q. Xiao, Y., & Wei, D. (2021). Advances in polymer-based matte coatings: A review. *Polymers for Advanced Technologies*, 1-15. http://doi.org/10.1002/pat.5508.
239. Yongqing, F. Hejun, D. Weimin, H. Sam, Z., & Min, H. (2010). *Advanced materials for micro and nano systems programme*. Nanyang: Nanyang Technological University.
240. Yu, A. Fang, S. Zhao, D., & Zheng, P. (2014). Ab initio calculation of the thermodynamic properties of wurtzite ZnS: Performance of the LDA and GGA. *Chalcogenide Letters*, **11**(12), 619-628.
241. Yuan, X. Chen, L. Zhao, Y. Di, H., & Zhu, F. (2014). Dependence of grain size on mechanical properties and microstructures of high manganese austenitic steel. *Procedia Engineering*, **81**, 143-148. https://doi.org/10.1016/J.PROENG.2014.09.141.
242. Zhang, J-M. Zhang, Y. Xu, K-W., & Ji, V. (2008). Young's modulus surface and Poisson's ratio curve for orthorhombic crystals. *Journal of Chemical Crystallography*, **38**(733), 733-741. https://doi.org/10.1007/s10870-008-9370-6.
243. Zhang, K-C. Li, Y-F. Liu, Y., & Zhu, Y. (2012). Ferromagnetism of Cd doped $SnO_2$: A first-principles study. *Journal of Applied Physics*, **112**, 1-4. https://doi.org/10.1063/1.4748146.
244. Zhang, S. B. & Wei, S-H. (2002). Self-doping of cadmium stannate in the inverse spinel structure. *Applied Physics Letters*, **80**(8), 1376-1378. https://doi.org/10.1063/1.1452789.
245. Zheng, B. Zhou, C. Wang, Q. X. Chen, Y., & Xue, W. (2013). Deposition of low stress Silicon nitride thin film and its application in surface micromachining device structures. *Advances in Materials Science and Engineering*, **2013**(D835942), 1-4. https://doi.org/10.1155/2013/835942.

246. Zheng, L-S. & Lu, M. S-C. (2007). A large-displacement CMOS micromachined thermal actuator with comb electrodes for capacitive sensing. *Sensors and Actuators A: Physical*, **136**(2), 697-703. https://doi.org/10.1016/j.sna.2007.01.006.

247. Zhou, J. & Switzer, A. (1996). Growth of cerium (IV) oxide films by the electrochemical generation. *Journal of Alloys and Compounds*, **237**, 1-5. https://doi.org/10.1016/0925-8388(95)02048-9.

248. Zhou, Y. L. Niinomi, M., & Akahori, T. (2004). Effects of Ta content on Young's modulus and tensile properties of binary Ti-Ta alloys for biomedical applications. *Material Science and Engineering A*, **371**. https://doi.org/10.1016/j.msea.2003.12.011.

249. Zhu, H. Yu, X. Rajamani, R., & Stelson, K. A. (2004). Active control of glass panels for reduction of sound transmission through windows. *Mechatronics*, **14**, 805-819. https://doi.org/10.1016/j.mechatronics.2004.03.001.

250. Zhu, Z. Du, Z. Liu, X. Zhang, Y. Wu, Q., & Lin, X. (2021). Cadmium stannate conductive layer with high optical transmittance and tenable work function. *Materials Research Express*, **8**, 016410. https://doi.org/10.1088/2053-1591/abdcbb.

# APPENDICES

***Appendix 1: The crystal structures of silicon and silicon carbide as viewed in Burai, a graphical user interface for quantum espresso. The brown spheres represent the silicon atoms, while the grey spheres represent the carbon atoms***

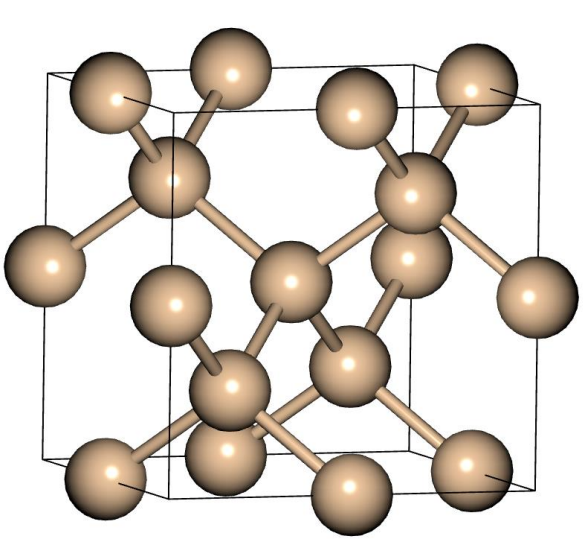

Si

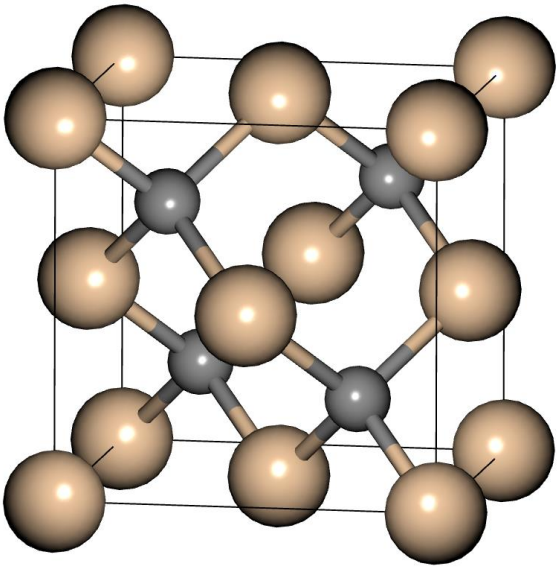

SiC

***Appendix 2: The crystal structures of CTO 1, CTO 2, CTO 3, and CTO 5***

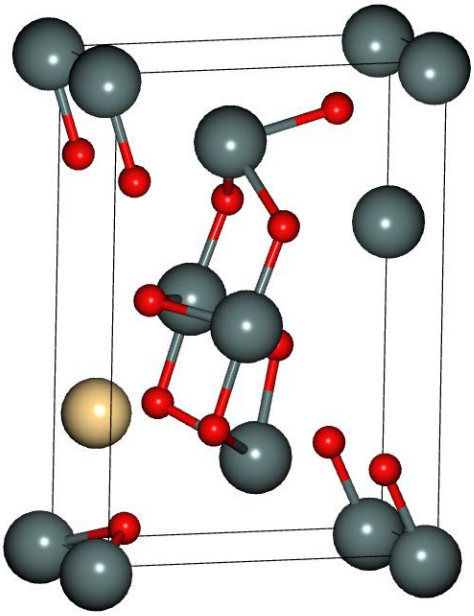

CTO 1

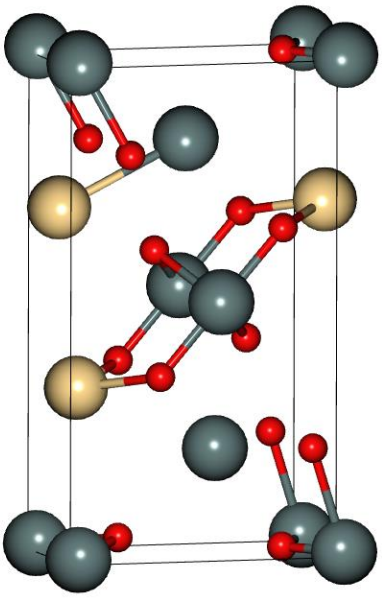

CTO 2

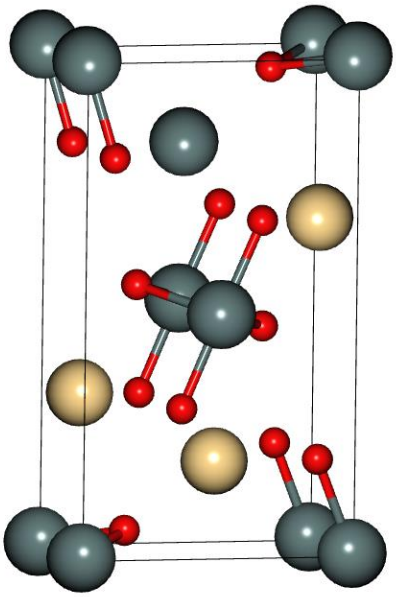

CTO 3

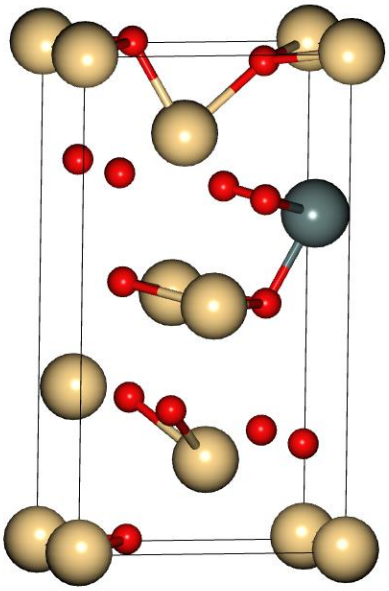

CTO 5

## *Appendix 3: Contents of the original input files of CTO 1, CTO 2, CTO ,3 and CTO 5, showing the original input parameters*

```
&CONTROL
calculation='scf'
prefix='CTO1'
pseudo_dir ='./'
outdir='./tmp'
tprnfor=.TRUE.
tstress=.TRUE.
/
&SYSTEM
celldm(1) = 12.584509349
celldm(2) = 1.4333565694
celldm(3) = 0.4884494871
degauss     =  0.02
ecutrho     = 400
ecutwfc     =  50
ibrav       = 8
nat         = 14
ntyp        = 3
occupations = "smearing"
smearing    = "gaussian"
/
&ELECTRONS
    conv_thr         =  1.00000e-06
    electron_maxstep = 200
    mixing_beta      =  7.00000e-01
    startingpot      = "atomic"
    startingwfc      = "atomic+random"
/
K_POINTS {automatic}
 5 3 9  0 0 0

ATOMIC_SPECIES
O      15.99940  O.pbesol-n-rrkjus_psl.0.1.UPF
Cd    112.40000  Cd.pbesol-dn-rrkjus_psl.0.2.UPF
Sn    118.69000  Sn.pbesol-dn-rrkjus_psl.0.2.UPF

ATOMIC_POSITIONS {angstrom}
Cd       0.275111899   2.700533055   1.626399160
Sn       6.117006816   6.181430277   1.626399160
Sn       3.513740249   1.719211801   1.626399160
Sn       2.887300059   7.852639001   1.626399160
Sn      -0.244990395  -0.138517595   0.000000000
Sn       2.710267053   4.548547136   0.000000000
O        0.390371458   7.449815637   0.000000000
O        5.566767214   1.671641830   0.000000000
O        3.423760179   6.459173523   0.000000000
O        2.087185742   2.570893336   0.000000000
O        0.883654338   0.450609735   1.626399160
O        5.038926897   8.423219476   1.626399160
O        3.910548348   3.885166302   1.626399160
O        1.318774582   4.843128076   1.626399160
```

CTO 1

```
&CONTROL
calculation='scf'
prefix='CTO2'
pseudo_dir ='./'
outdir='./tmp'
tprnfor=.TRUE.
tstress=.TRUE.
/
&SYSTEM
celldm(1) = 11.0231262
celldm(2) = 1.80955339
celldm(3) = 0.55634228
degauss     = 0.02
ecutrho     = 400
ecutwfc     = 50
ibrav       = 8
nat         = 14
ntyp        = 3
occupations = "smearing"
smearing    = "gaussian"
/
&ELECTRONS
    conv_thr         =  1.00000e-06
    electron_maxstep = 200
    mixing_beta      =  7.00000e-01
    startingpot      = "atomic"
    startingwfc      = "atomic+random"
/
K_POINTS {automatic}
 5 3 9  0 0 0

ATOMIC_SPECIES
O      15.99940  O.pbesol-n-rrkjus_psl.0.1.UPF
Cd    112.40000  Cd.pbesol-dn-rrkjus_psl.0.2.UPF
Sn    118.69000  Sn.pbesol-dn-rrkjus_psl.0.2.UPF

ATOMIC_POSITIONS {angstrom}
Cd       0.580968981   3.579723548   1.622325325
Cd       6.036377612   7.423354610   1.622317917
Sn       3.635042731   2.209055317   1.622218831
Sn       2.978007579   8.807624793   1.622215977
Sn       0.178142509   0.113470056  -0.000317091
Sn       3.306158190   5.499247061  -0.000297301
O        1.301664601   8.672873796  -0.000275305
O        5.321889660   2.336530780  -0.000270339
O        4.653791032   7.043001771  -0.000287270
O        1.968871426   3.943236235  -0.000274243
O        1.506629246   0.370894457   1.622325482
O        5.107837481  10.632245380   1.622335143
O        4.314721294   4.536387334   1.622339683
O        2.295082586   6.453336433   1.622339212
```

CTO 2

```
&CONTROL
calculation='scf'
prefix='CTO3'
pseudo_dir ='./'
Outdir='./tmp'
tprnfor=.TRUE.
tstress=.TRUE.
/
&SYSTEM
celldm(1) = 10.6973963
celldm(2) = 1.77929659
celldm(3) = 0.57172842
degauss     =  0.02
ecutrho     = 400
ecutwfc     =  50
ibrav       = 8
nat         = 14
ntyp        = 3
occupations = "smearing"
smearing    = "gaussian"
/
&ELECTRONS
    conv_thr         =  1.00000e-06
    electron_maxstep = 200
    mixing_beta      =  7.00000e-01
    startingpot      = "atomic"
    startingwfc      = "atomic+random"
/
K_POINTS {automatic}
 5 3 9  0 0 0

ATOMIC_SPECIES
O      15.99940  O.pbesol-n-rrkjus_psl.0.1.UPF
Cd    112.40000  Cd.pbesol-dn-rrkjus_psl.0.2.UPF
Sn    118.69000  Sn.pbesol-dn-rrkjus_psl.0.2.UPF

ATOMIC_POSITIONS {angstrom}
Cd       0.337993033   3.242002483   1.618225579
Cd       5.316409104   6.712153109   1.618225579
Cd       3.167139074   1.812429404   1.618225579
Sn       2.457968168   8.293973577   1.618225579
Sn      -0.037860690   0.069610477   0.000000000
Sn       2.838275688   4.951414352   0.000000000
O        0.576376665   8.154332752   0.000000000
O        4.877730054   1.985729989   0.000000000
O        3.671492607   6.844076958   0.000000000
O        2.029425206   3.053014677   0.000000000
O        1.308716293   0.438273709   1.618225579
O        4.259104407   9.779954805   1.618225579
O        4.147559386   4.531556530   1.618225579
O        1.504882213   5.411356170   1.618225579
```

CTO 3

```
&CONTROL
calculation='scf'
prefix='CTO5'
pseudo_dir ='./'
outdir='./tmp'
tprnfor=.TRUE.
tstress=.TRUE.
/
&SYSTEM
celldm(1) = 10.585334867
celldm(2) = 1.8077569526
celldm(3) = 0.5670357114
degauss     =  0.02
ecutrho     = 400
ecutwfc     =  50
ibrav       = 8
nat         = 14
ntyp        = 3
occupations = "smearing"
smearing    = "gaussian"
/
&ELECTRONS
    conv_thr         =  1.00000e-06
    electron_maxstep = 200
    mixing_beta      =  7.00000e-01
    startingpot      = "atomic"
    startingwfc      = "atomic+random"
/
K_POINTS {automatic}
 5 3 9  0 0 0

ATOMIC_SPECIES
O      15.99940  O.pbesol-n-rrkjus_psl.0.1.UPF
Cd    112.40000  Cd.pbesol-dn-rrkjus_psl.0.2.UPF
Sn    118.69000  Sn.pbesol-dn-rrkjus_psl.0.2.UPF

ATOMIC_POSITIONS {angstrom}
Cd       0.285513640   3.292578865   1.588130593
Sn       5.322310465   6.759347891   1.588130593
Cd       3.080679971   1.778711515   1.588130593
Cd       2.558789397   8.418418149   1.588130593
Cd       0.003220465   0.055483262   0.000000000
Cd       2.777818427   5.037263183   0.000000000
O        0.763443841   7.770114180   0.000000000
O        4.688714941   2.219755053   0.000000000
O        3.832510194   7.190301663   0.000000000
O        1.899849805   2.921607188   0.000000000
O        1.439927527   0.178205580   1.588130593
O        4.209240355   9.872735608   1.588130593
O        4.312069109   4.942654686   1.588130593
O        1.294200418   5.411996288   1.588130593
```

CTO 5

***Appendix 4: A flow chart showing the practical implementation of density functional theory***

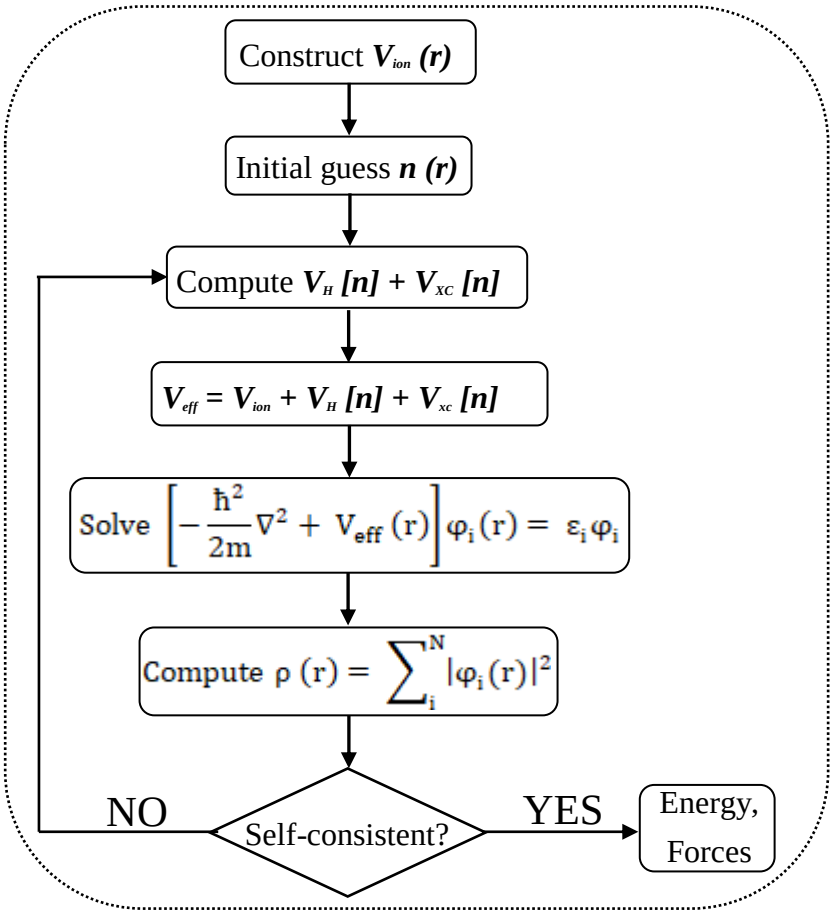

***Appendix 5: An input file (script) for the variable-cell relax calculation.***

```
&CONTROL
calculation   = 'vc-relax'
prefix        = 'CS'
pseudo_dir    = './'
outdir        = './tmp'
/
&SYSTEM
celldm(1)     = 10.48400
celldm(2)     = 1.787734
celldm(3)     = 0.573610
degauss       = 1.00e-02
ecutrho       = 400
ecutwfc       = 50
ibrav         = 8
nat           = 14
ntyp          = 3
occupations   = "smearing"
smearing      = "gaussian"
/
&ELECTRONS
   conv_thr           =  1.00000e-06
   electron_maxstep = 200
   mixing_beta        =  7.00000e-01
   startingpot        = "atomic"
   startingwfc        = "atomic+random"
/
&ions
ion_dynamics        = 'bfgs',
/
&cell
cell_dynamics       = 'bfgs'
press               = 0.0,
press_conv_thr      = 0.5,
/
K_POINTS {automatic}
 5 3 9 0 0 0

ATOMIC_SPECIES
O    15.99940  O.pbesol-n-rrkjus_psl.0.1.UPF
Cd   112.40000  Cd.pbesol-dn-rrkjus_psl.0.2.UPF
Sn   118.69000  Sn.pbesol-dn-rrkjus_psl.0.2.UPF

ATOMIC_POSITIONS {angstrom}
Cd     0.337949      3.279126      1.624684
Cd     5.326820      6.847977      1.624684
Cd     3.170333      1.784426      1.624684
Cd     2.494436      8.342677      1.624684
Sn     0.000000      0.000000      0.000000
Sn     2.832384      5.063552      0.000000
O      0.760654      8.186203      0.000000
O      4.904115      1.940900      0.000000
O      3.593038      7.004451      0.000000
O      2.071731      3.122652      0.000000
O      1.333101      0.394744      1.624684
O      4.331667      9.732359      1.624684
O      4.165486      4.668807      1.624684
O      1.499283      5.458296      1.624684
```

***Appendix 6: Sections of the output of Self Consistent Field calculations, showing the stresses on the cadmium-tin-oxide crystals for the -0.0075 strain. The elastic stiffness constants $c_{22}$, $c_{23}$, $c_{33}$, $c_{44}$, $c_{55}$, and $c_{66}$ are then read from the matrices as shown.***

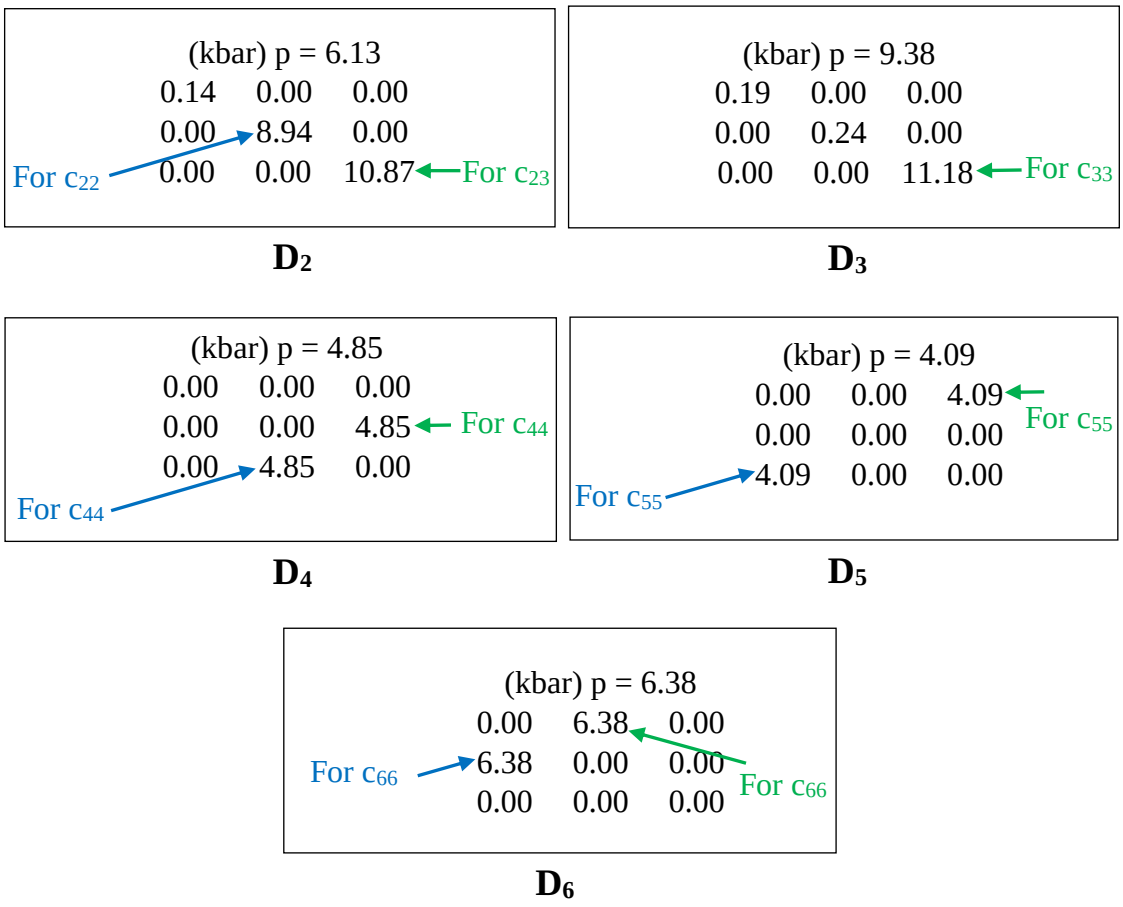

***Appendix 7: The Maple code and the corresponding matrix for the single-glazed glass laminated with the thin film of cadmium-tin-oxide***

```
with(LinearAlgebra): with(plots):

w := (x, t) → A · e^(I·k_p·x·sin(θ)) · e^(−I·ω·t); dt2w := (x) → −A · e^(I·k_p·x·sin(θ)) ω^2;

p_1 := (z, t) → (e^(−I·k_0·(z·cos(θ)−x·sin(θ))) + R · e^(I·k_0·(z·cos(θ)+x·sin(θ)))) · e^(−I·ω·t) · p_i;

dnp_1 := (z) → Ik_0 · (−cos(θ) · e^(−I·k_0·(z·cos(θ)−x·sin(θ))) + R · cos(θ) · e^(I·k_0·(z·cos(θ)+x·sin(θ)))) ·
p_i;

p_t := (z, t) → T · e^(−I·k_0·(z·cos(θ)−x·sin(θ))) · e^(−I·ω·t) · p_i;

dnp_t := (z) → −I · T · k_0 cos(θ) · e^(−I·k_0·(z·cos(θ)−x·sin(θ))) · p_i;

eqn1 := p_1(z, t) − p_t(z, t) = 𝔇 · diff(w(z, t), z$4) + ρ · h ·
diff(w(x, t), t$2); simplify(eqn1);

lhss := (z) → −p_1(−e^(−I·(k_0·z·cos(θ)−k_0 x·sin(θ))) − R · e^(I·(k_0·z·cos(θ)+k_0·x·sin(θ))) + T ·
e^(−I(k_0·z·cos(θ)−k_0·x·sin(θ)));

rhss := (z) → A(𝔇k_p^4 sin(θ)^4 e^(I(k_p x sin(θ))) − ρhω^2 e^(I(k_p x sin(θ))));

eqn := {lhss(0) − rhss(0), −ρ · dt2w(x) = dnp_t(0), dnp_t(0), dnp_1(0) = −ρ · dt2w(x)};

collect{(eqn), (A, R, T)}


AAA := {[ρe^(Ik_p x sin(θ)) ω^2, 0, I · k_0 cos(θ) e^(Ik_p x sin(θ)) · p_i], [ρe^(Ik_p x sin(θ)) ω^2, −I ·
k_0 cos(θ) e^(Ik_p x sin(θ)) · p_i, 0], [(𝔇k_p^4 sin(θ)^4 e^(I(k_p x sin(θ))) −
ρhe^(I(k_p x sin(θ))) ω^2), −p_i e^(I(k_0 x sin(θ))), p_i e^(I(k_0 x sin(θ)))]};

CCC := [0; −Ik_0 cos(θ) e^(I(k_0 x sin(θ))); p_i e^(I(k_0 x sin(θ)))]; res := LinearSolve(AAA, CCC)

collect{((−2ρω^2 + Ik_0 cos(θ)𝔇k_p^4 sin(θ)^4 − Ik_0 cos(θ) M_p ω^2) / (2ρω^2)), (k_0, cos(θ))}
```

$$1 + \frac{1}{2}\frac{\left(-(\theta)\mathfrak{D}k_p^4 \sin(\theta)^4 + M_p\omega^2\right)\cos(\theta)k_0}{\rho\omega^2}; eqn3 := \mathfrak{D}k_p^4 \sin(\theta)^4 = M_p\omega^2$$

$$1 + \frac{IM_p \cos(\theta)\, k_0}{2\rho}\left(1 - \frac{\mathfrak{D}k_p^4 \sin(\theta)^4}{M_p\omega^2}\right); 1 + \frac{IM_p \cos(\theta)\, k_0}{2\rho}\left(1 - \frac{\omega^2\mathfrak{D} \sin(\theta)^4}{M_p c^4}\right); eqn4 := \omega_c$$

$$= 2\pi f_c = sqrt\left(\frac{M_p c^4}{\mathfrak{D} \sin(\theta)^4}\right)$$

***Appendix 8: The Maple code and the corresponding matrix for the double-glazed glass laminated with the thin film of cadmium-tin-oxide***

with(Linear Algebra): with(plots):

$w_1 := (x,t) \to A_1 \cdot e^{I \cdot k_{p1} \cdot x \cdot \sin(\theta)} \cdot e^{-I \cdot \omega \cdot t}$; $dt2w1 := (x) \to -A_1 \cdot e^{I \cdot k_{p1} \cdot x \cdot \sin(\theta)} \omega^2$;

$w_2 := (x,t) \to A_2 \cdot e^{I \cdot k_{p2} \cdot x \cdot \sin(\theta)} \cdot e^{-I \cdot \omega \cdot t}$; $dt2w2 := (x) \to -A_2 \cdot e^{I \cdot k_{p2} \cdot x \cdot \sin(\theta)} \omega^2$;

$w_3 := (x,t) \to A_3 \cdot e^{I \cdot k_{p3} \cdot x \cdot \sin(\theta)} \cdot e^{-I \cdot \omega \cdot t}$; $dt2w3 := (x) \to -A_3 \cdot e^{I \cdot k_{p3} \cdot x \cdot \sin(\theta)} \omega^2$;

$p_1 := (z,t) \to \left(e^{-I \cdot k_0 \cdot (z \cdot \cos(\theta) - x \cdot \sin(\theta))} + R_1 \cdot e^{I \cdot k_0 \cdot (z \cdot \cos(\theta) + x \cdot \sin(\theta))}\right) \cdot e^{-I \cdot \omega \cdot t} \cdot p_i$;

$dnp_1 := (z) \to \left(-Ik_0 \cos(\theta) \cdot e^{-I \cdot k_0 \cdot (z \cdot \cos(\theta) - x \cdot \sin(\theta))} + IR_1 k_0 \cdot \cos(\theta) \cdot e^{I \cdot k_0 \cdot (z \cdot \cos(\theta) + x \cdot \sin(\theta))}\right) \cdot p_i$;

$p_2 := (z,t) \to T_1 \cdot e^{-I \cdot k_0 \cdot (z \cdot \cos(\theta) - x \cdot \sin(\theta))} \cdot e^{-I \cdot \omega \cdot t} p_i + R_2 T_1 \cdot e^{-I \cdot k_0 \cdot (-z \cdot \cos(\theta) - x \cdot \sin(\theta))} \cdot e^{-I \cdot \omega \cdot t} \cdot p_i$;

$dnp_2 := (z) \to -IT_1 k_0 \cos(\theta) \cdot e^{-I \cdot k_0 \cdot (z \cdot \cos(\theta) - x \cdot \sin(\theta))} p_i + IR_2 T_1 k_0 \cdot \cos(\theta) \cdot e^{-I \cdot k_0 \cdot (-z \cdot \cos(\theta) - x \cdot \sin(\theta))} p_i$;

$p_3 := (z,t) \to T_2 \cdot T_1 \cdot e^{-I \cdot k_0 \cdot (z \cdot \cos(\theta) - x \cdot \sin(\theta))} \cdot e^{-I \cdot \omega \cdot t} p_i + R_3 \cdot T_2 \cdot T_1 \cdot e^{-I \cdot k_0 \cdot (-z \cdot \cos(\theta) - x \cdot \sin(\theta))} \cdot e^{-I \cdot \omega \cdot t} \cdot p_i$;

$dnp_3 := (z) \to -IT_2 T_1 k_0 \cos(\theta) \cdot e^{-I \cdot k_0 \cdot (z \cdot \cos(\theta) - x \cdot \sin(\theta))} p_i + IR_3 T_2 T_1 k_0 \cdot \cos(\theta) \cdot e^{-I \cdot k_0 \cdot (-z \cdot \cos(\theta) - x \cdot \sin(\theta))} p_i$;

$p_{t3} := (z,t) \to T_3 \cdot T_2 \cdot T_1 \cdot e^{-I \cdot k_0 \cdot (z \cdot \cos(\theta) - x \cdot \sin(\theta))} \cdot e^{-I \cdot \omega \cdot t} \cdot p_i$;

$dnp_{t3} := (z) \to -I \cdot T_3 \cdot T_2 \cdot T_1 \cdot k_0 \cos(\theta) \cdot e^{-I \cdot k_0 \cdot (z \cdot \cos(\theta) - x \cdot \sin(\theta))} \cdot p_i$;

$deltp1 := (z,t) \to p_1(z,t) - p_2(z + h_1, t)$;

$mvtpl1 := (x,t) \to \mathfrak{D}_1 \cdot \mathrm{diff}(w_1(x,t), x\$4) + \rho_1 h_1 \cdot \mathrm{diff}(w_1(x,t), t\$2)$;

$deltp2 := (z,t) \to p_2(z,t) - p_3(z + h_2, t)$;

$mvtpl2 := (x,t) \to \mathfrak{D}_2 \cdot \mathrm{diff}(w_2(x,t), x\$4) + \rho_2 h_2 \cdot \mathrm{diff}(w_2(x,t), t\$2)$;

$deltp3 := (z,t) \to p_3(z,t) - p_{t3}(z + h_t, t)$;

$mvtpl3 := (x,t) \to \mathfrak{D}_3 \cdot \mathrm{diff}(w_3(x,t), x\$4) + \rho_3 h_3 \cdot \mathrm{diff}(w_3(x,t), t\$2)$;

$$\begin{aligned}\text{eqnbndc} := \{&\text{deltp1}(0,0) = \text{mvtpl1}(x,t), \text{deltp2}(d_1 + h_1, 0)\\ &= \text{mvtpl2}(x,t), \text{deltp3}(d_1 + h_1 + d_2 + h_2, 0) = \text{mvtpl3}(x,t), \text{dnp1}(0)\\ &= -\rho_f \cdot \text{dt2w1}(x), \text{dnp2}(h_1) = -\rho_f \cdot \text{dt2w1}(x), \text{dnp2}(d_1 + h_1)\\ &= -\rho_f \cdot \text{dt2w2}(x), \text{dnp3}(d_1 + h_1 + h_2)\\ &= -\rho_f \cdot \text{dt2w2}(x), \text{dnp3}(d_1 + h_1 + d_2 + h_2)\\ &= -\rho_f \cdot \text{dt2w3}(x), \text{dnp3}(d_1 + h_1 + d_2 + h_2 + h_3) = -\rho_f \text{dt2w3}(x)\};\end{aligned}$$

$$\text{collect}\big((\text{eqnbndc}), A_1, A_2, R_1, T_1, R_2, T_2, R_3, T_3\big)$$

$$\begin{aligned}\text{AAA} := \big[&0, 0, -\rho_f \cdot e^{Ik_{p3} x \sin(\theta)} \omega^2, 0, 0, 0, 0, 0, -I\\ &\cdot k_0 \cos(\theta)\, e^{-Ik_0((d_1+h_1+d_2+h_2+h_3)\cos(\theta) - x\sin(\theta))} p_i\big],\end{aligned}$$

$$\begin{bmatrix} 0, 0, -C \cdot e^{Ik_{p3} x \sin(\theta)}, 0, 0, 0, e^{-Ik_0(d_1+h_1+d_2+h_2)\cos(\theta) - x\sin(\theta)} p_i, \\ e^{-Ik_0(-(d_1+h_1+d_2+h_2)\cos(\theta) - x\sin(\theta)} p_i, e^{-Ik_0((d_1+h_1+d_2+h_2+h_3)\cos(\theta) - x\sin(\theta))} p_i \end{bmatrix},$$

$$\begin{bmatrix} -\rho_f \cdot e^{Ik_{p1} x \sin(\theta)} \omega^2, 0, 0, 0, -Ik_0 \cos(\theta)\, e^{-Ik_0(h_1 \cos(\theta) - x\sin(\theta))} p_i, \\ I \cdot k_0 \cos(\theta)\, e^{-Ik_0(-h_1 \cos(\theta) - x\sin(\theta))} p_i, 0, 0, 0 \end{bmatrix},$$

$$\begin{bmatrix} 0, -\rho_f \cdot e^{Ik_{p2} x \sin(\theta)} \omega^2, 0, 0, Ik_0 \cos(\theta)\, e^{-Ik_0((d_1+h_1)\cos(\theta) - x\sin(\theta))} p_i, \\ I \cdot k_0 \cos(\theta)\, e^{-Ik_0(-(d_1+h_1)\cos(\theta) - x\sin(\theta))} p_i, 0, 0, 0 \end{bmatrix},$$

$$\big[-\rho_f \cdot e^{Ik_{p1} x \sin(\theta)} \omega^2, 0, 0, Ik_0 \cos(\theta)\, e^{Ik_0 x \sin(\theta)} p_i, \quad 0, 0, 0, 0, 0\big],$$

$$\begin{bmatrix} 0, -\rho_f \cdot e^{Ik_{p2} x \sin(\theta)} \omega^2, 0, 0, 0, 0, -Ik_0 \cos(\theta)\, e^{-Ik_0((d_1+h_1+h_2)\cos(\theta) - x\sin(\theta))} p_i, \\ I \cdot k_0 \cos(\theta)\, e^{-Ik_0(-(d_1+h_1+h_2)\cos(\theta) - x\sin(\theta))} p_i, 0 \end{bmatrix},$$

$$\begin{bmatrix} 0, 0, -\rho_f \cdot e^{Ik_{p3} x \sin(\theta)} \omega^2, 0, 0, 0, -Ik_0 \cos(\theta)\, e^{-Ik_0((d_1+h_1+d_2+h_2)\cos(\theta) - x\sin(\theta))} p_i, \\ I \cdot k_0 \cos(\theta)\, e^{-Ik_0(-(d_1+h_1+d_2+h_2)\cos(\theta) - x\sin(\theta))} p_i, 0 \end{bmatrix},$$

$$\begin{bmatrix} 0, -B \cdot e^{Ik_{p2} x \sin(\theta)}, 0, 0, e^{-Ik_0((d_1+h_1)\cos(\theta) - x\sin(\theta))} p_i, \\ e^{-Ik_0((d_1+h_1+h_2)\cos(\theta) - x\sin(\theta))} p_i, -e^{-Ik_0(-(d_1+h_1+h_2)\cos(\theta) - x\sin(\theta))} p_i, 0 \end{bmatrix},$$

$$\begin{bmatrix} -A \cdot e^{Ik_{p1} x \sin(\theta)}, 0, 0, e^{Ik_0 x \sin(\theta)} p_i, -e^{-Ik_0(h_1 \cos(\theta) - x\sin(\theta))} p_i \\ -e^{-Ik_0(-h_1 \cos(\theta) - x\sin(\theta))} p_i, 0, 0, 0 \end{bmatrix},$$

$$CCC := \begin{bmatrix} 0 \\ 0 \\ 0 \\ 0 \\ Ik_0 \cos(\theta)\, e^{Ik_0 \, x \sin(\theta)} p_i \\ 0 \\ 0 \\ 0 \\ e^{Ik_0 \, x \sin(\theta)} p_i \end{bmatrix}$$

$$res := \text{LinearSolve}(AAA, CCC);$$

$$oto := \begin{bmatrix} A_1 \\ A_2 \\ A_3 \\ R_1 \\ T_1 \\ R_2 T_1 \\ T_1 T_2 \\ R_3 T_1 T_2 \\ T_1 T_2 T_3 \end{bmatrix}$$

$$A := \frac{\mathfrak{D}_1 k_{p1}^4 \sin(\theta)^4 - M_1 \cdot \omega^2;\ B := \mathfrak{D}_2 k_{p2}^4 \sin(\theta)^4 - M_2 \cdot \omega^2}{1 - I \cdot (A + 2B) \cos(\theta) \frac{k_0 \omega^2 \rho_f}{2\rho_f^2 \omega^4} - A \cdot B \cdot (1 - e^{-2Ik_0 d \cos(\theta)}) \frac{\cos(\theta)^2 k_0^2}{2\rho_f^2 \omega^4}}$$

$$1 + \frac{1}{2} \frac{\left(-\mathfrak{D} k_p^4 \sin(\theta)^4 + M_p \omega^2\right) \cos(\theta) k_0}{\rho \omega^2};\ eqn3 := \mathfrak{D} \cdot k_p^4 \sin(\theta)^4 = M_p \omega^2$$

$$1 + \frac{IM_p \cos(\theta)\, k_0}{2\rho} \left(1 - \frac{\mathfrak{D} k_p^4 \sin(\theta)^4}{M_p \omega^2}\right);\ 1 + \frac{IM_p \cos(\theta)\, k_0}{2\rho} \left(1 - \frac{\omega^2 \mathfrak{D} \sin(\theta)^4}{M_p c^4}\right);\ eqn4 := \omega_c$$

$$= 2\pi f_c = \text{sqrt}\left(\frac{M_p c^4}{\mathfrak{D} \sin(\theta)^4}\right)$$

## *Appendix 9: The Maple code and the corresponding matrix for the triple-glazed glass laminated with the thin film of cadmium-tin-oxide*

with(Linear Algebra): with(plots):

$w_1 := (x,t) \to A_1 \cdot e^{I \cdot k_{p1} \cdot x \cdot \sin(\theta)} \cdot e^{-I \cdot \omega \cdot t}$; $dt2w1 := (x) \to -A_1 \cdot e^{I \cdot k_{p1} \cdot x \cdot \sin(\theta)} \omega^2$;

$w_2 := (x,t) \to A_2 \cdot e^{I \cdot k_{p2} \cdot x \cdot \sin(\theta)} \cdot e^{-I \cdot \omega \cdot t}$; $dt2w2 := (x) \to -A_2 \cdot e^{I \cdot k_{p2} \cdot x \cdot \sin(\theta)} \omega^2$;

$w_3 := (x,t) \to A_3 \cdot e^{I \cdot k_{p3} \cdot x \cdot \sin(\theta)} \cdot e^{-I \cdot \omega \cdot t}$; $dt2w3 := (x) \to -A_3 \cdot e^{I \cdot k_{p3} \cdot x \cdot \sin(\theta)} \omega^2$;

$p_1 := (z,t) \to \left(e^{-I \cdot k_0 \cdot (z \cdot \cos(\theta) - x \cdot \sin(\theta))} + R_1 \cdot e^{I \cdot k_0 \cdot (z \cdot \cos(\theta) + x \cdot \sin(\theta))}\right) \cdot e^{-I \cdot \omega \cdot t} \cdot p_i$;

$dnp_1 := (z) \to \left(-I k_0 \cos(\theta) \cdot e^{-I \cdot k_0 \cdot (z \cdot \cos(\theta) - x \cdot \sin(\theta))} + I R_1 k_0 \cdot \cos(\theta) \cdot e^{I \cdot k_0 \cdot (z \cdot \cos(\theta) + x \cdot \sin(\theta))}\right) \cdot p_i$;

$p_2 := (z,t) \to T_1 \cdot e^{-I \cdot k_0 \cdot (z \cdot \cos(\theta) - x \cdot \sin(\theta))} \cdot e^{-I \cdot \omega \cdot t} p_i + R_2 T_1 \cdot e^{-I \cdot k_0 \cdot (-z \cdot \cos(\theta) - x \cdot \sin(\theta))} \cdot e^{-I \cdot \omega \cdot t} \cdot p_i$;

$dnp_2 := (z) \to -I T_1 k_0 \cos(\theta) \cdot e^{-I \cdot k_0 \cdot (z \cdot \cos(\theta) - x \cdot \sin(\theta))} p_i + I R_2 T_1 k_0 \cdot \cos(\theta) \cdot e^{-I \cdot k_0 \cdot (-z \cdot \cos(\theta) - x \cdot \sin(\theta))} p_i$;

$p_3 := (z,t) \to T_2 \cdot T_1 \cdot e^{-I \cdot k_0 \cdot (z \cdot \cos(\theta) - x \cdot \sin(\theta))} \cdot e^{-I \cdot \omega \cdot t} p_i + R_3 \cdot T_2 \cdot T_1 \cdot e^{-I \cdot k_0 \cdot (-z \cdot \cos(\theta) - x \cdot \sin(\theta))} \cdot e^{-I \cdot \omega \cdot t} \cdot p_i$;

$dnp_3 := (z) \to -I T_2 T_1 k_0 \cos(\theta) \cdot e^{-I \cdot k_0 \cdot (z \cdot \cos(\theta) - x \cdot \sin(\theta))} p_i + I R_3 T_2 T_1 k_0 \cdot \cos(\theta) \cdot e^{-I \cdot k_0 \cdot (-z \cdot \cos(\theta) - x \cdot \sin(\theta))} p_i$;

$p_{t3} := (z,t) \to T_3 \cdot T_2 \cdot T_1 \cdot e^{-I \cdot k_0 \cdot (z \cdot \cos(\theta) - x \cdot \sin(\theta))} \cdot e^{-I \cdot \omega \cdot t} \cdot p_i$;

$dnp_{t3} := (z) \to -I \cdot T_3 \cdot T_2 \cdot T_1 \cdot k_0 \cos(\theta) \cdot e^{-I \cdot k_0 \cdot (z \cdot \cos(\theta) - x \cdot \sin(\theta))} \cdot p_i$;

$deltp1 := (z,t) \to p_1(z,t) - p_2(z + h_1, t)$;

$mvtpl1 := (x,t) \to \mathfrak{D}_1 \cdot \mathrm{diff}(w_1(x,t), x\$4) + \rho_1 h_1 \cdot \mathrm{diff}(w_1(x,t), t\$2)$;

$deltp2 := (z,t) \to p_2(z,t) - p_3(z + h_2, t)$;

$mvtpl2 := (x,t) \to \mathfrak{D}_2 \cdot \mathrm{diff}(w_2(x,t), x\$4) + \rho_2 h_2 \cdot \mathrm{diff}(w_2(x,t), t\$2)$;

$deltp3 := (z,t) \to p_3(z,t) - p_{t3}(z + h_t, t)$;

$$\text{mvtpl3} := (x,t) \to \mathfrak{D}_3 \cdot \text{diff}(w_3(x,t), x\$4) + \rho_3 h_3 \cdot \text{diff}(w_3(x,t), t\$2);$$

$$\begin{aligned}\text{eqnbndc} := \{&\text{deltp1}(0,0) = \text{mvtpl1}(x,t), \text{deltp2}(d_1 + h_1, 0)\\ &= \text{mvtpl2}(x,t), \text{deltp3}(d_1 + h_1 + d_2 + h_2, 0) = \text{mvtpl3}(x,t), \text{dnp1}(0)\\ &= -\rho_f \cdot \text{dt2w1}(x), \text{dnp2}(h_1) = -\rho_f \cdot \text{dt2w1}(x), \text{dnp2}(d_1 + h_1)\\ &= -\rho_f \cdot \text{dt2w2}(x), \text{dnp3}(d_1 + h_1 + h_2)\\ &= -\rho_f \cdot \text{dt2w2}(x), \text{dnp3}(d_1 + h_1 + d_2 + h_2)\\ &= -\rho_f \cdot \text{dt2w3}(x), \text{dnp3}(d_1 + h_1 + d_2 + h_2 + h_3) = -\rho_f \text{dt2w3}(x)\};\end{aligned}$$

$$\text{collect}\big((\text{eqnbndc}), A_1, A_2, R_1, T_1, R_2, T_2, R_3, T_3\big)$$

$$\begin{aligned}\text{AAA} := \big[&0, 0, -\rho_f \cdot e^{I k_{p3} x \sin(\theta)} \omega^2, 0, 0, 0, 0, 0,\\ &-I \cdot k_0 \cos(\theta)\, e^{-I k_0 ((d_1+h_1+d_2+h_2+h_3)\cos(\theta) - x\sin(\theta))} p_i\big],\end{aligned}$$

$$\begin{bmatrix} 0, 0, -C \cdot e^{I k_{p3} x \sin(\theta)}, 0, 0, 0, e^{-I k_0 (d_1+h_1+d_2+h_2)\cos(\theta) - x\sin(\theta)} p_i, \\ e^{-I k_0 (-(d_1+h_1+d_2+h_2)\cos(\theta) - x\sin(\theta)} p_i, e^{-I k_0 ((d_1+h_1+d_2+h_2+h_3)\cos(\theta) - x\sin(\theta))} p_i \end{bmatrix},$$

$$\begin{bmatrix} -\rho_f \cdot e^{I k_{p1} x \sin(\theta)} \omega^2, 0, 0, 0, -I k_0 \cos(\theta)\, e^{-I k_0 (h_1 \cos(\theta) - x\sin(\theta))} p_i, \\ I \cdot k_0 \cos(\theta)\, e^{-I k_0 (-h_1 \cos(\theta) - x\sin(\theta))} p_i, 0, 0, 0 \end{bmatrix},$$

$$\begin{bmatrix} 0, -\rho_f \cdot e^{I k_{p2} x \sin(\theta)} \omega^2, 0, 0, -I k_0 \cos(\theta)\, e^{-I k_0 ((d_1+h_1)\cos(\theta) - x\sin(\theta))} p_i, \\ I \cdot k_0 \cos(\theta)\, e^{-I k_0 (-(d_1+h_1)\cos(\theta) - x\sin(\theta))} p_i, 0, 0, 0 \end{bmatrix},$$

$$\big[-\rho_f \cdot e^{I k_{p1} x \sin(\theta)} \omega^2, 0, 0, I k_0 \cos(\theta)\, e^{I k_0 x \sin(\theta)} p_i, \quad 0, 0, 0, 0, 0\big],$$

$$\begin{bmatrix} 0, -\rho_f \cdot e^{I k_{p2} x \sin(\theta)} \omega^2, 0, 0, 0, 0, -I k_0 \cos(\theta)\, e^{-I k_0 ((d_1+h_1+h_2)\cos(\theta) - x\sin(\theta))} p_i, \\ I \cdot k_0 \cos(\theta)\, e^{-I k_0 (-(d_1+h_1+h_2)\cos(\theta) - x\sin(\theta))} p_i, 0 \end{bmatrix},$$

$$\begin{bmatrix} 0, 0, -\rho_f \cdot e^{I k_{p3} x \sin(\theta)} \omega^2, 0, 0, 0, -I k_0 \cos(\theta)\, e^{-I k_0 ((d_1+h_1+d_2+h_2)\cos(\theta) - x\sin(\theta))} p_i, \\ I \cdot k_0 \cos(\theta)\, e^{-I k_0 (-(d_1+h_1+d_2+h_2)\cos(\theta) - x\sin(\theta))} p_i, 0 \end{bmatrix},$$

$$\begin{bmatrix} 0, -B \cdot e^{I k_{p2} x \sin(\theta)}, 0, 0, e^{-I k_0 ((d_1+h_1)\cos(\theta) - x\sin(\theta))} p_i, \\ e^{-I k_0 ((d_1+h_1+h_2)\cos(\theta) - x\sin(\theta))} p_i, -e^{-I k_0 (-(d_1+h_1+h_2)\cos(\theta) - x\sin(\theta))} p_i, 0 \end{bmatrix},$$

$$\begin{bmatrix} -A \cdot e^{I k_{p1} x \sin(\theta)}, 0, 0, e^{I k_0 x \sin(\theta)} p_i, -e^{-I k_0 (h_1 \cos(\theta) - x\sin(\theta))} p_i \\ -e^{-I k_0 (-h_1 \cos(\theta) - x\sin(\theta))} p_i, 0, 0, 0 \end{bmatrix},$$

$$CCC := \begin{bmatrix} 0 \\ 0 \\ 0 \\ 0 \\ Ik_0 \cos(\theta)\, e^{Ik_0\, x \sin(\theta)} p_i \\ 0 \\ 0 \\ 0 \\ -e^{Ik_0\, x \sin(\theta)} p_i \end{bmatrix}$$

$$res := \text{LinearSolve}(AAA, CCC);$$

$$oto := \begin{bmatrix} A_1 \\ A_2 \\ A_3 \\ R_1 \\ T_1 \\ R_2 T_1 \\ T_1 T_2 \\ R_3 T_1 T_2 \\ T_1 T_2 T_3 \end{bmatrix}$$

$$A := \frac{\mathfrak{D}_1 k_{p1}^4 \sin(\theta)^4 - M_1 \cdot \omega^2;\ B := \mathfrak{D}_2 k_{p2}^4 \sin(\theta)^4 - M_2 \cdot \omega^2}{1 - I \cdot (A + 2B) \cos(\theta) \frac{k_0 \omega^2 \rho_f}{2\rho_f^2 \omega^4} - A \cdot B \cdot (1 - e^{-2Ik_0 d \cos(\theta)}) \frac{\cos(\theta)^2 k_0^2}{2\rho_f^2 \omega^4}}$$

$$1 + \frac{1}{2} \frac{\left(-\mathfrak{D} k_p^4 \sin(\theta)^4 + M_p \omega^2\right) \cos(\theta) k_0}{\rho \omega^2};\ eqn3 := \mathfrak{D} \cdot k_p^4 \sin(\theta)^4 = M_p \omega^2$$

$$1 + \frac{IM_p \cos(\theta)\, k_0}{2\rho} \left(1 - \frac{\mathfrak{D} k_p^4 \sin(\theta)^4}{M_p \omega^2}\right);\ 1 + \frac{IM_p \cos(\theta)\, k_0}{2\rho} \left(1 - \frac{\omega^2 \mathfrak{D} \sin(\theta)^4}{M_p c^4}\right);\ eqn4 := \omega_c$$

$$= 2\pi f_c = \text{sqrt}\left(\frac{M_p c^4}{\mathfrak{D} \sin(\theta)^4}\right)$$

*Appendix 10a: 2-Dimensional directional Young's moduli of the cadmium-tin-oxide samples along the {1 0 0} direction. (a) CTO 1, (b) CTO 2, (c) CTO 3, and (d) CTO 5.*

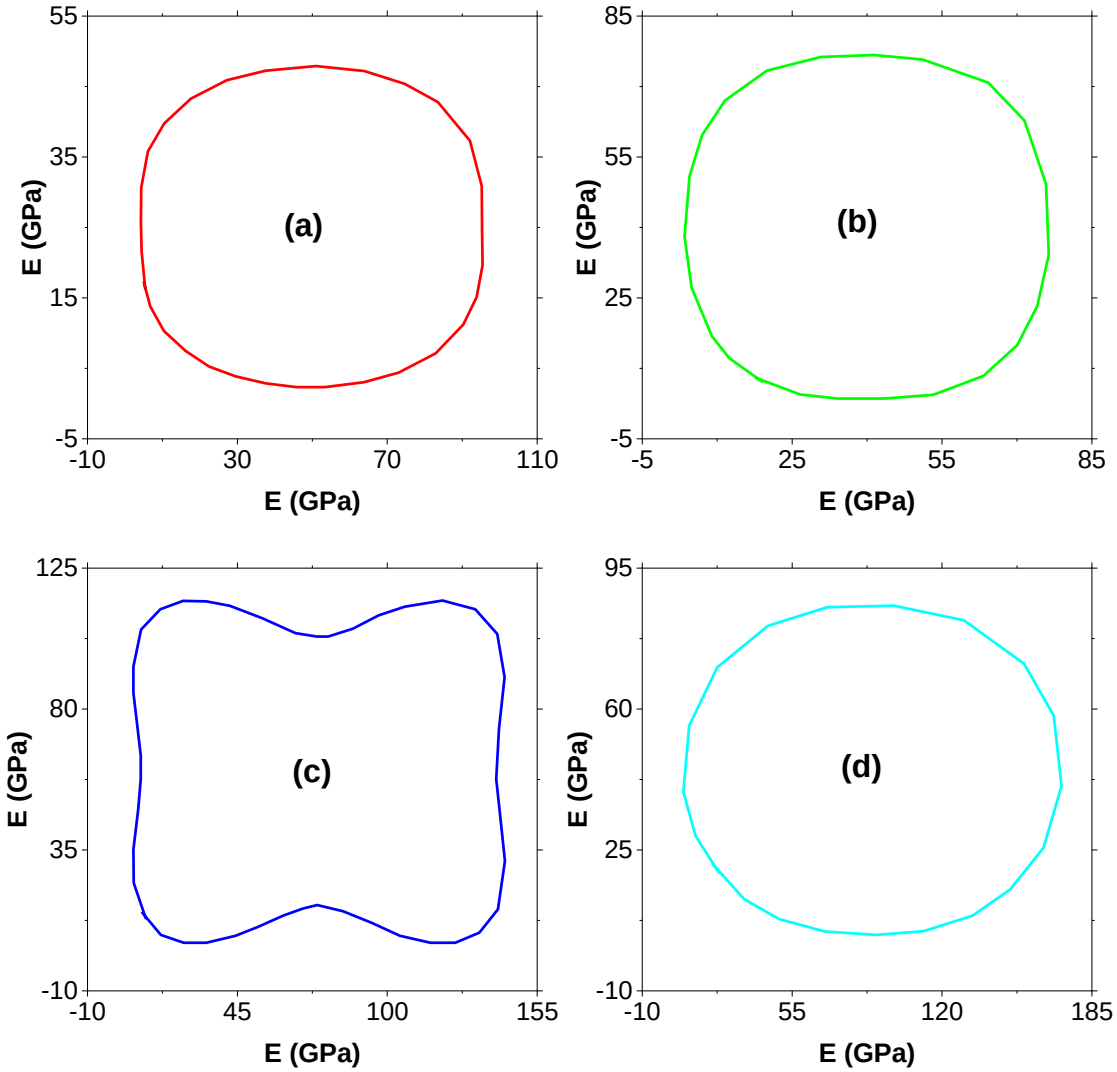

*Appendix 10b: 2-Dimensional directional Young's moduli of the cadmium-tin-oxide samples along the {1 1 0} direction. (a) CTO 1, (b) CTO 2, (c) CTO 3, and (d) CTO 5.*

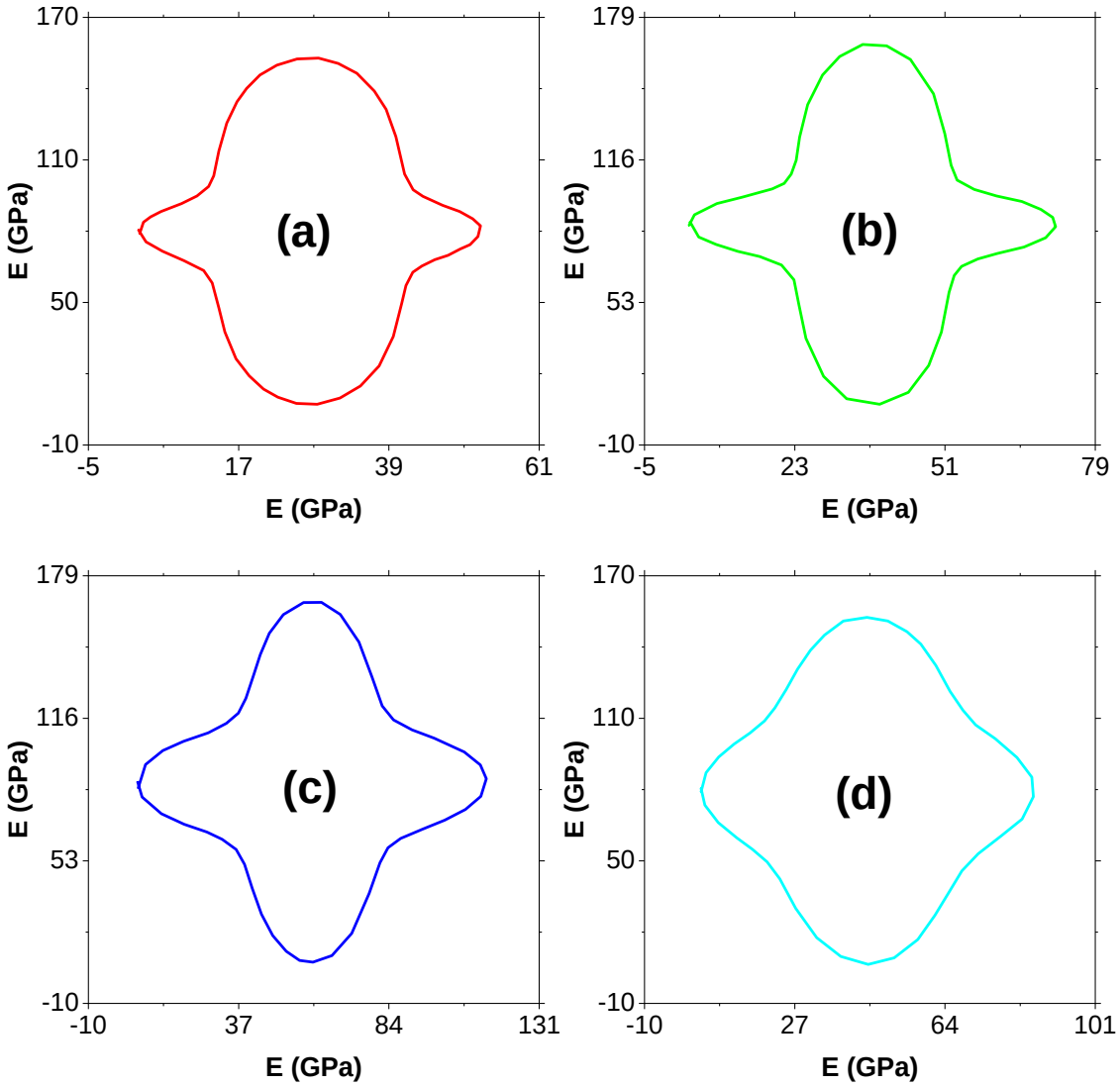

***Appendix 10c: 3-Dimenisonal directional Young's moduli of the cadmium-tin-oxide samples: (a) CTO 1, (b) CTO 2, (c) CTO 3, and (d) CTO 5***

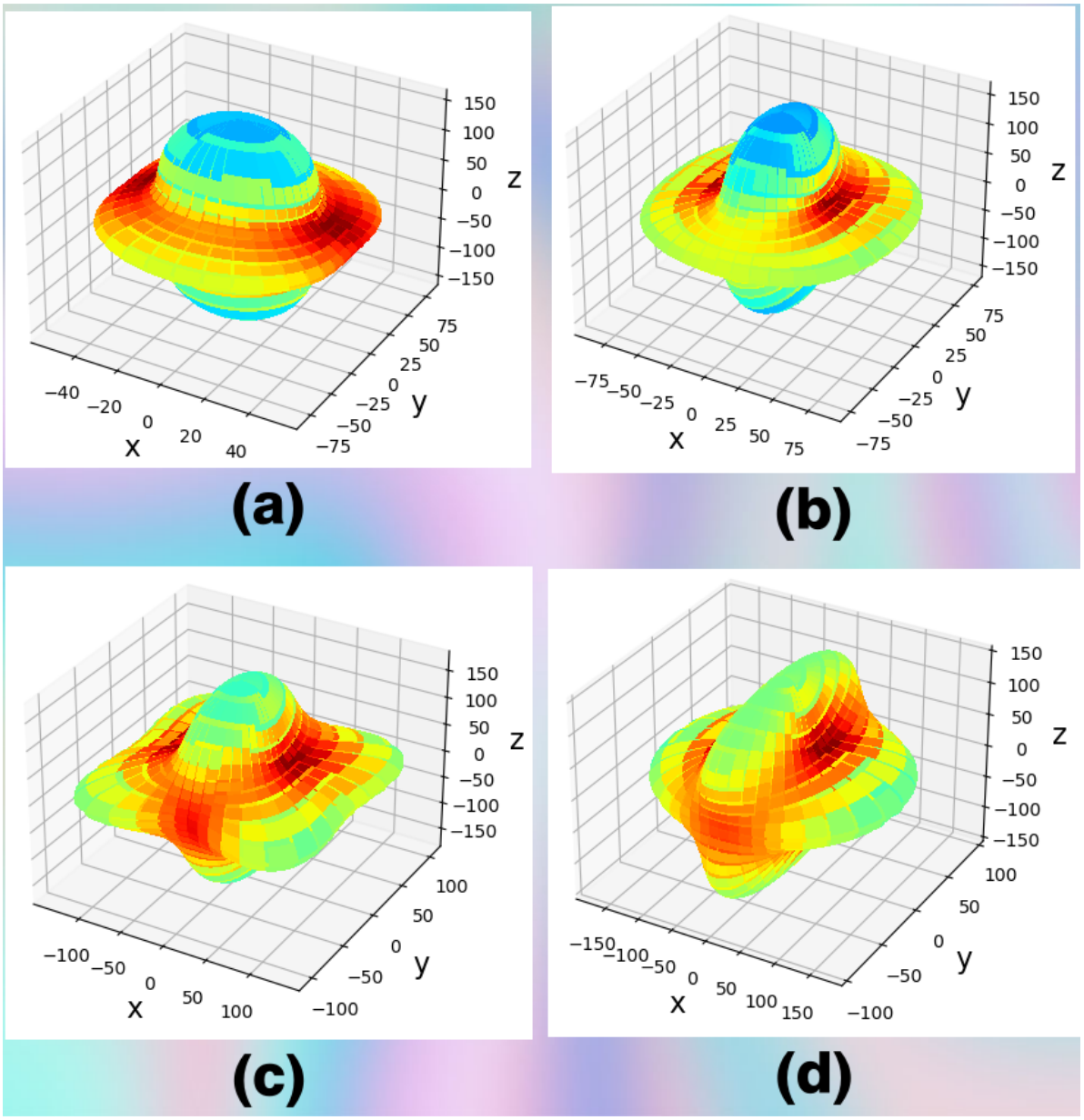

***Appendix 11: Publications***

**Arising from this thesis**

1. **Ongwen, N**. Ogam, E. Fellah, Z.E.A. Otunga, H. Oduor, A. & Mageto, M. *Accurate Ab-initio calculation of elastic constants of anisotropic binary alloys: A case of Fe–Al*, ***Solid State Communications (Elsevier)***, Volume **353**, 114879(1-6). https://doi.org/10.1016/j.ssc.2022.114879.
2. **Ongwen, N**. Ogam, E. Otunga, H. Oduor, A. Z. E. A. Fellah & Mageto M. *Temperature-Dependent Elastic Constants of Substrates for Manufacture of Mems Devices*, ***Kabarak Journal of Research & Innovation***, Volume **12** (1), 30-35, 2022. http://ojs.kabarak.ac.ke/index.php/kjri/article/view/524.
3. **Ongwen, N**., Chanbi, D. Ogam, E. Otunga, H. Oduor, A. & Z. E. A. Fellah, *Microstructural and Elastic Properties of Stable Aluminium-rich TiAl and $TiAl_2$ Formed Phase Intermetallics*, ***Materials Letters (Elsevier),*** Volume **287**, 129295 (1-4), 2021. https://doi.org/10.1016/j.matlet.2020.129295.
4. **Ongwen, N**., Ogam, E & Otunga, H. (2020). *Ab initio study of elastic properties of cadmium stannate as a substrate for the manufacture of MEMS devices*, ***Materials Today Communications (Elsevier),*** Volume **26** (101822), 2021. https://doi.org/10.1016/j.mtcomm.2020.101822.

**Others**

1. Bouchendouka, A., Fellah, Z. E. A., Larbi, Z., **Ongwen, N. O**., Ogam, E., Fellah, M., & Depollier, C. *Flow of a Self-Similar Non-Newtonian Fluid Using Fractal Dimensions*, ***Fractal and Fractional (MDPI)***, Volume **6** (582), 1-11, 2022. https://doi.org/10.3390/fractalfract6100582.
2. Benmorsli, D., Fellah, Z. E. A., Belgroune, D., Ongwen, N. O., Ogam, E., Depollier, C., & Fellah, M. *Transient Propagation of Longitudinal and Transverse Waves in Cancellous Bone: Application of Biot Theory and Fractional Calculus*, ***Symmetry (MDPI)***, Volume **14** (10), 1-29, 2022. https://doi.org/10.3390/sym14101971.
3. Fellah, Z. E. A., Fellah, M., Ronsen, R., **Ongwen, N.,** Ogam, E., & Depollier, C. *Transient Propagation of Spherical Waves in Porous Material: Application to Fractal Calculus*, ***Symmetry (MDPI)***, Volume **14** (233), 1-12, 2022. https://doi.org/10.3390/sym14020233.
4. Fellah, Z. E. A., Ronsen, R., **Ongwen, N.,** Ogam, E., Fellah, M. & Depollier, C. *Influence of Higher Order Viscous and Thermal Effects on an Ultrasonic Wave Reflected from the First Interface of a Porous Material*, ***Materials (MDPI)***, Volume **15** (3), 1-15, 2022. https://doi.org/10.3390/ma15030798.
5. Fellah, Z.E.A., Fellah, M., **Ongwen, N.,** Ogam, E. & Depollier, C. *Acoustics of Fractal Porous Material and Fractional Calculus*, ***Mathematics (MDPI)***, Volume **9** (15) (1-16), 2021. https://doi.org/10.3390/math9151774.
6. Ogam, E., Fellah, Z.E.A., Ogam, G., **Ongwen, N.** & Oduor, A., *Investigation of Long Acoustic Waveguides for the Very Low Frequency Characterization of Monolayer and Stratified Poroelastic Materials*, ***Applied Acoustics (Elsevier)***, Volume **182**, 108200 (1-13), 2021. https://doi.org/10.1016/j.apacoust.2021.108200.